GRID MODERNIZATION LABORATORY CONSORTIUM
U.S. Department of Energy

MODELS AND METHODS FOR ASSESSING THE VALUE OF HVDC AND MVDC TECHNOLOGIES IN MODERN POWER GRIDS

Annual Report

September 2019

ORNL[1]: S Debnath, M Chinthavali, J Sun, P Marthi, S Chinthavali, M Lee
PNNL[2]: MA Elizondo, YV Makarov, Q Huang, M Vallem, Y Liu, AA Tbaileh, Q Zhang, N Samaan, H Kirkham
NREL[3]: J Novacheck, J Lau

[1] Oak Ridge National Laboratory
[2] Pacific Northwest National Laboratory
[3] National Renewable Energy Laboratory

Models and Methods for Assessing the Value of HVDC and MVDC Technologies in Modern Power Grids

Annual Report

ORNL[1]: S Debnath, M Chinthavali, J Sun, P Marthi, S Chinthavali, M Lee
PNNL[2]: MA Elizondo, YV Makarov, Q Huang, M Vallem, Y Liu, AA Tbaileh, Q Zhang, N Samaan, H Kirkham
NREL[3]: J Novacheck, J Lau

September 2019

[1] Oak Ridge National Laboratory
[2] Pacific Northwest National Laboratory
[3] National Renewable Energy Laboratory

Executive Summary

Evolution of today's predominantly alternating current (ac) transmission grid in to mixed ac transmission – high-voltage direct current (HVdc) systems is expected with the decreasing costs of and advancements in power electronics technologies. The recent technological advancements include the development of more efficient and compact voltage source converters (VSCs) that can provide fast response. Because of their controllability and fast response, HVdc systems provide the ability to enhance reliability of the ac transmission grid through frequency support, voltage control, and congestion relief. The HVdc systems can also provide other ancillary services to enhance the economics and reliability of the ac transmission grids, and to optimize their performance. The tools, models, and methods developed to evaluate their benefits will be key enablers to understanding the value proposition introduced by the fast-acting HVdc systems.

The main motivation of this work was to develop models and methods to explore and quantify the technical and economic benefits of HVdc systems and fast response VSC technologies in the future grid of United States. The models and methods explore the benefits of HVdc systems through provision of controlled active/reactive power and fast response. The fast response can provide much-needed multi-objective services to the grid (e.g., frequency response, voltage control) while moving blocks of energy. The models and methods can be applied to study other power electronics technologies and scenarios such as those undertaken in ongoing studies led by the North American Electric Reliability Corporation (NERC) Inverter-based Resource Performance Task Force (IRPTF). The IRPTF studies identify the problems associated with power electronics-based technologies as they are integrated into the bulk power system (or the ac transmission system).

Objectives

The main objective of this work included the following:

1. Develop high-fidelity dynamic models of VSCs to enable the study of the fast control response that they can provide. The models that were developed enable planners to make informed choices of the required HVdc technologies (e.g., line-commuted converter [LCC], VSCs) in the future grid expansion using HVdc systems.
2. Include other HVdc control algorithms such as the voltage control algorithm that is feasible due to the introduction of fast-acting and controllable VSCs, in addition to the developments by Makarov et al. (2017). Evaluate the multi-objective control algorithms using the high-fidelity models of VSCs and hybrid simulation of HVdc–ac transmission grid dynamics. The evaluation methods that were developed can be used to identify the improved performance of the ac transmission grid due to the presence of the fast-acting VSCs. The methods can be applied to assess the impact of other fast-acting power electronics technologies on the grid, such as those being evaluated in the NERC-led IRPTF studies.
3. Develop up to seven-terminal multiterminal dc (MTdc) system models with multiple points of injection in asynchronous ac transmission grids based on high-fidelity models of VSCs. Develop multi-objective control methods such as the multiple point-of-injection fast frequency support and voltage control in the MTdc systems. The methods that were developed provide enhanced reliability services that increase the value of MTdc systems and can be applied to future dc technologies and systems.

4. Develop and evaluate different scenarios of HVdc system penetrations in the future grid, thus facilitating the comparison of their benefits. Evaluate technical benefits for frequency and congestion management of several HVdc lines over a continental-level North American power grid model based on utility industry models.
5. Develop advanced models to address computational challenges of high-fidelity models when models need to expand over a large geographic area, such as HVdc Macrogrids. Create two types of modeling approaches: (a) develop reduced, lumped models able to capture voltage behavior near HVdc terminals and (b) configure advanced hybrid co-simulation between high-fidelity, electromagnetic transient models for HVdc and lower-fidelity electromechanical transient models for the continental-level grid.
6. Evaluate economic benefits associated with fast-acting and controllable HVdc systems. The methods applied to identify economic benefits can be extended to identify the benefits of providing fast reliability services in the grid by power electronics technologies or other technologies.

Value proposition

The value proposition of this project includes the following:

1. Enable decision-makers, planners, and investors to make better-informed decisions regarding the HVdc systems as an important grid development option. These decisions usually concern major investments and require multiple analyses of the benefits that can be provided. The analyses carried out in previous studies did not include the technical and economic benefits offered by advanced control methods in VSC-HVdc configurations that connect Eastern Interconnection (EI), Western Interconnection (WI), and Electric Reliability Council of Texas (ERCOT) grids. This project has demonstrated the benefits of these advanced control methods in VSC-HVdc configurations, and different penetrations and configurations of HVdc systems (such as the MTdc systems).
2. Quantify the fidelity requirements of HVdc system – ac transmission grid models as advanced fast control methods are integrated in to VSCs that may further enhance the reliability and reduce operating reserve margins. In this process, the following questions are answered:
    a) Why do we need higher-fidelity models of VSCs? What are the implications of high-bandwidth control methods? What are the trade-offs in speed vs. fidelity? The faster control methods applied to the high-fidelity models of VSC-HVdc technologies exploit the capabilities of the hardware to a greater extent than the conservative slower control methods. The conservative slower control methods can be applied to the lower-fidelity models. These methods have been shown to reduce the benefits that can be extracted from the HVdc system–ac transmission grid. For example, lesser frequency reserves may be shared across interconnections if the slower control methods are utilized, reducing the associated economic benefits.
    b) Why do we need simulation algorithms that speed up the simulation of higher-fidelity models? The simulation of higher-fidelity models takes much longer than today's existing planning models that use lower-fidelity models. This limits the acceptance of the higher-fidelity models. Hence, speedup of the simulation of high-fidelity models is critical for their acceptance in the industry.
3. Identify the methods to evaluate the fast control methods in VSCs. The following questions were answered in this analysis:
    a) How do we perform hybrid simulation of the higher-fidelity models of HVdc systems with the traditional high-fidelity models of the ac transmission grid to identify the impact of the reliability services that can be provided by VSCs? The reliability services provided are based on the multi-objective control methods to provide frequency and voltage support. The traditional high-fidelity

models of the ac transmission grid are in transient stability simulators (e.g., PSS®E), and the higher-fidelity models are developed in an electromagnetic transient (EMT) simulator (e.g., PSCAD). Three tools have been identified to perform hybrid simulation: PSCAD, E-Tran, and PSS®E. The limitations identified in this work that are associated with performing hybrid simulations have been identified with methods proposed to overcome the limitations.

b) What are the alternatives to hybrid simulation to evaluate the performance of the fast control methods like frequency and voltage support provided by VSCs? Methods to develop an equivalent ac transmission grid model in an EMT simulator that adequately represent frequency and voltage dynamics have been identified. The developed models can then be simulated with the higher-fidelity models of VSCs in one simulator (e.g., PSCAD). The equivalent ac transmission grid models that are required for simulation of the complete grid model in an EMT simulator are extremely expensive (in computational costs and time taken to simulate).

4. Research multiple objectives that can be achieved with advanced HVdc configurations (e.g., VSC-HVdc, MTdc systems) and legacy HVdc systems (e.g., line-commuted converter–LCC HVdc systems), answering the following questions:

   a) Can VSC-HVdc systems provide adequate voltage support? What are gaps in such analysis? In this work, it was identified that VSC-HVdc systems can provide adequate voltage support to improve the reliability of the existing grid, especially the fast response requirements under fault circumstances. The load models in traditional ac transmission grid models need to be updated to accurately represent fault-induced delayed voltage recovery (FIDVR) issues.

   b) How do we control a radial MTdc system with multiple points of injection into an asynchronous ac grid to provide ancillary services? Optimal control methods to provide fast frequency support across multiple points of injection in different asynchronous ac grids (EI, WI, and ERCOT) have been developed in this work.

   c) How do we provide simultaneous frequency and congestion relief? A combined decentralized and centralized control strategy has been developed in this work to address the same and show the feasibility of the method.

5. Evaluate economic benefits associated with providing reliability services such as fast frequency support. Essentially, identify methods to evaluate the impact of fast control methods using high-fidelity models on the ac transmission grid and the associated economic benefits.

Approach and Outcomes

The overview of the approach and the corresponding outcomes in this project is provided below:

1. A suite of high-fidelity EMT dynamic models of three multilevel VSCs with up to 10,000 states and the required simulation algorithms was developed. The three multilevel VSCs include an alternate-arm converter (AAC), a cascaded two-level converter (CTL), and a modular multilevel converter (MMC). The MMC dynamic model was developed by Makarov et al. (2017). The multilevel converters are shown in Fig. Ex-1. The simulation algorithms applied include the following characteristics:
   a. A numerical stiffness-based separation of states is applied, as shown in Fig. Ex-2. The simulation of the dynamics of capacitor voltages are separated from those of the inductor currents in AACs and CTLs.
   b. A hybrid discretization algorithm is applied to the separated states. This algorithm reduces the matrix inversion requirements. The reduced matrix inversion requirements reduce the computational burden associated with applying homogeneous algorithms to all the states.

c. Multi-rate algorithms are applied to the simulation of states in the CTL. The switching frequency of individual switches in the CTL are higher than the corresponding switches in the AAC or MMC. The higher switching frequency affects the dynamics of the capacitor voltages. The multi-rate algorithms further reduce the computational burden imposed as compared to the homogeneous time-step algorithms applied to all states.

A speedup of up to 12× was observed with these algorithms. The models and algorithms developed to simulate AACs and CTLs have been compared with the simulation in traditional simulators. An error of less than 1% was observed with one of the comparison studies shown in Fig. Ex-3. Further speedup may be achieved through temporal parallelization (of up to *N* times with *N* available cores). The speedup is necessitated due to the very long time (on the order of days) taken to simulate the high-fidelity models of large power electronic systems.

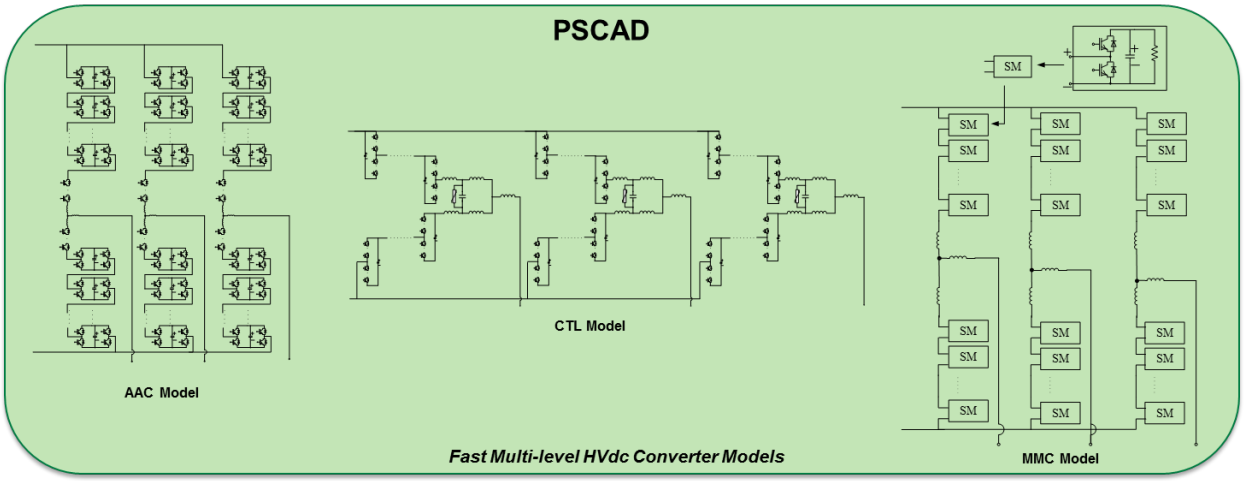

Figure Ex-1: Suite of VSC models available in the PSCAD EMT simulator. SM: submodule.

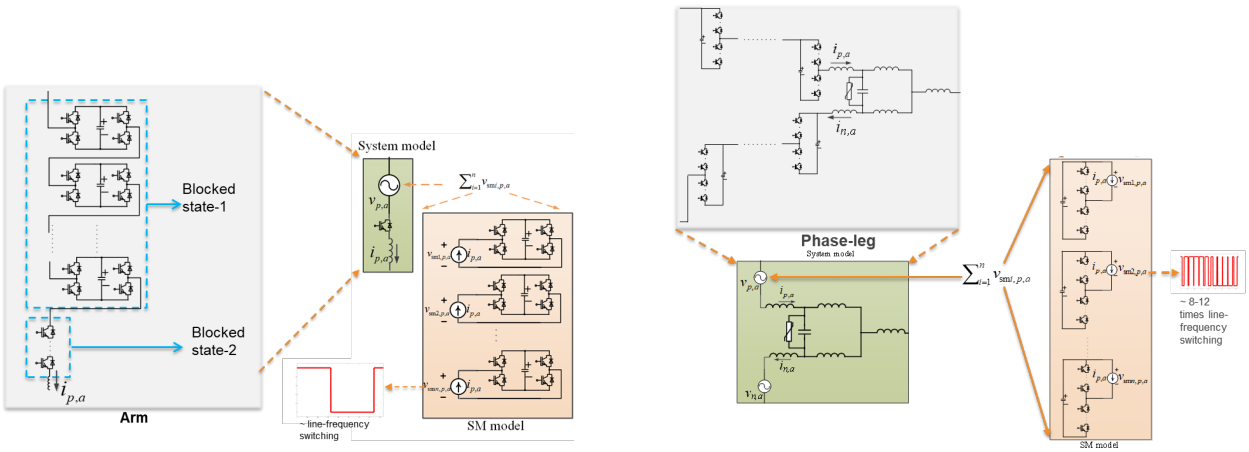

(a) (b)

Figure Ex-2: Simulation algorithm applied to speed-up the simulation of (a) AACs and (b) CTLs.

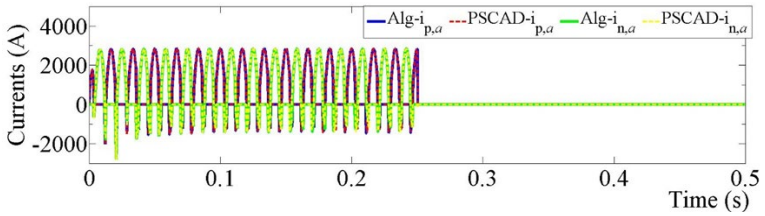

Figure Ex-3: Simulation of AAC-HVdc under blocked scenario.

2. The simulation tools and fidelity of models required to study fast control methods in VSCs (e.g., voltage control) and their effect on ac transmission grids were established through the scenario shown in Fig. Ex-4. The chosen scenario was based on the replacement of one of the point-to-point LCC-HVdc systems from the HVdc macrogrid described by Makarov et al. (2017) by a point-to-point VSC-HVdc system. The location chosen for the VSC-HVdc system was based on the strength of ac transmission grid and the previous study completed by Midcontinent Independent System Operator (MISO) (MISO 2014). The VSC considered in this scenario is an MMC.

   The use cases to evaluate the fast voltage control methods in VSCs were transmission line faults and tripping of shunt compensators and generators. The following requirements were identified (and summarized in Fig. Ex-4) to accurately capture the impact of fast control methods in VSCs on the ac transmission grids during the defined use cases:

   a. High-fidelity EMT dynamic models of VSC-HVdc systems with their fast control methods (e.g., the voltage control method developed in this study).
   b. EMT dynamic models of buffer zones. The buffer zones are regions near the VSC-HVdc terminals. They are extracted from the transient stability (TS) dynamic model of the ac transmission grid. The extraction uses a sensitivity-based method through injection of reactive power at the VSC-HVdc terminals.
   c. A distributed line model of transmission lines in the EMT dynamic models of the buffer zones and VSC-HVdc systems. The characteristics of the distributed line model with respect to the lumped line model are highlighted in Fig. Ex-4 in the “Transmission Line Fidelity” plot. The plot indicates the differences observed in the characteristics at higher frequencies that correspond to the bandwidth of the fast control methods.
   d. Hybrid simulation of EMT-TS models that include the TS dynamic model of the rest of the ac transmission grids and the EMT dynamic models mentioned in points a-c above.

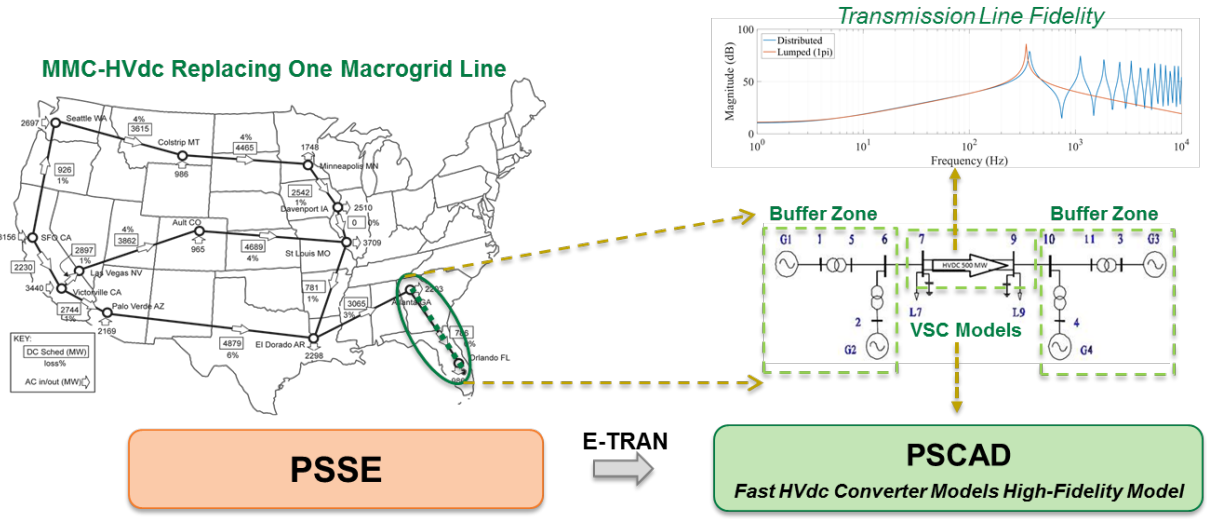

Figure Ex-4: Hybrid simulation framework to simulate VSC-line commuted converter (LCC) HVdc macrogrid as the VSC provides voltage control.

In this study, the EMT dynamic models were developed in PSCAD, the TS dynamic models were based in PSS®E, and the hybrid simulation of EMT-TS models was facilitated using E-Tran. The TS dynamic models were converted to EMT dynamic models using E-Tran. The conversion is required to extract buffer zone models.

The following tests were performed to evaluate the necessity of the requirements identified above:

a. **Evaluate Lower-fidelity Model of VSCs**: Multi-rate simulation methods were applied to the high-fidelity EMT dynamic models of VSC-HVdc system. The VSC considered in this study was the MMC. The multi-rate simulation of MMCs reduced the fidelity of the model. The lower fidelity was due to the lower sampling rate of the external measured signals in the multi-rate simulation of MMCs. The multi-rate simulation methods reduced the imposed computational burden. The comparison of the states observed is performed with the high-fidelity model of VSCs (that is, MMCs in this case). The corresponding results are shown in Fig. Ex-5, which highlights the instability observed in the VSC-HVdc control system when simulated with a lower-fidelity model. The instability was observed in the reactive power, as shown in Fig. Ex-5. The instability is not observed with a high-fidelity model of VSCs.

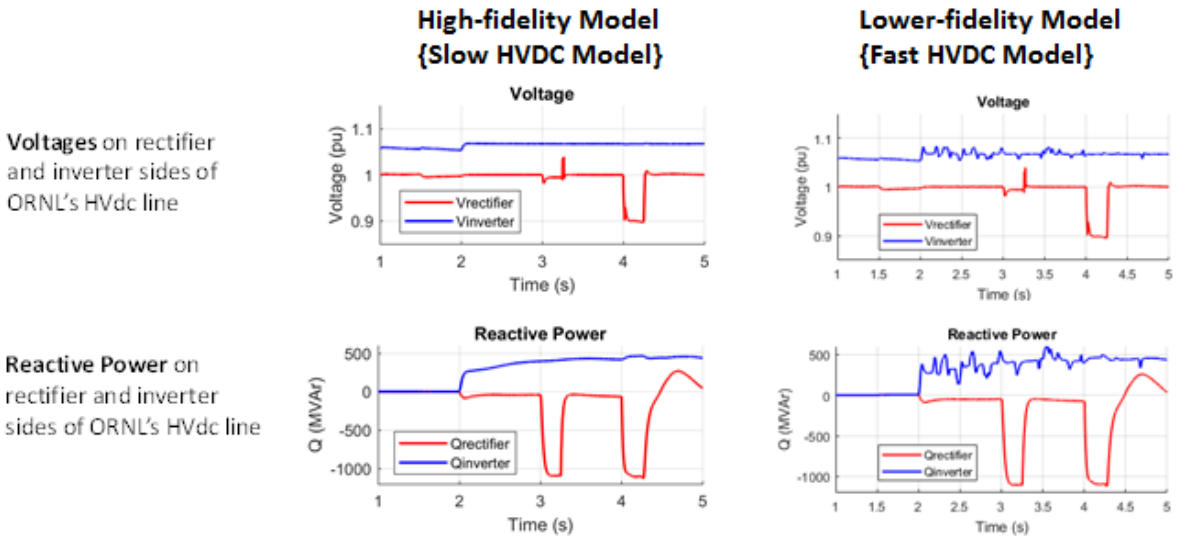

Figure Ex-5: Comparison of states observed in simulation of high and lower fidelity models of MMCs.

b. **Buffer Zone Size Reduction**: Size of the buffer zone was varied in hybrid simulations to identify the sensitivity to the size of buffer zones. A comparison between the states observed in hybrid simulation of the systems with a small buffer zone and with a large buffer zone was performed, and the corresponding results are shown in Fig. Ex-6. The results indicate that variations are observed in the dynamics of the VSC-HVdc control system, as highlighted in Fig. Ex-6.

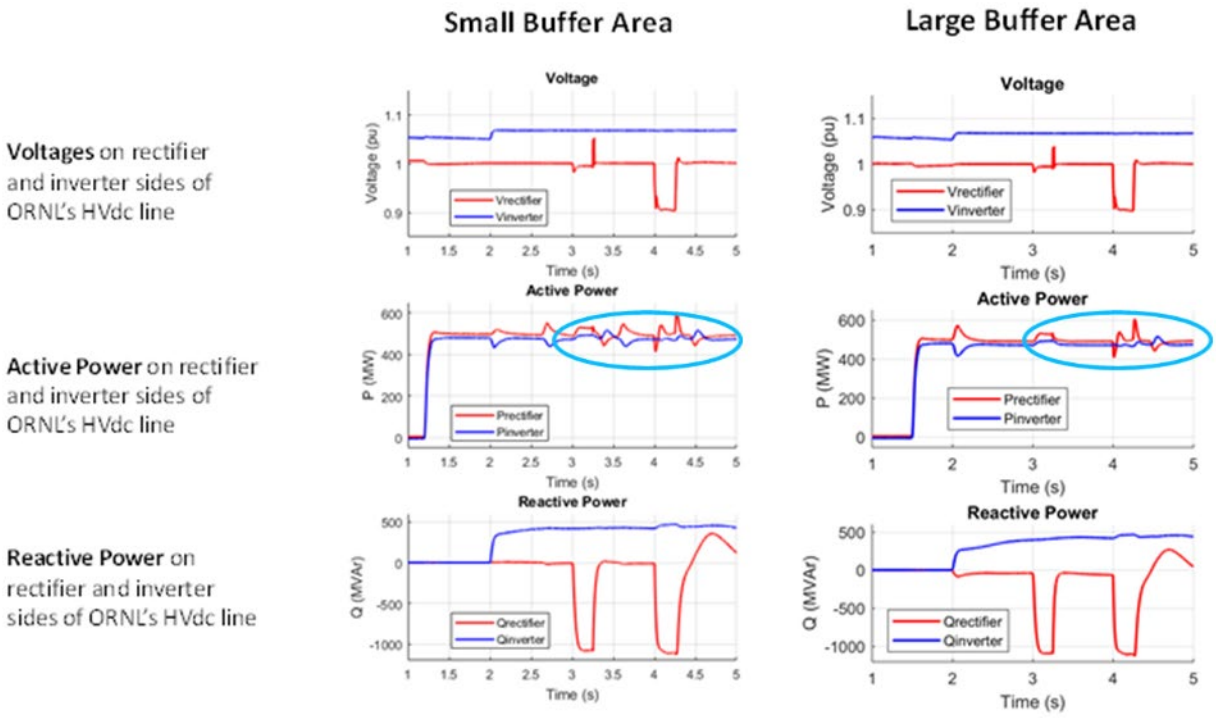

Figure Ex-6: Comparison of states observed in EMT simulation only and hybrid EMT-TS simulation.

c. **Reduced Fidelity of Transmission Lines**: Lumped line models were applied to the transmission line models in a smaller Kundur two-area system with a point-to-point VSC-HVdc system. The VSCs included the fast voltage control method. The states observed in the simulation of the system with lumped line model were compared to that observed in the system with the distributed line model. The corresponding results are shown in Fig. Ex-7. The results indicate that the system with a distributed line model is stable, whereas the system with a lumped line model is not stable. This difference can be attributed to the higher damping in the response observed in the distributed line model as compared to the lumped line model at the bandwidth of the control system.

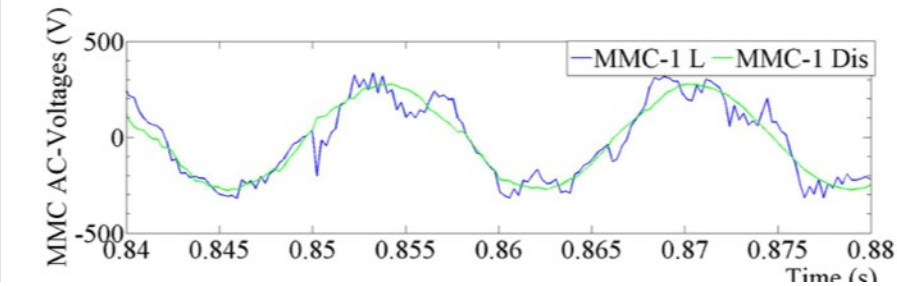

Figure Ex-7: Comparison of the response of a point-to-point VSC-HVdc system with fast control methods utilizing a lumped line model (MMC-1 L) and a distributed line model (MMC-1 Dis) in the transmission lines in the buffer zones of a small system (known as the Kundur two-area system).

d. **EMT Simulation Only**: EMT dynamic simulation only is performed in PSCAD, neglecting the response of the rest of the ac transmission grid. The comparison is performed with the states observed in hybrid simulation with respect to simulation only in PSCAD. The corresponding results are highlighted in Fig. Ex-8. The comparison of the results indicates varied dynamic performance of the VSC-HVdc control system during contingency events as highlighted in Fig. Ex-8. The varied dynamic performance affects the tuning of the VSC-HVdc control system.

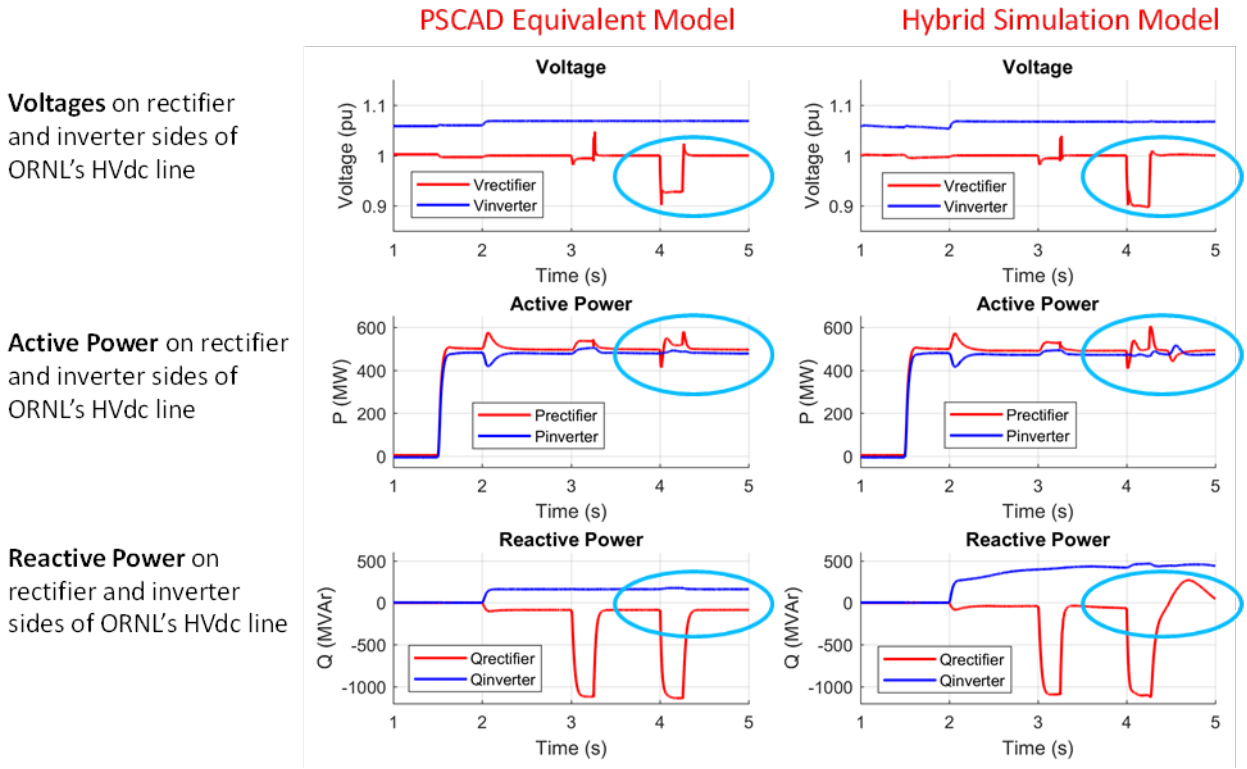

Figure Ex-8: Comparison of states observed in EMT simulation only and hybrid EMT-TS simulation.

The highlights of the computational performance of PSCAD-PSS®E hybrid simulation are summarized below:

a. About seventy-seven percent of computational burden was imposed by the EMT simulation in PSCAD, and ~23% was imposed by the TS simulation in PSS®E and communication between PSS®E and PSCAD.
b. The lower-fidelity point-to-point VSC-HVdc system model with the multirate simulation method resulted in up to 3.9× speed-up in hybrid simulation and up to 6× speed-up in Kundur two-area simulation in PSCAD only.
c. A speedup of up to 1.9× was observed with a smaller buffer zone model.

The highlights on accuracy of the PSCAD-PSS®E hybrid simulation are summarized below:

a. The multirate simulation methods applied to the simulation of VSC-HVdc systems (or, lower fidelity model) showed instability in the controller of the VSC-HVdc systems. The instability occurred as a fast voltage control method with a higher sampling rate was utilized. The instability was not observed in the simulation of the high-fidelity models of VSC-HVdc systems. The instability was not observed as the higher sampling rate is accurately captured, indicating the need for high-fidelity models for these studies.
b. The simulation results of the states from a smaller and larger buffer zone indicated the requirement of buffer zones. The larger buffer zone adequately captured the dynamics of the VSC-HVdc control system that is important to tune controller parameters, which influences the effect on the ac transmission grid.
c. The lumped line model of transmission lines does not adequately capture the high-frequency dynamics in the system. The high-frequency dynamics arise from the fast control methods in VSC-HVdc systems. They are also necessary to tune the controller parameters.

d. There are differences observed in the dynamics of the states observed in PSCAD-only and hybrid simulations. These differences arise due to the interaction of the fast control methods in VSCs with the other portions of the ac transmission grid. These components are not adequately captured in the PSCAD-only simulation. One possible solution is to convert a very large buffer zone from the ac transmission grid model in PSS®E to PSCAD. However, this solution imposes a large computational burden. The other solution is to perform hybrid simulation for such studies.

Limitations have been identified in hybrid simulation and model conversion using E-Tran:

a. Machine parameter Xp = X'p is not allowed in PSCAD (PSS®E does not have a problem with those reactances being equal). This issue was fixed by making these reactances different for a few generators.
b. Some generator output set with excessive reactive power can cause initialization problems for some exciter's models in PSCAD.
c. E-Tran by default defines several measurement channels per generator, when converting from PSS®E to PSCAD. When the system model in PSS®E has many generators (e.g., the EI lumped model has 300 generators), the total number of channels becomes unmanageable by PSCAD. An efficient and automated method has been suggested to fix the problem by the PSCAD support team to remove all the channels.
d. E-Tran software was not initially set up to handle the full PSS®E WI-EI-HVdc macrogrid model with over 100,000 buses. Only full nodal EI model has been used in this work.
e. Zero resistance lines are converted into PSCAD as ideal lines. When some of these lines are in a loop configuration, the model presents problems when executing PSCAD simulations (this configuration has no problem in PSS®E).
f. Negative loads in PSS®E are converted into PSCAD as voltage sources. Voltage sources significantly modify the dynamic behavior of the system, distorting the frequency response. This problem is avoided by identifying and eliminating or replacing negative loads.
g. HVdc systems in PSS®E are not directly translated into PSCAD with E-Tran. Instead, E-Tran places an ideal voltage source at each substation terminal. E-Tran currently cannot represent CDC6T model. The user is expected to include HVdc models in PSCAD.

3. Models and methods to evaluate the fast response that could be provided by MTdc systems were established. MTdc systems are one of the futuristic HVdc–ac transmission grid scenario. Six- and seven-terminal MTdc system EMT dynamic models were developed based on the high-fidelity EMT dynamic models of the VSC (like MMC utilized in this study). These models were applied on a portion of the HVdc macrogrid shown in Fig. Ex-9. The six-terminal MMC-based MTdc system connecting EI and WI grids is shown in Fig. Ex-9. The additional seventh terminal in the seven-terminal MMC-based MTdc system was considered in the ERCOT grid.

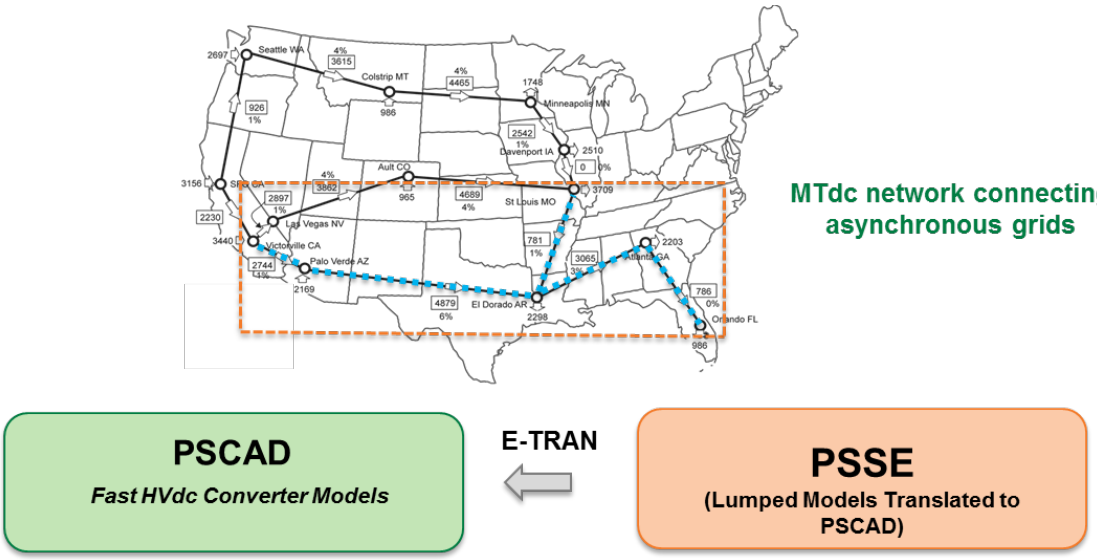

Figure Ex-9: Models of seven-terminal MTdc system and lumped ac transmission grid EMT dynamic models.

The MTdc system can provide fast frequency support across multiple asynchronous interconnections based on the application of fast control methods in the VSCs (like MMCs in this study). The use of slower control methods in the HVdc macrogrid (or the MTdc system in this study) reduces the reduction in primary reserves. A comparison of the fast and slow control methods in HVdc systems is shown in Fig. Ex-10. The reduction in primary reserves is improved by 33% by the use of fast control methods, indicating the value of applying fast optimal control methods in MTdc systems. The faster control methods optimally exploit the capabilities of the HVdc hardware better than the conservative slower control methods. While the slower control methods can be studied on lower fidelity models, the fast control methods require high-fidelity models of the HVdc technologies (like the MTdc system in this study). The frequency support can also be provided through multiple points of injection in each interconnection, rather than only at the interconnection boundaries. This feature improves the reliability of the system with greater probability to share primary reserves across interconnections under various operating conditions. That is, in the event of the terminals at the interconnection boundaries being fully loaded, other terminals can provide means to share primary reserves.

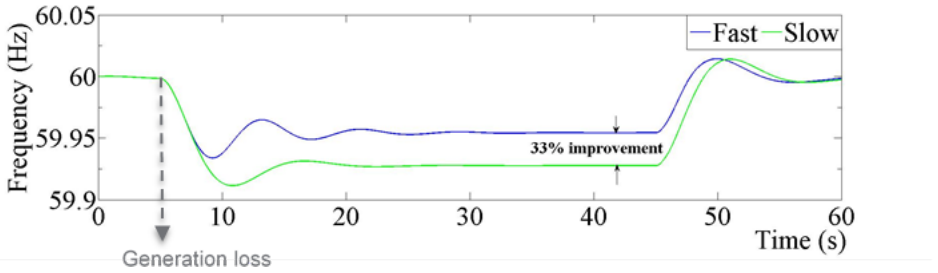

Figure Ex-10: Comparison of the frequency support provided by fast and slow control methods in HVdc systems.

The multi-objective optimal control method arises from the need to meet multiple objectives of high-efficiency operation and provision of fast frequency support across asynchronous interconnections. The constraints involved include the limits placed on dc-link voltage and power processed at each terminal. The conflicting multiple objectives and the constraints are summarized in Fig. Ex-11.

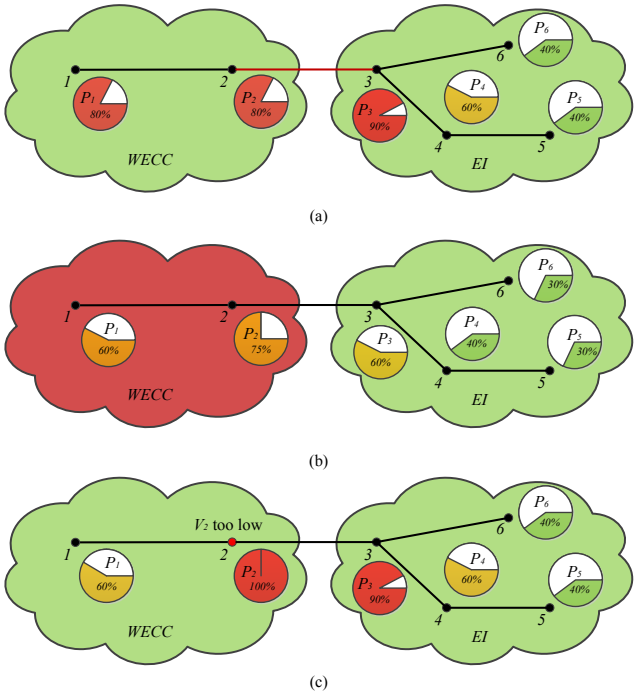

Figure Ex-11: Conceptual diagram of six-terminal MTdc system: (a) stress on line-23 is high; (b) frequency deviation is too high, not sufficient power provided; (c) voltage on terminal-2 is too low. Pie charts indicates the percentage of potential active power utilized in a converter. Red and black lines indicate the transmission line is over-loaded and within limits, respectively. Green and red clouds indicate that the frequency deviation is low and high, respectively. Red and black converter terminal dot indicate that dc-link voltage is out of bounds and within bounds, respectively.

One of the methods to evaluate the fast control methods in VSCs (and by extension in MTdc systems) is to perform EMT simulations of combined dynamic models presented below. This method is an alternative to the hybrid simulation of EMT dynamic models of VSCs and buffer zones, and TS models of rest of the ac transmission grids. Lumped ac transmission grid EMT dynamic models of EI, WI, and ERCOT grids were developed to represent the frequency dynamics of the grids. These models were used to evaluate the impact of multi-objective optimal control in MTdc systems. The optimal control provided fast frequency support at multiple points in an asynchronous grid. The lumped models were needed as the full nodal models of the grids cannot be simulated in EMT simulators (like PSCAD) due to the large size of the model and the time taken to simulate them. These models were developed based on conversion of models from PSS®E to PSCAD, as summarized in Fig. Ex-9. They can simulate up to 100× faster than the full nodal models of the grid. To incorporate the voltage behavior of the ac transmission grid at the MTdc terminals, combined dynamic model of the grid was developed. The combined dynamic model was developed based on incorporation of buffer zones at the MTdc terminals in to the lumped models. The buffer zones provided adequate representation of the dynamic voltage behavior of the local ac transmission grid.

The multi-objective optimal control in MTdc systems can provide up to 64% improvement in the frequency response, as shown in Fig. Ex-12. This method can be applied to other dc technologies.

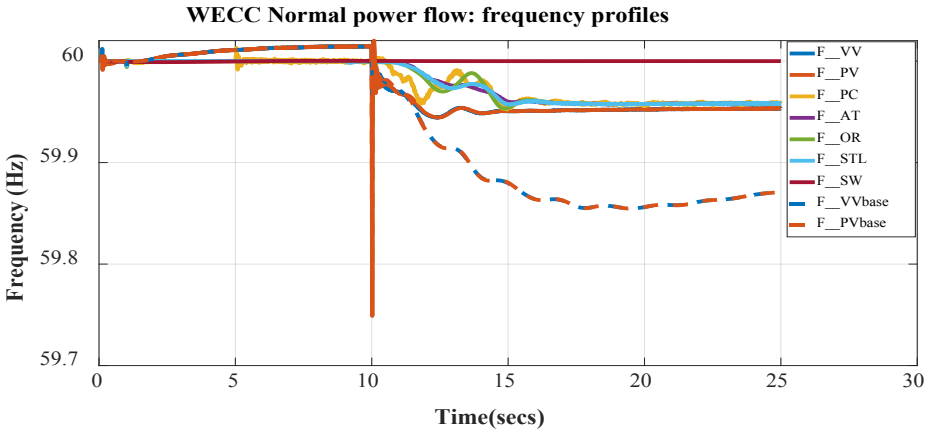

Figure Ex-12: Comparison of frequency response of the WI grid with and without the frequency support provided by the MTdc system. In the figure, F_VV and F_PV are the frequency measured at Victorville and Palo Verde from simulation of MTdc system with the ability to provide frequency support. Similarly, F_VVbase and F_PVbase are the corresponding frequencies measured without the frequency support being provided in the WI grid. The other frequencies are measured in the EI grid when providing frequency support to the WI grid through the MTdc system.

In future, expansion of the MTdc system to all the nodes of the HVdc macrogrid to create an MTdc macrogrid can be considered. The MTdc macrogrid can provide higher reliability due to the meshed architecture, as compared to the radial 7-terminal MTdc system in Fig. Ex-9. The MTdc macrogrid can also be evaluated to identify other value models like resilience and security through firewalling disturbances using the HVdc network. The same can be achieved through the ability of MTdc macrogrids to provide islanding capability, black-start, voltage support, and negative-sequence based control.

4. Several HVdc penetration scenarios were evaluated and compared with the HVdc macrogrid for a scenario in 2025–2026 with respect to the ability to provide congestion relief and frequency support. The various penetration scenarios studied provide an understanding of the benefits provided by the increased presence of dc lines in the system. The various penetration scenarios studied are shown in Fig. Ex-13. For topology 1 to be feasible in the 2025–2026 scenario, significant ac transmission grid upgrades are required. And, topology 2 is an intermediate scenario to topology 3 with potential major reliability problems caused by the outage of one of the East-West HVdc lines. Hence, only topology 3 is studied in detail and compared with the HVdc macrogrid. The HVdc lines and terminals in topology 3 are sized to maintain similar power transfer capability between the East and the West of the HVdc macrogrid. Both the topology 3 and HVdc macrogrid are able to provide similar frequency support (or have similar capability to share primary reserves across EI and WI grids). The HVdc macrogrid can provide better congestion relief due to the presence of a larger number of HVdc lines, as shown by the study in Fig. Ex-14.

Figure Ex-13: Summary of HVdc penetration scenarios evaluated.

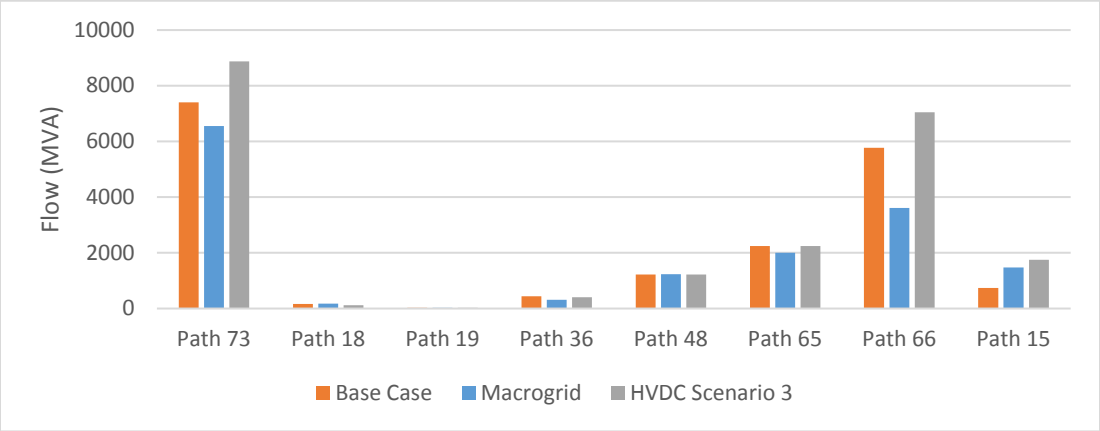

Figure Ex-14: Congestion relief provided by various HVdc configurations. Topology 3 and 4 are referred to as HVDC Scenario 3 and Macrogrid, respectively, in the figure.

Combined congestion management and frequency support is explored in both topology 3 and HVdc macrogrid. The combined method utilizes a combination of centralized and decentralized controller shown in Fig. Ex-15. The decentralized controller consists of the frequency controller that locally controls the lines crossing the interconnection borders during a frequency event. The centralized controller can perform fast rescheduling of all HVdc lines to reduce congestion after the decentralized controller completed its operation.

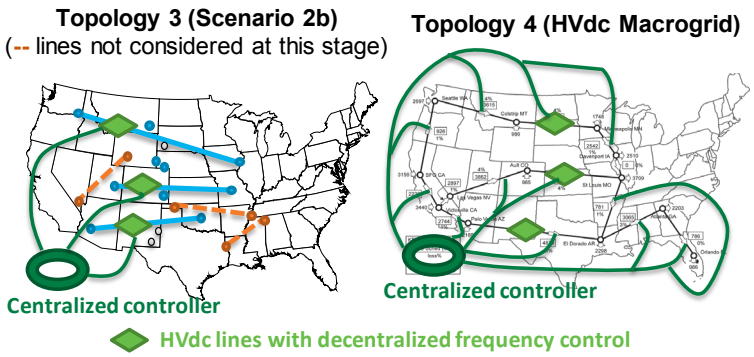

Figure Ex-15: Decentralized controller implemented in HVdc lines that cross the WI and EI borders and centralized controller providing schedules to all HVdc lines.

The combined congestion management and frequency response can further enhance the reliability of the existing grid. The corresponding results are shown in Fig. Ex-16. A comparison of the power "before central" and "after central" in the figures show that the combined control method reduces the stress on the lines while the power is exchanged between the East and West to provide frequency support. Topologies 3 and 4 provide similar frequency response benefit. Topology 4 provides greater congestion management through fast rescheduling of more HVdc lines across the full continental-level power grid.

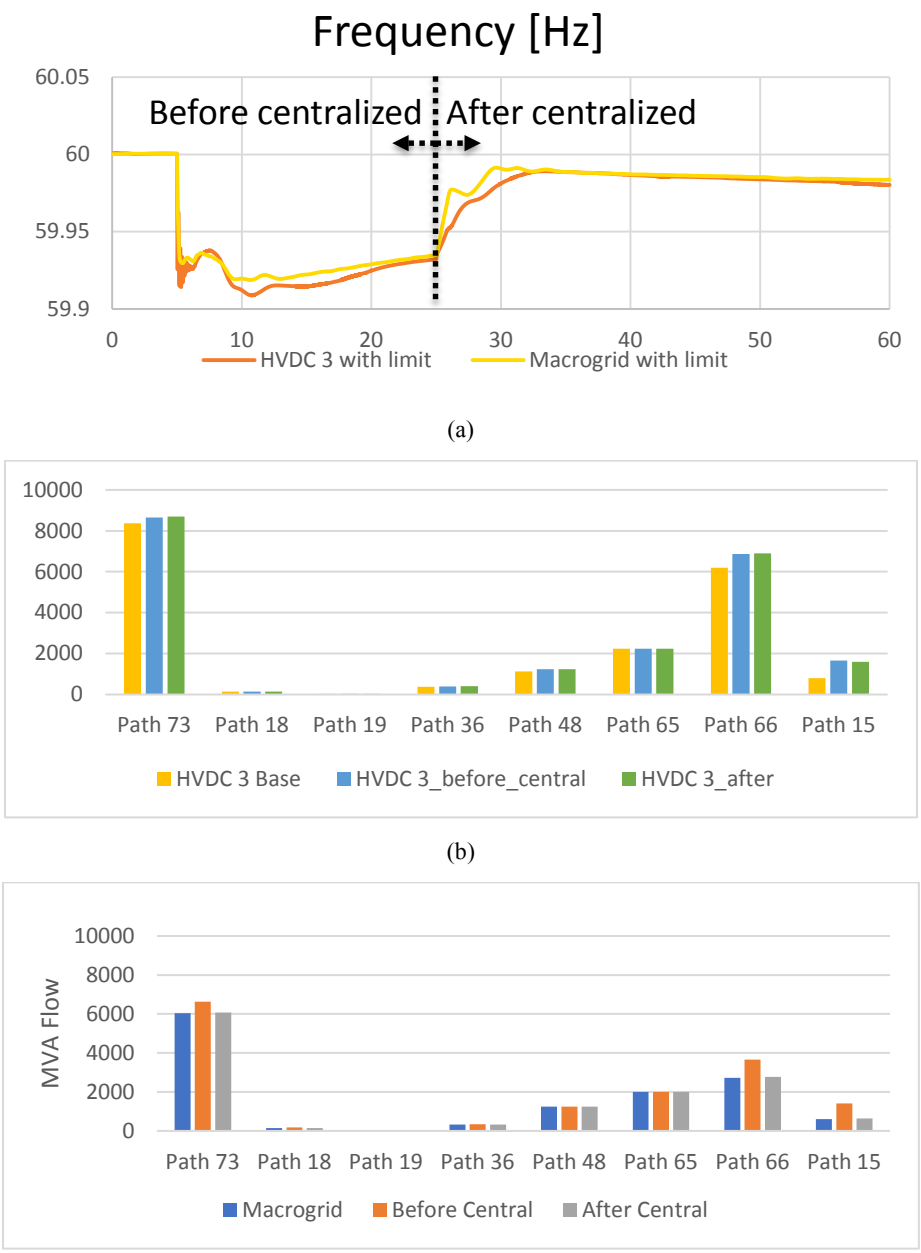

Figure Ex-16: Results of combined frequency control and congestion management (a) Frequency of WI after generation contingency, (b) MVA flows in main WI paths for topology 3 scenario, (c) MVA flows in main WI paths for topology 4 (Macrogrid) scenario.

5. Updates in PIDG 2.0, the tool that enables model conversion from PSS®E to PLEXOS, resulted in 10x speed-up. The speed-up acts as an enabler to convert large systems from PSS®E to PLEXOS like the over 100,000 bus models of EI and WI grids. PLEXOS is a tool used to simulate production costs associated with operating the grids.

6. The impact of a HVdc national network and accompanying HVdc controls were evaluated in economic and operational context over a simulated year in PCM, as summarized in Fig. Ex-17. This

study found potential impacts from the studied scenarios and sensitivities, such as improved resource usage efficiency, decreased production cost, changes to transmission congestion patterns, and decreased spinning reserve requirements. The value of providing fast frequency support has been evaluated through a sensitivity analysis on spinning reserve reduction with the results shown in Fig. Ex-18. Two spinning reserve reductions have been considered that has shown $105 million benefits annually with a 2 GW reduction and $241 million benefits annually with a 6 GW reduction. The former reduction can be obtained using the seven-terminal MTdc system studied and with the fast frequency support. The sensitivity analysis provides an understanding of the advantages of greater spinning reserve reduction using fast frequency support.

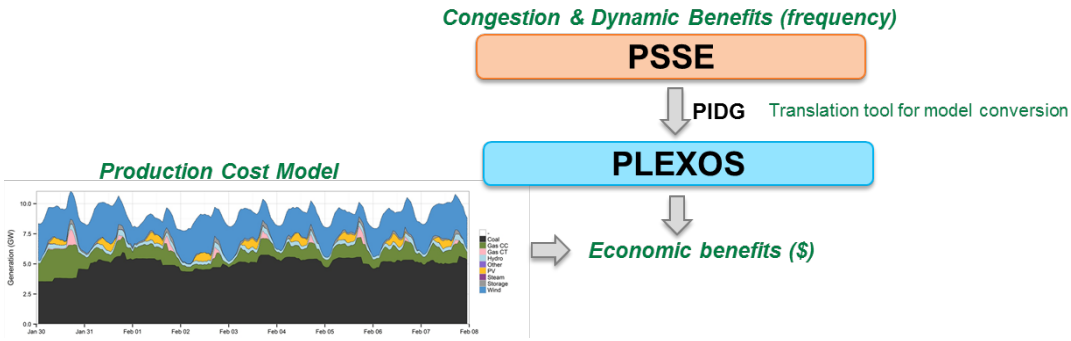

Figure Ex-17: Economic benefits evaluation from congestion relief and frequency support provided by HVdc macrogrid.

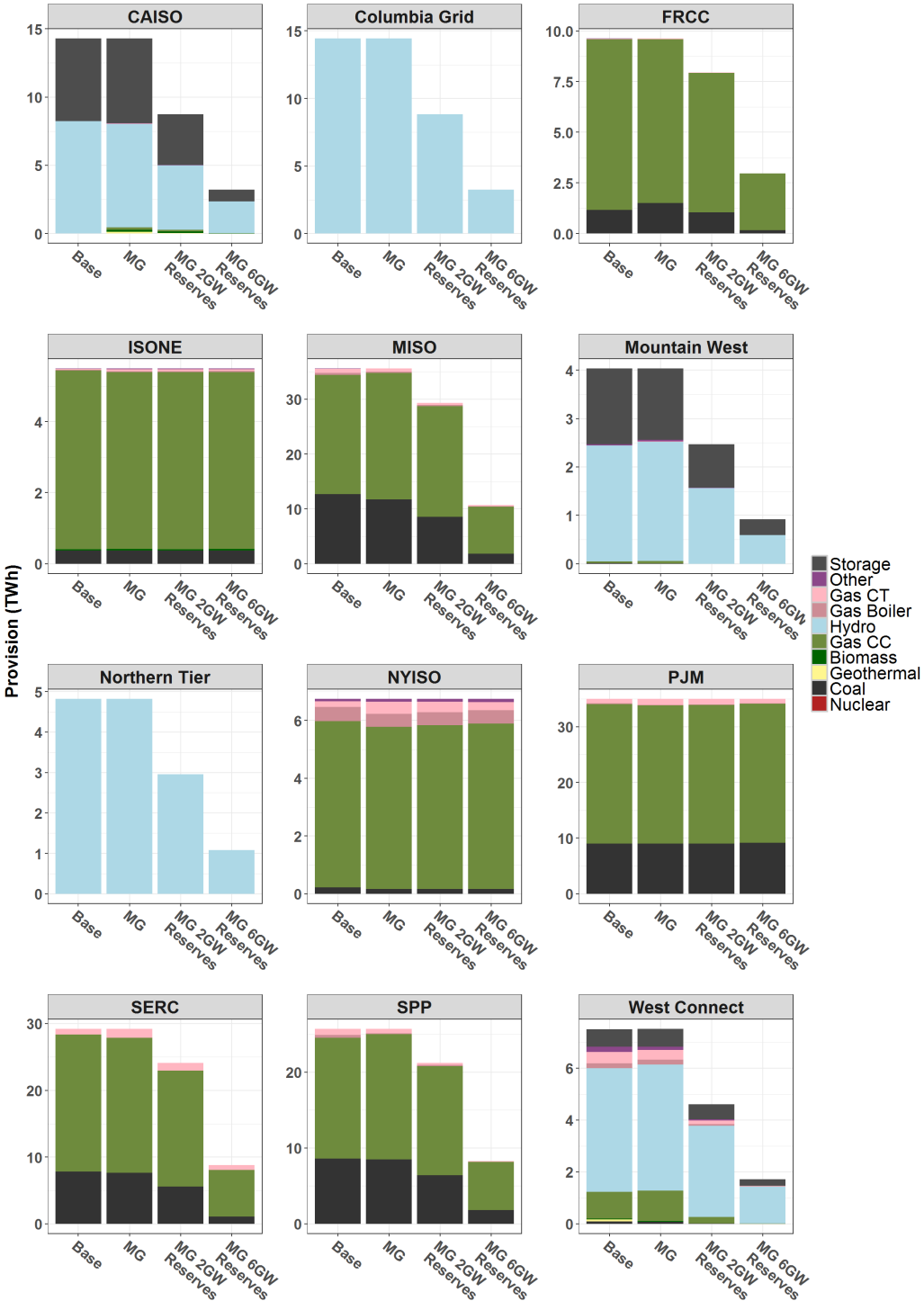

Figure Ex-18: Spinning reserves provisions by fuel type and technology across two scenarios and two sensitivities.

Impact & Challenges

The MMC models developed are being utilized by two Universities for research on MTdc systems. There are ongoing discussions with multiple industry partners on ways by which they can access the VSC and

MTdc systems models and the various control methods developed in this work. Based on the work completed in hybrid simulation, suggestions have been provided to Electranix Corporation to improve the hybrid simulation tool.

The results from this work have been published in a journal and three conference papers. There are at three more journal papers that have been submitted. The results have also been presented at five conferences. The results disseminated will aid in utilizing the models and methods developed in this work.

The challenges faced in this project include identifying stable means of parallelization in simulation of power electronics and compatibility issues in use of tools across multiple domains. Some of the challenges associated with linking the tools have been identified like:

1. Compatibility of models in different tools like PSCAD, PSS®E, and PLEXOS;
2. Limitations with respect to the size of the models utilized in individual tools while translating to another tool or co-simulating the models while performing hybrid simulation.

Lessons Learned

Several HVdc penetration scenarios like a 7-terminal MTdc systems, VSC-LCC HVdc macrogrids, and point-to-point HVdc systems were studied in this work utilizing multiple tools (PSCAD, PSS®E, and PLEXOS). The requirement of high-fidelity models of these penetration scenarios to understand the stability and impact of advanced control methods like voltage and frequency control on ac transmission grid were identified. The models required included EMT switched system and hierarchical control system models of VSCs, distributed line model of transmission lines, EMT dynamic models of buffer zones in the region with VSCs, and TS model of ac transmission grids. The buffer zones are regions near the VSC-HVdc terminals. The EMT dynamic models of the buffer zones enable the understanding of the high-bandwidth dynamics associated with VSCs and the corresponding stability of such systems. The EMT dynamics models take a long time (or, more computational resources) to simulate, and there is a requirement for advanced simulation and modeling of components as has been performed with the EMT dynamic model of VSCs in this work. Future extensions of this work could include detailed EMT dynamic modeling and fast simulation of other components as well as buffer zones. It could also consider temporal parallelization that has been briefly studied in this project.

The tools required to quantify the impact of the advanced control methods on ac transmission grid include PSCAD, E-Tran, and PSS®E. While the EMT dynamic models were simulated in PSCAD, the TS dynamic models were simulated in PSS®E. The co-simulation between the EMT and TS dynamic models were enabled by E-Tran. The E-Tran tool also enabled model conversion from TS dynamic model to EMT dynamic model, which was useful to develop EMT models of buffer zones.

Economic benefits were quantified from the impact of the advanced control methods in MTdc system/ HVdc macrogrid on the ac transmission grid. The tools utilized for the same included PSS®E, PIDG 2.0, and PLEXOS.

The ability to utilize information across multiple tools have been successfully demonstrated in this work, with the capability to identify economic benefits associated with advanced control methods applied to power electronics. This is summarized in Fig. Ex-19. One of the successes included the capability to identify the impact of advanced control in power electronics on the underlying ac transmission grid. The other included the means to evaluate the economic benefits associated with such advanced control

methods through the impact quantified in ac transmission grids. While the former was achieved through hybrid simulation using E-Tran, the latter was achieved using PIDG 2.0.

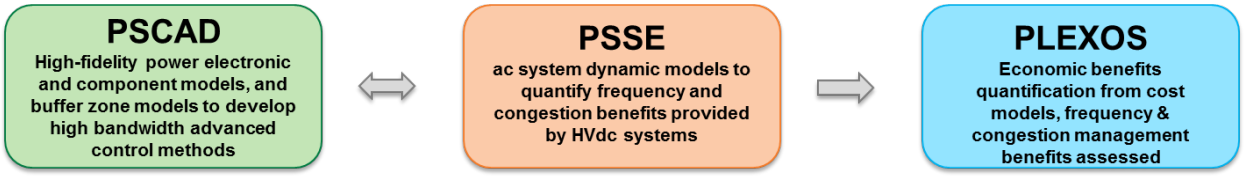

Figure Ex-19: Tools and relationship to establish economic benefits from advanced control methods applied to large-scale HVdc-ac systems.

The feasibility of utilizing MTdc systems to provide fast frequency response at multiple points of injections have also been demonstrated in this project. The ability to provide combined congestion management and frequency response utilizing a higher penetration HVdc system (like the HVdc macrogrid) has also been demonstrated.

Future Work

Future extensions of this work could include the following:

1. Large-scale HVdc-ac system model that incorporates up to 15-terminal MTdc systems that will be needed in the MTdc macrogrid (or, higher as desired for other HVdc configurations) with vendor agnostic VSC configurations. These models would provide means to explore other applications of MTdc grids like transportation electrification, integration of renewables (solar, wind), and others.
2. Detailed EMT dynamic modeling and fast simulation of other components (like HVdc breakers, transmission lines) as well as buffer zones. This work could also explore the advanced dynamic load models required for this type of analysis. These modeling efforts would equip planners to incorporate dc technologies into future grids.
3. Parallel-in-time simulation algorithm application to EMT simulations and/or hybrid simulations. The algorithm can speed-up simulation and incorporate higher fidelity models that can be simulated in reasonable time-frame. The higher fidelity models provide means to evaluate value models that are not explorable with lower fidelity models like the fast frequency support demonstrated in this work.
4. Contingency analysis in MTdc-ac systems with fault identification mechanism and post-fault operation methods. This analysis would provide further insights in to the reliability of dc-ac systems from contingency studies in the dc systems, beyond the reliability aspects studied in the ac system in this work.
5. Hybrid simulation with large-scale HVdc-ac systems that incorporates advancements in hybrid simulation tools and simulation methods to enable and speed-up such simulations. Such simulations to study contingencies in HVdc and ac systems to understand reliability and resiliency. This analysis enhances the tools to study large-scale dc-ac systems, studies in the NERC-led IRPTF, and others.
6. Develop dynamic models for futuristic scenarios (like 2038 grid) that include high-penetration of inverter-based resources (like generation and loads).
7. Additional modeling and analysis on the HVdc controls is necessary to expand industry expertise in the indirect benefit of reduced reserve requirements due to frequency support provided by HVdc. Another opportunity is to investigate coordinated control of multiple dc lines, both existing and future facilities. These opportunities could be explored not only from the point of view of automatic dynamic control in short time scales, but also including coordinated scheduling in longer terms and HVdc interactions and their roles in real-time electricity markets.

Acknowledgments

The authors would like to acknowledge the support and feedback from Kerry Cheung (U.S. DOE) and the industry advisory board (IAB) participants.

The authors would like to also thank the participants of the IAB: Reynaldo Nuqui and Roger N. Rosenqvist (ABB), Sakshi Mishra (American Electric Power [AEP]), Ebrahim Rahimi (California Independent System Operator [CAISO]), Ram Adapa (Electric Power Research Institute [EPRI]), Jose Conto (Electric Reliability Council of Texas [ERCOT]), Sharma Kolluri (Entergy), Maryam Saeedifard (Georgia Institute of Technology), Jared Alholinna (Great River Energy), Dale Osborn (Independent), Armando Figueroa-Acevedo and Brandon Heath and James Okullo and Jordan Bakke and Maire Boese and Nihal Mohan and Yifan Li (Midcontinent Independent System Operator [MISO]), Hassan Ghoudjehbaklou (San Diego Gas and Electric), Divya (Siemens), Raul Perez Guerrero (Southern California Edison), Shih-Min Hsu (Southern Company), Harvey Scribner and Jay Caspary (Southwest Power Pool [SPP]), David Orser (University of Minnesota), Madhav Manjrekar (University of North Carolina Charlotte), James Hirning (Western Area Power Administration).

Acronyms and Abbreviations

AAC	alternate-arm converter
ABB	ASEA Brown Boveri
ac	alternating current
AEP	American Electric Power
BPA	Bonneville Power Administration
CAISO	California Independent System Operator Corporation
CC	combined cycle
CEMS	continuous emissions monitoring systems
CIGRE	Conseil International des Grands Réseaux Électriques
CPAAUT	Frequency Sensitive Auxiliary Signal Model in PSS®E
CT	combustion turbine
CTL	cascaded two-level
DAE	differential algebraic equations
dc	direct current
DOE	US Department of Energy
EI	Eastern Interconnection
EMT	electromagnetic transient
EMTDC	electromagnetic transients and DC algorithms used in PSCAD software
EPA	Environmental Protection Agency
EPRI	Electric Power Research Institute
ERCOT	Electric Reliability Council of Texas
FIDVR	fault induced delayed voltage recovery
GMLC	Grid Modernization Laboratory Consortium
GW	giga watt
HVdc	high voltage direct current
IAB	industry advisory board
IGBT	insulated-gate bipolar junction transistor

INELFE	Interconnexion électrique France-Espagne
IRPTF	Inverter-Based Resource Performance Task Force
LCC	line commutated converter
LCL	inductor-capacitor-inductor
MG	macrogrid
MISO	Mid-Continent Independent System Operator
MMC	modular multilevel converters
MTdc	multi-terminal direct current
MVDC	medium voltage direct current
MVA	mega volt ampere
NERC	North American Electric Reliability Corporation
NREL	National Renewable Energy Laboratory
ORNL	Oak Ridge National Laboratory
PCM	production cost modeling
PIDG	Private Infrastructure Development Group
PNNL	Pacific Northwest National Laboratory
PSCAD	Power Systems Computer-Aid Design Software
PSS®E	Siemens Power System Simulator
PWM	pulse-width modulation
QSS	quasi steady state
RTO	Regional Transmission Organization
SERC	SERC Reliability Corporation
SM	submodule
SPP	Southwest Power Pool
SRF-PLL	synchronous reference frame phase-locked loop
TARA	transmission adequacy and reliability assessment
TS	transient stability
TWh	tera watt hours

VSC	voltage source converter
WECC	Western Electricity Coordinating Council
WI	Western Interconnection

Contents

Figures

Executive Summary

Chapters

Appendix A

Appendix B

Appendix C

Appendix D

Tables

Chapters

Appendix C

Chapter 1 Introduction

Today's predominantly alternating-current (ac) transmission grid is increasingly evolving into mixed ac–direct current (dc) transmission systems with the decreasing costs of and advancements in power electronics technology [Makarov 2017]. The recent high-voltage (HV) dc technological advancements include the development of more efficient and compact voltage source converters (VSCs). Some of the VSC technologies include the modular multilevel converter (MMC), the cascaded two-level converter (CTL), and the alternate-arm converter (AAC) topologies. The MMC HVdc technology was used in the Trans-Bay Cable project in San Francisco. Because they offer the advantages of flexibility and controllability, dc technologies provide the ability to (i) connect asynchronous grids to share primary reserves; (ii) integrate renewable energy sources; (iii) enable underground transmission, (iv) transfer large blocks of energy over long distances, and (v) provide additional services to the grid such as frequency response, voltage control, congestion relief, and others. The dc technologies can also provide other ancillary services to enhance the economics and reliability and to optimize the performance of ac transmission grids.

Several projects are under development in the United States, such as the Southern Cross, TransWest Express Transmission, Plains & Eastern Clean Line, and New England Clean Power Link. The Southern Cross Transmission Project will connect Electric Reliability Council of Texas (ERCOT) to the southeastern United States with a 400 mi HVdc transmission line. It will deliver cost-effective wind power while providing both regions with improved reliability and economic benefit [RUSK-PANOLA 2019]. The TransWest Express Transmission Project will transfer wind power from Wyoming to the Desert Southwest region (California, Nevada, Arizona) using a 730 mi HVdc transmission line [TransWest 2019]. It is well-known that dc lines over certain distances are less expensive than ac lines.

The main motivation of this work was to maximize the technical and economic benefits of HVdc systems as they overlap with the ac transmission systems based on multiple services that they could provide. The benefits are maximized by using the flexibility of dc systems in terms of active/reactive power control and fast response. The fast response can provide essential and much-needed services to the grid (e.g., frequency response, voltage control) while moving blocks of energy. Models and methods to explore and quantify the technical and economic benefits of dc technologies in the future grid of United States were developed in this work.

The development of a mixed ac-dc grid model using a HVdc macrogrid connecting Eastern Interconnection (EI) and Western Interconnection (WI) is documented in [Makarov 2017]. The HVdc macrogrid is based on point-to-point line-commuted-converter (LCC) dc technology. The model use WI 2025 heavy summer case and EI multiregional modeling working group 2026 summer peak case. The models showed that the HVdc macrogrid relieved congestion and mitigated loop flows in ac transmission networks and provided up to 24% improvement in frequency responses. They showed that the current infrastructure can accommodate HVdc injections. This work also developed high-fidelity dynamic models of MMCs, one of the VSC dc technologies. It also developed a high-fidelity model and control algorithms of a three-terminal dc system connecting EI, WI, and ERCOT. The ac transmission grid models of EI, WI, and ERCOT were developed based on data that are available from the North American Electrical Reliability Corporation (NERC). The developed models showed up to 45% improvement in frequency response with the connection of the three asynchronous interconnections in the United States using fast and advanced dc technologies such as the multi-terminal dc (MTdc) system.

Preliminary economic analysis showed improved cost benefits associated with MTdc systems as compared to multiple point-to-point LCC-dc systems [Makarov 2017]. Despite the cost benefits of MTdc systems, LCC-dc systems are still required for bulk power transfers (> 4 GW)., In this work, the analysis of various scenarios of penetrations of dc systems and the economic benefits provided by these systems is performed. Various VSCs (e.g., CTL and AAC) were modeled to understand the feasibility of multiple vendors participating in the future developments of dc-ac systems. Other ancillary services, such as voltage control by individual VSC substations and multi-objective frequency control with multiple points of injection in MTdc systems, were studied. Economic and reliability benefits derived from these services were quantified through understanding enhancements in grid reliability. The project team aimed at capturing the value of the flexibility and controllability introduced by the HVdc systems into the ac large interconnections.

1.1. Project Objectives

The main objective of this work was to develop models and methods to evaluate the performance of HVdc technologies and their advanced control methods across large interconnect ac systems. The major objectives of this work included the following:

1. Develop high-fidelity dynamic models of VSCs to enable the study of the fast control response that they can provide. The developed models enable planners to make informed choice of the required HVdc technologies (e.g., LCC, VSCs) in the future grid expansion using HVdc systems.
2. Include other HVdc control algorithms, such as a voltage control algorithm; such inclusion is feasible due to the introduction of fast-acting and controllable VSCs in addition to the developments in [Makarov 2017]. Evaluate the multi-objective control algorithms using the high-fidelity models of VSCs and hybrid simulation of HVdc–ac transmission grid dynamics. The evaluation methods that were developed can be used to identify the improved performance of the ac transmission grid due to the presence of the fast-acting VSCs. The methods can be applied to assess the impact of other fast-acting power electronics technologies on the grid, such as the NERC-led IRPTF studies.
3. Develop up to seven-terminal MTdc system models with multiple points of injection in asynchronous ac transmission grids based on high-fidelity models of VSCs. Develop multi-objective control methods like the multiple-point-of-injection, fast-frequency support and voltage control in the MTdc systems. The developed methods provide enhanced reliability services that increase value of MTdc systems, and can be applied to other future dc technologies and systems.
4. Develop and evaluate different scenarios of HVdc system penetrations in the future grid, thus facilitating the comparison of their benefits. Evaluate technical benefits for frequency and congestion managements of several HVdc lines over a continental-level North American power grid model, based on utility industry models.
5. Develop advanced models to address computational challenges of high-fidelity models when models need to expand over large geographic areas, such as HVdc macrogrids. Create two modeling approaches: (a) develop reduced, lumped models able to capture voltage behavior near HVdc terminals and (b) configure advanced hybrid co-simulation between high-fidelity, electromagnetic transient models for HVdc, and lower-fidelity electromechanical transient models for the continental-level grid.
6. Evaluate the economic benefits associated with fast-acting and controllable HVdc systems. The methods applied to identify economic benefits can be extended to identify the benefits of providing fast reliability services in the grid by power electronics technologies or other technologies.

1.2. Project Participants and Industry Advisory Board Members

The project team was formed by national laboratories, including Oak Ridge National Laboratory (ORNL), Pacific Northwest National Laboratory (PNNL), and National Renewable Energy Laboratory (NREL), whose members effectively collaborated and produced significant results in a short time. The project team organized biweekly teleconference meetings and weekly meetings (if needed) to coordinate work across institutions. The project team presented intermediate progress to an industry advisory board (IAB). The IAB assisted the national laboratories with building accurate, realistic cases for simulations. There were three IAB meetings with participants from the following institutions: ASEA Brown Boveri (ABB), American Electric Power (AEP), California Independent System Operator (CAISO), Electric Power Research Institute (EPRI), ERCOT, Entergy, Georgia Institute of Technology, Great River Energy, Southwest Power Pool (SPP), Midcontinent Independent System Operator (MISO), San Diego Gas and Electric, Siemens, Southern California Edison, Southern Company, Xcel Energy, the University of Minnesota, the University of North Carolina at Charlotte, Western Area Power Administration, ORNL, PNNL, and NREL. The members in the IAB also completed a survey to assist in dc penetration scenarios and system analysis, and technology developments. Feedback from the IAB members during the meetings and through a survey were obtained on development of models, methods to develop hybrid simulation studies, scenarios of study, use cases, and events of interest.

Chapter 2 Advanced Modeling and Simulation of HVdc VSCs

Development of the high-fidelity models of VSCs, namely the AAC and the CTL, is discussed in this chapter. The high-fidelity models were based on electromagnetic transient (EMT)-type switched system models. Advanced simulation algorithms were applied to these models to reduce the computational burden imposed to simulate the models. The developed models and simulation algorithms were evaluated in a benchmark system that is based on the Interconnexion électrique France-Espagne (INELFE) project. The AAC and CTL converters and their control systems were designed based on the project. The errors observed in the developed models and simulation algorithms based on the benchmark system with respect to the conventional reference models/simulation algorithms are below 1%. The speedup observed is up to 12×.

2.1 AAC

The circuit diagram of the AAC VSC is shown in the Fig. 2-1. Only phase *a* notation is shown in Fig. 2-1. Phases *b* and *c* follow a similar notation as phase *a*. The AAC consists of three phase legs. Each phase leg consists of two arms: the upper arm and the lower arm. Each arm consists of "N" series connected H-bridge submodules (SMs), a director switch, and an inductor. The value of "N" ranges from several hundred today and could range up to a few thousand with increase in the dc voltage in HVdc systems in the near future. The director switch is a series connection of "N_{ds}" insulated-gate bipolar junction transistors (IGBTs) with an antiparallel diode, with the number of such serial connections, "N_{ds}", dependent on the dc-link and ac transmission grid voltages. The inductor and SM capacitor were sized based on the circulating current and voltage ripple requirements, respectively [Merlin 2014].

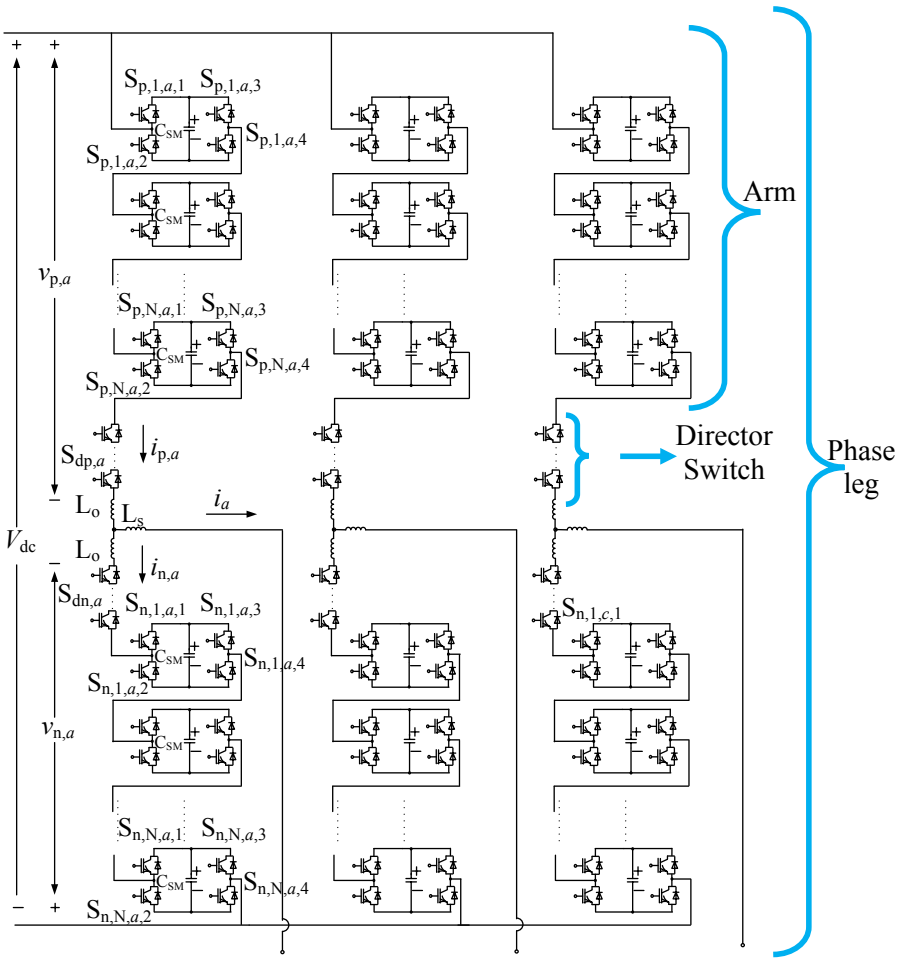

Figure 2-1: AAC-VSC circuit configuration.

The EMT high-fidelity dynamic modeling of AAC considers the arm currents and capacitor voltages as stated in the model, resulting in a total of "6N+6" states. Additionally, there are "24N + 6N_{ds}" switching states based on the number of IGBTs in H-bridges and director switches. From the calculated states, it can be observed that several thousands of states are present. The presence of a large number of diodes in H-bridges and director switches introduces numerical stiffness in the simulation models of the AAC. These challenges along with the use of small simulation time-steps (in the order of microseconds) to accurately capture the harmonics present in such systems result in the requirement of advanced simulation algorithms to speed up the simulation.

The models of AACs described in this chapter have been developed based on differential algebraic equations (DAEs) that describe the dynamics of the system. The developed models are separated based on numerical stiffness and time constants. The separation allows the application of hybrid discretization and multi-rate simulation algorithms that reduced the computational burden imposed in simulation of such systems. The hybrid discretization algorithm is based on explicit and implicit discretization algorithms without and with stiff decay properties, respectively. To enhance the stability of the separated systems, relaxation algorithms were applied to the interfaces created between the separated systems.

2.1.1 Terminal Models

An example of a point-to-point VSC-HVdc system is shown in Fig. 2-2. The VSCs shown in Fig. 2-2 can represent an AAC or a CTL converter. The three and two slanted lines represent the three-phase ac and dc lines (or cables), respectively. The DAEs formulated for this system could be separated based on time constants under the assumption that the ac and dc lines are sufficiently long. The states measured at the ends of the long ac and dc lines had much larger time constants than those of the dynamics of the VSCs. This assumption is particularly valid with the long HVdc lines connecting EI and WI.

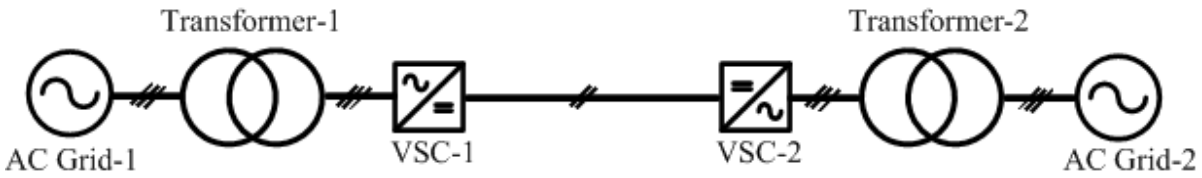

Figure 2-2: Two-terminal point-to-point VSC-HVdc system.

The separated DAEs were equivalently represented by the circuit shown in Fig. 2-3. The terminal voltage sources shown in Fig. 2-3 are based on the voltage-behind-reactance model that allows stable separation based on time constants. Since the control systems for the VSCs utilize measured voltages from an ac transmission grid and a dc link, voltage-behind-reactance models are considered to represent the ac transmission grid and dc links in the VSC-HVdc separated portion of the system. The equivalent representation of the VSC model in the power system (ac and dc systems in Fig. 2-3) was based on current source. The current-source-based models were used to represent the current controlled by the VSCs in an ac transmission grid and a dc link. The cables or overhead lines are implemented based on a distributed resistor-inductor-capacitor traveling wave model (a frequency-dependent model) [Morched 1999] [Gustavsen 1999] in the ac transmission grid and dc link.

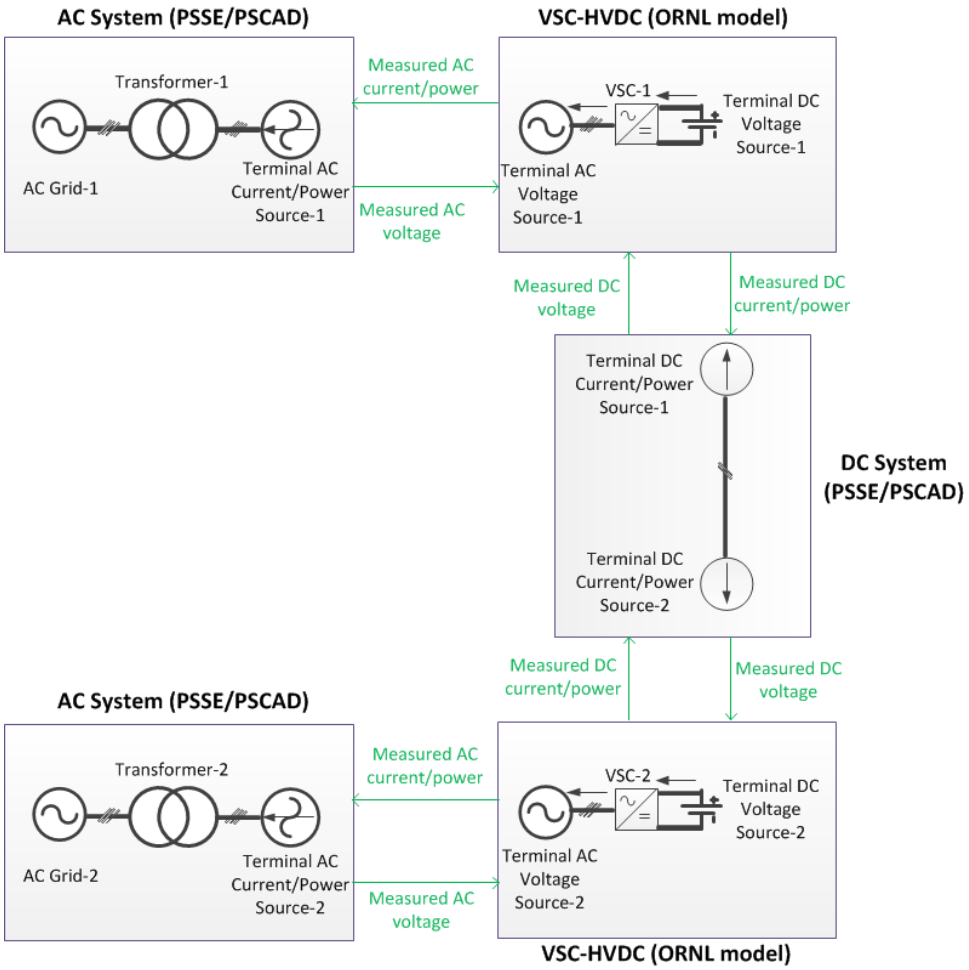

Figure 2-3: VSC terminal models in hybrid (dc-ac) grids.

The ac transmission grids in the ac system shown in Fig. 2-3 can be represented by simple ac voltages with reactors or by large system models such as the 2025/2026 EI and WI models.

The developed terminal models allow the implementation of hybrid discretization and multi-rate simulation algorithms to simulate the ac transmission grid and dc systems. For instance, the ac transmission grids and dc systems can be discretized using the trapezoidal method with a time-step of the order of several tens to hundreds of microseconds (or higher based on the timescales being studied in the power system networks). The trapezoidal method is used to ensure stability of and high accuracy in the simulation of the ac transmission grids and dc systems. The VSC-HVdc EMT dynamic models were discretized using a combination of stiff and non-stiff decay algorithms with a time-step of the order of a few microseconds or nanoseconds, respectively.

The developed terminal models can be implemented in various HVdc configurations: point-to-point, radial multi-terminal, and meshed multi-terminal. Several of the configurations were noticed in the planned HVdc macrogrid across the EI and WI [Makarov 2017] as well as in several other HVdc systems being planned in United States [MISO 2014].

2.1.2 EMT Model and Simulation Algorithm

AAC-HVdc Model: The EMT dynamic model of H-bridge SM-based AAC-HVdc system captures the dynamics of the 6N+6 states present. The states captured include the 6N capacitor voltages and the 6 arm currents. From Fig. 2-1, the arm currents' dynamics are given by

$$(L_o + L_s)\frac{di_{p,j}}{dt} - L_s\frac{di_{n,j}}{dt} = -(R_o + R_s)\,i_{p,j} + R_s\,i_{n,j} + \frac{V_{dc}}{2} - v_j - v_{cm} - v_{p,j}\,, \forall j \in (a,b,c), \quad (2.1a)$$

$$(L_o + L_s)\frac{di_{n,j}}{dt} - L_s\frac{di_{p,j}}{dt} = -(R_o + R_s)\,i_{n,j} + R_s\,i_{p,j} + \frac{V_{dc}}{2} - v_j - v_{cm} - v_{n,j}\,, \forall j \in (a,b,c), \quad (2.1b)$$

$$v_{y,j} = \begin{cases} \sum_{l=1}^{N} v_{sm,y,l,j} \text{ if } (S_{d\,y,j} = 1 \text{ and H-bridges unblocked}) \\ \sum_{l=1}^{N} v_{c\,y,l,j} \text{ if } (S_{d\,y,j} = 1, \text{ H-bridges blocked, } i_{y,j} > 0) \\ -\sum_{l=1}^{N} v_{c\,y,l,j} \text{ if } (\text{H-bridges blocked, } i_{y,j} < 0) \\ \text{based on circuit conditions if } (S_{d\,y,j} = 0,\ i_{y,j} \geq 0) \end{cases}, \forall j \in (a,b,c), y \in (p,n) \quad (2.1c)$$

$$v_{sm,y,l,j} = \{S_{y,l,j,1}\,S_{y,l,j,4}\,(1 - S_{y,l,j,2})(1 - S_{y,l,j,3}) - S_{y,l,j,2}\,S_{y,l,j,3}\,(1 - S_{y,l,j,1})(1 - S_{y,l,j,4}) + (1 - S_{y,l,j,1})(1 - S_{y,l,j,4})(1 - S_{y,l,j,2})(1 - S_{y,l,j,3})\,\text{sgn}(i_{y,j})\}\,v_{c\,y,l,j}, \forall j \in (a,b,c), y \in (p,n), l \in (1,N), \quad (2.1d)$$

$$\text{sgn}(x) = \begin{cases} 1 \text{ if } x > 0 \\ -1 \text{ if } x < 0 \end{cases}, \qquad v_{cm} = \frac{1}{6}\sum_{j\in(a,b,c)}(v_{n,j} - v_{p,j}), \qquad \sum_{j\in(a,b,c)} i_{p,j} = \sum_{j\in(a,b,c)} i_{n,j} \quad (2.1e)$$

The SM capacitor voltages' dynamics are given by

$$C_{SM}\frac{dv_{c\,y,l,j}}{dt} = -\frac{v_{c\,y,l,j}}{R_p} + \{S_{y,l,j,1}\,S_{y,l,j,4}\,(1 - S_{y,l,j,2})(1 - S_{y,l,j,3}) - S_{y,l,j,2}\,S_{y,l,j,3}\,(1 - S_{y,l,j,1})(1 - S_{y,l,j,4}) + (1 - S_{y,l,j,1})(1 - S_{y,l,j,4})(1 - S_{y,l,j,2})(1 - S_{y,l,j,3})\,\text{sgn}(i_{y,j})\}\,i_{y,j}, \forall j \in (a,b,c), y \in (p,n), l \in (1,N) \quad (2.2)$$

The blocked state of the H-bridge SMs in (2.1) is defined as the state in which all the semiconductor devices in the H-bridge are in OFF state. Equations (2.1) and (2.2) represent a semi-explicit DAE with numerical stiffness introduced due to the presence of sgn function and the variations shown in $v_{y,j}$. The sgn function and the variations in $v_{y,j}$ arise from the modeling of various diodes that are present in the AAC-HVdc.

The separation of the model representing the arm currents' dynamics from the model representing the SM capacitor voltages' dynamics was achieved using an explicit discretization algorithm. However, due to the numerical stiffness observed, explicit discretization cannot be applied to both the models. The separation of the models was based on numerical stiffness and a hysteresis relaxation algorithm.

Hybrid Discretization Algorithm: The numerical stiffness is observed only in the arm currents' dynamics because the sgn function in the SM capacitor voltages' dynamics were treated as an external input. That is, the arm currents' dynamics given in (2.1) was discretized using backward Euler, which has a stiff-decay property. The SM capacitor voltages' dynamics in (2.2) was discretized using forward Euler, which is an explicit discretization algorithm. The use of hybrid discretization resulted in inverting only a 5 × 5 matrix at every instant in the simulation of the proposed AAC VSC model. In the conventional simulation of AAC VSC models, the simulation of AAC VSC required the inversion of a (6N+5) ×

(6N+5) matrix. Thus, the computational burden imposed by the simulation of the proposed AAC VSC model was significantly reduced.

An interface was created to exchange information between the two DAEs because the DAEs representing the arm currents' dynamics depends upon the state of the capacitor voltages and vice versa. A hysteresis relaxation algorithm is applied at the interface for stable simulation across different external conditions.

Hysteresis Relaxation Algorithm: At any instant, the director switches in AAC can be in the ON or OFF state and the H-bridges can be in the blocked state based on the control methodology adopted. Under these conditions, there is numerical stiffness associated with the DAEs representing arm currents' dynamics. To reduce the numerical stiffness and for ease of discretization, a hysteresis loop is defined for the sgn function term in (2-1d), as shown in Fig. 2-4. The sgn function in (2-1d) is reflective of the blocked state of H-bridges with the director switch in the ON state. The relaxation algorithm is also applied to other conditions that introduce numerical stiffness, as shown in Fig. 2-5. The said conditions include (a) H-bridge SMs are in the blocked state and the director switch is in the OFF state and (b) H-bridge SMs are in the unblocked state and the director switch is in the ON state.

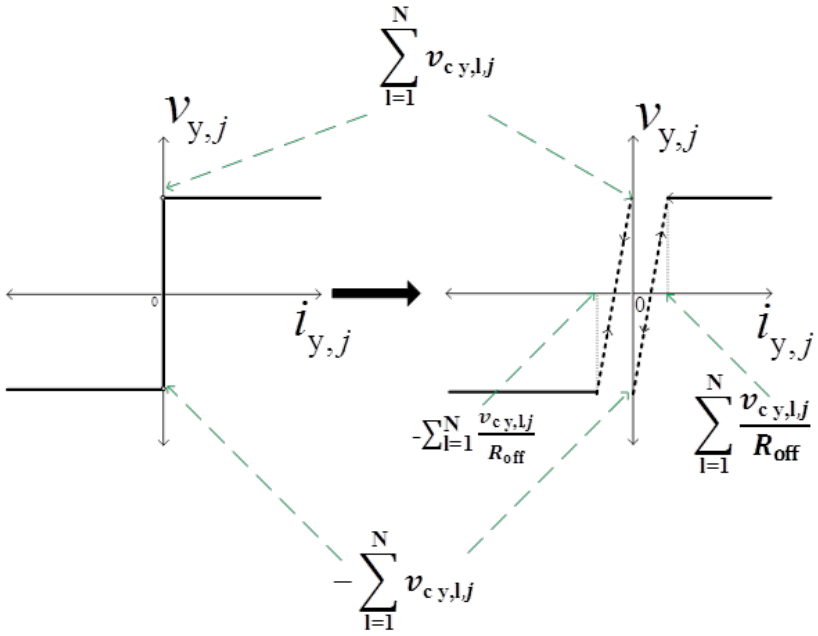

Figure 2-4: Hysteresis relaxation applied to arm currents' dynamics during H-bridge SMs blocked state with the director switch in the ON state.

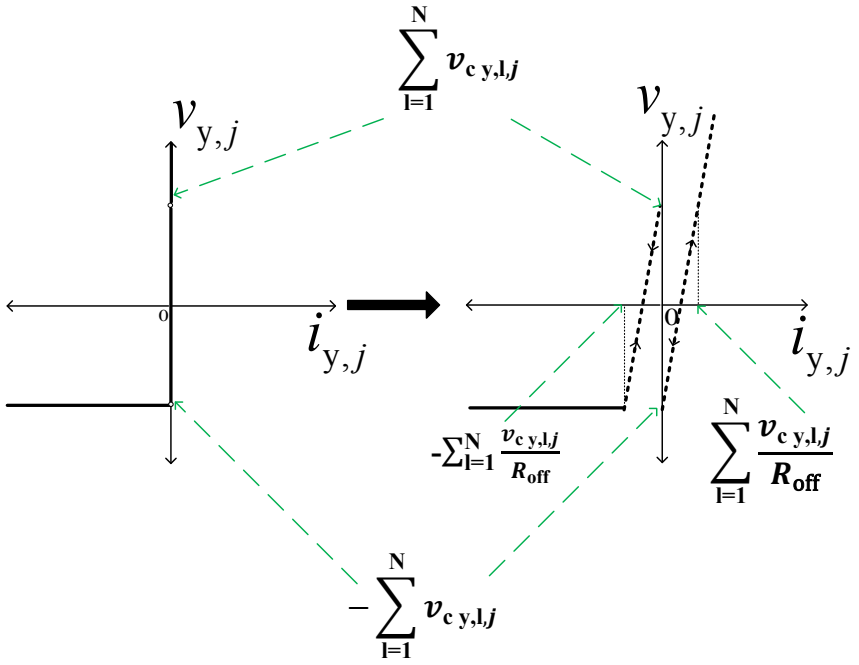

(a)

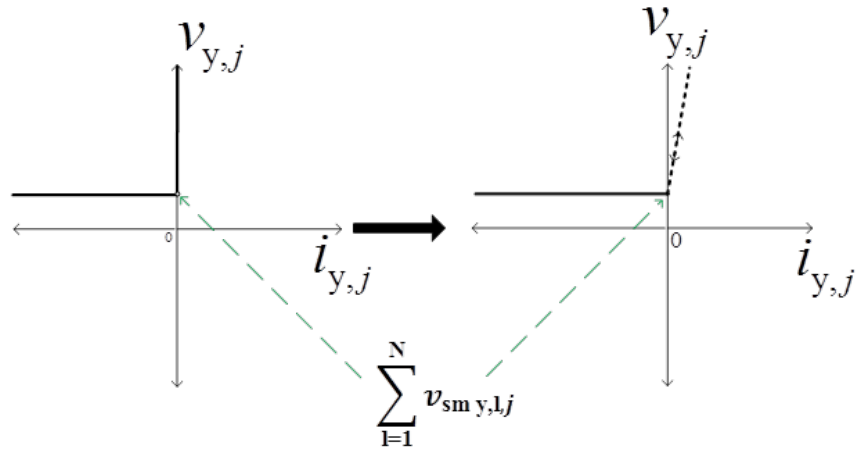

(b)

Figure 2-5: Hysteresis relaxation applied to arm currents' dynamics when (a) H-bridge SMs are in the blocked state and the director switch is in the OFF state and (b) H-bridge SMs are unblocked and the director switch is in the OFF state

Although the hysteresis relaxation reduces the numerical stiffness in the DAEs representing the arm currents' dynamics, the DAEs representing the arm currents' dynamics still require an implicit discretization with a stiff decay property like backward Euler. The use of backward Euler discretization allowed a higher slope in the hysteresis loop; the higher slope increased the accuracy of the simulation and avoided the requirement of very low time-steps (of the order of nanoseconds).

2.2 CTL Converters

The circuit diagram of the CTL VSC is shown in the Fig. 2-6. Phase *a* notation is only shown in Fig. 2-6. Phases *b* and *c* followed the similar notation as phase *a*. The CTL consists of three phase legs. Each phase leg consists of two arms: the upper arm and the lower arm. Each arm consists of "N" series connected half-bridge SMs and an inductor-capacitor-inductor (LCL) filter. Each switch in the half-bridge SMs uses eight series-connected press-pack IGBTs with antiparallel diodes [Jacobson 2010]. The press-pack IGBT offers short-circuit mode of failure, which provides safe operation of the CTL when one of the IGBTs fails. The LCL filter is sized to remove the second harmonic circulating current and limit fault currents. The value of "N" ranges from 50 today and can range up to a few hundred in the near future for HVdc applications with an increase in the dc voltage range.

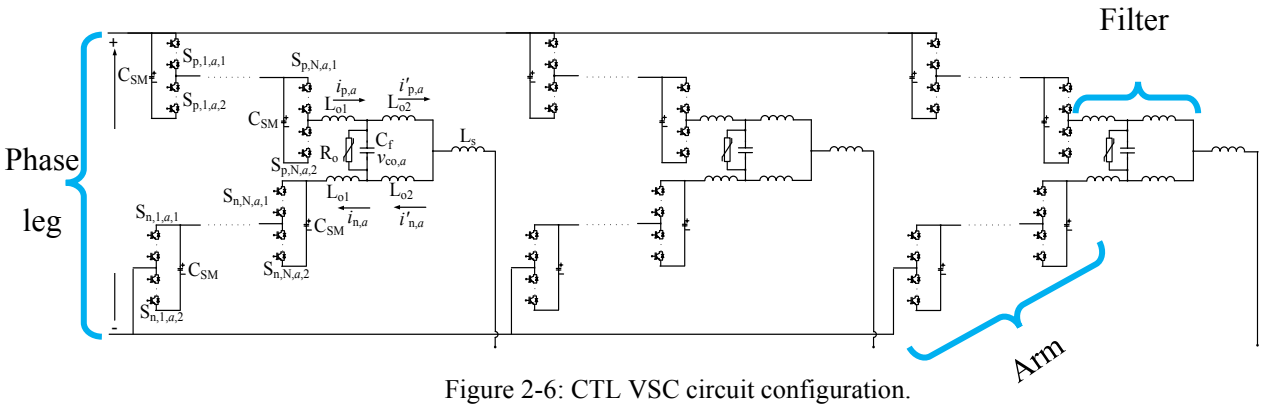

Figure 2-6: CTL VSC circuit configuration.

The differences between MMC and CTL arise in the switch configuration, the number of SMs per arm, the modulation strategy to control SMs, and the filter design in each arm. The switch in the SM of an MMC uses one power module that consists of an IGBT with an antiparallel diode. The power module has an open-circuit failure mode. It requires additional circuitry to ensure safe operation of the MMC when one of the IGBTs fails. The number of SMs per arm in CTL is one-eighth that of the MMC when connected to the same dc-side voltage. The difference arises due to the different switch configurations. The modulation strategy in the MMC is based on nearest level control that switches the SMs at nearly 60 Hz frequency (or, ac-side frequency). The modulation strategy in the CTL uses pulse-width modulation (PWM) with several hundred Hertz switching of each SM to get dynamic performance that is similar to that of the MMC. Compared to the LCL filter in the CTL, the filter in an MMC uses only an inductor. These differences made it imperative to model and simulate the CTL with a different approach to that of the MMC to reap significant computational gains.

The state-space modeling of CTL considers the arm currents, filter capacitor voltage, and SM capacitor voltages as the states, resulting in a total of "6N+12" states. Additionally, there are "12N" switching states based on the number of IGBTs in half-bridge SMs. From the calculated states, it was observed that several hundred to a few thousand states were present. The presence of a large number of diodes introduced numerical stiffness in the simulation models of the CTL. Moreover, the PWM applied to each CTL SM required very small time-steps (of the order of nanoseconds) to accurately identify switching pulses. These challenges resulted in a requirement for advanced simulation algorithms.

In this work, models of CTLs were developed to efficiently simulate large hybrid grids. The models were developed based on the formulation of the DAEs that describe the dynamics of the system. The developed

models were separated based on stiffness and time constants to allow hybrid discretization and multi-rate simulation that reduce the computational burden imposed. The hybrid discretization algorithm is based on explicit and implicit discretization algorithms without and with stiff decay properties. To enhance the stability of the separated systems, relaxation algorithms were applied to the interfaces created between the separated systems.

The terminal models developed for the CTL have already been explained earlier in Section 2.1.1.

2.3 EMT Model and Simulation Algorithm

CTL-HVdc Model: The EMT model of half-bridge-based CTL VSC system captures the dynamics of the 6N+12 states present. The states captured include the 6N capacitor voltages and the 12 inductor currents. From Fig. 2-6, the arm currents' dynamics are given by

$$(L_{o2}+L_s)\frac{di'_{p,j}}{dt}-L_s\frac{di'_{n,j}}{dt}+L_{o1}\frac{di_{p,j}}{dt}=-(R_{o2}+R_s)i'_{p,j}+R_s i'_{n,j}-R_{o1}i_{p,j}+\frac{V_{dc}}{2}-v_j-v_{cm}-v_{p,j},\forall j\in(a,b,c), \tag{2.3a}$$

$$(L_{o2}+L_s)\frac{di'_{n,j}}{dt}-L_s\frac{di'_{p,j}}{dt}+L_{o1}\frac{di_{n,j}}{dt}=-(R_{o2}+R_s)i'_{n,j}+R_s i'_{p,j}-R_{o1}i_{n,j}+\frac{V_{dc}}{2}+v_j+v_{cm}-v_{n,j},\forall j\in(a,b,c), \tag{2.3b}$$

$$v_{y,j}=\begin{cases}\sum_{l=1}^{N}v_{sm,y,l,j} & \text{if (SMs unblocked)}\\ \sum_{l=1}^{N}v_{c\,y,l,j} & \text{if (SMs are blocked and } i_{y,j}>0)\\ 0 & \text{if (SMs are blocked and } i_{y,j}<0)\\ \text{based on circuit conditions} & \text{if } (i_{y,j}=0)\end{cases},\forall j\in(a,b,c),\ y\in(p,n) \tag{2.3c}$$

$$v_{sm,y,l,j}=\{S_{y,l,j,1}S_{y,l,j,4}(1-S_{y,l,j,2})(1-S_{y,l,j,3})-S_{y,l,j,2}S_{y,l,j,3}(1-S_{y,l,j,1})(1-S_{y,l,j,4})+(1-S_{y,l,j,1})(1-S_{y,l,j,4})(1-S_{y,l,j,2})(1-S_{y,l,j,3})\,\mathrm{sgn}(i_{y,j})\}v_{c\,y,l,j},\forall j\in(a,b,c),\ y\in(p,n),\ l\in(1,N), \tag{2.3d}$$

$$L_{o2}\frac{di'_{p,j}}{dt}+L_{o2}\frac{di'_{n,j}}{dt}=-R_{o2}i'_{p,j}-R_{o2}i'_{n,j}+v_{c\,o,j},\forall j\in(a,b,c), \tag{2.3e}$$

$$i'_{p,j}-i'_{n,j}=i_{p,j}-i_{n,j} \tag{2.3f}$$

$$\mathrm{sgn}(x)=\begin{cases}1 \text{ if } x>0\\ 0 \text{ if } x<0\end{cases},\qquad v_{cm}=\frac{1}{6}\sum_{j\in(a,b,c)}(v_{n,j}-v_{p,j}),\qquad \sum_{j\in(a,b,c)}i_{p,j}=\sum_{j\in(a,b,c)}i_{n,j} \tag{2.3g}$$

The SM capacitor voltages' dynamics are given by

$$C_{SM}\frac{dv_{c\,y,l,j}}{dt}=-\frac{v_{c\,y,l,j}}{R_p}+\{S_{y,l,j,1}(1-S_{y,l,j,2})+(1-S_{y,l,j,1})(1-S_{y,l,j,2})\,\mathrm{sgn}(i_{y,j})\}i_{y,j},\forall j\in(a,b,c),y\in(p,n),l\in(1,N) \tag{2.4}$$

Equations (2.3) and (2.4) represent a semi-explicit DAE with numerical stiffness introduced due to the presence of a sgn function. The sgn function arises from the modeling of diodes that are present in the CTL VSC system.

The separation of the DAEs representing the arm currents' dynamics from the DAEs representing the capacitor voltages' dynamics were easily achieved using an explicit discretization algorithm. However,

due to the numerical stiffness observed, explicit discretization cannot be applied to both the DAEs. The proposed separation of the DAEs is based on numerical stiffness and a hysteresis relaxation algorithm.

Hybrid Discretization Algorithm: The model of CTL is separated based on the numerical stiffness associated with the DAEs representing the dynamics of the states. The DAEs representing the dynamics of the separated states are discretized using hybrid discretization. While the DAEs representing the dynamics of SM capacitor voltages were discretized using non-stiff explicit discretization algorithm like forward Euler, the DAEs representing the dynamics of arm current dynamics were discretized using an implicit discretization algorithm with stiff-decay property like backward Euler. The separated DAEs were interfaced using a relaxation algorithm that is explained in the "Hysteresis Relaxation Algorithm" section below.

The use of hybrid discretization resulted in inverting only a 11×11 matrix at every instant in the simulation of the proposed CTL VSC model. In the conventional simulation of CTL VSC models, the simulation of CTL VSC will require the inversion of a $(6N+12) \times (6N+12)$ matrix. Thus, the computational burden imposed by the simulation of the proposed CTL VSC model is significantly reduced.

Hysteresis Relaxation Algorithm: In normal operating conditions, one of the switches in the half-bridge SM is in the ON state. If the upper switch is in the ON state, the SM is said to be in the ON state. If the lower switch is in the ON state, the SM is said to be in the OFF-state. When the SM is in the ON/OFF state, the sgn functions in (2.3) and (2.4) are no longer present. Hence, there is no numerical stiffness associated with the DAEs representing the arm currents' dynamics.

In the blocked condition, both the switches in the half-bridge SM are in the OFF state. The blocked condition arises during external faults. Under this condition, the sgn function present in (2.3) introduces numerical stiffness in the DAEs representing the arm currents' dynamics. To reduce the numerical stiffness and for ease of discretization, a hysteresis loop was defined for sgn function term in (2.3), as shown in Fig. 2-7.

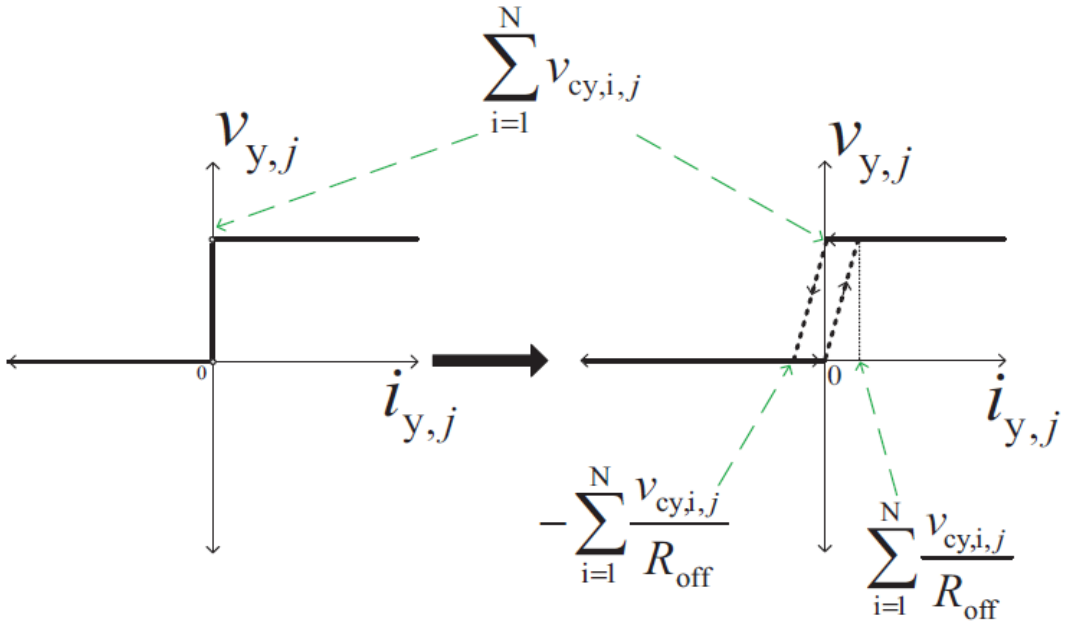

Figure 2-7: Hysteresis relaxation applied to arm currents' dynamics.

Although the hysteresis relaxation reduces the numerical stiffness in the DAEs representing the arm currents' dynamics, the DAEs representing the arm currents' dynamics still required an implicit discretization with a stiff decay property like backward Euler. The use of backward Euler discretization allowed a higher slope in the hysteresis loop that increased the accuracy of the simulation and avoided the requirement of very small time-steps (of the order of nanoseconds).

Multi-Rate Simulation: In addition to the hybrid discretization and relaxation algorithms, multi-rate simulation was adopted to reduce the burden imposed by the very small time-steps requirement. A smaller time-step was adopted for the PWM applied to each CTL SM and the corresponding capacitor voltage-balancing control method. A larger time-step was adopted for the updates provided to the upper-level CTL control. The upper-level control algorithms typically adopt a larger time-step. The use of hybrid discretization reduced the matrix inversion requirements by applying a larger time-step to evaluate the dynamics of the arm currents, thus reducing the computational requirements in simulating CTLs.

2.4 Detailed Power System Computer Aided Design (PSCAD) reference models

The benchmarking case study to validate the developed AAC and CTL VSC models was based on the HVdc interconnection link between France and Spain (the INELFE project). The INELFE project can transmit a rated power of 1 GW with a transmission voltage of ±320 kV dc with two MMCs [Abdel-Moamen 2017]. The ratings of INELFE converter station are tabulated in Table 2-1. The MMCs in the project are replaced by AAC and CTL substations in the benchmarking case studies.

Table 2-1: Parameter ratings of INELFE converter station.

Parameter	Alternate Arm Converter
Power	1 GW
dc Voltage (V_{dc})	±320 kV
ac Voltage (V_{ac})	333 kV

2.4.1 AAC Design

The circuit parameters that needed to be identified in AAC are the number of SMs, arm inductance, SM capacitance, and the corresponding voltage ratings. The number of SMs in one arm of the AAC was given by [Wickramasinghe 2017]:

$$N_{\text{sm}} = 1.1 \times \frac{2}{\pi} \times \frac{V_{\text{dc}}}{V_{\text{C}}} = 1.1 \times \frac{2}{\pi} \times \frac{640}{1.6} = 280.113 \cong 280, \tag{2.5}$$

where V_{dc} is dc-link voltage and V_{C} is SM capacitor voltage.

In the AAC, the arm inductance mainly depends on the requirements of the circulating current control. The two limiting factors in the circulating current control were redundant voltage and maximum overlap period. Redundant voltage (V_{r}) is defined by difference between the SM capacitor voltages and half the dc-link voltage [Wickramasinghe 2017].

The overlap period is the time period of switching on both the arm in the AAC and is explained in detail under the "AAC Control" section. Under the assumption that 50% of redundant voltage is available for an overlap period of $t_{\text{ov}}/2$, the arm inductance can be calculated as given below [Wickramasinghe 2017]

$$L \leq \frac{3V_{\text{dc}}V_{\text{r}}}{4\pi\omega S} \sin^{-1}\left(\frac{\widehat{m_a}-1}{m_a}\right), \tag{2.6}$$

where m_{a} is the modulation index at normal operating point, $\widehat{m_a}$ is the modulation index at the sweet spot, and S is the apparent power rating of the converter station. The sweet spot is the operating condition of AAC with inherent energy balance between the SMs in the arms.

The sizing of the SM capacitor depends mainly on the peak-to-peak energy deviation. The peak-to-peak energy deviation is the difference between the maximum and minimum energy deviations [Merlin 2015]. The energy requirements of the AAC are comparatively lower than that of the MMC and approximately equal to a third of the typical stored energy of the MMC. The stored energy of the AAC (E_{AAC}) is set to 11 kJ/MVA to achieve the same ripple target [Abdel-Moamen 2017] [Wickramasinghe 2017]. The required SM capacitance was determined as

$$C = \frac{SE_{AAC}}{3NV_C{}^2} = \frac{1000\times11}{3\times281\times1.6^2} = 5.097\ \text{m}F, \tag{2.7}$$

where E_{AAC} is the stored energy in AAC. Voltage across the director switch is the difference between the converter voltage and the voltage across the nonconducting SMs. The maximum voltage over the director switches was given by [Merlin 2014] [Najmi 2015]

$$V_{\text{DS max}} = \frac{4+\pi}{2\pi} V_{\text{dc}} - \frac{V_{\text{dc}}}{2} \tag{2.8}$$

The number of series IGBTs in a director switch was obtained by the ratio of V_{DSmax} to Vc. The designed circuit parameters for AAC are tabulated in Table 2-2.

Table 2-2: AAC design parameters.

Parameter	**Value**
Number of SMs per arm	280
Arm inductance	12.31 mH
Capacitor value for a SM	5.115 mF
Redundant voltage (V_{r})	128.179 kV
Maximum director switch voltage (V_{DS})	407.437 kV
Capacitor SM voltage (V_{C})	1.6 kV
IGBT voltage rating	3.3 kV
Cell capacitor deviation	10%
Stored energy	11 J/MVA

2.4.2 AAC Control

The overview of the control system of the AAC is shown in Fig. 2-8.

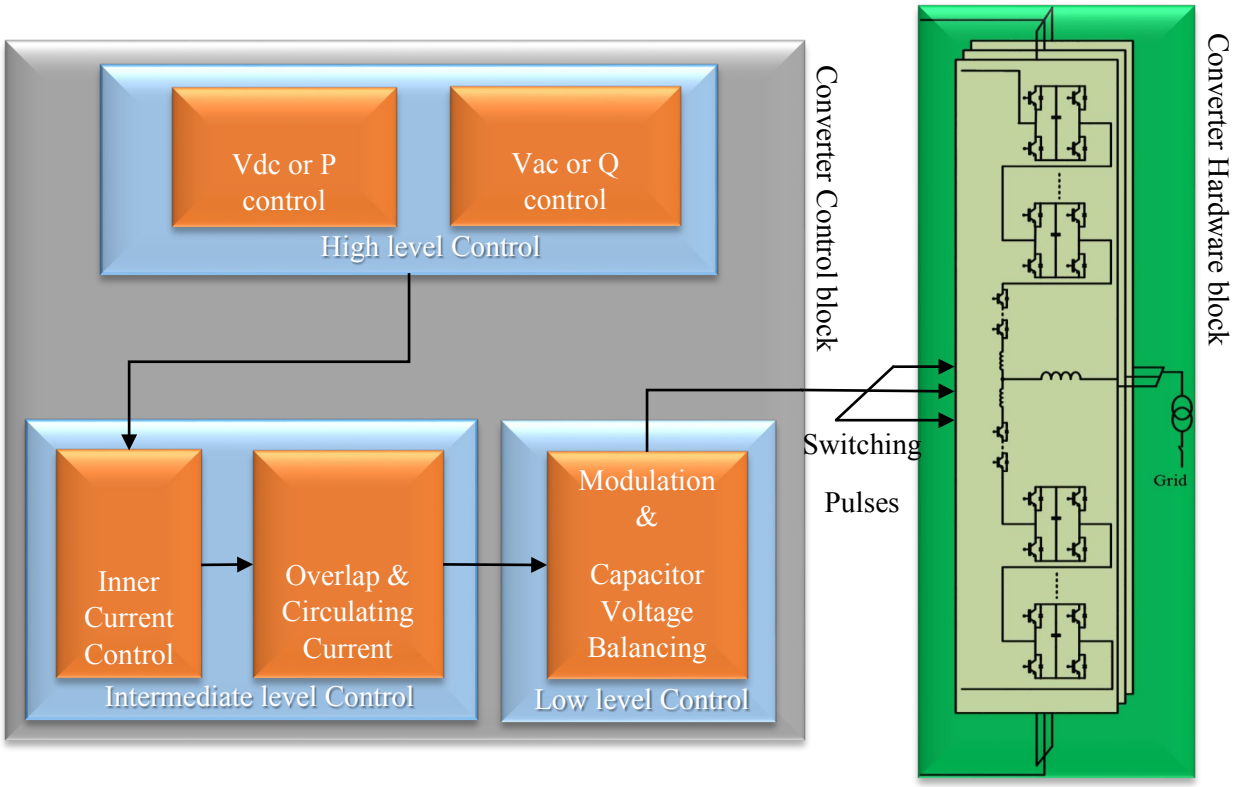

Figure 2-8: Control system of AAC [Wickramasinghe 2017].

The intermediate-level control functions include inner current control (or, ac-side current control) and provides the output modulation index reference. The modulation index is the normalized arm voltage reference. The intermediate-level control functions also include the overlap period, circulating current control, and director switch control. The normal mode of operation of a phase leg of the AAC is such that the director switches operate alternately, each conducting the ac-side current during half of the fundamental cycle. The upper and lower arms conduct during the positive and negative half cycles of the ac-side voltage, respectively. AAC has inherent energy balance between the SMs in the arms at one operating point $\widehat{m_a} = \frac{4}{\pi} \approx 1.27$, known as "the sweet spot" [Merlin 2014], but the energy balance does not occur at other operating points. To balance the energy, a short time period, known as an "overlap time period," was introduced to exchange the energy from upper arm to lower arm and vice versa. This overlap period reduces the divergence of SM capacitor voltage from its reference. The overlap period was determined based on the control of the average SM capacitor voltage error within the phase-leg [Najmi 2015, Mathew 2014, Wickramasinghe 2016], as shown in Fig. 2-9. The overlap period was distributed evenly across the zero-crossing point of the ac-side voltage reference. In this overlap period, the circulating current is controlled based on the reference current, which is proportional to the peak ac-side current, and on the sign of the voltage error. The overview of the circulating current control is shown in Fig. 2-10(a). The low-level control includes the SM capacitor voltage balancing algorithm and arm modulation index generator.

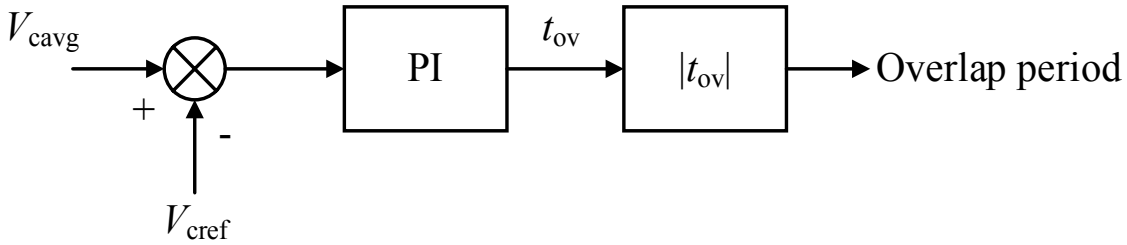

Figure 2-9: Overlap period control.

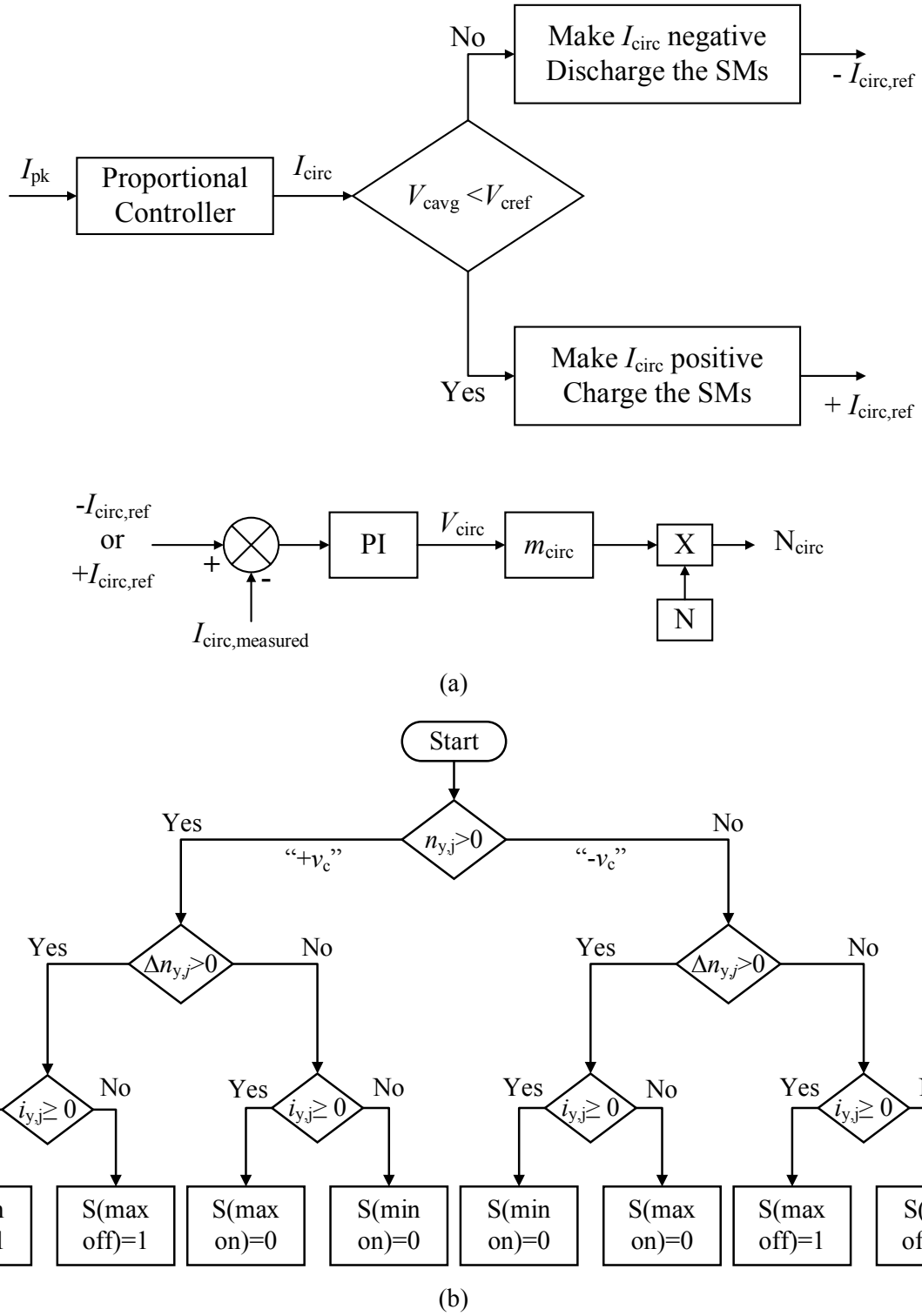

Figure 2-10: AAC control system: (a) Circulating current control, (b) Flowchart for the SM capacitor voltage balancing algorithm

The modulation indices of the upper and lower arms are given below

$$m_{p,j} = \begin{cases} \left(\frac{1-m_j}{2}\right) \times \frac{\pi}{2*1.1} & \forall \quad 0 \le \omega t < \frac{T}{2} - \frac{t_{ov}}{2} \\ \left(\frac{1-m_j}{2} + m_{circ,j}\right) \times \frac{\pi}{2*1.1} & \forall \quad \left(\frac{T}{2} - \frac{t_{ov}}{2}\right) \le \omega t \le \left(\frac{T}{2} + \frac{t_{ov}}{2}\right) \end{cases}, \tag{2.9a}$$

$$m_{n,j} = \begin{cases} \left(\frac{1+m_j}{2}\right) \times \frac{\pi}{2*1.1} & \forall \quad \left(\frac{T}{2} + \frac{t_{ov}}{2}\right) < \omega t \le T \\ \left(\frac{1+m_j}{2} + m_{circ,j}\right) \times \frac{\pi}{2*1.1} & \forall \quad \left(\frac{T}{2} - \frac{t_{ov}}{2}\right) \le \omega t \le \left(\frac{T}{2} + \frac{t_{ov}}{2}\right) \end{cases}, \tag{2.9b}$$

where m_j represents the modulation index of phase-*j* generated from inner current control, and $m_{circ,j}$ represents the modulation index of phase-*j* generated from the circulating current control.

Based on the arm modulation indices, the number of SMs inserted in arm-y, phase-j is given by

$$n_{y,j} = \lfloor \mathrm{N} m_{y,j} \rfloor \quad (2.10)$$

where $\lfloor . \rfloor$ denotes the floor operation.

Each SM in an AAC was positively inserted, bypassed, and negatively inserted. The corresponding SM voltage contributions to the arm voltage are $+v_c$ positively inserted 0 bypassed, and $-v_c$ negatively inserted. The mapping of the switch states to the SMs of each arm was performed based on the SM capacitor voltage balancing algorithm [Debnath 2015a]. The algorithm relies on the following

1. the sign of $n_{y,j}$;
2. the difference in the number of inserted SMs in each arm, within the present and the previous sampling period;
3. the direction of the arm current; and
4. the measured SM capacitor voltages.

The sign of $n_{y,j}$ determines whether the SMs are positively inserted or negatively inserted. The difference in the number of inserted SMs specified whether additional SMs would need to be bypassed or inserted. The difference in the number of inserted SMs is given by

$$\Delta n_{y,j}[k] = n_{y,j}[k] - n_{y,j}[k-1] \quad (2.11)$$

where $n_{y,j}$ [k] and $n_{y,j}$ [k-1] represent the present and previous sample of $n_{y,j}$, respectively. The direction of the arm current determines whether the SM module is charged ($i_{y,j} > 0$) or discharged ($i_{y,j} < 0$) when positively inserted. The decision to insert or bypass the SMs is made on the following:

1. If $n_{y,j}$ [k] > 0 and $\Delta n_{y,j}[k] > 0$, from the bypassed SMs, $\Delta n_{y,j}[k]$ SMs with the highest (lowest) capacitor voltages are positively inserted, if $i_{y,j} < 0$ ($i_{y,j} \geq 0$) , i.e. S(max off) = 1, S(min off) = 1.
2. If $n_{y,j}$ [k] > 0 and $\Delta n_{y,j}[k] < 0$, from the inserted SMs, $\Delta n_{y,j}[k]$ SMs with the lowest (highest) capacitor voltages are bypassed, if $i_{y,j} < 0$ ($i_{y,j} \geq 0$) , i.e. S(min on) = 0, S(max on = 0.
3. If $n_{y,j}$ [k] < 0 and $\Delta n_{y,j}[k] > 0$, from the negatively inserted SMs, $\Delta n_{y,j}[k]$ SMs with the lowest (highest) capacitor voltages are bypassed, if $i_{y,j} \geq 0$ ($i_{y,j} < 0$), i.e. S(min on) = 0, S(max on) = 0.
4. If $n_{y,j}$ [k] < 0 and $\Delta n_{y,j}[k] < 0$, from the bypassed SMs, $\Delta n_{y,j}[k]$ SMs with the highest (lowest) capacitor voltages are negatively inserted, if $i_{y,j} \geq 0$ ($i_{y,j} < 0$), i.e. S(max off) = 1, S(min off) = 1.

The detailed flowchart for the capacitor voltage balancing algorithm is shown in Fig. 2-10(b).

2.4.3 Validation & Comparison of Proposed AAC Model with Reference

A comparison of the proposed AAC model with a reference model developed in PSCAD was performed. The proposed model was developed in FORTRAN90 language and embedded within PSCAD. The detailed reference AAC model was developed based on SM models from Conseil International des Grands Réseaux Électriques (CIGRE) B4 models and other basic building blocks in PSCAD like IGBTs, diodes, and inductors. The parameters that describe the use case are listed in Tables 2-1 and 2-2. The simulation parameters are shown in Table 2-3.

Table 2-3: Simulation parameters of AAC.

Parameter	Value
h	4 µs
R_{on}	1 mΩ
R_{off}	1 MΩ

The errors observed between the states of the AAC in the simulation of the proposed AAC and the reference models are less than 1%. The errors are calculated as a difference between the values of the state in the developed method with respect to the reference method. The corresponding states are shown in Figs. 2-11, 2-12, and 2-13 for steady-state operation, dynamic operation, and blocked operations, respectively. The results in the figure show similarities between the developed model and the reference model. The time taken to simulate the reference PSCAD model based on existing modeling methods took 350 s to simulate 0.5 s, as compared to 31 s taken by the developed method. The speedup observed is 11.5×.

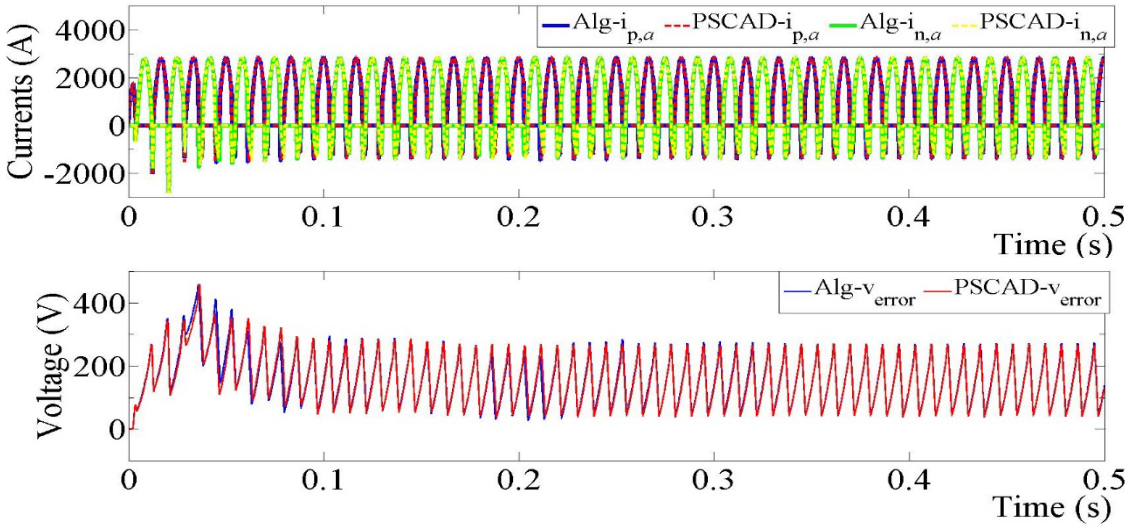

Figure 2–11: Simulation of AAC-HVdc in steady state: (top) arm currents and (bottom) voltage error as a difference of SM capacitor voltage with respect to reference voltage.

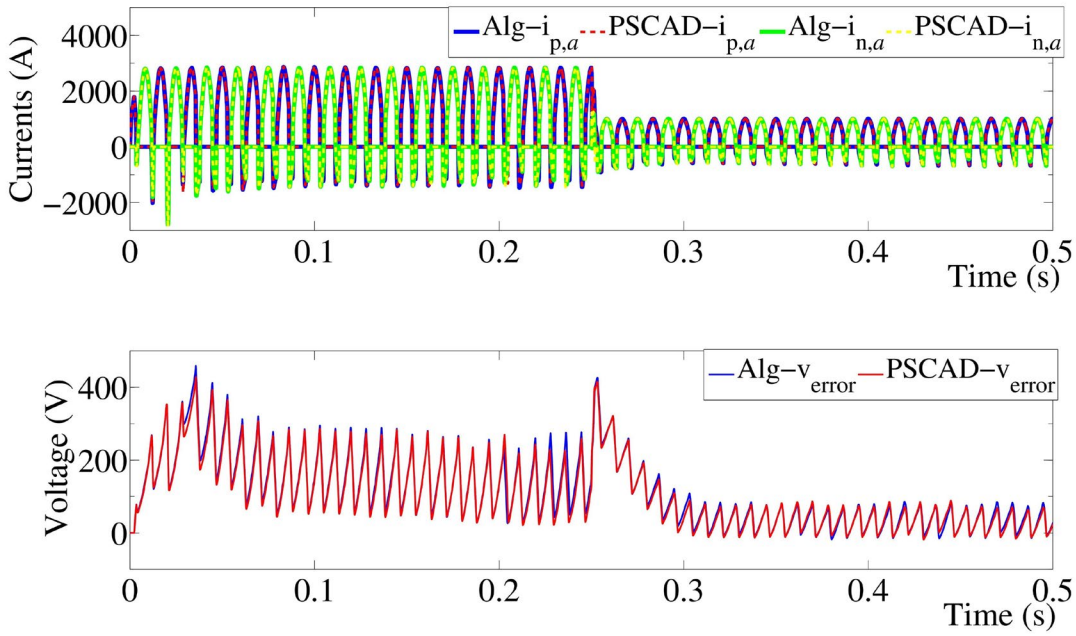

Figure 2-12: Simulation of AAC-HVdc under step-change in current reference: (top) arm currents and (bottom) voltage error as a difference of SM capacitor voltage with respect to reference voltage.

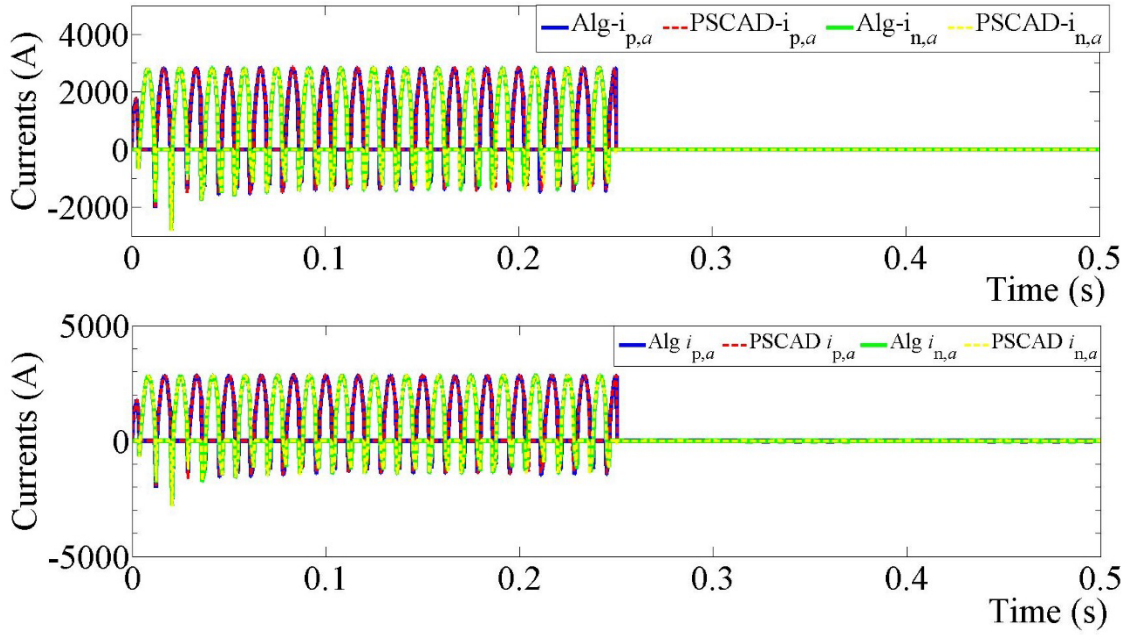

Figure 2-13: Simulation of AAC-HVdc under different blocked scenarios: (top) arm currents under director switches unblocked and SMs blocked scenario and (bottom) arm currents in the director switches and SMs blocked scenario

2.4.4 CTL Design

Based on the INELFE project's specifications (provided in Table 2-1) and the fact that 8 series connected IGBTs represent one switch in an SM, the voltage rating and switching frequency of the SM in a CTL are tabulated in Table 2-4.

Table 2-4: Parameter ratings of an SM in a CTL.

Parameter	Value
IGBT Voltage Rating	3.3 kV
No. of Modules	50
Sub Module Switching Frequency	360 Hz
Capacitor Voltage (V_C)	12.8 kV

The LCL filter in the CTL was designed based on the requirement to eliminate the second harmonic component of the circulating currents. The equivalent circuit representation of the LCL filter to identify its dependence on the circulating currents in AAC is shown in Fig. 2-14.

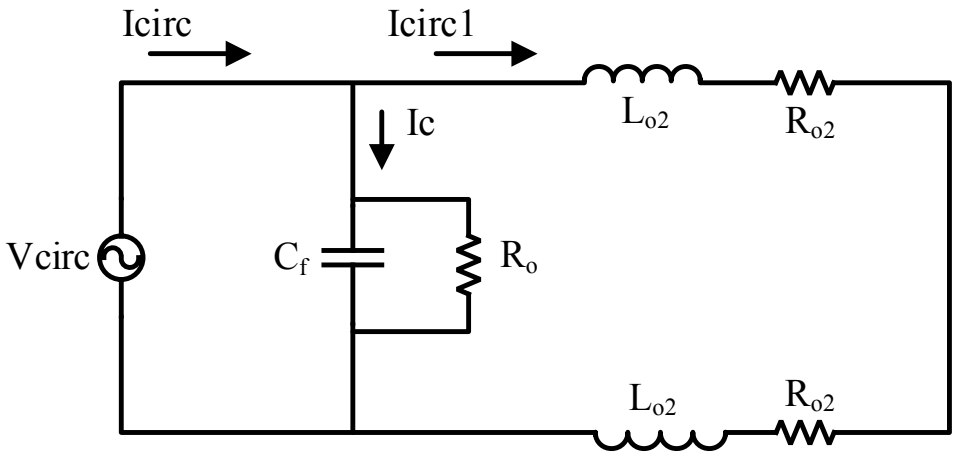

Figure 2-14: Equivalent circuit of the LCL filter in AAC.

The following procedure was used to determine the size of the filter components:

The admittance ($\frac{I_{circ}}{V_{circ}}$) for the circuit in Fig. 2-14 is given by

$$\frac{R+2s^2L_2RC+2sL_2+2sCRR_2+2R_2}{4s^3L_1L_2RC+4s^2(L_2R_1RC+L_1R_2RC+L_1L_2)+2s(L_1R+L_2R)+4s(L_2R_1+L_1R_2+R_1R_2RC)+(4R_1R_2)} \quad (2.12)$$

The reactors L_1 and L_2 are 50 mH and 15 mH; R is 20 kΩ. This assumption was based on the fact that the arm inductors chosen for the CTL should be similar to that of the INELFE project's arm inductors. The arm reactor of the MMC is 65 mH. The value of the R is designed so high to incur very low losses.

The admittance of the circuit at second harmonic frequency was calculated for the circuit shown in Fig. 2-14 and was kept at a small value. The small value of the admittance eliminated the second harmonic circulating current. The capacitor C can then be calculated as following

$$C = \frac{1}{(8\omega^2 L_2)} = 58.632\ \mu F \tag{2.13}$$

Assuming E = 33 kJ/MVA, the required SM capacitance can be determined as

$$C_{\mathrm{SM}} = \frac{SE}{3NV_C{}^2} = \frac{1{,}000\times 33}{3\times 50\times 12.8^2} = 1.3\ mF \tag{2.14}$$

The parameters of CTL are summarized in Table 2-5.

Table 2-5: CTL design parameters.

Component	Value
Reactor L_1	50 mH
Reactor L_2	15 mH
Reactor Resistance R_1	0.8 Ω
Reactor Resistance R_2	0.8 Ω
LCL filter resistance R	20 kΩ
LCL filter capacitor C	58.632 µF
C_{SM}	1.3 mF

2.4.5 CTL Control

The control system of the CTL consists of two levels [Jacobson 2010] and is shown in Fig. 2-15:

- An upper-level control that calculates the arm modulation indices from various measurements of system variables and the inner current control and
- A lower-level control that performs the SM capacitor voltage control at each SM and the PWM generation.

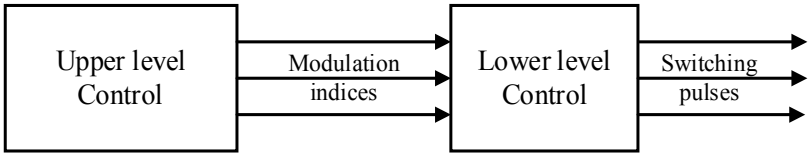

Figure 2-15: Block diagram for upper-level and low-level Submodule control

The inner current control in the upper-level control is the same as the inner current control implemented for AAC. The modulation indices of the upper and lower arms are given below:

$$m_{p,j} = -\frac{m_j}{2} + m_{circ,j}$$

$$m_{n,j} = \frac{m_j}{2} + m_{circ,j} \tag{2.15}$$

The arm modulation indices generated at the upper-level control were sent to each SM. The SM capacitor voltage control in the lower-level control introduced an additional term in each SM's modulation index. The additional term was based on maintaining SM capacitor voltage at its reference. This term is small enough to minimize distortions to the ac-side voltage and was set proportional to the error between the SM-voltage reference and the individual SM voltage. Based on phase-shifted PWM, the switching signals for each SM was generated using the modulation index determined in the SM. The carrier frequency in PWM is taken to be 360 Hz.

2.4.6 Validation & Comparison of Proposed CTL Model with Reference

A comparison of the proposed CTL model with a reference model developed in PSCAD was performed. The proposed model was developed in FORTRAN90 language and embedded within PSCAD. The detailed reference CTL model was developed based on SM models from CIGRE B4 models. The parameters that describe the use case are listed in Tables 2-4 and 2-5. The simulation parameters are shown in Table 2-6.

Table 2-6: Simulation parameters of CTL.

Parameter	Value
h	60 µs
R_{on}	1 mΩ
R_{off}	1 MΩ

The errors observed between the states of the CTL in the simulation of the proposed CTL and the reference models are less than 1%. The corresponding states are shown in Figs. 2-16 and 2-17 for dynamic operation and blocked operations. The results in the figure show similarities between the developed model and the reference model. The time taken to simulate the reference PSCAD model based on existing modeling methods took 83 s to simulate 1 s, as compared to 6.8 s taken by the developed method. The speedup observed is 12.2×.

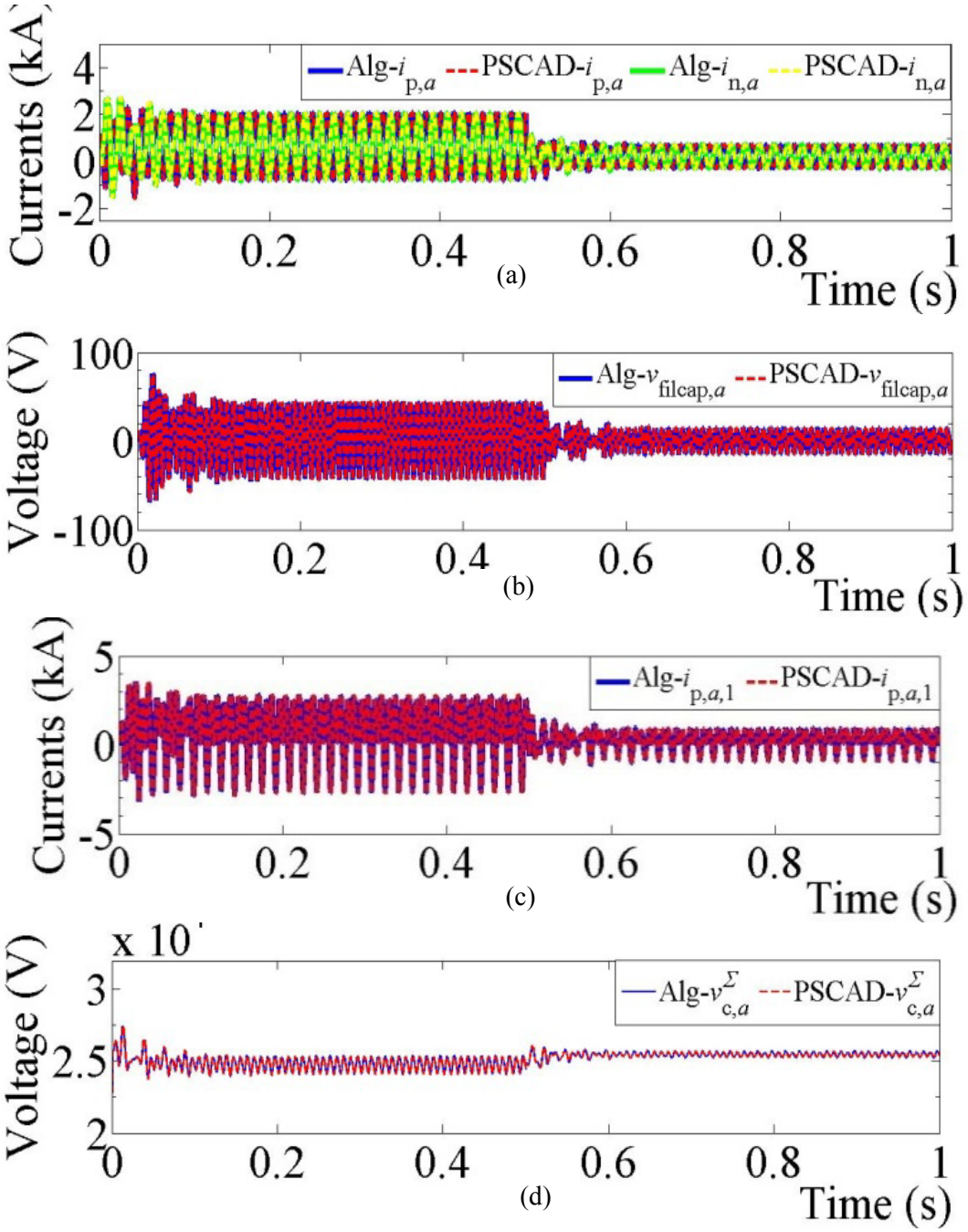

Figure 2–16: Simulation results from developed model and reference models of CTL under step-change in current reference: (a) arm currents, (b) filter capacitor voltages, (c) filter currents, and (d) SM capacitor voltages.

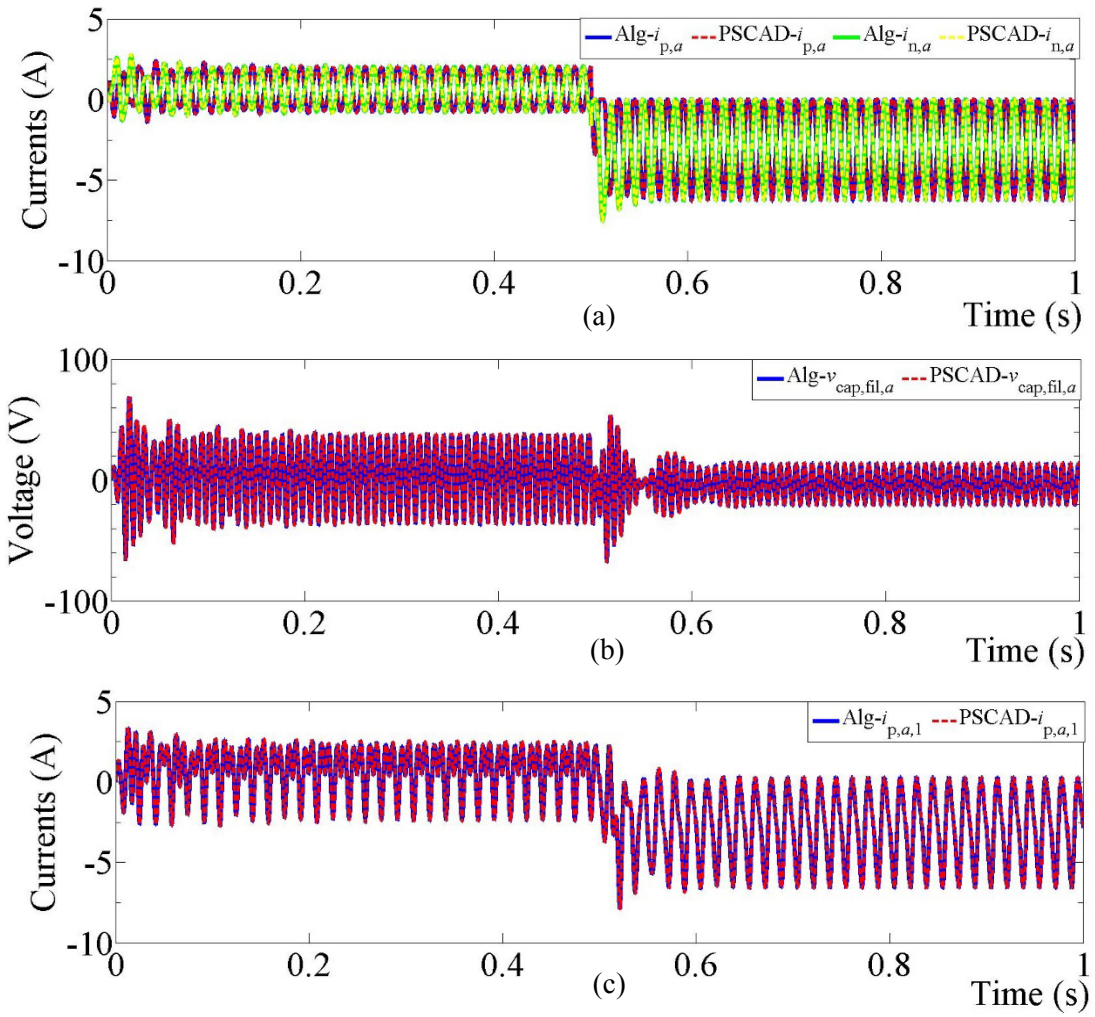

Figure 2-17: Simulation results from developed model and reference models of CTL during blocked scenario: (a) arm currents, (b) filter capacitor voltages, and (c) filter currents.

Application of parallel-in-time simulation algorithms to EMT simulation of MMCs is briefly introduced in Appendix A. Further work on application of parallel-in-time simulation algorithms to EMT simulation of VSCs will be considered as part of future work.

Chapter 3 Hybrid Simulation to Study Voltage Control in VSC-HVdc Systems

Hybrid simulation is defined as the co-simulation of EMT models with electromechanical transient stability (TS) models. In this chapter, the impact of the voltage control method in a point-to-point VSC-HVdc (in particular, MMC-HVdc) system on the wider ac system behavior (in particular, the EI ac transmission grid) was studied using hybrid simulation. The dynamics of the wider ac system are represented by the TS model in PSS®E. The dynamics of the point-to-point VSC-HVdc and the local ac systems are represented by the EMT model in PSCAD. The local ac systems, or buffer zones, are regions near the VSC-HVdc terminals. The dynamics of the local ac system are represented by the EMT model to accurately capture high-bandwidth dynamics and voltage behavior in the regions. The requirement to capture the high-bandwidth dynamics in the buffer zone arose from the need to understand the stability of the high-bandwidth advanced control methods (like voltage control) in a point-to-point VSC-HVdc system. Other advanced control methods, such as provision of virtual inertia, provision of support during symmetrical and asymmetrical ac faults using negative sequence injections, black start capability, and power oscillation damping, can also be studied in the future through the hybrid simulation platform developed. The requirements of and challenges associated with hybrid simulation are identified in this chapter. The requirements include the identification of the fidelity of models and the size of the buffer zones. The challenges include speed of simulation (or equivalently, the computational burden) and the limitations in software. The speed of simulation was resolved using multi-rate simulation methods for power electronics (like VSCs in this study).

The results from hybrid simulations in PSCAD and PSS®E show that capturing the high-bandwidth dynamics is relevant to studying the impact of advanced control methods in VSCs, such as voltage control. In these simulations, a significant computational burden was imposed by PSCAD; the burden was mitigated using multi-rate simulation methods for power electronics.

3.1 Hybrid Simulation Case Study

The ac system voltage control provided by a point-to-point VSC-HVdc system connecting Atlanta, Georgia, to Orlando, Florida, was studied in this chapter. The point-to-point VSC-HVdc system may be considered as part of the larger HVdc macrogrid, as shown by the blue dashed line in Fig. 3-1. The VSC substation in this study is based on an MMC. The impact of the ac voltage control provided by the point-to-point MMC-HVdc system was evaluated using hybrid simulation. The dynamics of the point-to-point MMC-HVdc system are represented by EMT models in PSCAD. Additionally, buffer zones are defined in the regions surrounding the points of injection of MMC-HVdc substations, that is, Atlanta, Georgia, and Orlando, Florida. The dynamics of these buffer zones were also represented by EMT models in PSCAD to accurately capture the high-bandwidth dynamics associated with the control of the MMC-HVdc substation. The defined buffer zones also accurately captured the dynamics of the voltage. The dynamics of the rest of the system in EI and WI are represented by TS models in PSS®E. The hybrid simulation of the models in PSCAD and PSS®E was performed using E-Tran software.

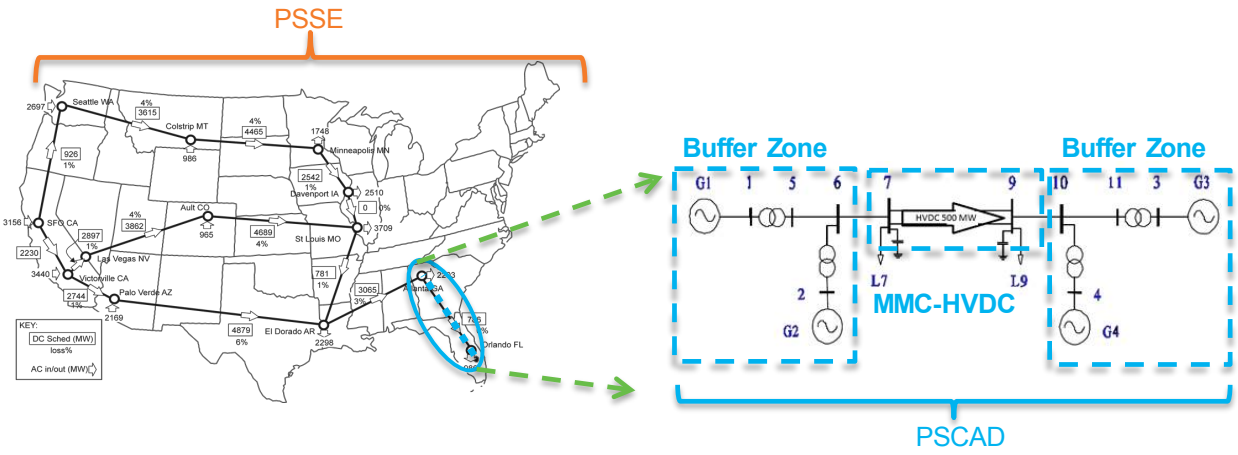

Figure 3-1: PSS®E-PSCAD hybrid simulation of one line of the HVdc Macrogrid model.

3.2 Point-to-Point MMC-HVdc Substation Model and Voltage Control

The EMT models of and the control methods used in MMC-HVdc substation are explained in this section. In addition to the accurate high-fidelity EMT dynamic model of MMC-HVdc substation and the corresponding simulation algorithms presented in [Makarov 2017], there is a fast simulation algorithm explained in this section based on multi-rate methods to speed up large system simulations.

3.3 MMC-HVdc Substation Models & Simulation Algorithms

The circuit diagram of a three-phase MMC is shown in Fig. 3-2. It consists of six arms with *N* series connected SMs and an inductor. The basic operation of the MMC is explained in detail in [Debnath 2016a]. The dynamics of MMC are based on the dynamics of the arm currents and SM capacitor voltages.

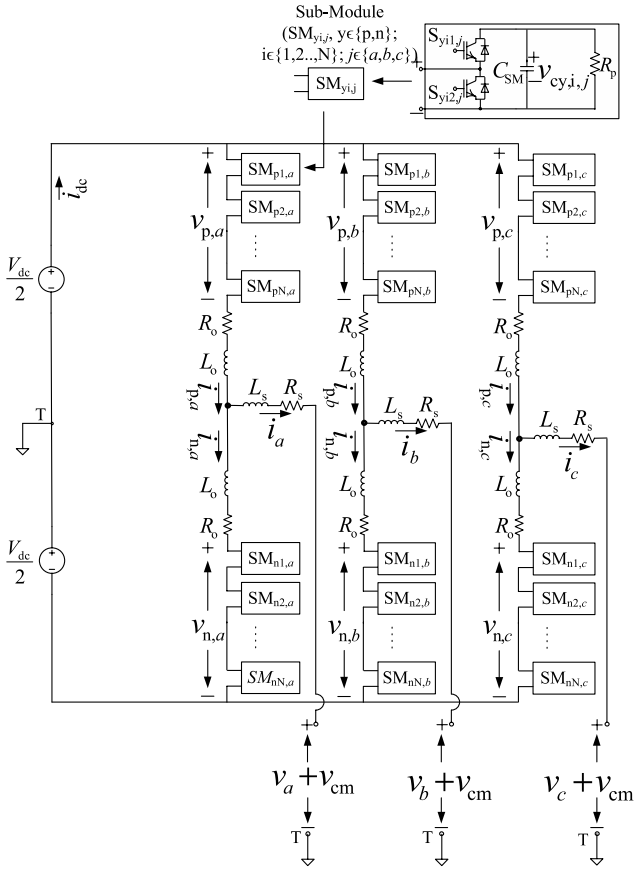

Figure 3-2: Circuit diagram of an MMC.

The dynamics of the arm currents and SM capacitor voltages of the MMC shown in Fig. 3-1 are explained in detail in [Haileselassie 2012]. They form a set of semi-explicit DAEs that represent the overall dynamics of the MMC. There was numerical stiffness observed in the DAEs that describe the arm currents' dynamics. Hence, the dynamics of the arm currents are discretized using algorithms like backward Euler that possess the stiff-decay property. As no numerical stiffness was observed in the DAEs that represent the SM capacitor voltage dynamics, they are discretized using non-stiff algorithms like forward Euler. A more detailed description of the hybrid discretization algorithm based on the numerical stiffness associated with the DAEs and relaxation algorithms can be found in [Haileselassie 2012].

3.3.1 MMC-HVdc Substation Control Strategies

The hierarchical control in an MMC-HVdc substation consists of (1) an inner control system to control ac transmission grid currents, dc-link currents, circulating currents, and SM capacitor voltages and (2) an outer control system to control ac transmission grid voltage and mean of SM capacitor voltages. The inner control system in MMC-HVdc substation has been explained in [Debnath 2016b] and is summarized in Figs. 3-3 and 3-4. The ac transmission grid currents, dc-link currents, and circulating currents' control strategy is shown in Fig. 3-3. The SM capacitor voltage-balancing algorithm is shown in Fig. 3-4.

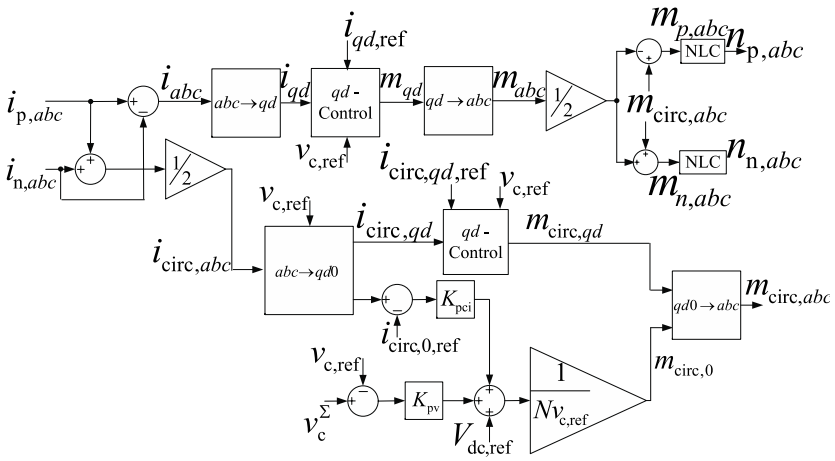

Figure 3-3: MMC-HVdc substation's current control.

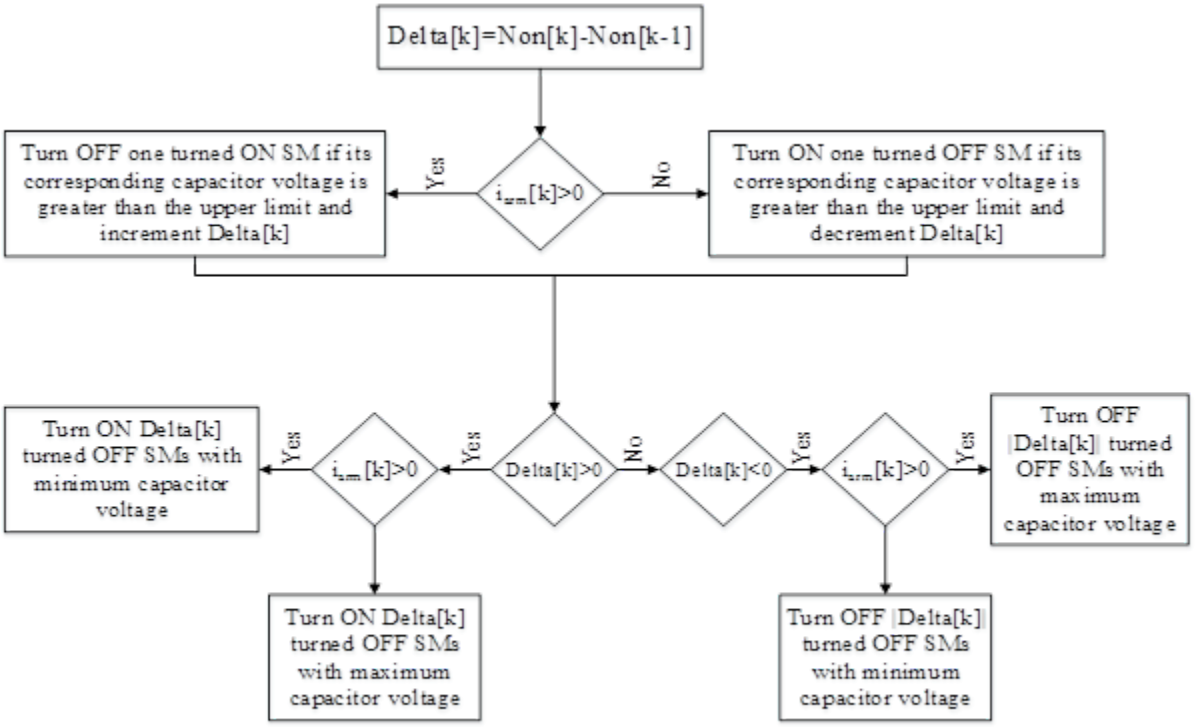

Figure 3-4: SM capacitor voltage-balancing algorithm.

The outer control system controls the ac transmission grid voltage and the mean of the SM capacitor voltages, as shown in Fig. 3-5 [Debnath 2018a]. The ac transmission grid frequency and angle in the inner and outer control systems were estimated based on digital implementation of a synchronous reference frame phase-locked loop (SRF-PLL). The SRF-PLL uses the measured ac transmission grid voltages as input. The ac transmission grid voltage control was based on voltage support through a filter and proportional control or through a resettable integrator (shown by "*I*" in the figure). The use of a proportional controller alone resulted in insufficient voltage compensation with low gains and oscillatory behavior with high gains. The resettable integrator provided the required stability based on the external connected ac system [Debnath 2018a].

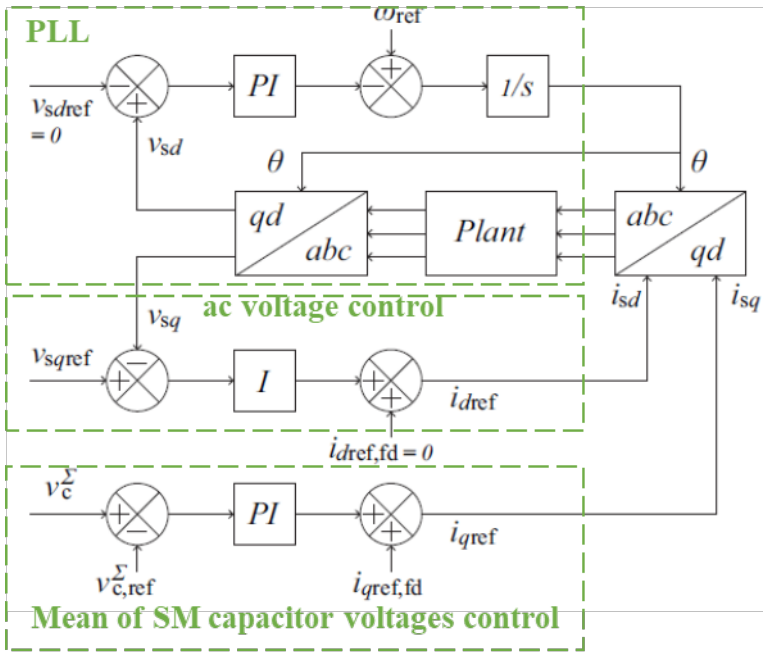

Figure 3-5: MMC-HVdc substations' outer control system and PLL accurate high-fidelity MMC simulation overview.

The overall implementation of the MMC-HVdc substation's simulation and control algorithms is summarized in Fig. 3-6 [Haileselassie 2012, Makarov 2017]. In the figure, $\mathbf{v_c}$ refers to the vector consisting of all the SM capacitor voltages, $\boldsymbol{z}_{\mathrm{n}}$ refers to the vector of all arm voltages, $\mathbf{r}_{\mathrm{arm}}$ refers to the vector consisting of $R_{\mathrm{y},j}$, i refers to the vector containing all the arm currents, and $\mathbf{u}$ refers to the vector of SM states in all arms. Parallel implementation of the SM capacitor voltage system and the SM capacitor voltage balancing in each arm is feasible if a multicore CPU is used.

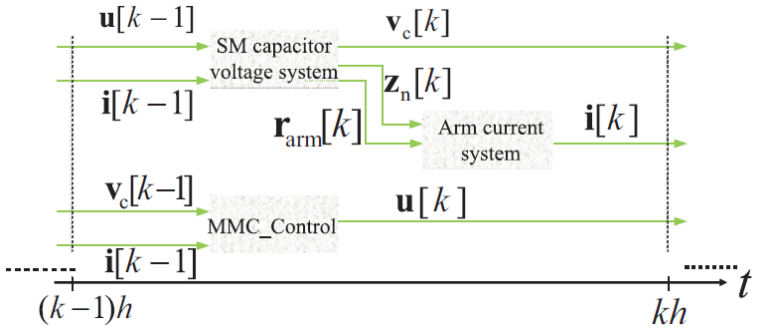

Figure 3-6: Summary of MMC-HVdc substation simulation and control algorithm implementation.

3.3.2 Fast Simulation of High-Fidelity MMC Offline Simulation

A multi-rate simulation approach was developed to speed up the simulation of the complete system that includes an MMC-HVdc substation with the external connected ac/dc systems. The approach is summarized in Fig. 3-7. The dynamic models are simulated in two loops: the inner loop and the outer loop. The corresponding simulation time steps are h_{inner} and h_{outer}, respectively. The smaller time step, h_{inner} (e.g., 4 μs), was selected as a multiple of the larger time step, h_{outer} (e.g., 60 μs). In the accurate implementation described in the previous section, both the MMC-HVdc substation dynamic model and the rest of the

system's dynamic model were simulated at the same time-step of h_{inner}. In the fast implementation, only the MMC-HVdc substation dynamic model was simulated at the smaller step, h_{inner}. The rest of the system was updated at the larger time-step, h_{outer}. Since the rest of the ac/dc system (i.e., transmission lines, generators, loads) are relatively computationally expensive, the fast implementation speeds up the simulation of the complete system. However, the states that were measured at the h_{inner} time-step in the inner and outer control systems of the MMC-HVdc substation from the external ac/dc systems were approximated to be measured at h_{outer}. This approximation results in stable and accurate fast simulation if the variation in measured states is insignificant within each h_{outer} time-step and the slower sampling doesn't interfere with the dynamics of the control system. With this approach, a speedup of up to 6× was observed in the simulation of an example Kundur 2-area system [Kundur 1994] with a MMC-HVdc line.

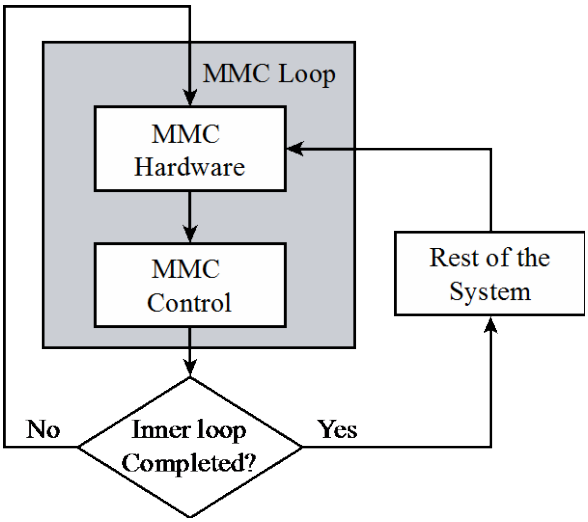

Figure 3-7: Implementation of the fast simulation algorithm.

3.4 Fidelity Requirements in Buffer the Zone

In addition to the high-fidelity EMT dynamic models of MMC-HVdc substations, high-fidelity models of the connected transmission ac and dc systems (like the buffer zone) are also of importance. These models assist in the analysis of stability and benefits provided by the high bandwidth control systems in MMC-HVdc substations [Debnath 2018a]. The high-fidelity models of the connected ac and dc systems include the models of transmission lines. Transmission lines can be modeled based on a lumped transmission line model or a frequency-dependent distributed transmission line model (also known as a distributed transmission line model) [Chaudhuri 2011]. Unlike the distributed transmission line model, the lumped transmission line model (e.g. π-section model) failed to provide adequate accuracy. The lack of accuracy was pronounced when high-frequency dynamics greater than 1 kHz were observed in the states measured in simulation. The high-frequency dynamics are associated with the high-bandwidth VSC-HVdc substations' control systems. While the accuracy of simulation was improved by the distributed transmission line model, the simulation became less efficient due to the increased computation time. This trade-off should be carefully considered when determining the type of transmission line model to be used in the dynamic simulations.

The length of the transmission line in the system of interest is another important criterion to determine the fidelity of the transmission line model to be used in the dynamic simulations. The frequency response of lumped and distributed transmission line models with different line lengths is shown in Fig. 3-8. It was

observed that the accuracy of the lumped transmission line model decreases with increase in the length of the transmission line. Considering a target frequency of 1 kHz, when the line is longer than 100 km, lumped transmission line model is not sufficiently accurate.

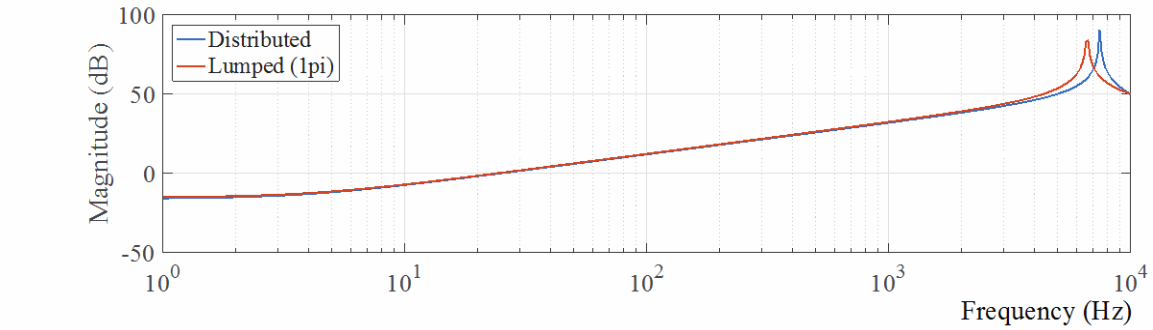

(a)

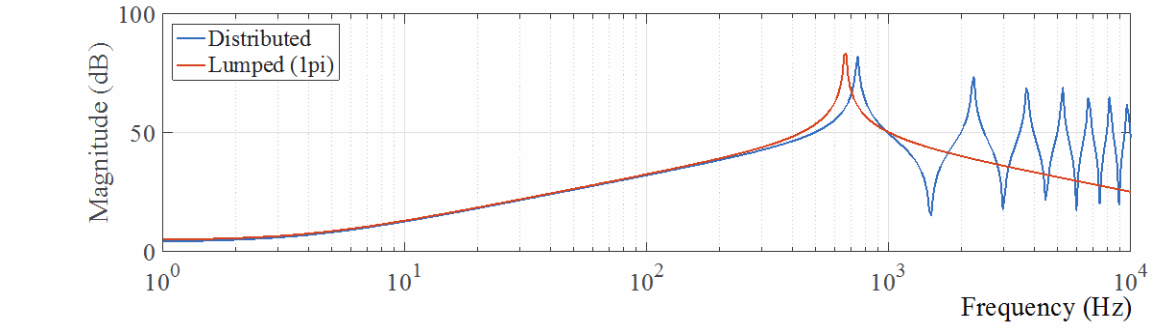

(b)

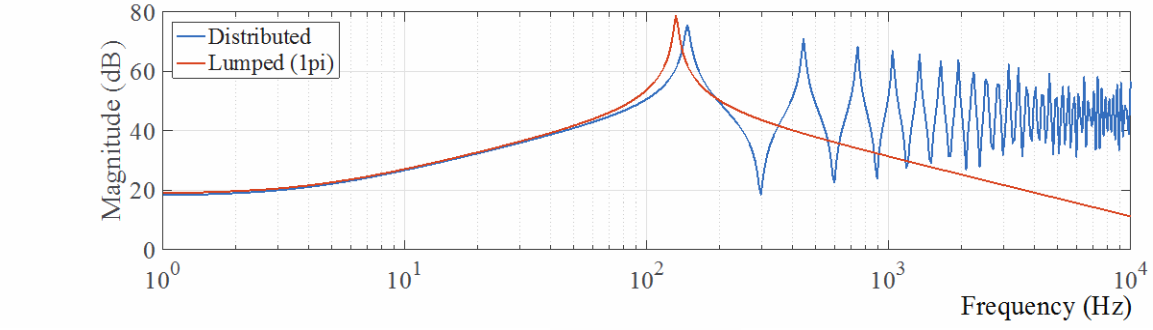

(c)

Figure 3-8: Frequency response of lumped and distributed transmission line models with different line length: (a) 10 km, (b) 100 km, and (c) 500 km.

An example case study of a Kundur two-area system was utilized to understand the models required to accurately simulate the fast dynamics associated with MMC-HVdc substations. One of the ac transmission lines in the Kundur two-area system was replaced with a point-to-point MMC-HVdc system, as is shown in Fig. 3-9. The 220 km ac transmission line connecting bus-7 and bus-9 are simulated with both lumped and distributed transmission line models. Different voltage controllers, namely the proportional and filter controller and an integral controller, were tested under various operating conditions

to understand the fidelity requirements. The corresponding results are shown in Figs. 3-10 and 3-11. The transients associated with enabling the proportional and filter ac transmission grid voltage controller in the MMC-HVdc substations are shown in Fig. 3-10. In Fig. 3-10, the simulation results obtained with the distributed transmission line models are marked "Distributed," and the simulation results obtained with the lumped transmission line models are marked "RLC," which means resistor-inductor-capacitor. The results in Fig. 3-10 indicate stable operation of the point-to-point MMC-HVdc system if a lumped transmission line model is used in the simulation, and unstable operation of the system if a distributed transmission line model is used in the simulation. The transients associated with utilizing an integrator-type ac transmission grid voltage controller in the MMC-HVdc substations are shown in Fig. 3-11. The results in Fig. 3-11 are marked by "MMC-1 D" and "MMC-1 L" for simulation of the modified Kundur two-area system with distributed and lumped transmission line models, respectively. The stable operation of the point-to-point MMC-HVdc system, if simulated with lumped transmission line model, is observed in Fig. 3-11(b) and (c) under transmission line fault and reactive load change, respectively. The operation of the system is observed to be unstable if simulated with the distributed transmission line model. The results in Fig. 3-11(a) indicate stable operation of the system if simulated with the distributed transmission line model as compared to the lumped transmission line model. The differences observed in the stability of the point-to-point MMC-HVdc system can be related to the different damping observed in the frequency responses of the different transmission line models [Debnath 2018a]. The damping provided by the distributed transmission line model is higher at certain high frequencies and lower at certain high frequencies as compared to the damping provided by the lumped transmission line model.

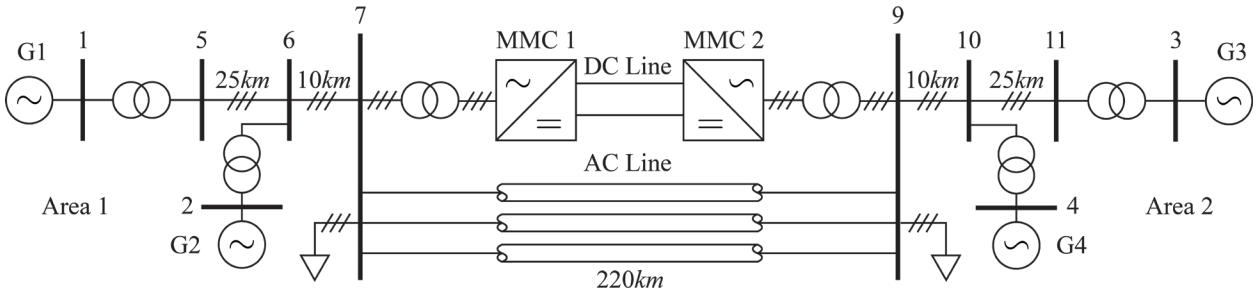

Figure 3-9: Modified Kundur two-area system with a point-to-point MMC-HVdc system.

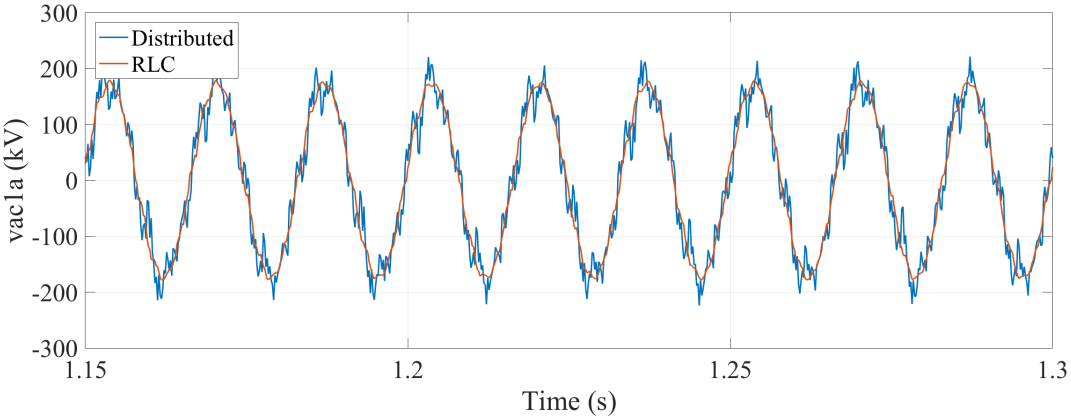

(a)

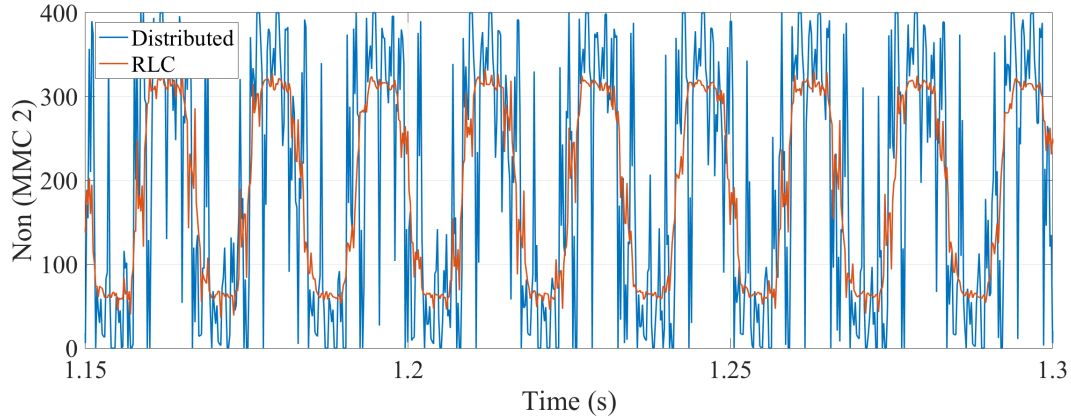

(b)

Figure 3-10: Transient response to enabling a voltage controller with proportional and filter controller: (a) MMC-1 phase-a instantaneous voltage, (b) MMC 1 phase-a upper arm Non.

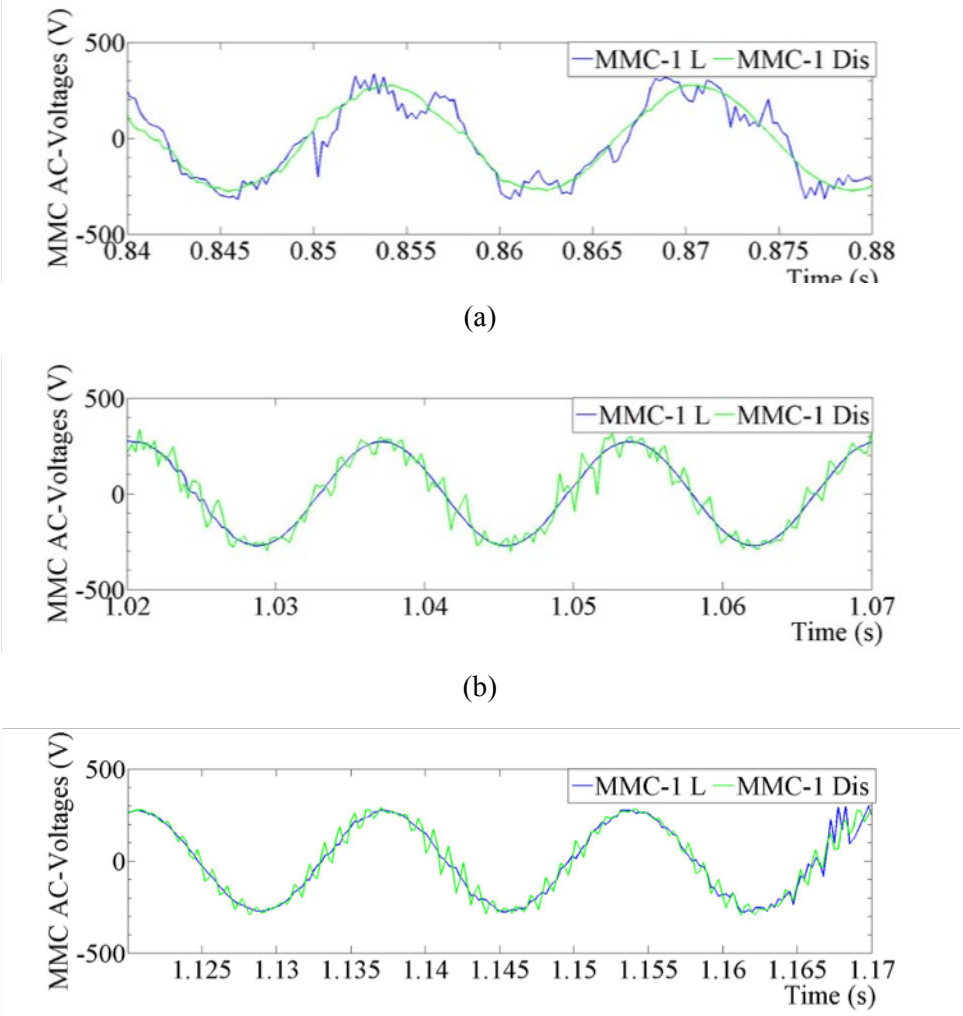

Figure 3-11: Transient response to enabling a voltage controller with integrator behavior: (a) ac-side voltage controller enabled, (b) Transmission line fault, and (c) Reactive power load change.

The EMT dynamic models of the buffer zones in Atlanta, Georgia, and Orlando, Florida, were established through translation of a portion of the dynamic model of the EI grid in PSS®E to PSCAD using E-Tran. The type of transmission line models used in these simulations was important to capture the high-bandwidth dynamics that were observed in the states measured during the simulation of the buffer zones with the MMC-HVdc substation. Such an option is present while performing model conversion. The study in this section provided insights into the length of the transmission line that triggers the requirement for distributed transmission line model to represent the dynamics of the corresponding line. In the case of short transmission lines, the lumped transmission line model is used to represent the dynamics of the line.

3.5 Buffer Zone Model Extraction

Buffer zones were identified to accurately simulate the voltage behavior and the high-bandwidth dynamics observed in the states measured in the system close to the HVdc substations. To obtain the buffer zones, a sensitivity-based methodology was developed. A reactive power injection source was placed at the rectifier and inverter buses as shown in Fig. 3-12, and the change in the voltage was

observed in the surrounding buses. A voltage deviation criterion was defined to determine the buses to be included within the buffer zones. The procedure is summarized by the following steps:

1. Inject some amount of reactive power (ΔQ) into an adjacent bus near rectifier or inverter bus
2. Solve power flow to calculate the change in voltage (ΔV) in the buses adjacent to the reactive power injection (ΔQ) bus
3. Define criteria to rank buses based on ΔV and select buses for which the calculated ΔV values are in the defined range as defined in the voltage deviation criteria.

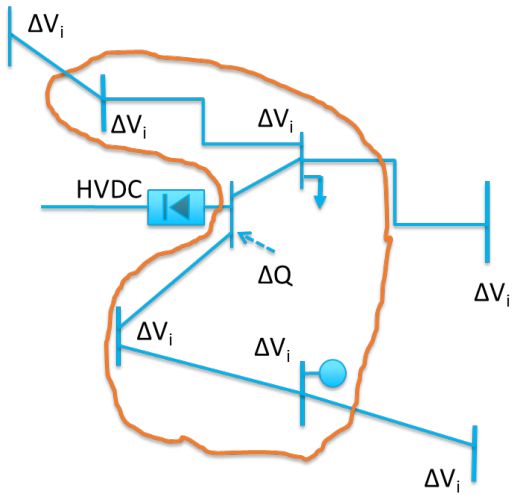

Figure 3-12: conceptual illustration of buffer areas selected by reactive power injection and voltage sensitivity method.

In this work, an injection of 1,000 MVAr was used in the sensitivity study. The voltage deviation range is defined as ±1.4% about the nominal voltage. If the changes in voltage in the buses were greater than the voltage deviation range, the corresponding buses were selected as part of the buffer zone. Based on this approach, the number of buses in each buffer area was identified as the following:

- Rectifier side (Atlanta): 29 buses
- Inverter side (Orlando): 12 buses

To study sensitivity on the size of the buffer zones, a smaller buffer zone was defined with the following number of buses:

- Rectifier side (Atlanta): 8 buses
- Inverter side (Orlando): 7 buses

The corresponding EMT dynamic models of the buffer zones were converted from the dynamic model of EI grid in PSS®E to PSCAD using E-Tran.

The scenario selected to extract the buffer zones was EI2WECC, where WECC stands for Western Electricity Coordinating Council. EI2WECC is defined as the scenario in which power is being exported from EI to WECC. EI2WECC is more challenging to EI as the export of power by the HVdc system is seen as a large load to EI, and voltage control is in general more challenging for loaded systems.

3.6 Use Cases for Voltage Control Evaluation

The EMT dynamic model of the point-to-point MMC-HVdc system is integrated into the dynamic models of the buffer zones. The use cases to evaluate the ac transmission grid voltage controller in the MMC-HVdc substation is developed in this section. The change in voltages in the buffer zones was evaluated to identify use cases of interest.

One of the use cases identified is a fault in the transmission lines that created a voltage sag of up to 10%. The simulation results of a node voltage near Atlanta in this use case with and without the ac transmission grid voltage controller in the MMC-dc substation is shown in Fig. 3-13. As shown in the figure, up to 38% improvement was observable in the voltage profile with the use of the ac transmission grid voltage controller.

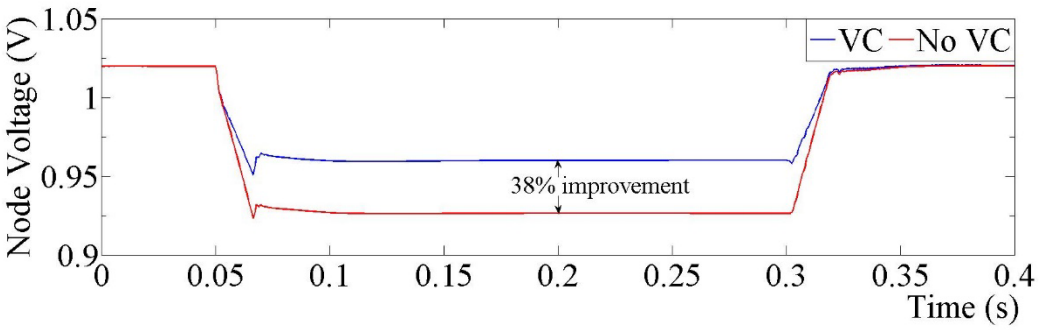

Figure 3-13: Impact of voltage control in MMC-dc system in a defined use-case.

Other use cases of interest include tripping of shunt compensators and generators near Atlanta. The variation in voltages observed upon tripping a 1,200 MVAr shunt capacitor at Atlanta-El Dorado HVdc substation (as a part of the HVdc macrogrid) is shown in Fig. 3-14(a). Based on the voltage responses, these use cases were identified for evaluation of the ac transmission grid voltage controller in the MMC-HVdc substations. Further detailed modeling of loads may be required to identify other use cases in voltage, as has been shown in the preliminary work performed on dynamic load modeling in Appendix B.

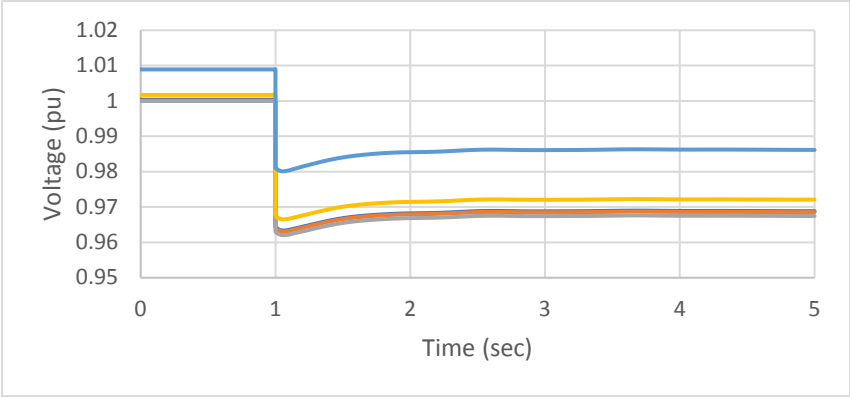

Figure 3-14: Voltage response after a large shunt capacitor is tripped.

3.7 Hybrid Simulation of EI with Point-to-Point MMC-HVdc System in Atlanta-Orlando

The EMT dynamic model of the point-to-point MMC-HVdc system from Atlanta to Orlando was integrated into the dynamic model of the corresponding buffer zones in PSCAD. Different sizes of buffer zones, as explained in Section 3.4, are considered in this study to identify sensitivity of the size of buffer zone to faster dynamic models within the zone (like the MMC-HVdc substation here). Two different MMC-HVdc substation dynamic models were also considered: (a) slow (or, the accurate high-fidelity model), and (b) fast models. The EI grid model in PSS®E was interfaced with the PSCAD models through boundary buses using ETRAN Plus to perform hybrid simulations. The boundary buses were the buses at the edge of the buffer zones. These simulations were used to evaluate the ac transmission grid voltage controller under various defined use cases. The hybrid simulation cases studied here are summarized below:

1. Small Buffer Area – Fast HVdc Model (simulation time-step = 60 μs)
2. Small Buffer Area – Slow HVdc Model (simulation time-step = 4 μs)
3. Large Buffer Area – Fast HVdc Model (simulation time-step = 60 μs)
4. Large Buffer Area – Slow HVdc Model (simulation time-step = 4 μs)

Two type of contingencies were used to test the model:

a) Trip of a 1,241 MVAr shunt capacitor at t = 3 s and reconnection at t = 3.25 s

b) Application of a three-phase-to-ground fault (or, transmission line fault) at t = 4 s and clear it at t = 4.25 s

- In addition to the hybrid simulation, simulations were also carried out only in PSCAD. In the PSCAD equivalent model, the EMT dynamic models of the point-to-point MMC-HVdc system and the buffer zones were modeled with the external system being represented by an equivalent voltage source in PSCAD. This additional simulation model provided a means to compare the different methods to simulate the described system in this chapter.
- The simulation methods are summarized below:

a) PSCAD Equivalent Model: The point-to-point MMC-HVdc system and buffer areas are modeled in PSCAD, the external system (representing the rest of the EI grid) is modeled as equivalent voltage sources in PSCAD.

b) Hybrid Simulation Model: The point-to-point MMC-HVdc system and buffer areas are modeled in PSCAD, the external system (or, the rest of the EI grid) is modeled in PSS®E and interfaced to PSCAD through boundary buses.

The various simulation case studies are summarized in Table 3-1. The information on time-steps used in PSCAD and PSS®E are also provided in the table. The small and large buffer zones in PSCAD with the point-to-point MMC-HVdc system's dynamic EMT model and two of the contingencies are illustrated in Figs. 3-15 and 3-16, respectively. The voltage magnitude and the active and reactive power dynamic response for the various case studies are shown in Figs. 3-17–3-20. The circled portions of the dynamic response in Fig. 3-17 can be compared with the corresponding portions in Figs. 3-18–3-20. The results in Fig. 3-20, from a model that used a large buffer zone with the slow MMC-HVdc model, presents the most accurate representation with high-fidelity representation of both the buffer zone and MMC-HVdc models. A comparison of the results in Figs. 3-17 and 3-18 shows that the fast MMC-HVdc model, with respect to

the slow MMC-HVdc model, adequately represents the dynamics of the measured reactive power and ac transmission grid voltages. However, the dynamics associated with the measured active power is noticed to have differences. Similarly, a comparison of the results in Figs. 3-19 and 3-20 shows that the measured reactive power is more stable when simulated with the slow MMC-HVdc model. The other measured quantities were similar between the two models. The differences observed in the simulation results from fast MMC-HVdc model when compared with the corresponding results from the slow MMC-HVdc model arose due to the different sampling rates of the measured states (and the corresponding interference with the control system of the MMC-HVdc substation). However, most of the measured variables appeared to be adequately represented by the fast MMC-HVdc model in these studies.

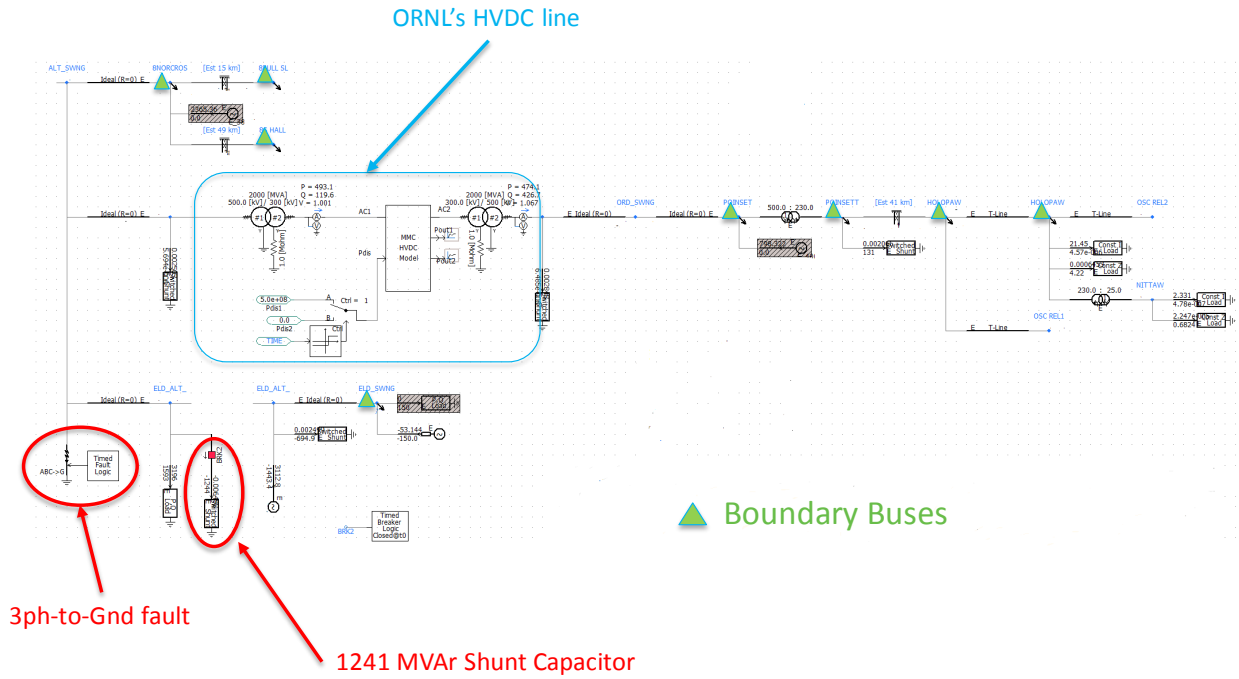

Figure 3-15: Small buffer zone, point-to-point MMC-HVdc system model, marked by ORNL's HVDC line (blue), and location of two contingencies in PSCAD (red).

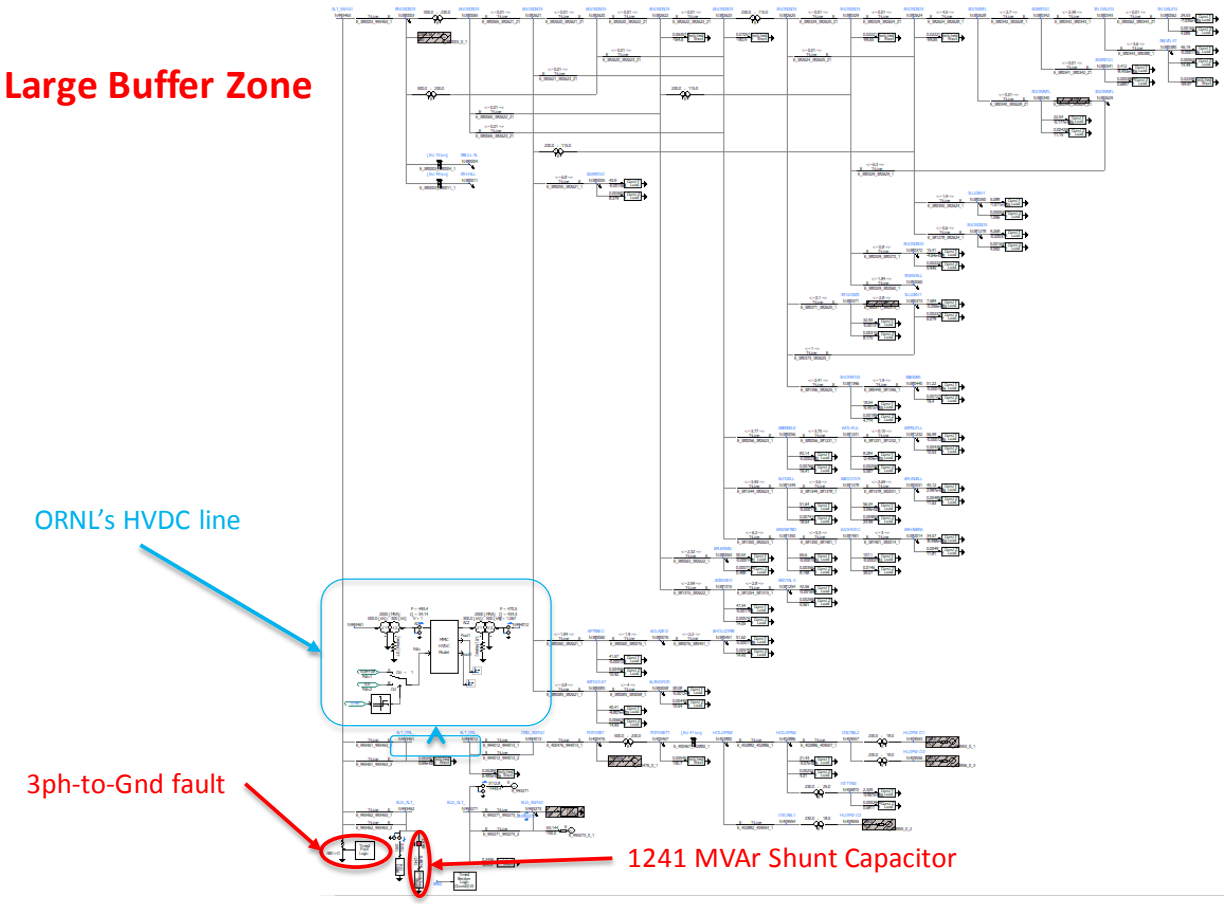

Figure 3.16: Large buffer zone, point-to-point MMC-HVdc system model, marked by ORNL's HVDC line (blue), and location of two contingencies in PSCAD red).

Voltages on rectifier and inverter sides of ORNL's HVdc line

Active Power on rectifier and inverter sides of ORNL's HVdc line

Reactive Power on rectifier and inverter sides of ORNL's HVdc line

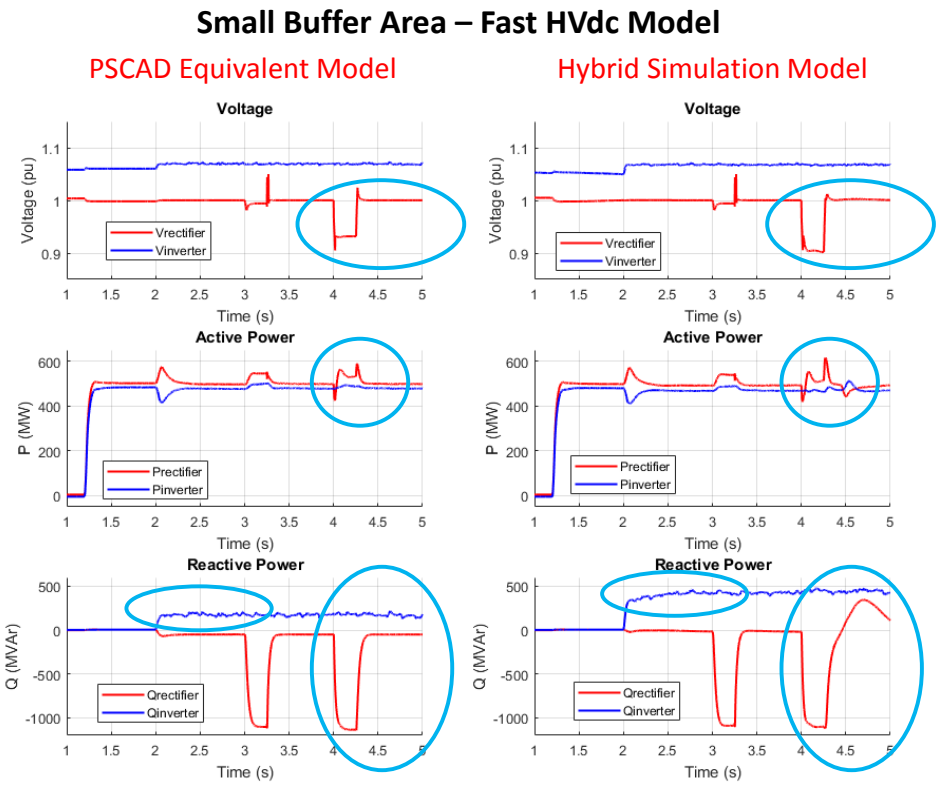

Figure 3-17: Simulation results for shunt capacitor trip (at t = 3 s) and reconnection (at t = 3.25 s), followed by a short-circuit fault (at t = 4 s) and cleared (at t = 4.25 s) for a model consisting of small buffer zone and fast MMC-HVdc system model. The circles in the figure can be compared with the dynamic response observed in the results in Figs. 3-18 to 3-20.

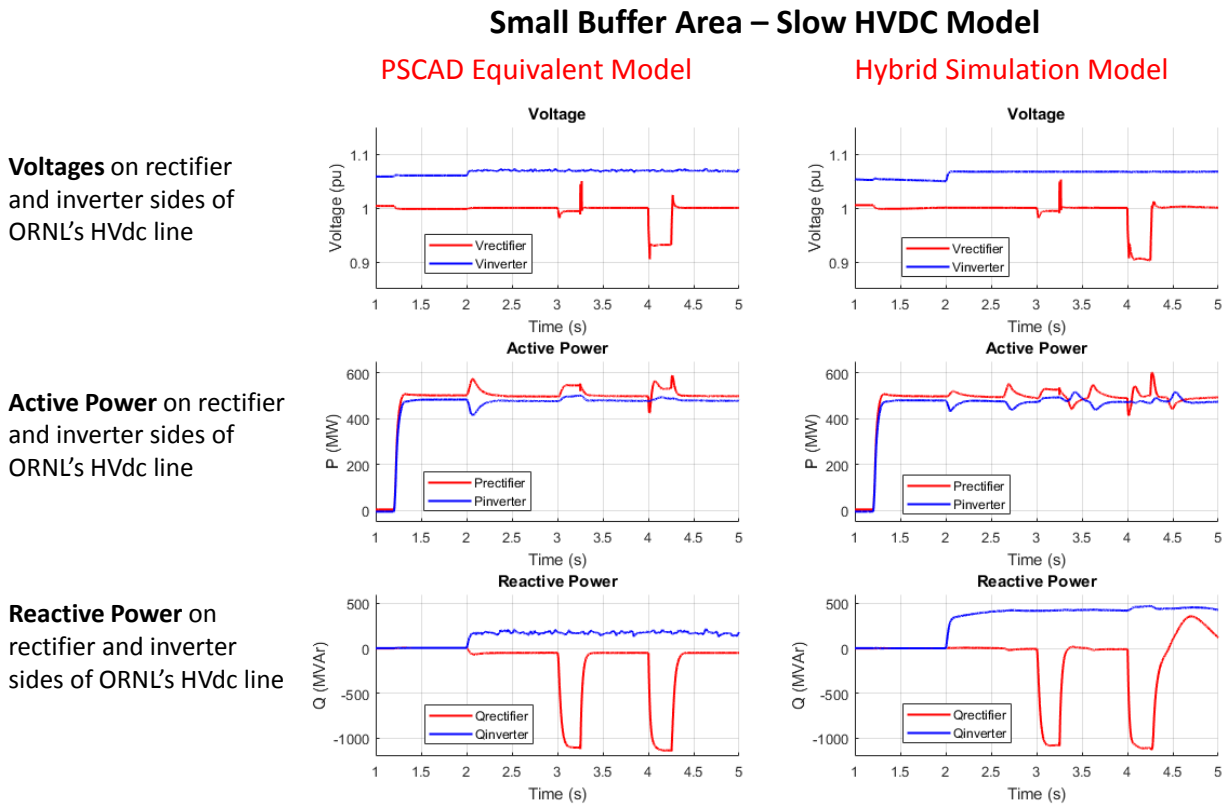

Figure 3-18: Simulation results for shunt capacitor trip (at t = 3 s) and reconnection (at t = 3.25 s), followed by a short circuit fault (at t = 4 s) and cleared (at t = 4.25 s) for a model consisting of small buffer zone and slow MMC-HVdc system model.

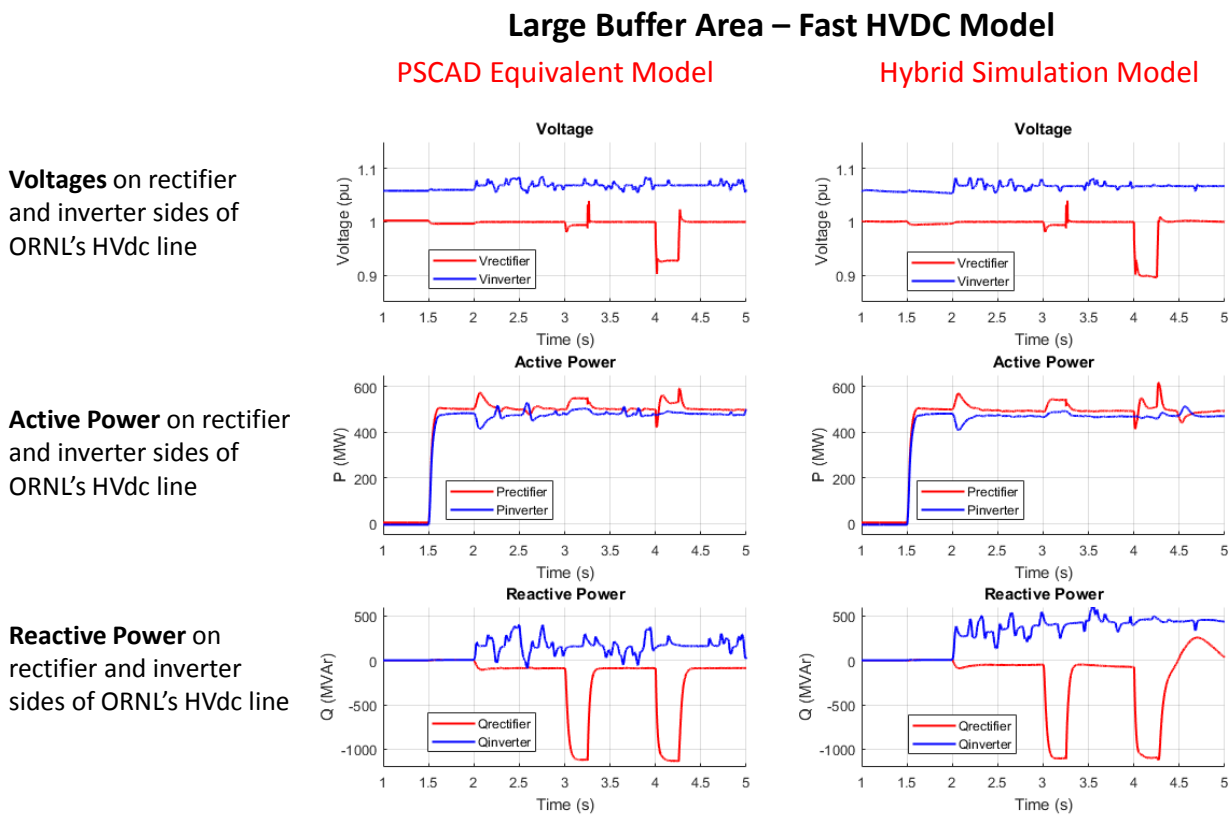

Figure 3-19: Simulation results for shunt capacitor trip (at t = 3 s) and reconnection (at t = 3.25 s), followed by a short circuit fault (at t = 4 s) and cleared (at t = 4.25 s) for a model consisting of large buffer zone and fast MMC-HVdc system model.

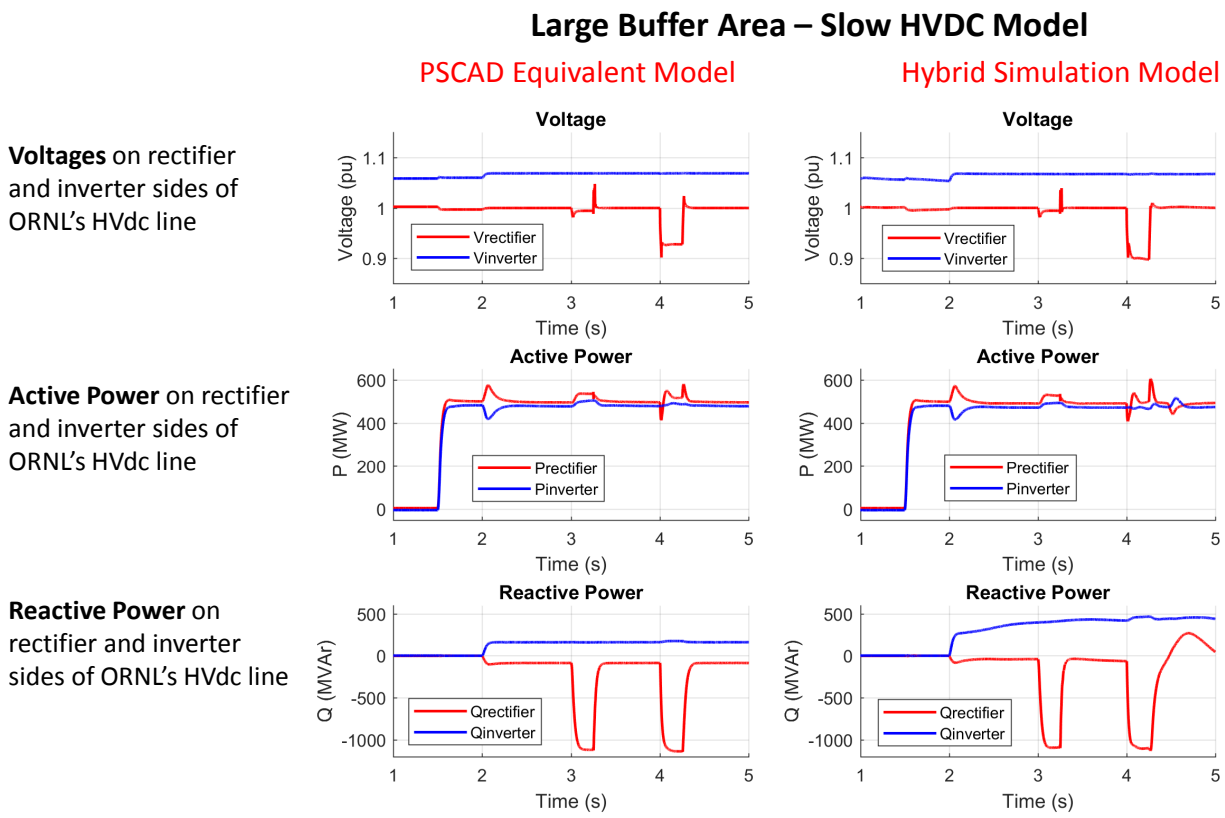

Figure 3-20. Simulation results for shunt capacitor trip (at t = 3 s) and reconnection (at t = 3.25 s), followed by a short circuit fault (at t = 4 s) and cleared (at t = 4.25 s) for a model consisting of large buffer zone and slow MMC-HVdc system model.

The differences between hybrid simulations (on the right) and simulations performed only on PSCAD (sub-figures on the left) are also shown in Figs. 3-17–3-20. The most noticeable differences were in reactive power and voltage dip (as marked by areas encircled in Fig. 3-17). There are also smaller differences observed in the active power's dynamics. These observed differences were due to the additional dynamic effects introduced by the external system (represented by the dynamic TS model in PSS®E) in the hybrid simulation. The simulations only performed in PSCAD had a static external system, represented by a static multiport Thevenin equivalent, with the dynamic effects not well quantified.

The differences between simulation results using small and large buffer zones can be observed when Figs. 3-20 and 3-18 are compared. There were transient variations (due to potential instability in the substation dynamics) observed in voltages and reactive power measured in the PSCAD-only simulation with the smaller buffer zone. The corresponding instabilities were not observed in the PSCAD-only simulation with a larger buffer zone. There were also differences observed in the active power between results obtained from hybrid simulations shown in Figs. 3-20 and 3-18. Transient events were observed in the active power in the hybrid simulation with a small buffer zone. These events were not observed in the results of the hybrid simulation with a large buffer one. It can be concluded from these tests that the simulation with the larger buffer zone is more accurate, especially when comparing the active powers and evaluating stability of advanced control methods in VSC-HVdc substations.

The comparison of the computational performance of the four simulation case studies is shown in Table 3-1. The computer used for the simulation was an Intel® CORE™ i7-6820HQ CPU @ 2.70GHz, with 16.0 GB (15.7 GB) usable RAM, 64-bit Operating System, and an x64-based processor. The PSCAD version was 4.6.2; the PSS®E version 33.7.

Table 3-1: Summary of computational performance for 5 s simulation length with various models.

Buffer zone size		**Type of simulation**	**PSCAD time step - ORNL's line model**	**PSS®E time step**	**Simulation time**	**Speedup**
Smaller	17 buses, 8 boundary buses	PSCAD with equivalent	60 µs – Fast	-	247 s	2.4×
			4 µs – Slow	-	610 s	
		PSCAD-PSS®E co-simulation	60 µs – Fast	4.16 ms	287 s	2.4×
			4 µs – Slow	4.16 ms	706 s	
Larger	62 buses, 25 boundary buses	PSCAD with equivalent	60 µs – Fast	-	303 s	3.9×
			4 µs – Slow	-	1,189 s	
		PSCAD-PSS®E co-simulation	60 µs – Fast	4.16 ms	391 s	3.4×
			4 µs – Slow	4.16 ms	1,351 s	

The following accuracy highlights were derived from the above PSCAD-PSS®E hybrid simulation:

- Converter controller parameters' tuning needs high fidelity model around converter to capture high-frequency voltage dynamics (that includes the need for EMT dynamic model for buffer zones and distributed transmission line model for transmission lines in the buffer zones)
- PSCAD-PSS®E hybrid simulation captured voltage/reactive power dynamics more accurately

The highlights of the computational performance of PSCAD-PSS®E hybrid simulation and the models developed are provided below:

- ~77% of computation burden by PSCAD, and ~23% by PSS®E and communication between PSS®E and PSCAD
- The fast point-to-point MMC-HVdc system model resulted in up to 3.9× faster computation time
- The speedup of up to 1.9× was observed with a smaller buffer zone model

3.8 Summary of Issues Faced with Using ETRAN for Hybrid Simulations and for Converting Models from PSS®E to PSCAD

Several issues were faced when using ETRAN for hybrid simulations and for converting models from PSS®E to PSCAD. The following list summarizes all the issues faced, some of which have been resolved through close cooperation with the developers of ETRAN – Electranix.

- Machine parameter Xp = X'p is not allowed in PSCAD (PSS®E does not have a problem with those reactances being equal). This issue was fixed by making these reactances different for a few generators.
- Some generator output set with excessive reactive power can cause initialization problems for some exciter's models in PSCAD
- ETRAN by default defines several measurements channels per generator, when converting from PSS®E to PSCAD. When the system model in PSS®E has many generators (e.g., the EI lumped model has 300 generators), the total number of channels becomes unmanageable by PSCAD. An efficient and automated method has been suggested to fix the problem by the PSCAD support team to remove all the channels.
- ETRAN software could not handle the full PSS®E WECC-EI-HVdc macrogrid model with over 100,000 buses. Only full nodal model of EI has been used.
- Zero resistance lines are converted into PSCAD as ideal lines. When some of these lines are in a loop configuration, the model presents problems when executing PSCAD simulations (this configuration has no problem in PSS®E).
- Negative loads in PSS®E are converted into PSCAD as voltage sources. Voltage sources significantly modify the dynamic behavior of the system, distorting the frequency response. This problem is avoided by identifying and eliminating negative loads in PSS®E, or as part of the conversion through ETRAN.
- HVdc systems in PSS®E are not directly translated into PSCAD with ETRAN. Instead ETRAN places an ideal voltage source at each substation terminal. ETRAN currently cannot represent CDC6T model.

Chapter 4 MTdc System Scenario Connecting Asynchronous Interconnections in The United States

The objective of this part of the work was to model and study the impact of advanced control methods in a seven-terminal MMC-based MTdc systems that connect various asynchronous interconnections in the United States. The advanced control methods include inertial/primary frequency support and ac-side voltage control. The frequency support was considered through multiple points of injection in each interconnection and was not limited to the single point of injection through the substation closest to the interconnection border. The ability to provide support in multiple substations in an interconnection provided greater flexibility and stability across various operating conditions. The frequency support included providing inertial and primary frequency responses using an expert system–based high-bandwidth implementation. The formulation of the expert system was the outcome of a gradient-descent based co-simulation algorithm that solves a minimum distance problem. This problem was solved as an equivalent of a minimum time problem to optimize the bandwidth of the system and provide maximum frequency support. It was based on the formulation of multiple equivalent local optimization problems that attempted to converge the results from the global optimization problem.

This study involves three asynchronous interconnection grids in United States: the EI, WI, and ERCOT grids. Multiple-area lumped models of the interconnections were developed to capture the main power flows among the regions and to enable the understanding of multiple points of injection of power from the MTdc system through frequency support control methods. These models did not adequately represent the local voltage behavior. The buffer zone models described in Chapter 3 were incorporated into the multi-area lumped models to adequately capture the local voltage behavior. The dynamic models of the buffer zone based on the high-fidelity models of components described in Chapter 3. The dynamic models of MTdc systems were based on high-fidelity models of MMCs. The high-fidelity dynamic models considered enable the understanding of the impact and stability of advanced control methods utilized in MTdc systems. The advanced control methods in MTdc systems provided up to 63% and 64% improvement in the observed frequency response in the simulations during defined contingency events.

4.1 MMC-Based MTdc System Scenarios and Models

Two MTdc systems connecting various asynchronous interconnections in the United States were considered in this study: (i) a six-terminal MTdc system connecting EI and WI grids, and (ii) a seven-terminal MTdc system connecting the EI, ERCOT, and WI grids. These systems may be considered as a part of the larger HVdc macrogrid studied in [Makarov 2017].

4.1.1 Six-Terminal MTdc Connecting EI and WI Grids

The six-terminal MTdc system connecting EI and WI grids is shown in Fig. 4-1. The location of the substations in the MTdc system are provided below:

- Palo Verde, Arizona, and Victorville, California, in the WI region;
- Panola County, Texas, St. Louis, Missouri, Atlanta, Georgia, and Orlando, Florida in the EI region.

Each MMC substation in the six-terminal MTdc system is rated at 2 GW and connected to a 500 kV ac line and to a ±525 kV dc line. The transmission line information between each substation is tabulated in Table 4-1.

Figure 4-1: Terminal MTdc system.

Table 4-1: Transmission line information.

From	To	Length(km)
Victorville	Palo Verde	454.18
Palo Verde	Panola County	1,724.1
St. Louis	Panola County	808.22
Panola County	Atlanta	938.07
Atlanta	Orlando	645.92

4.1.1 Seven-Terminal MTdc with EI, ERCOT, and WI

In addition to the six-terminal MTdc system that connects EI and WI grids, another scenario to connect ERCOT grid to EI and WI grids was considered using a seven-terminal MTdc system. The additional seventh terminal in the seven-terminal MTdc system is located at Sweetwater, TX, in the ERCOT region. The seven-terminal MTdc system is shown in Fig. 4-2. The transmission line information between the terminals is tabulated in Table 4-2.

Table 4-2: Transmission line information.

From	To	Length (km)
Victorville	Palo Verde	454.18
Palo Verde	Sweetwater	1,395
Sweetwater	Panola County	634
St. Louis	Panola County	808.22
Panola County	Atlanta	938.07
Atlanta	Orlando	645.92

Figure 4-2: Multiple point of injection 7 terminal HVdc system.

The dynamic models of the various scenarios of MTdc system were developed in PSCAD/EMTDC. These models were based on the high-fidelity dynamic switched system models of MMC substations as described in [Makarov 2017]. The dc lines in the MTdc system were modeled based on distributed transmission line model.

4.2 Control of the MTdc System

The control of MTdc systems included control of internal states of the MMC and of external states. The internal states include ac-side currents, dc-side current, circulating currents, and SM capacitor voltages. The control of internal states is explained in detail in [Debnath 2016b] and is not explained here. The external states include ac-side active and reactive power, dc-side voltage, ac-side frequency, and ac-side voltage. The control system of external states consisted of (i) droop control on dc-side voltage, (ii) expert system–based frequency support, and (iii) ac-side voltage support.

4.2.1 Droop Control in MTdc Systems

The active power in each substation in an MTdc system was controlled using droop control on dc-link voltage. The formulation of the droop control was based on the equivalent model developed for the MTdc system. The model developed is described below.

The equivalent circuit representation of the six-terminal MTdc is shown in Fig. 4-3. In this representation, the lumped model of the dc transmission lines is considered for simplicity and representation of steady-state and low-frequency dynamics.

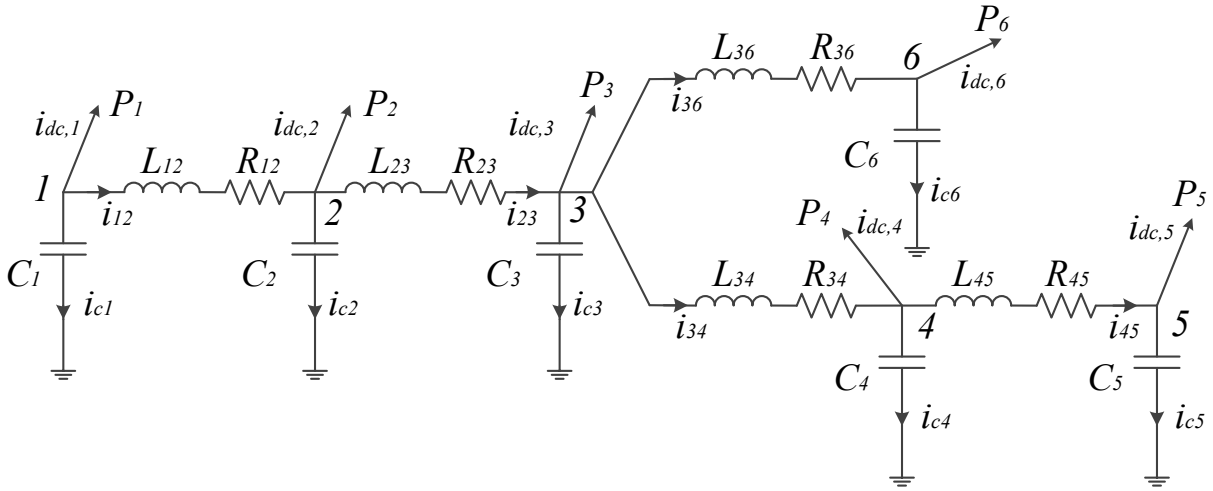

Figure 4-3: Six-terminal system diagram with dc lines and terminal capacitors

The droop controller on each converter results in the following formulation

$$V_{\mathrm{dc},i} = V_{\mathrm{dc,ref}} - K_{pc,i}\left(\frac{P_{\mathrm{dc},i}}{3V_{\mathrm{dc,ref}}} - \frac{i_{\mathrm{dc},i}}{3}\right) + \frac{2}{3}R_0 i_{\mathrm{dc},i} = \frac{P_{\mathrm{dc},i}}{i_{\mathrm{dc},i}}, \tag{4.1}$$

where $K_{pc,i}$ is the droop constant on the terminal, $P_{\mathrm{dc},i}$ is the active power processed by the converter, $V_{\mathrm{dc,ref}}$ is the reference dc-link voltage, and $i_{\mathrm{dc},i}$ is the dc-link current processed by the converter. Rearranging the terms in (4.1) and using the net current balance equation (based on KCL) for the six-terminal system is

$$\sum_{i=1}^{6} i_{\mathrm{dc},i} = \sum_{i=1}^{6} \frac{V_{\mathrm{dc},i} - A_i}{B_i} = 0, \tag{4.2}$$

where $A_i = V_{\mathrm{dc,ref}} - \frac{K_{\mathrm{pc},i} P_{\mathrm{dis},i}}{3V_{\mathrm{dc,ref}}}$, $B_i = \frac{K_{pc,i}}{3} + \frac{2}{3}R_o$.

The steady-state voltage drop on a dc transmission line between terminals i and j can written as

$$V_{\mathrm{dc},i} - V_{\mathrm{dc},j} = R_{ij} i_{ij} \tag{4.3}$$

Solving for $V_{\mathrm{dc},i}$ from the line equations in (4.3) and the net current balance equation in (4.2), the nominal values of terminal dc-side voltages can be obtained. Considering the proper distribution of nominal dc-side voltages to within their rated range, droop gains $K_{\mathrm{pc},i}$ are determined.

4.2.2 Expert System–Based Frequency Support in MTdc System

The control of ac-side frequency is based on an expert system implemented on the dc-side voltage and ac-side frequency based on the single point of injection [Makarov 2017]. The expert system is based on the following:

- If the measured frequency is within the dead-band settings and the dc-side voltage is outside the dead-band setting, active power is modulated based on dc-side voltage.
- If the measured frequency is outside the dead-band settings and the dc-side voltage is within the dead-band setting, active power is modulated based on frequency.
- If both the measured frequency and dc-side voltage are beyond their respective dead-band settings, the frequency support is withdrawn.

In this work, the expert system is expanded and varied to provide multiple points of injection of frequency support to the different asynchronous interconnection (EI, ERCOT, WI) grids. The inclusion of multiple points of injection poses the following challenges:

- Identifying the substations that inject power to support the frequency variations.
- Minimizing the losses in the system.
- Limitations imposed by the power rating of each substation.
- Limitations imposed by the voltage rating of lines/cables and substations.

The trade-offs between the frequency variations, losses, voltage deviations, and power processed by the substations are visualized in Fig. 4-5. In Fig. 4-5(a), a large amount of power is sent from EI grid to WI grid though line 23 to reduce the frequency deviations, resulting in high stress on the line. If the power sent though line 23 is reduced, as shown in Fig. 4-5(b), the frequency deviation in WI grid will be large. In Fig. 4-5(c), the power sent from EI grid to WI grid minimizes the frequency deviations but results in a large dc-side voltage deviation. As a result, the substation voltage on converter-2 is too low, which may impact the stability of the system.

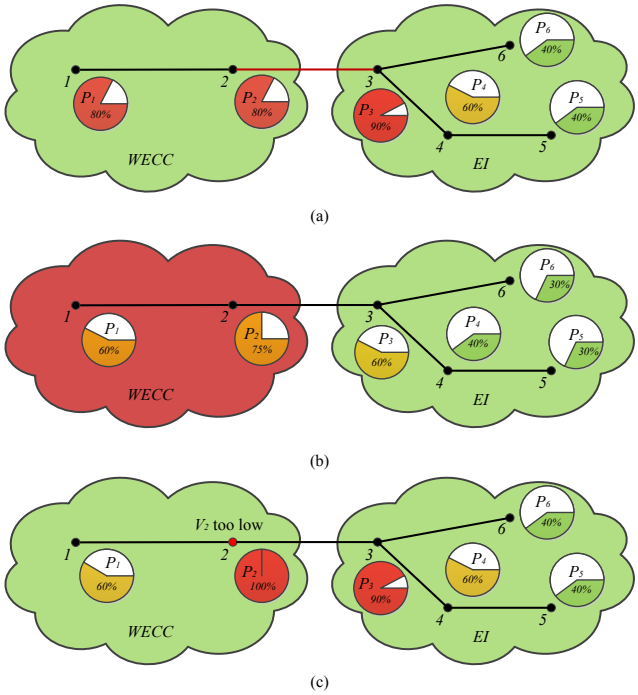

Figure 4-4: Conceptual diagram of six-terminal MTdc system: (a) stress on line 23 is high; (b) frequency deviation is too high, not sufficient power provided; (c) voltage on terminal-2 is too low. Pie charts indicates the percentage of potential active power utilized in a converter. Red and black lines indicate the transmission line is over-loaded and within limits, respectively. Green and red clouds indicate that the frequency deviation is low and high, respectively. Red and black converter terminal dot indicate that dc-link voltage is out of bounds and within bounds, respectively.

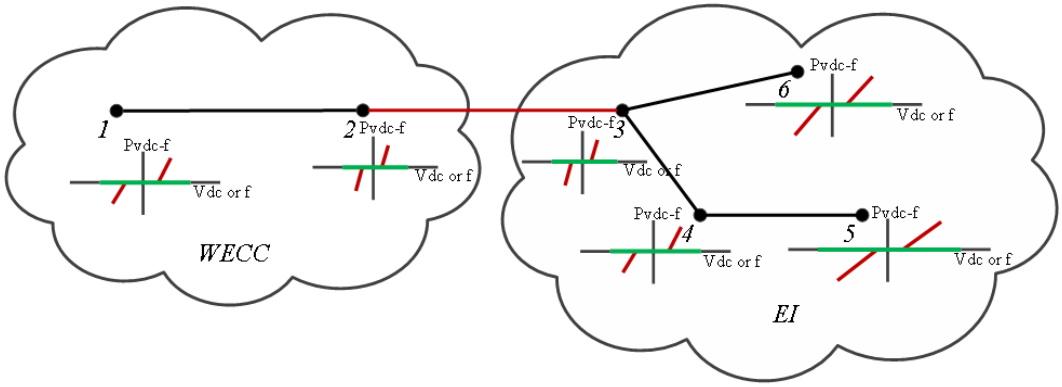

Figure 4-5: Illustration of dead-band and gain settings at each terminal in multiple point injection six-terminal MTdc system

The aforementioned challenges lead to the constrained multi-objective optimization with dynamic constraints. The dynamic constraints were imposed by time-varying voltage, power, and frequency constraints that involve small time constants (of the order of milliseconds). This problem is summarized in (4.4), with the dynamic models explained below.

$$\min_{\{P_{\text{vdc-f},1},P_{\text{vdc-f},2},P_{\text{vdc-f},3},P_{\text{vdc-f},4},P_{\text{vdc-f},5},P_{\text{vdc-f},6}\}} \lambda_1\{\text{loss}\} + \lambda_2\{\text{frequency deviation}\} \tag{4.4}$$

s.t

$$V_{i,\min} \le V_i \le V_{i,\max}$$

$$P_{\text{vdc-f},i,\min} \le P_{\text{vdc-f},i} \le P_{\text{vdc-f},i,\max}$$

where V_i is the dc-side voltage at substation-i and $P_{\text{vdc-f},i}$ is the additional active power processed at substation-i due to the implemented expert system.

The dynamics of frequency behavior in EI and ERCOT grids are modeled based on second-order dynamic system models and using the available National Energy Reliability Council (NERC) data. The corresponding models are summarized by

$$F(s) = F_{\text{nom}}(s) + \frac{G}{1+2\frac{\delta}{\omega_n}s+\frac{s^2}{\omega_n^2}}(P_{\text{gen}} - P_{\text{load}}) \tag{4.5}$$

where F_{nom} is the nominal frequency, P_{gen} is the generation in the interconnection, and P_{load} is the load in the interconnection.

The frequency dynamics in WI, based on WSEIG1, can be modeled by

$$\Delta f(s) = \frac{\Delta P - \Delta f(s)H(s)}{P_{ref}}\frac{1}{T_1 s}, \tag{4.6}$$

where T_1 is the time constant of one of the system models, ΔP is the effective generator-load mismatch, and $H(s)$ is the transfer function of the fifth-order frequency model. The transfer function is given by

$$H(s) = \frac{m_1 s + m_2}{k_0 + k_1 s + k_2 s^2 + k_3 s^3 + k_4 s^4}, \tag{4.7}$$

where m_i and k_i are parameters of the fifth-order system.

The dynamics of the dc-side voltage is determined based on Fig. 4-3. At each substation, the dynamics of the capacitor voltages are given by

$$C_i \frac{\mathrm{d}\Delta V_i}{\mathrm{dt}} = -\Delta i_{\text{dc},i} + \sum_{ij} \Delta i_{ij}, \tag{4.8}$$

where Δi_{ij} is the small-signal line currents in the lines adjacent to the converter substation-i, C_i is the terminal capacitor, $\Delta i_{\text{dc},i}$ is the small-signal dc-link current into the i^{th} converter substation, and $V_{\text{dc},i}$ is the small-signal dc-link voltage of the i^{th} converter substation.

The small-signal variables are derived with respect to the corresponding pre-event values, with the event defined by the frequency excursions. The dc transmission line dynamics are given by

$$\Delta V_i - \Delta V_j = L_{ij}\frac{\mathrm{d}\Delta i_{ij}}{\mathrm{dt}} + R_{ij}\Delta i_{ij}, \tag{4.9}$$

where i and j are the two substations connecting to the specific line.

The optimization problem in (4.4) with the dynamics in (4.5)–(4.9) is solved using gradient-descent and co-simulation-based optimization method that can be used to solve optimization problems with dynamic constraints, as described in detail in [Haileselassie 2012]. The constrained optimization problem in (4.4)

is converted into the multi-objective unconstrained formulation in (4.10). The constraints in (4.4) are loosely represented in the optimization function in (4.10) using small associated weights.

$$\min_{\{\Delta P_1,\Delta P_2,\Delta P_3,\Delta P_4,\Delta P_5,\Delta P_6\}} \lambda_1\{\text{loss}\} + \lambda_2\{\text{frequency deviation}\} + \lambda_3\{\text{voltage deviation}\} + \lambda_4\{\text{frequency rate of change}\} + \lambda_5\{\text{power limit}\} + \lambda_6\{\text{power rate of change}\} \quad (4.10)$$

where $\lambda_1, \lambda_2, \lambda_3, \lambda_4, \lambda_5, \lambda_6$ are the weights for multi-objective optimization, ΔP_i is the power processed at substation-i. The loss term in (4.10) is given by

$$\text{loss} = \sum_{ij\in\{12,23,34,45,36\}} \left(i_{ij,nom} + \Delta i_{ij}\right)^2 R_{ij}, \quad (4.11)$$

The frequency deviation term is represented by the square of frequency deviation compared to the base frequency in WI, EI, and ERCOT grids, respectively. The voltage deviation term is the summation of square of voltage difference compared to nominal dc voltage on each dc bus. With the consideration of practical implementation, the rate of changes in frequency and output power, as well as the output power itself, are limited within their reasonable ranges. The expert system developed from the optimization problem in (4.10) results in the formulation shown in Fig. 4-5.

4.2.3 Voltage Control in MTdc Systems

The reactive power provided by each MMC substation is varied to control ac-side voltage. The ac-side voltage at the point of common coupling (PCC) is approximately given by [Haileselassie 2012]

$$\widehat{V_s} = \widehat{V_C} + \left(\frac{P+Q\omega L}{V_x}\right). \quad (4.14)$$

The strong dependence of the ac-side voltage on reactive power (Q) is indicated in (4-14). The reactive power in the qd-frame of reference is given by

$$Q_{qd} = -\frac{3}{2} V_{sq} i_d, \quad (4.15)$$

where V_{sq} is the q-axis voltage of the measured ac-side voltage at the substation terminals and i_d is the d-axis ac-side current.

The reactive power can be controlled by the reactive current (i_d), as indicated in (4-15). However, the reactive current is limited based on the current rating of the converter (i_{rated}). Based on the limits, the reactive current is constrained by

$$i_{d,\max} = \sqrt{i_{\text{rated}}^2 - i_{q,\text{ref}}^2} \quad (4.16)$$

The other limitation on the reactive current is introduced by the relationship between the dc-side and the ac-side voltages. The block diagram of the ac-side voltage control using the reactive power compensation is illustrated in Fig. 4-6.

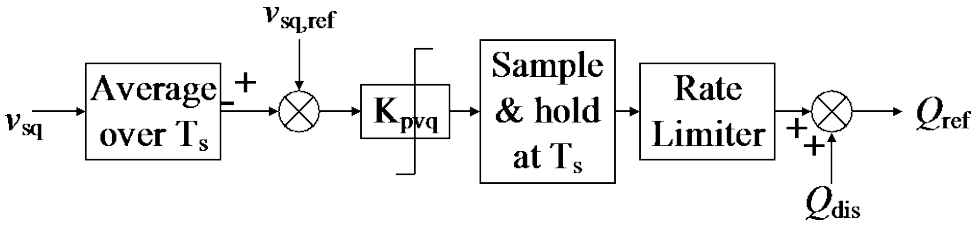

Figure 4-6: Voltage control in MMC.

The voltage support provided by the converter consists of a filter, resettable integrator, and a proportional controller. The use of proportional controller alone resulted in insufficient voltage compensation with low gains and oscillatory behavior with high gains. The resettable integrator provided the required stability. The inclusion of resettable integrator resulted in sampling the output of the voltage control at a different timescale compared to the rest of the states. The sampled time provides enough time to integrate the measured ac-side voltage. The overview of the control is shown in Fig. 4-6.

4.3 Development of Multi-Area Lumped Models

Dynamic ac transmission grid models for EI, ERCOT, and WI grids were required to evaluate the performance of the MTdc system as the system provided frequency support or other advanced support like dynamic voltage control. The full nodal ac transmission grid models of EI and WI represented a large of number buses (~100,000s) in the system, which is difficult to simulate in EMT simulators like PSCAD. The full nodal ac transmission grid models were based on a future scenario (2025/2026). Hence, lumped ac transmission grid models were developed to capture the frequency behavior of the full nodal ac transmission grid models.

The approach to develop the lumped ac transmission grids was based on tuning the existing lumped models to obtain acceptable frequency and voltage dynamic behaviors. The lumped ac transmission grid models of EI and WI were developed based on the following procedure:

1. Prepared the ac power flow lumped model with total generation and total load matching those of the main EI and WI areas (using the full nodal models) in PSS®E (or electro-mechanical transient simulators)
2. Tuned the dynamic models to match frequency response of the full nodal models
3. Compared the dynamic performance of lumped models against full nodal models
4. Translated the developed lumped models from PSS®E to PSCAD

The following existing lumped models and their corresponding characteristics are summarized below:

1. WI grid lumped model like 179-bus WI model(http://web.eecs.utk.edu/~kaisun/Oscillation/index.html)
    a. The frequency dynamics of the grid were represented using 29 machines
    b. No governors and exciters were included in the original lumped models
    c. Total load and generation of original model was about 42,000 MW as the model was created in 1980s probably representing minimum load
2. EI grid lumped models based on 68-bus model created for production cost modeling (PCM) [GMLC 2019]
    a. Several generators at each bus with no dynamics are represented (see Fig. 4-7)
3. ERCOT model based on [Makarov 2017]

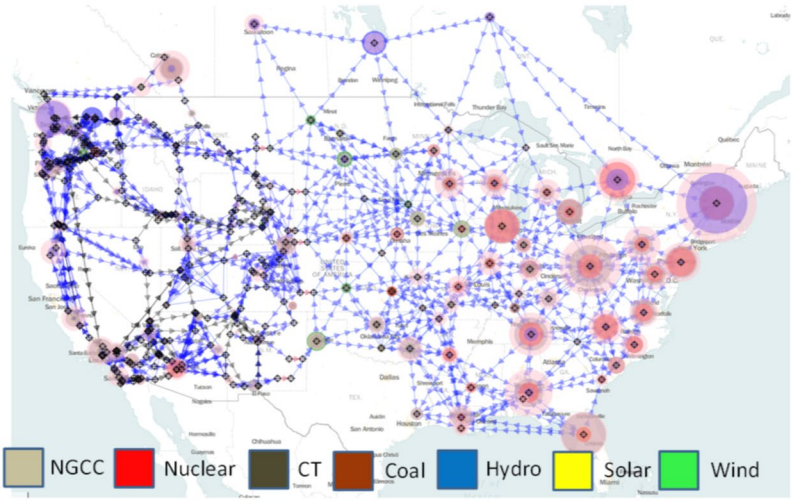

Source: Seams study, GM 1.3.33

Figure 4-7: Lumped model used for production cost modeling in project GM 1.3.33.

4.3.1 Lumped Model of EI Grid

The existing lumped EI model is based on the static dc power flow model (also referred to as the bubble model) [GMLC 2019] for PCM. This model does not preserve voltage, reactive power, or frequency dynamics of the full nodal model.

To build and tune the EI lumped dynamic model, dynamic data available for full EI planning model was used as a reference. Generators were lumped based on information available from bubble model on generation technologies and dynamic model types (specifically the type of governors' models). This process was followed to bring frequency response behavior of the lumped model to match that of the full EI planning model.

An initial lumped model was created with 57 large equivalent generators. The 57 large generators were divided into smaller generators using the 14 technologies defined in the EI static lumped model for each of the areas. The dynamic full nodal models of EI grid in PSS®E for 2026 scenario were also used to split generators into smaller generators. The type of governor in each of the lumped generators was also selected based on technologies defined in the bubble model and the governor models of the full nodal EI grid dynamic model in PSS®E.

4.3.2 Lumped Model of WI Grid

The existing 179 bus dynamic model of WI (or, lumped dynamic model of WI) does not contain governors and exciters in generators. The governors were added and tested together with exciters for stability and acceptable dynamic response. Governor and exciter model types were selected so that the lumped model contains similar proportions to the types of models contained in the full model. The existing lumped dynamic model of WI has a total load and generation of about 42 GW. The total load is low compared to the 170 GW of total load in the full nodal model of WI based on the 2025 scenario. The existing lumped dynamic model of WI was created in the 1980s and probably represented minimum load conditions. Therefore, the total load and generation of the existing lumped dynamic model was appropriately scaled to 170 GW. The loads and generations were made gradually and checked for model

convergence at each incremental step. The existing lumped dynamic model has negative loads representing HVdc inverters and some generators. These negative loads in PSS®E get converted into infinite buses in PSCAD upon conversion using E-Tran that raises accuracy concerns. This particular issue was resolved by replacing the negative loads by generator models.

4.3.3 Performance Evaluation Criteria of Lumped Models

NERC-BAL-003-1 criteria and guidance was used to compare the dynamic performance of the lumped models with the corresponding performance of the full nodal models upon a defined loss of generator. The frequency measured from each model was specifically compared at three points upon a loss of generator: FA, FB, and FC based on NERC's guidelines. The corresponding checkpoints (FA, FB, and FC) for quantifying the accuracy of system frequency response from different models are shown in Fig 4-8.

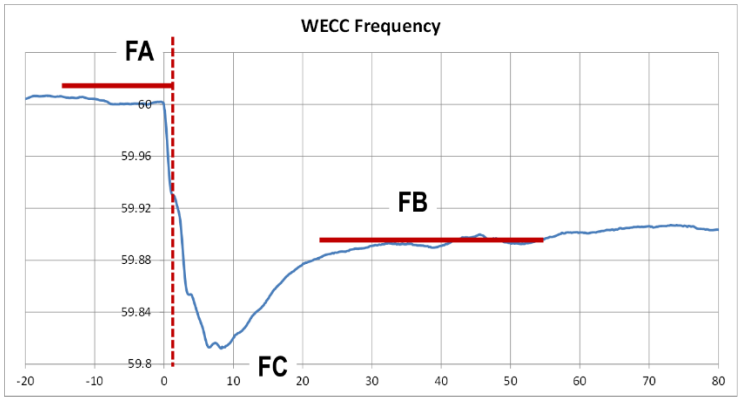

Figure 4-8: NERC-BAL-003-1 criteria for evaluating performance of power system frequency response.

4.3.4 Tuning of EI and WI Lumped Dynamic Models

The EI and WI lumped dynamic models were tuned to meet the performance criteria established in Section 4.3.3. This was a challenging effort due to the presence of hundreds of parameters in the equivalent generators of the 68-bus lumped model of EI grid and 179-bus lumped model of WI grid, in contrast to tuning a single or few machine models as in other efforts provided in the literature, such as in [Anderson 1990].

The EI grid lumped model and the WI grid lumped model were successfully tuned in PSS®E. The tuning process in PSS®E can be summarized with the following main points:

- Adjust Pgen for all bubbles
- Adjust base MVA for all generators and bubbles
- Adjust machine inertia for all generators and bubbles
- Verify proportion of each type of governor with respect to the proportions in the full nodal models
    - Type of governors such as IEEEG1, IEEESGO, TGOV1, GAST
- Adjust governor droops for all generators and bubbles

    - Typical values are 3-5% for individual generators, however lumped generators are not within this range to take into consideration the limitations of aggregation
- Represent deadband in EI model
    - NERC has reported frequency deadbands that exist in many speed governors in EI
    - Previous works on EI model demonstrated a more realistic match by considering deadbands of about 36 mHz [Kou 2016]
    - Replace IEEEG1, IEEESGO, and TGOV1 with WSIEG1
- Additional tuning of dynamic parameters
    - Turning on/off power system stabilizers
    - Selection of synchronous machine models
    - Tuning of stabilizers and governors

The frequency responses observed in the EI and WI grids based on a defined loss of generator in each interconnection are shown in Figs. 4-9(a) and (b). The responses shown in the figures include the observations from the simulation of both the full nodal and lumped models in PSS®E. It can be seen in the figures that the frequency responses observed in the lumped models approximate the frequency response observed in the full nodal model very well based on the performance criteria explained in Section 4.3.3.

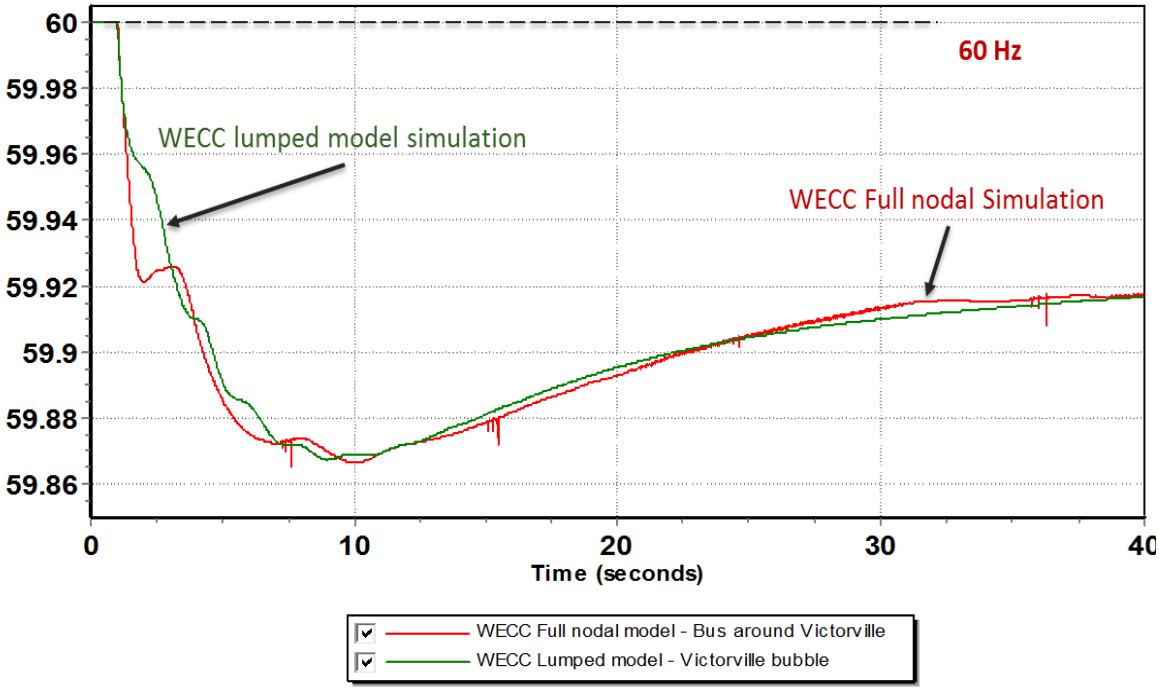

(a)

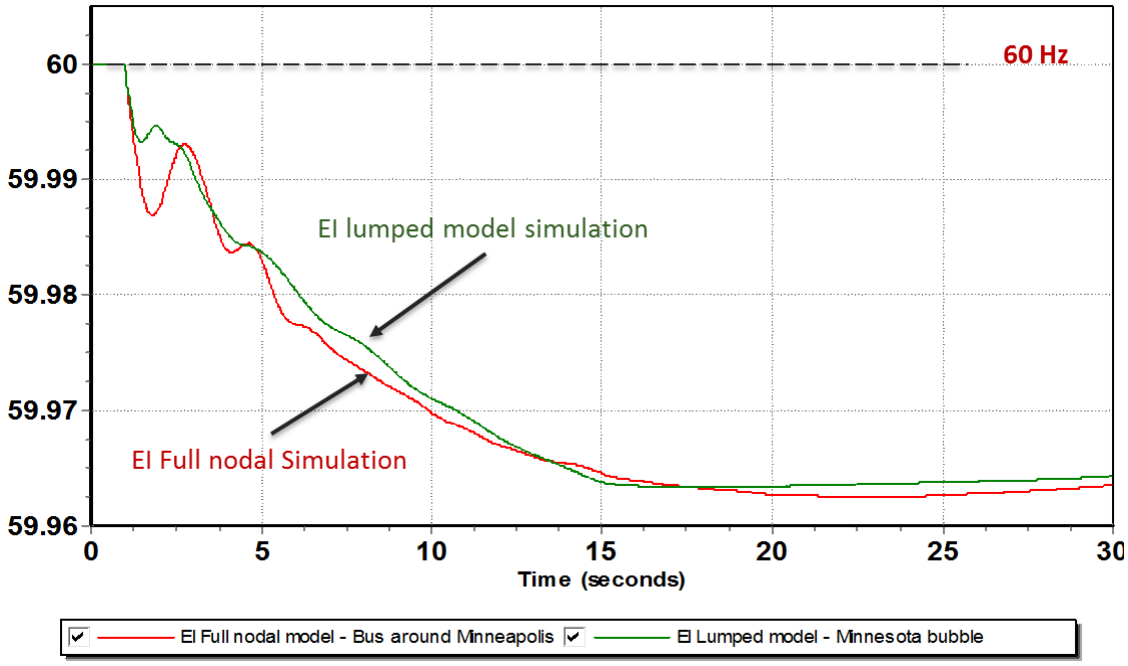

(b)

Figure 4-9: Final results of lumped model tuning compared with results from full industry-grade models for (a) Western interconnection and (b) Eastern interconnection.

4.3.5 Model Translation from PSS®E to PSCAD

The lumped models were initially developed in PSS®E as it had many functionalities for analyzing and debugging such large systems. With the detailed EMT dynamic models of MTdc systems developed in PSCAD, the evaluation of the advanced control methods in MTdc systems required lumped dynamic models of the ac transmission grids in PSCAD that adequately represent the voltage and frequency dynamics of the grids. Hence, the final step in developing the lumped models in PSCAD was to translate the models in PSS®E to the corresponding models in PSCAD-PSS®E using E-Tran. The translation process is not simple and needed various fixes due to differences in modeling of individual components in PSCAD and PSS®E. The following were the issues faced while translating the WI and EI lumped dynamic models in PSS®E to the corresponding models in PSCAD:

- The first test of the WI lumped dynamic model in PSCAD showed some numerical issues with generators due to two main reasons
    - Machine parameter Xp = X'p was not allowed in PSCAD, whereas it is allowed in PSS®E. This issue was fixed by making these reactances different for the few generators where this problem appeared.
    - Some generator outputs were producing excessive reactive power causing initialization problems in some of the exciters in PSCAD. The reactive power was reduced by selecting a different voltage setting or modifying nearby capacitors.
- The EI lumped dynamic model included 300 generators. E-Tran, by default, defined several measurements channels per generator when a model in PSS®E was converted to the corresponding model in PSCAD. When the dynamic model in PSS®E was converted to the model in PSCAD, it resulted in a large, unmanageable number of measurement channels in PSCAD. This problem was fixed by limiting the number of observable channels.
- The frequency response observed in the lumped dynamic model of EI grid in PSCAD does not match that of the model in PSS®E. The following issues have been identified:
    - Some shunt compensations were being translated as infinite bus, significantly affecting the frequency response of the system – this problem was corrected by manually modifying the shunts settings before the conversion
    - The model in PSCAD shows some instabilities when the simulation was run for longer time – this issue will be investigated in future work

Upon resolution of the majority of the aforementioned issues, the WI and EI lumped dynamic models in PSCAD provided similar dynamic performance. The dynamic performance is quantified by the frequency response measured in the system upon a loss of generator.

4.3.6 Additional Observations on the Developed Lumped Models

The following observations were important to the usage of the lumped models:

1. The lumped dynamic models were tuned and developed to mimic the frequency response (including inertial response) observed in the full nodal models of both WI and EI grids in the 2025/2026 scenario upon a loss of generator. They may not mimic the voltage response observed in the full nodal models during contingencies.
2. The lumped dynamic models were tested and verified to provide satisfactory frequency response under the two most common generation outages analyzed in EI and WI as provided below:
    a. EI model—Cook double generator outage (1,060 MW), XCEL generation outage (560 MW)
    b. WI model—Palo Verde double generator outage (2,756 MW), Diablo double generator outage (2400 MW)

3. Generator outages, where the size of the generator is larger than the ones mentioned above, were not guaranteed to produce stable frequency responses.

4.3.7 Computational Performance of the Lumped and Full Nodal Models

The comparison of the computation time taken to simulate the lumped dynamic models and full nodal models of WI and EI grids in PSS®E is listed in Table 4-3. The computation times were obtained from simulations on a Windows PC with an Intel(R) Core (TM) i7-6600U CPU @ 2.60GHz 2.80 GHz, RAM 16.0 GB (15.7 GB usable), 64-bit operating system.

Table 4-3: Computation time comparison of full models and lumped models in PSS®E.

Interconnection	**Full model in PSS®E**	**Lumped model in PSS®E**
WI	720 s (12 min)	6 s (0.1 min)
EI	2,160 s (36 min)	22 s (0.36 min)

4.3.8 Adding Voltage Behavior to Lumped Model

A practical approach to integrate detailed dynamic model of buffer zones that accurately represented local voltage behavior into a lumped dynamic model of a large power system is explained in this section. The buffer zones in each location can be extracted based on the procedure described in Chapter 3. The resulting integrated model were used to design advanced control methods in MTdc systems. These models were also used to study the impact of the control methods on local voltage and global effects such as frequency and regional ac power flows. The integration approach was directly applicable to practical power system models because it uses commercial E-Tran, PSS®E, and PSCAD software. This approach was demonstrated by combining the lumped dynamic model of the EI grid with buffer zones around the HVdc terminals in EI. The combined model provided a test bed to evaluate MTdc systems and their advanced control methods.

The conceptual approach taken to combine dynamic model of buffer zones and lumped dynamic model of grids is summarized below:

- The dynamic model of buffer zones and lumped dynamic model of grids were connected through several equivalent lines to conserve power flows, voltages, and short circuit ratio as much as possible.
- Equivalent line parameters were defined using an equivalencing process applied to the full nodal dynamic models with tools like E-Tran and PSS®E.
- Tested and refined the approach as needed.

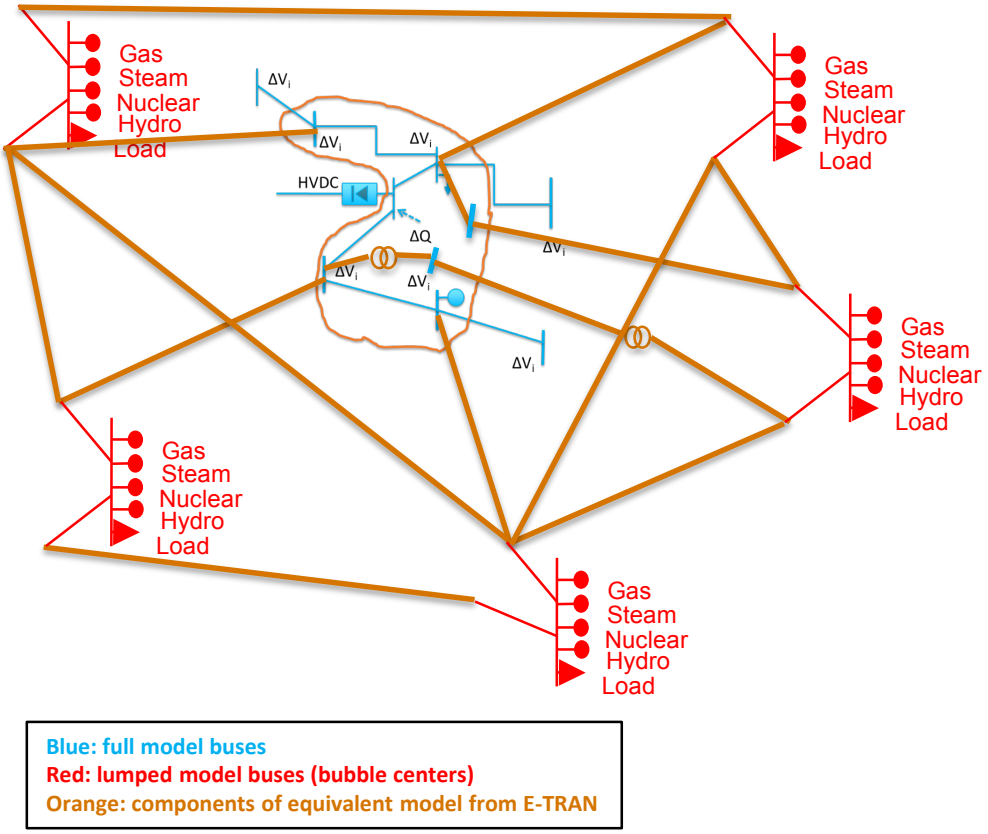

Figure 4-10: Combination of multi-area ac lumped model with detailed buffer zones.

This approach is graphically shown in an example case in Fig. 4-10 and it is applied to Atlanta and Orlando buffer zones. It may be applied to other buffer zones in the future. The equivalencing process can be based on identifying bubble centers in E-Tran to develop the equivalent lines. The equivalent lines can connect the dynamic model of the buffer zones in Atlanta and Orlando to the lumped dynamic model of EI grid. The strong buses in the full nodal dynamic model of the EI grid in PSS®E that are near the buffer zones were adopted as the bubble centers. The equivalencing process resulted in an equivalent model with 42 buses, as shown in Fig. 4-11. The 42 buses include the 6 buses selected as bubbles near the buffer zones. The buffer zones originally defined are marked in Fig. 4-11 by stars. This equivalent model was created successfully in PSCAD using E-Tran.

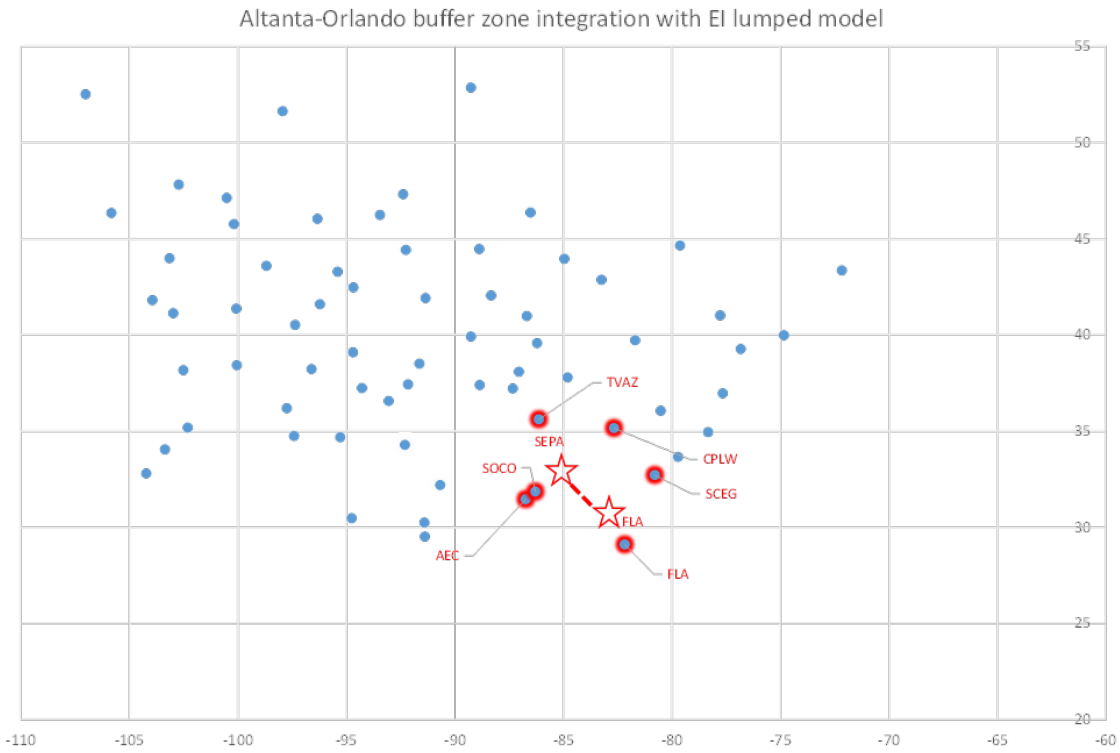

Figure 4-11: Selected buses in the full nodal dynamic model of EI grid as bubble centers to form buffer zones plus equivalent lines to connect to lumped dynamic model of EI grid.

The next step was to export the equivalent model in PSCAD into PSS®E. The equivalent model in PSS®E was then be combined with the lumped dynamic model of the EI grid. E-Tran does not have the ability to convert models from PSCAD to the corresponding models in PSS®E. Python scripts were developed to perform this conversion using the PSCAD tabular functions.

The overview of the approach explained in this section is illustrated in Fig. 4-12.

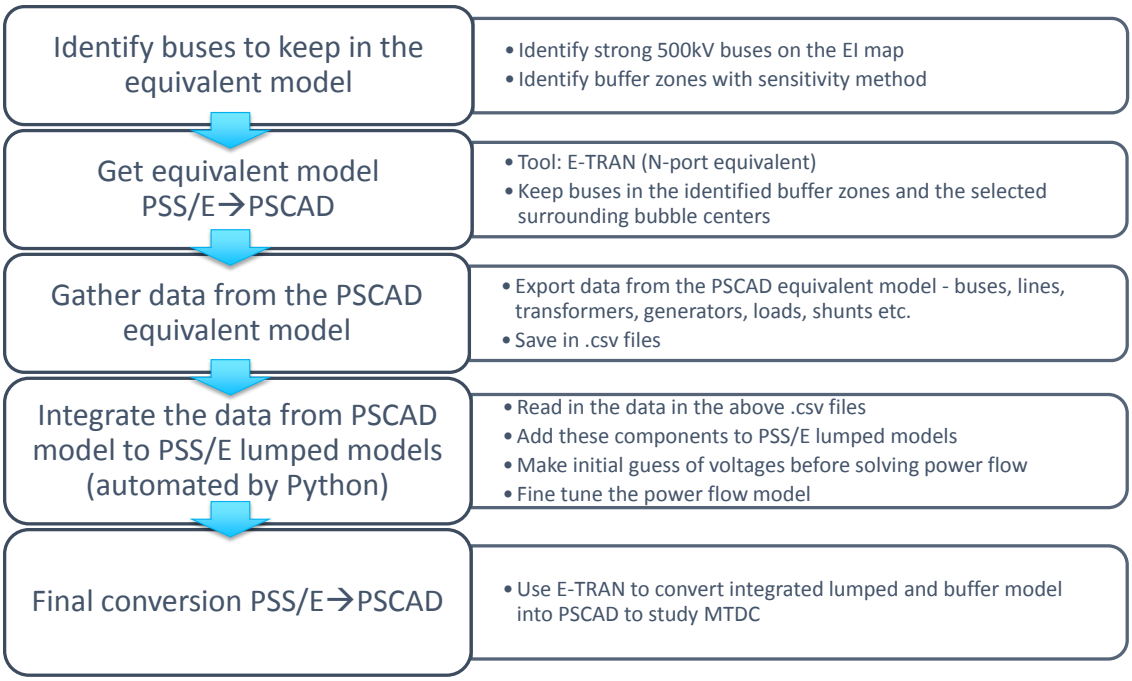

Figure 4-12: Flowchart of the integration procedure.

The combined lumped dynamic model of the EI grid with the dynamic models of Atlanta and Orlando buffer zones is hereafter termed as the combined dynamic model. The steady-state voltages of the buffer zone buses in the combined dynamic model were compared to the corresponding buses in the full nodal model of the EI grid. The percentage difference in the comparison is shown in Fig. 4-13. The differences in the steady-state voltages were within ± 6.39%.

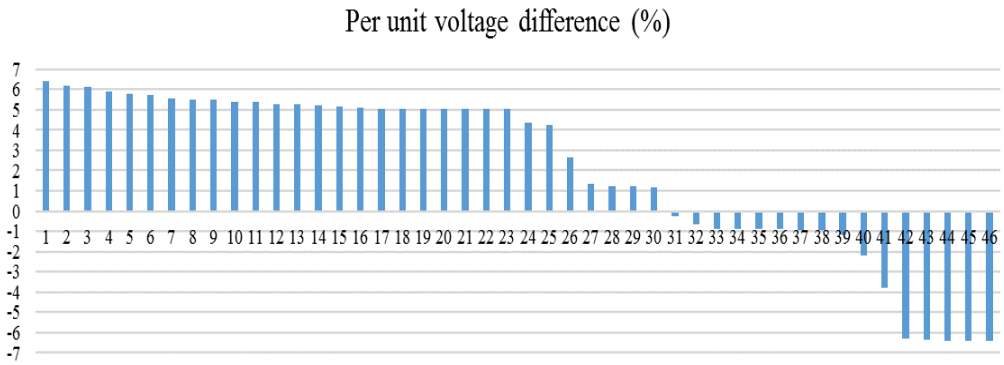

Figure 4-13: Steady state voltage comparison for the buffer zone buses between combined dynamic and full nodal dynamic model of the EI grid.

In addition to the combined model approximating the full model, it is also of interest to show that the combined model does not drastically modify the original dynamics of the lumped model. To evaluate this performance, the dynamic voltage measured in the combined dynamic model was compared with that measured in the lumped dynamic model of EI grid in PSS®E during a generation loss contingency. The contingency used was tripping of a 1,200 MW generator in Minnesota. The corresponding results for three of the buses are shown in Fig. 4-14. It can be observed in the figure that the measured voltages in

Area 4 and Area 5 from the simulation of both the models were similar. For the measured voltages in Area 2, there is a steady state difference between the results observed from the simulation of the models.

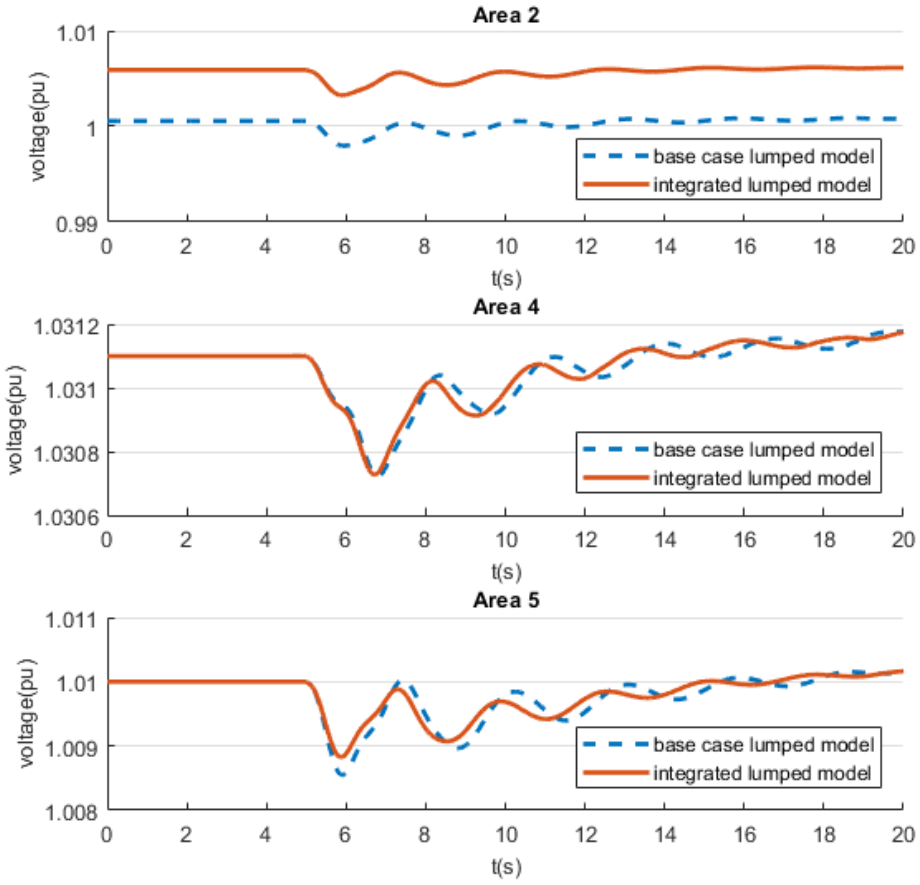

Figure 4-14: Dynamic voltage response comparison.

4.3.9 Lumped Model of ERCOT Grid

The simplified dynamic model of ERCOT grid is based on the developments in [Makarov 2017] and is summarized here as

$$F(s) = F_{\text{nom}}(s) + \frac{G}{1+2\frac{\delta}{\omega_n}s+\frac{s^2}{\omega_n^2}}(P_{\text{gen}} - P_{\text{load}}), \tag{4.17}$$

where F_{nom} is the nominal frequency, P_{gen} is the generation, and P_{load} is the load in the interconnection. The dynamic performance of this model has been verified in [Makarov 2017].

4.4 Case Studies Evaluating Advanced Control Methods in MTdc Systems

4.1.1 Advanced Frequency Control

The optimization problem formulated in Section 4.2.2 to develop the optimal expert system for MTdc systems is solved for the following two case studies:

- 2 GW ±525 kV seven-terminal MTdc system with normal power flow (i.e., power flow from WI grid to EI grid),

- 2 GW ±525 kV seven-terminal MTdc system with reverse power flow (i.e., power flow from EI grid to WI grid).

The seven-terminal MTdc system is shown in Fig. 4-2, where two terminals connect to the WI grid, four terminals connect to the EI grid, and one terminal connects to the ERCOT grid. The results of the optimization problem for the six-terminal MTdc system is not discussed in this chapter as this system is a subset of the seven-terminal MTdc system without the MMC-HVdc substation terminal in the ERCOT grid. In each case-study mentioned above, multiple contingencies were considered that include loss of generation in EI, loss of generation in WI, and loss of generation in ERCOT. Six use cases were studied in this section.

The initial and final optimized gains of the expert system are provided in the Appendix C for all use cases. The performance of the optimization problem formulated is evaluated by comparing the performance of the expert system with initial gains and optimized gains in the MTdc systems. The comparison is performed based on the frequency responses observed in the simulation of the simplified models used in the optimization problem (as described in Section 4.2.2). Based on these comparisons, it is highlighted that the frequency deviation caused by the loss of generation in an asynchronous interconnection is reduced by use of the optimized gains in the expert system. The optimized gains in the expert system enable the transfer of maximum amount of power between asynchronous interconnections. The corresponding comparison in the performance is shown in Fig. 4-15 for the normal power flow case with a 500 MW loss of generation in the ERCOT grid. As shown in Fig. 4-15(b), the frequency deviation in the ERCOT grid upon the loss of generation converges to -0.048, compared to -0.07 in Fig. 4-15(a). The nadir in the frequency deviation in the ERCOT grid is seen to improve from -0.08 to -0.06 from the figures. The settling point and the nadir in the frequency response improve by 31% and 25%, respectively.

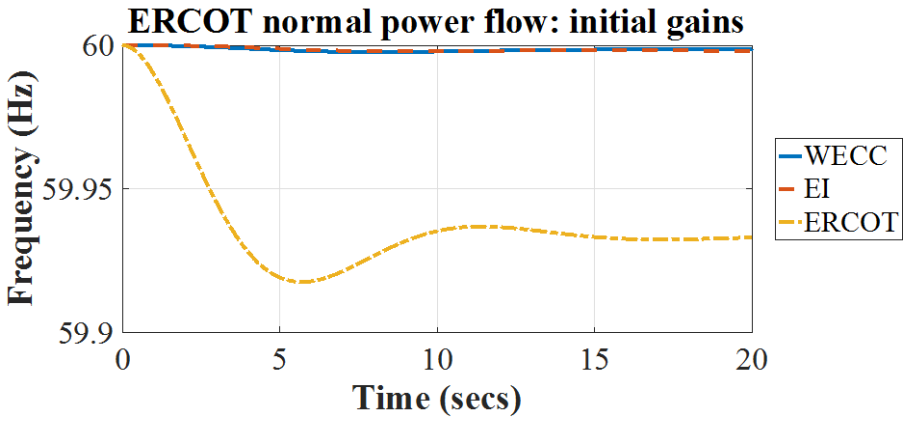

(a)

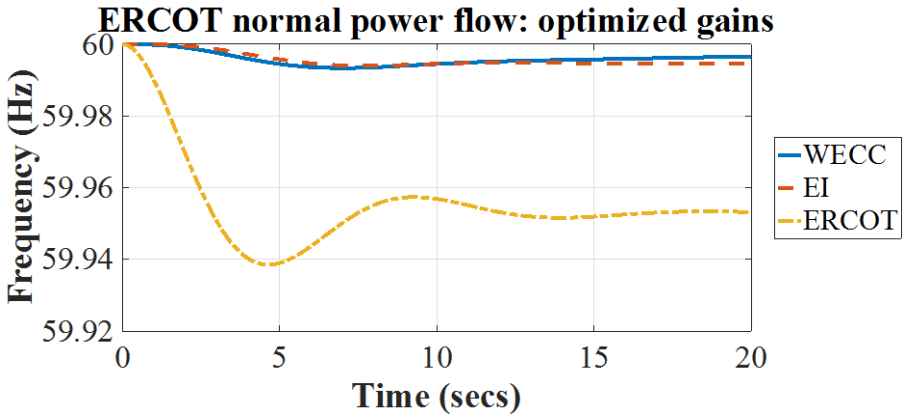

(b)

Figure 4-15: Frequency response based on (a) initial gains, (b) optimized gains in the expert system of the MTdc system with loss generation in the ERCOT grid.

The comparison in the performance of frequency response is shown in Fig. 4-16 for the normal power flow case with a 2,756 MW loss of generation in WI grid. The loss of generation represented the double Palo Verde loss of generation in the WI grid. As shown in Fig. 4-16(b), the frequency deviation in the WI grid upon the loss of generation converges to -0.07, compared to -0.1 in Fig. 4-16(a). The nadir in the frequency deviation in the WI grid is seen to improve from -0.15 to -0.09 from the figures. The settling point and nadir in the frequency deviation improved by 30% and 40%, respectively.

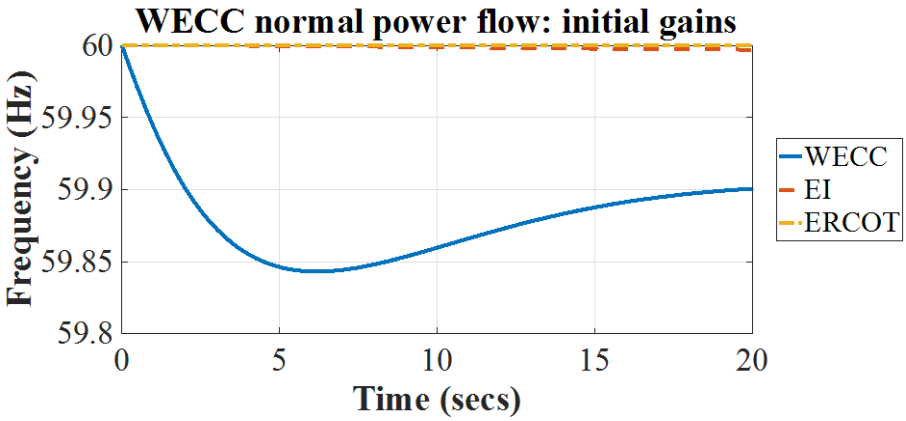

(a)

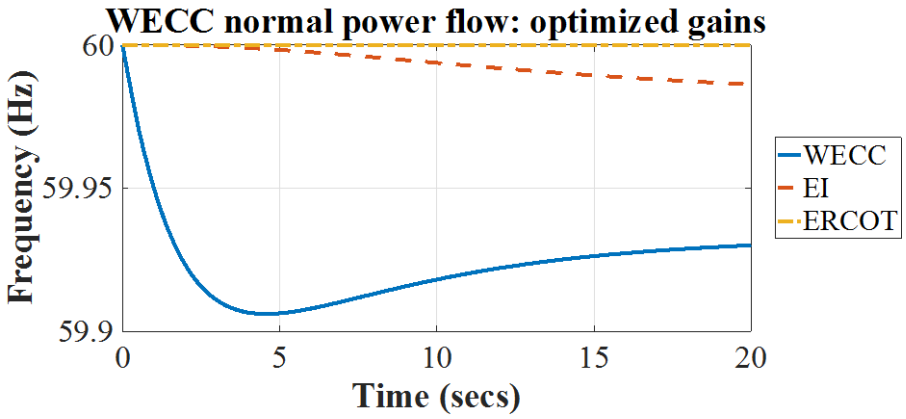

(b)

Figure 4-16: Frequency response based on (a) initial gains and (b) optimized gains in WI loss of generation.

The results of all the use cases along are shown in Appendix C. The improvement in the settling point of the frequency response was observed to be ranging between 25% and 31%.

The EMT model of the seven-terminal MTdc system scenario described in Section 4.1 is integrated into the multi-area lumped EMT models of the EI, ERCOT, and WI grids developed in Section 4.3. The MTdc systems are integrated into the grids at the locations identified in Section 4.1. This EMT model was utilized to evaluate the performance of the advanced frequency control based on the optimized gains identified.

The 500 MW loss of generation in the ERCOT grid with the MTdc system connecting the asynchronous grids was simulated using EMT simulation; the corresponding results from the simulation are shown in Fig. 4-17. F_VV, F_PV, F_PC, F_AT, F_OR, F_STL, and F_SW indicate the frequency measured at substation terminals Victorville (VV), Palo Verde (PV), Panola County (PC), Atlanta (ATL), Orlando (ORL), St Louis (STL), and Sweetwater (SW), respectively, in Fig. 4-17(a). F_VVbase, F_PVbase, and F_SWbase are the frequency profiles at the substation terminals in VV, PV, and SW, respectively, without any primary frequency support. Pout1-Pout7 in Fig. 4-17(b) indicate the output power profiles at substation terminals VV through SW as in the same order tabulated in Appendix C.Vdc1-Vdc7 in Fig. 4-17(c) indicate the output dc voltage profiles of the terminals VV through SW as in the same order

tabulated in Appendix C. idc1-idc7 in Fig. 4-17(d) indicate the output current profiles of terminals VV through SW as in the same order as tabulated in Appendix C.

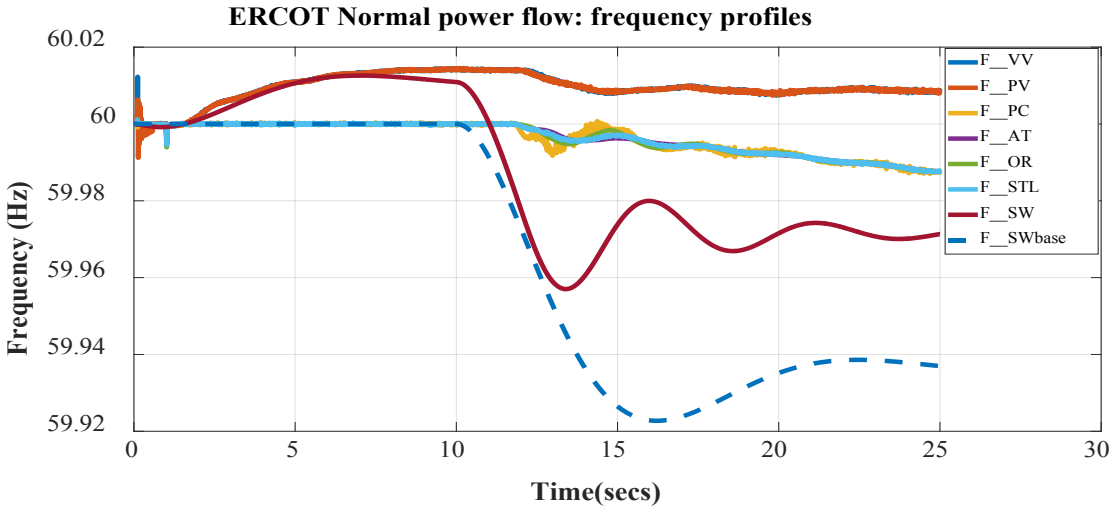

(a)

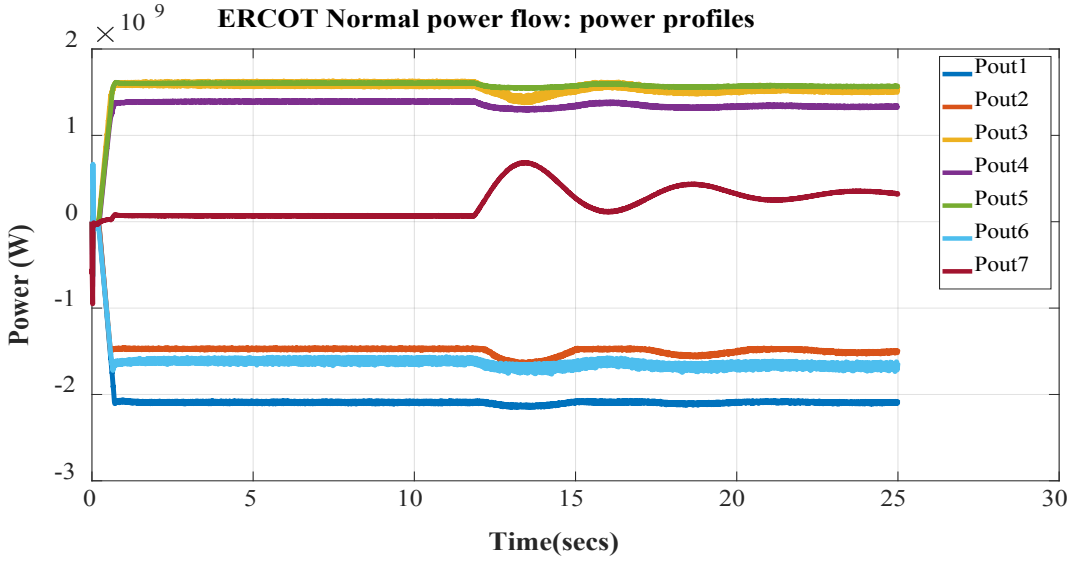

(b)

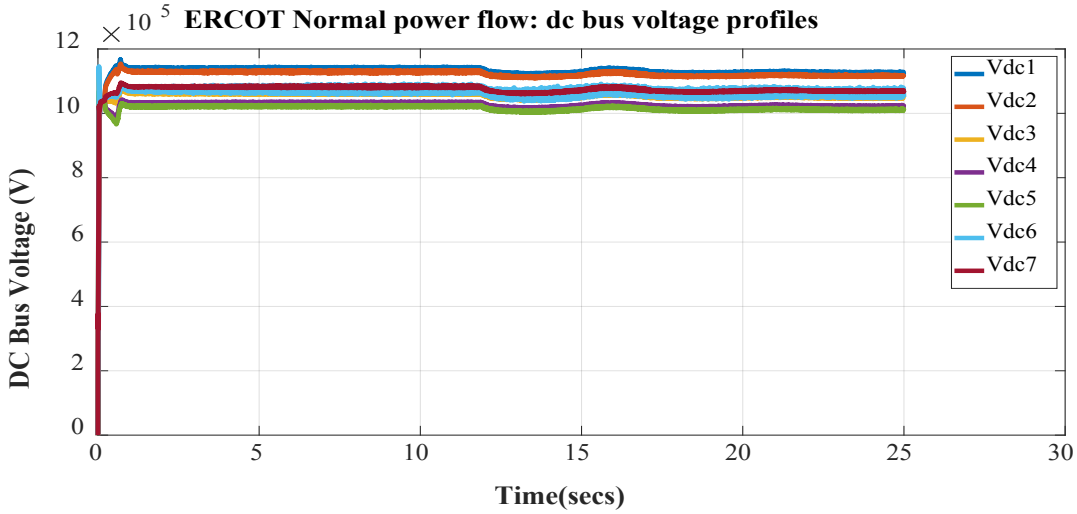

(c)

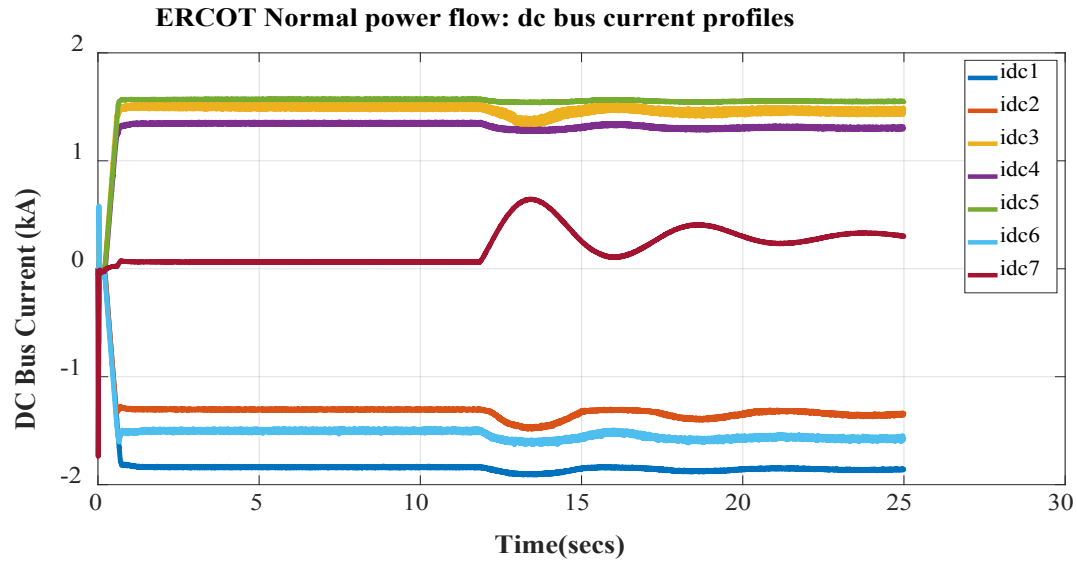

(d)

Figure 4-17: Loss of generation in the ERCOT grid in normal power flow case study: (a) frequency profiles with and without WI and EI support, (b) output power profiles, (c) dc bus voltage profiles, and (d) dc bus current profiles.

From Fig. 4-17(a), it can be noticed that the inclusion of advanced frequency control in the MTdc system improved the frequency response. Frequency response of the ERCOT grid was improved by up to 38.8% in the nadir and 44.4% in the settling point. It can be observed from Figs. 4-17(b) and (d) that in the event of generation loss in ERCOT grid, the support is provided to the grid by changing the power and current flow through the MTdc system. During the contingency, the dc voltages at all the MTdc substation terminals are within the defined permissible limits, as seen from Fig. 4-17(c).

The 2,756 MW loss of generation in WI grid with the MTdc system connecting the asynchronous grids was simulated using EMT simulation. The corresponding results from the simulation are shown in Fig. 4-18. From Fig. 4-18(a), it can be noticed that the inclusion of advanced frequency control in the MTdc system improved the frequency response. Frequency response of the WI grid was improved by up to

62.5% in the nadir and 64.3% in the settling point. In the event of generation loss in the WI grid, the support is provided to WI by the MTdc substation terminals in the EI grid. This phenomenon can be clearly noticed in Figs. 4-18(b) and (d). The dc voltages at all MTdc substation terminals are within the defined permissible limits, as seen in Fig 4-18(c).

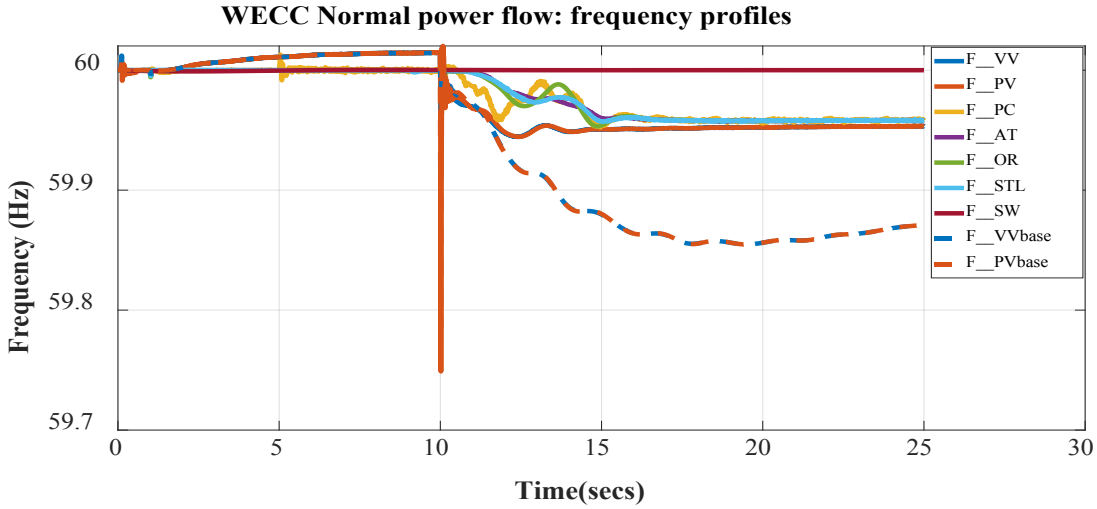

(a)

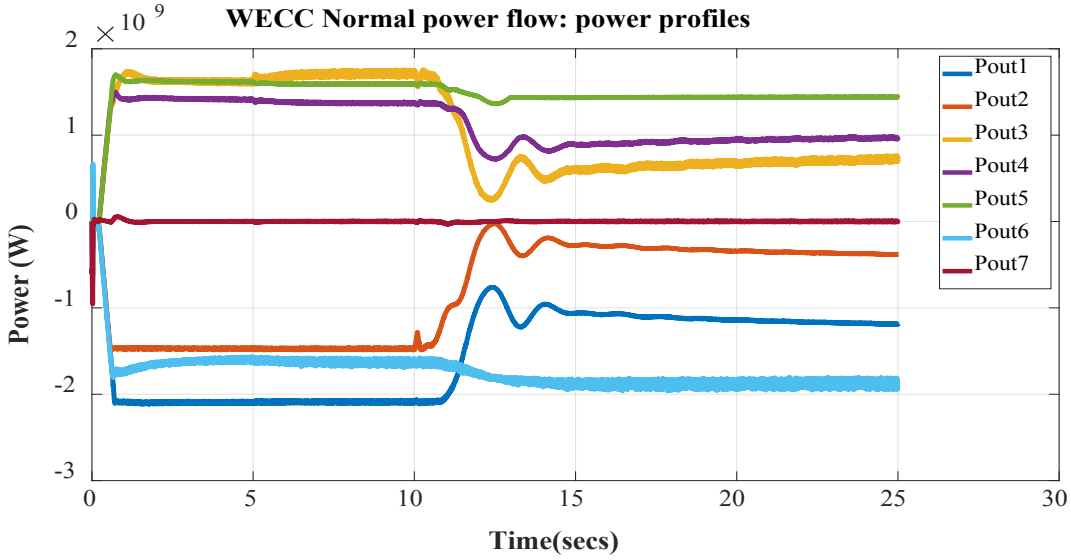

(b)

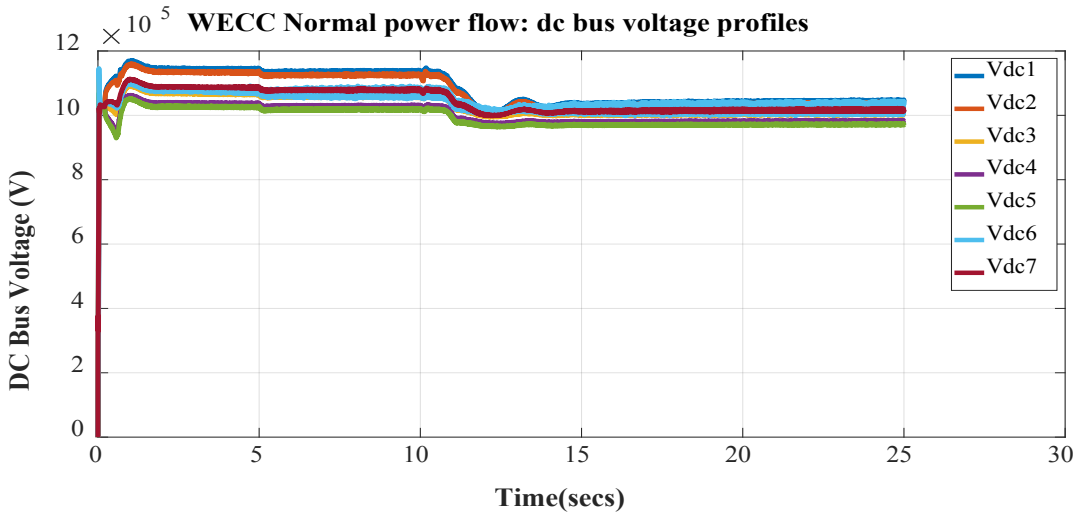

(c)

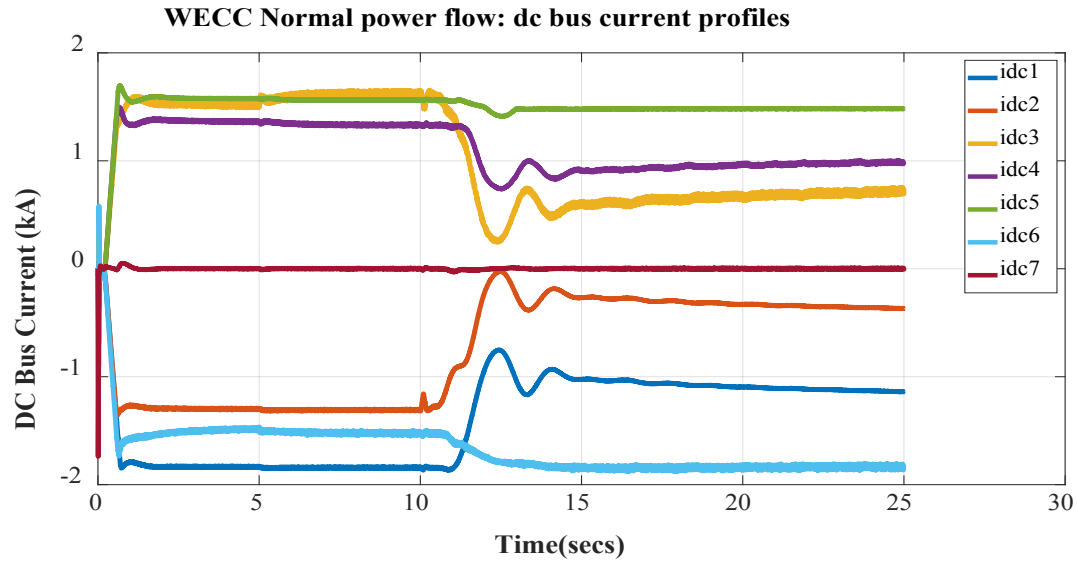

(d)

Figure 4-18: Loss of generation in the WI grid in normal power flow case study: (a) frequency profiles with and without EI and ERCOT support (b) output power profiles (c) dc bus voltage profiles (d) dc bus current profiles.

All the simulated use case results from the detailed EMT simulation of the MTdc system with the combined grid models are documented in Appendix C. From the figures in the Appendix, it is observed that up to 64% improvement is observed in the nadir and 63% improvement in the settling point of the frequency response.

To understand the constrained multi-objective optimization applied to the control of MTdc systems to enable sharing of primary frequency reserves in asynchronous interconnections in United States, a preliminary work on creating a visualization framework has been started. The framework enables the ability to visualize multiple datasets that are being utilized in the control of MTdc systems while preserving the system reliability. The preliminary framework is shown in Appendix C.

4.1.2 Voltage Control and Evaluation of Combined Lumped-Buffer Zone Models

The EMT model of the MTdc system for the seven-terminal scenario described in Section 4.1 was integrated into the combined model of the EI grid (with Atlanta and Orlando buffer zones) and multi-area lumped models of the WI and ERCOT grids. The combined model of EI grid was based on the model developed in Section 4.3.8. The MTdc system was integrated into the grids at the locations identified in Section 4.1. This EMT model was utilized to evaluate the performance of the voltage control described in Section 4.2.3 and to evaluate the performance of the combined model of the EI grid.

The voltage profile of a bus near Atlanta is shown in Fig. 4-19 during a three-phase transmission line fault. The profiles observed were recorded from simulation of Atlanta buffer zone alone and the combined model without the MTdc system model. A steady-state difference of 7% was observed between the voltage profiles. The transient behavior observed in the voltages during the three-phase transmission line fault was also observed in the figure. The transient behavior was important to understand the stability and impact of the voltage control methods developed in MTdc systems.

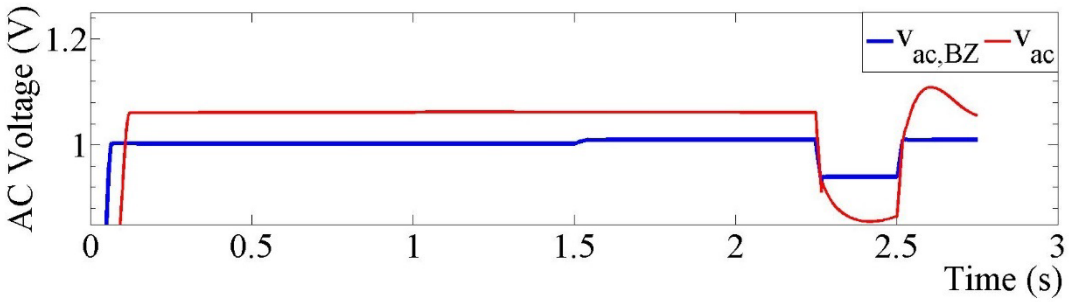

Figure 4-19: Voltage profiles of a bus near Atlanta (without the MTdc system) when transmission line fault occurs at t = 2.25 s. “vac,BZ” and “vac” are the voltages observed in the buffer zone only and the combined model, respectively.

The EMT model of the MTdc system for the seven-terminal scenario described in Section 4.1 was integrated into the combined model of the EI grid (with Atlanta and Orlando buffer zones) and multi-area lumped models of the WI and ERCOT grids. The combined model of the EI grid was based on the model developed in Section 4.3.8. The MTdc system was integrated into the grids at the locations identified in Section 4.1. This EMT model was utilized to evaluate the performance of the voltage control described in Section 4.2.3 and evaluate the performance of the combined model of EI grid. The states observed near Atlanta during a three-phase transmission line fault (at t = 3.0 s) are shown in Fig. 4-20. The states observed are recorded from simulation of Atlanta buffer zone alone and the combined model with the MTdc system model. The voltage control in the MMC substation terminal at Atlanta was activated at t = 2.0 s. There is a steady-state voltage difference of 7% observed when comparing the two models before t = 2.0 s. This steady-state difference in the voltages resulted in different reactive powers observed after t = 2.0 s, once the voltage control was enabled in the MMC substation terminal at Atlanta. There were also differences observed in the dynamics of the reactive power during the three-phase transmission line fault between the two models.

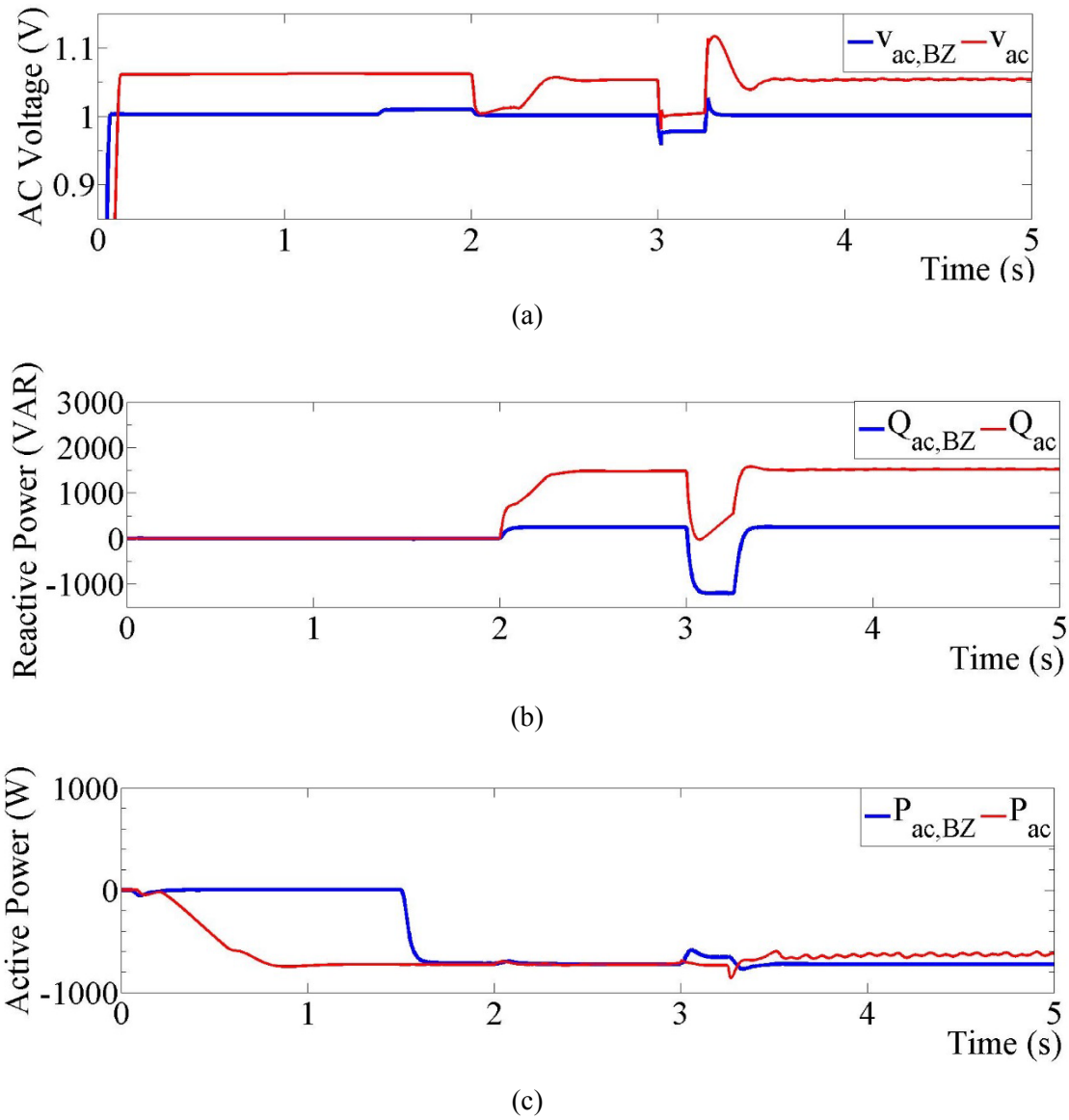

Figure 4-20: State profiles of a bus near Atlanta when transmission line fault occurs at t = 3.0 s: (a) voltage, (b) reactive power, and (c) active power. "xac,BZ" and "xac" are the states observed in the buffer zone only and the combined model, respectively. "x" represents voltage, reactive power, and active power.

The active power in the MMC substation at Atlanta was turned on differently in the two models, resulting in the differences observed in the active power profiles before t = 2.0 s. That is, the differences observed in the active power before t = 2.0 s were not related to the models utilized. However, the differences observed in the active power after t = 2.0 s were related to the models utilized. There were differences observed like the ripple in the active power and the dynamics observed in the active power after the application of the three-phase transmission line faults. The ripple observed in the active power measured from the combined model was due to saturation in the controlled states in the MMC substation terminal at Atlanta.

There were differences observed with the response of the voltage controller in the MMC substation terminal at Atlanta when simulated with two different ac transmission grid models: (i) buffer zone of

Atlanta alone and (ii) the combined EI grid model that includes the lumped model of EI grid and the buffer zones of Atlanta and Orlando. The results from the combined model are expected to be more accurate due to a detailed representation of the ac transmission grid.

Chapter 5 Models & Advanced Control Methods for Different HVdc Penetration Scenarios

The modeling of and the control coordination in various HVdc penetration scenarios to provide primary frequency response and congestion management in a North American continental-level power system are described in this chapter. Scenarios of different levels of HVdc penetration were defined, where the lines were considered as strengthening the interconnection between the two largest North American power system interconnections: EI and WI. Power flow static and electromechanical dynamic models were built for the scenarios based on industry-grade models and databases. HVdc lines were modeled as being controlled with both centralized power schedules and decentralized controllers to support the primary frequency responses. Congestion management was modeled as HVdc fast centralized rescheduling. The primary frequency response performance in one interconnection can be improved by immediately bringing support from the other interconnection. Additionally, HVdc lines can be used to alleviate congestion in the underlying ac system, especially when fast centralized rescheduling is used after a large generation contingency in combination with decentralized HVdc control. The model and simulations demonstrated the technical benefits of having more controllable HVdc lines in place in the system in addition to the benefits of transfers of large blocks of energy among regions.

5.1 HVdc Penetration Scenarios

Scenarios with various levels of HVdc penetration were defined and studied in this work. The largest two North American electrical interconnections, the EI and the WI (also referred to as WECC), were considered in this study. This study focused on the HVdc lines that strengthen the interconnections between EI and WI and the lines close to the seams between these two interconnections.

The following three main sources of data were used to define the HVdc penetration scenarios:

1. HVdc macrogrid initially proposed by MISO: This macrogrid scenario was updated and the corresponding models were built using 2025/2026 ac transmission grid models and developing power flow and dynamic ac/macrogrid HVdc models [Makarov 2017 and Elizondo 2017].
2. Project GM 1.3.33 “Seams study:” The latest preliminary results (December 2017) were obtained from the Grid Modernization Laboratory Consortium [GMLC 2019].
3. Industry-proposed HVdc lines: Currently proposed HVdc lines (as of December 2017) were surveyed using project information available online. The proposed lines were selected based on the highest likelihood of actual construction and proximity to the EI-WI borders.

The data sources to build the new dc scenarios are illustrated in Fig. 5-1. For data from source 1, the reader can refer to [Makarov 2017]. The identified HVdc lines from scenario 2.b from [GMLC 2019], or data from source 2, are shown in Table 5-1. The HVdc lines proposed by industry that were selected for the dc penetration scenarios, or data from source 3, are shown in Table 5-2.

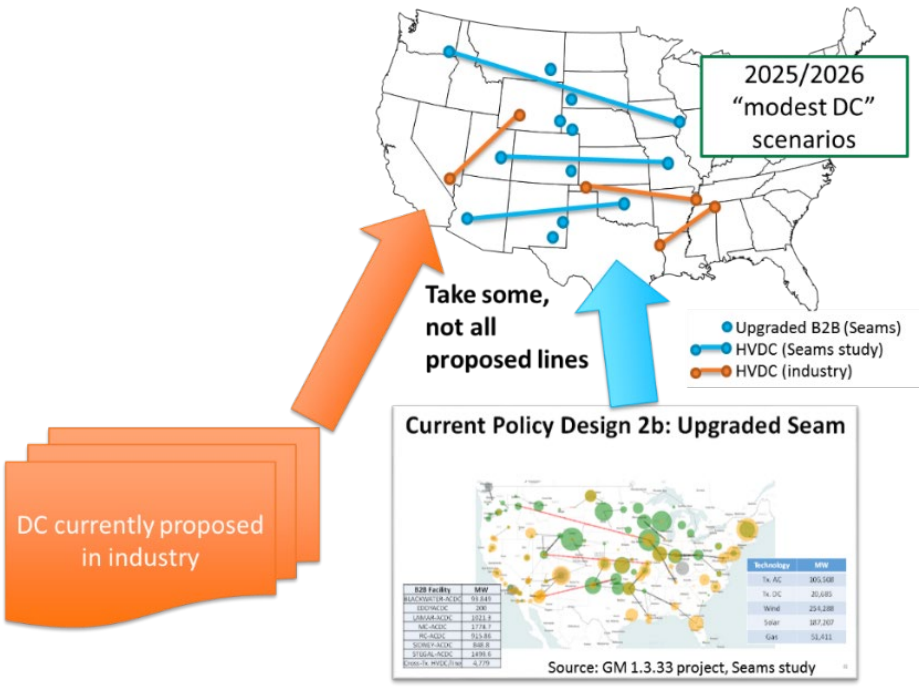

Figure 5-1: Sources of data for building dc penetration scenarios.

Table 5-1: Preliminary data from identified scenario 2.b from [GMLC 2019].

Scenario #	dc Lines Information					Information Required or Missing
	Locations	**Type**	**Voltage Rating (kV)**	**Power Rating (MW)**	**Stage of Implementation (ongoing/short-term/future)**	
Seams 2.b	Artesia, NM	Back-to-back (B2B)	82	200	Existing	
	Blackwater, NM	B2B	57	94	Existing (200MW)	
	Lamar, CO	B2B	64	1,021	Future (210 MW existing)	Voltage and technology for desired power rating - models
	Sidney, NE	B2B	50	849	Future (200 MW existing)	Voltage and technology for desired power rating - models
	Stegall, NE	B2B	50	1,494	Future (200 MW existing)	Voltage and technology for desired power rating - models
	Rapid City, SD	B2B	13	916	Future (200 MW existing)	Voltage and technology for desired power rating - models
	Miles City, MT	B2B	82	1,775	Future (200 MW existing)	Voltage and technology for desired power rating - models
	Hanford, WA – Davenport, IA	LCC	800	4,779	Future, 1,800 mi	Conductor, preferred losses, usage capacity factor
	Intermountain, UT – St. Louis, MO	LCC	800	4,779	Future, 1,330 mi	Conductor, preferred losses, usage capacity factor
	Palo Verde, AZ - Seminole, OK	LCC	800	4,779	Future, 1,060 mi	Conductor, preferred losses, usage capacity factor

Table 5-2: Identified HVdc projects proposed by industry.

Name	Location	Length	Voltage	Capacity	Cost
Southern Cross	Desoto Parish (Texas border) - Northeast Mississippi	400 mi	500 kV	2,000 MW	N/A
Plains & Eastern Clean Line	Panhandle, OK - Memphis, TN	720 mi	600 kV	4,000 MW	$2.5 B
TransWest	Wyoming - Desert Southwest region (California, Nevada, Arizona)	730 mi	500 kV	3,000 MW	$3 B(*)

(*) this estimate includes both a 500kV ac line and an HVdc line

The models corresponding to 2025/2026 industry scenarios for the EI and WI systems were utilized in the studies performed in this project. The corresponding dynamics models built in [Makarov 2017] were leveraged in these studies. It is important to highlight that the 2025/2026 industry dynamic models of EI and WI already contain existing dc lines as of 2018. The HVdc macrogrid model built in [Makarov 2017] was considered as one of the scenarios of the study.

The new HVdc lines and back-to-back (B2B) reinforcements proposed in [GMLC 2019] were designed for a 2038 scenario. The challenge in this project was to select the HVdc lines and B2B reinforcements that are compatible with the existing grid in the 2025/2026 scenarios and based on 2025/2026 load and generation. The 2025/2026 scenarios did not include all generation additions and transmission reinforcements suggested in 2038 model. In this project power transfers between EI and WI were adjusted to levels that do not raise major reliability or feasibility concerns.

Three new HVdc penetration scenarios were studied in this project (see Fig. 5-2):

- Topology 1, incorporating B2B dc upgrades;
- Topology 2, based on two dc lines connecting EI and WI; and
- Topology 3, based on three dc lines connecting EI and WI.

As part of this project, the three new scenarios were compared with the macrogrid scenario described in [Makarov 2017] (Topology 4 in Fig. 5-2). The new HVdc topologies were proposed so that they gradually add dc infrastructure. A lesser priority was assigned to Topology 2 because it is an intermediate scenario with potential major reliability problems caused by one of East-West HVdc lines being forced out. Hence, topology 2 is being studied no further.

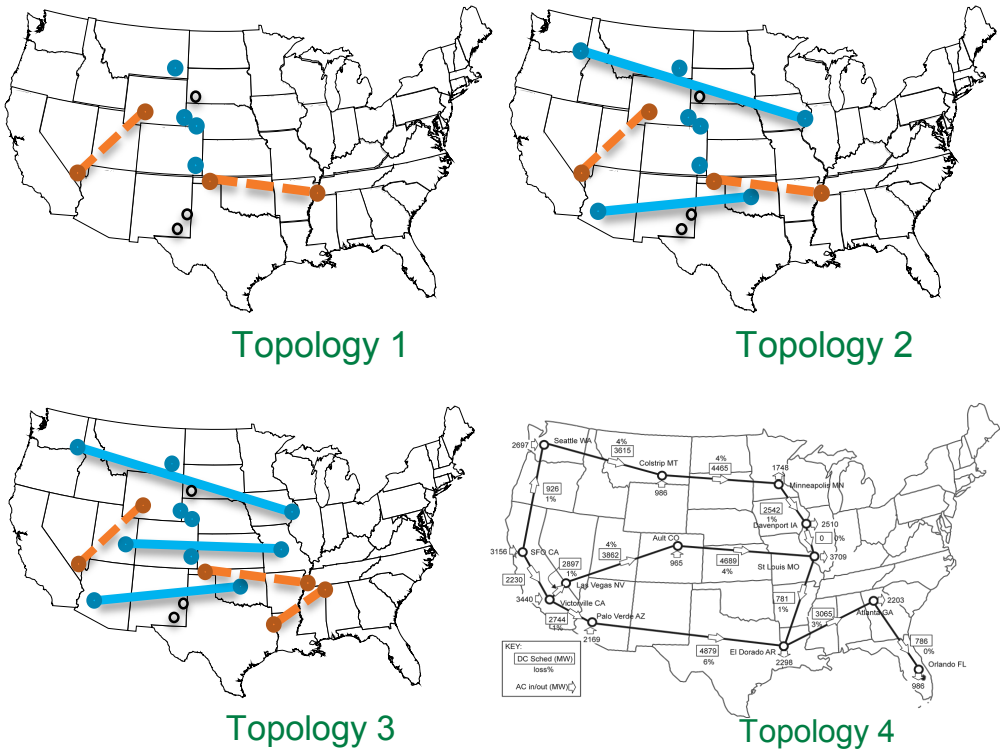

Figure 5-2: Four HVdc penetration scenarios proposed for this work.

5.2 Modeling of Continental-Level EI and WI Grids Connected through HVdc Topologies

The power flow and dynamic models of the two defined HVdc penetration scenarios (topologies) were built. The corresponding models of the macrogrid scenario were built in [Markarov 2017]. A high-level summary of the process to build the models is as follows:

1. *Power flow (steady-state) combined models:* As part of the process of building the power flow models, power flow studies were performed to identify limitations on capacity and location of HVdc lines and B2B connections. Additionally, generation was modified to accommodate the power transfers between EI and WI. The manual process followed here is based on the process followed in [Makarov 2017].
2. *Dynamic combined models:* The dynamic models for HVdc lines were developed. The dynamic models of EI and WI were tested individually. The dynamic model of EI was corrected to make the simulated frequency response characteristics similar to those of the measured response. The dynamics models were combined in a single model of both EI and WI connected through the HVdc dynamic models.

The following subsections provide additional details of the modeling process.

5.2.1 Topology 1: Identification of B2B Capacity Reinforcements for 2025/2026 Scenario

Topology 1 is based on reinforcing the existing B2B dc connections between the EI and WI. The main bottleneck of this type of reinforcement is the current ac transmission grid around the B2B connections. The grid is currently not well developed near these connections to accept the injections defined in [GMLC

2019]. In order to identify the amount of capacity that can be increased in the existing B2B dc connections for the 2025/2026 scenarios, an initial power flow feasibility study was performed. It appears most likely that not all the capacity proposed for year 2038 in Table 5-1 [GMLC 2019] will be feasible in 2025/2026 scenarios.

The original operating powers and dc voltages of the identified B2B dc ties are tabulated in Table 5-3. In Table 5-3, the operating powers have been taken from the 2025/2026 planning models (including 0 MW on the Blackwater B2B).

Table 5-3: Current operating values of and results of maximum power transfer feasible from identified B2B dc line.

Locations	Operating dc Voltage (kV)	Operating Power (MW)	Max Power Transfer Feasible (MW)
Blackwater, NM	55	0	200
Lamar, CO	87.5	99	120
Sidney, NE	57	196	240
Stegall, NE	50	110	150
Miles City, MT	78.3	126	236
Rapid City, SD	82	130	230

Figure 5-3: Example showing the loading condition of the adjacent dc line.

The objective of this part of the work is to explore the maximum operating powers of the identified B2B HVdc lines under current operating dc voltages. Two factors that constrained the power transfer capability of each HVdc line were the limits of the power ratings of adjacent ac lines and the levels of terminal bus voltages of the corresponding dc tie. The under-voltage conditions induced by increasing the operating power of the dc B2B ties were improved by compensating the shunt capacitance at the terminals. To explore the maximum allowable power transfer of each dc tie, the operating power of the dc line was increased and proportionally compensated the shunt capacitance at the terminals of that line. The operating power of the investigated dc line was increased until at least one of the adjacent ac lines approached the power rating limits. The change in loading condition of the 239 MVA ac line when the operating power of the Miles City dc line increases from 126 MW to 236 MW is shown in Fig. 5-3. The results of the explored maximum operating power of each dc line are provided in Table 5-3. As reported in Table 5-3, the 2025/2026 EI-WI model can only take small increments of B2B power transfer.

If the B2B connections were to be increased to the levels proposed in [GMLC 2019], significant ac transmission grid reinforcements would be required. Defining such reinforcements is outside the scope of

this project. Therefore, for this project, the B2B maximum capacities, indicated in the last column of Table 5-3, were used.

The nominal changes in the maximum power transfer capability means that Topology 1, shown in Fig. 5-2, might not result in significant technical benefits in terms of congestion relief and frequency response. No further studies were performed on Topology 1.

5.2.2 Topology 3: Modeling of New dc Lines for Power Flow and Dynamic Studies HVdc Power Flow Model

The power flow models of the HVdc lines in Topology 3 were developed. The parameters were calculated for the three lines crossing EI-WI in Table 5-1 based on the preliminary results from [GMLC 2019] in November 2017.

It is important to highlight that later results from Seams study [GMLC 2019] gave HVdc lines with about twice the capacity shown on Table 5-1. For this project, it was decided to stay with the capacities of Table 5-1 because of the following reasons:

1. This project is based on 2025/2026 planning cases, while the results in [GMLC 2019] are based on 2038 scenarios where generation looks significantly different.
2. To implement the HVdc twice as large as that of Table 5-1, significant reinforcements of ac transmission grid will be needed.
3. This project used HVdc macrogrid model built in [Makarov 2017], which transferred about 14 GW between EI and WECC. By using capacities of Table 5-1, topology 3 of this project was comparable to the 14 GW transfers considered in [Makarov 2017]. Therefore, there was a more direct comparison between the different topologies.

Industry-proposed lines, represented by the orange lines in Figs. 5-1 and 5-2, can be included in the model depending on the technical benefits evaluation. For example, if in the congestion management benefit evaluation, it is determined that the lines could provide additional benefits, the lines were included in the model. The inclusion of industry-proposed lines was not considered in this report because their potential benefit was not identified in the studies of this report. These lines could be considered in future work.

To identify the HVdc parameters, an Excel Spreadsheet developed by MISO in [Makarov 2017] is utilized in this project.

The main assumptions to obtain HVdc parameters are LCC technology; 5% losses target; 800 kV nominal voltage; capacity of 5,400 MW; and the conductors were assumed to be Cumberland with six conductor bundles.

The calculated parameters for HVdc conductors based on six Cumberland conductors per line are shown in Table 5-4. In addition to line parameters, converter parameters for power flow models were identified based on typical parameters for the lines assumed, as it was done previously in [Makarov 2017].

Table 5-4: Parameters calculated for three new lines crossing EI-WECC interconnection.

HVdc Location	HVdc Link From	HVdc Link To	Approx. Geo Dist (miles)	Rdc (Ohms) (75^0 C)	Rdc (Ohms) per pole	Bi-Pole dc Calculated (MW)	Estimated Losses for Bipole (MW)	Power Received @ To End (MW)	Estimated Loss on Bi-Pole
Hanford, WA (HANF)	HANF	DVN	1,800	0.0575	17.94	4,779	320	4,459	6.7%
Intermx (INTERMX)	INTERMX	CPS	1,330	0.0575	13.26	4,779	237	4,542	4.9%
Palo Verde (PALV)	PALV	SEMINOL	1,060	0.0575	10.56	4,779	189	4,590	3.9%

Note: CPS = St. Louis substation; *DVN* = Davenport Substation.

HVdc Dynamic Model

The CDC6T model was used to represent the converter dynamics. The parameters of the dynamic models were assumed based on the parameters used in [Makarov 2017]. The parameters are shown in Fig. 5-4. The power flow and dynamic models of the HVdc lines were tested and were found to produce expected stable behavior, similar to the models of existing HVdc lines.

	Con Value	Con Description
1	5.0000	ALFDY (degrees)
2	15.0000	GAMDY (degrees)
3	0.0500	TVDC (sec)
4	0.0200	TIDC (sec)
5	0.1500	VBLOCK (pu)
6	0.3500	VUNBL (pu)
7	0.0500	TBLOCK (sec)
8	0.1500	VBYPAS (kV)
9	0.3500	VUNBY (pu)
10	0.0500	TBYPAS (sec)
11	0.0000	RSVOLT (kV)
12	160.0000	RSCUR (amp)
13	5.0000	VRAMP (pu/sec)
14	5.0000	CRAMP (pu/sec)
15	168.7500	C0 (amp)
16	0.0000	V1 (kV)
17	337.5000	C1 (amp)
18	2000.0000	V2 (kV)
19	8437.5000	C2 (amp)
20	2000.0000	V3 (kV)
21	8437.5000	C3 (amp)
22	0.0500	TCMODE (sec)
23	-99.0000	VDEBLK (pu)
24	99.0000	TDEBLK (sec)
25	0.1000	TREBLK (sec)
26	-99.0000	VINBLK (pu)
27	0.0000	TCOMB (sec)
28	-99.0000	VACBYP (pu)
29	99.0000	TDEBYP (sec)
30	0.0000	TINBLK (sec)
31	0.1000	TINBYP (sec)
32	0.0500	TVRDC (sec)

Figure 5-4: Parameters of dynamic model CDC6T.

5.2.3 Power Flow Models of EI, WI, and HVdc Topologies

Generation and Load Modification

To model the injections by the HVdc lines, the EI and WI generations and loads were modified. Models for both EI2WI and WI2EI transfer directions were built. The total level of transfers between EI and WI were about 14.4 GW in total, similar to those implemented in the HVdc macrogrid in [Makarov 2017].

The loads were scaled to represent an off-peak condition in the system that is exporting power. This operating condition is consistent with the capacity exchange application assumed in [Makarov 2017], where the power is imported to supply peak load, and power is exported when the load is at off-peak condition. The loads were scaled on loads marked as scalable in PSS®E, with non-scalable loads being left intact. As the loads were modified, the injections by the HVdc lines were also gradually modified until the desired injection levels were reached.

The generations were modified to support the HVdc line injections in the importing side of the lines. The generations were modified in a similar way as it was performed in [Makarov 2017]. The HVdc injection was increased by the same amount as the decrease in the generation. This was also performed gradually.

In this process the power flow solution was moved gradually to avoid convergence problems in the large models.

Combined EI, WI, and HVdc Power Flow Models

The HVdc power flow model of Topology 3 was combined with the EI and WI power flow models containing the corresponding injections. The convergence of the combined power flow model was verified. The final values of the injections are shown in Table 5-5. The total transfer between EI and WI of about 14.4 GW was divided equally between the three lines, at their sending end.

Table 5-5: HVdc injections in combined EI, WECC and HVdc power flow models.

	Topology 3		
	HVdc line 1	**HVdc line 2**	**HVdc line 3**
Bus at WI	SiteWECC 1	SiteWECC 2	SiteWECC 3
Bus at EI	SiteEI 1	SiteEI 2	SiteEI 3
Export (sending end) (MW)	4,779	4,779	4,779
Import (receiving end) (MW)	4,459	4,590	4,542

Location of HVdc Substations

To identify the location of the HVdc converter substations, power flow studies in N-0 and N-1 conditions in the ac transmission grid were performed in the proximity of the HVdc converter substations. Two sets of locations, both having strong buses in the region of interest, were evaluated: (1) locations that the project team initially selected based on engineering judgement and (2) locations that the project team identified in [GMLC 2019]. Some locations remained the same as initially proposed (set one), and some locations were changed to the buses in [GMLC 2019]. The final locations of the HVdc converter substations are summarized in Table 5-6. The reason for the changes in Table 5-6 was because the new locations have more connections and higher line ratings. Major overloads existed in N-0 for locations initially selected. The new locations identified in Table 5-6 have no major overloads in N-0 and N-1 conditions.

Table 5-6: Locations of HVdc Converter Substations, selected in collaboration between teams of this report and the team of project [GMLC 2019].

	Hanford to Davenport	**Palo Verde to Seminole**	**InterMT to St Louis**
Bus at WI	Same as assumed initially	Same as assumed initially	Changed to location selected in [GMLC 2019]
Bus at EI	Changed to location selected in [GMLC 2019]	Changed to location selected in [GMLC 2019]	Changed to location selected in [GMLC 2019]
Load at Export (MW)	4,779	4,779	4,779
Gen at Import (MW)	4,459	4,590	4,542

The power flow model of Topology 4 developed in [Makarov 2017] is utilized in this study.

5.2.4 Combined Dynamic Models of WI, EI, and HVdc Lines

The following dynamic models were tested individually: (i) EI, (ii) WI, (iii) HVdc lines by themselves, (iv) EI with HVdc injections, and (v) WI with HVdc injections.

For the EI dynamic model, a correction was applied to the models of speed governors in generators so that the frequency response had the characteristics similar to the observations in measurements. Similar corrections were applied to the EI dynamic model with the HVdc macrogrid topology in [Makarov 2017]. The frequency responses for the EI dynamic model before and after applying the deadband corrections are shown in Fig. 5-5. Significant differences are observed in the frequency responses shown in Fig. 5-5. The model with corrected deadbands approximates the response observed in the actual system, as discussed in detail in [Makarov 2017].

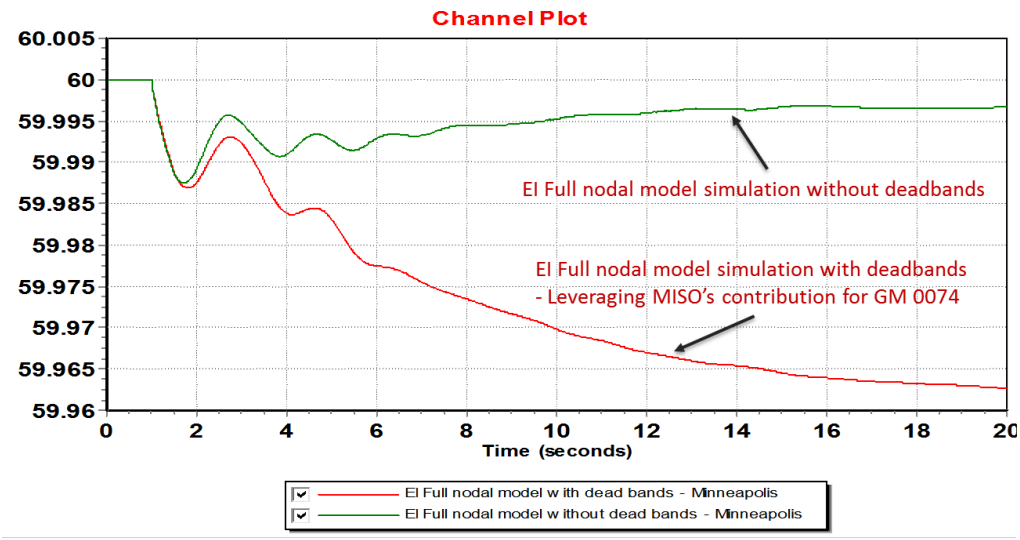

Figure 5-5: Frequency response of EI original dynamic model and after applying deadband modeling corrections, leveraging MISO's contribution to project [Makarov 2017].

After the models were tested individually, a single combined dynamic model was developed and tested. The results of the tests in the combined model are shown in Fig. 5-6. The results show the frequency response in several buses in EI and WI, for generator trips (defined contingencies) in EI and WI, respectively. The frequency responses observed in these simulations are reasonable and stable, displaying the expected result of a working model upon the defined contingencies. This final model of the EI grid is used as the base model for the technical benefit demonstration of frequency control and congestion management.

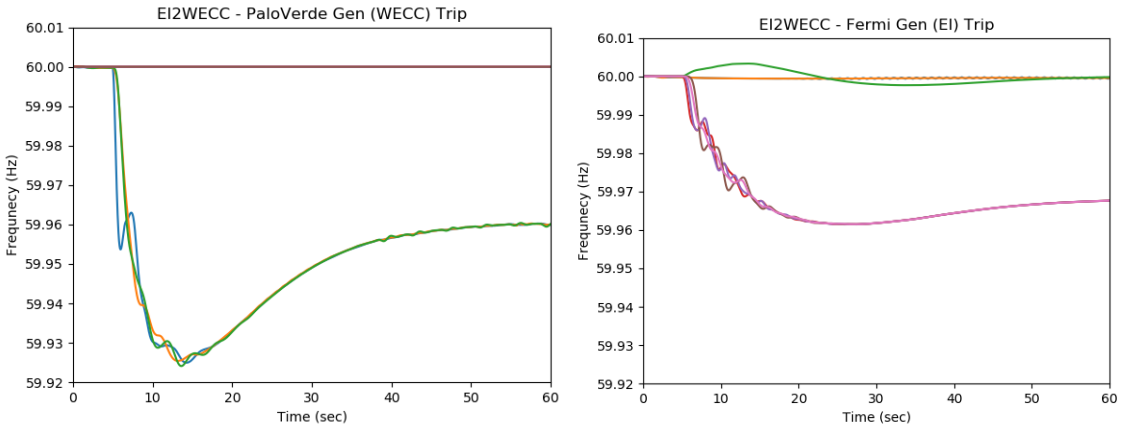

(a) (b)

Figure 5-6: Frequency deviation after large generation trip in (a) WECC system and (b) EI system with HVdc injections modeled; these simulations correspond to the final EI-WECC-HVdc combined dynamic model.

5.3 Frequency Response Comparison

The frequency response of Topology 3 is compared with the HVdc macrogrid topology in this section.

The HVdc lines connecting EI and WI were used to provide faster frequency recovery upon loss of generation in each interconnection through a decentralized HVdc frequency controller. In this study, the case with power flow from EI to WI was investigated for a contingency in WI. This case represents a worst-case scenario as the import from EI displaces responsive generation in WI. In this way, the spinning reserves in EI can be used to support WI in the event of generation loss in WI.

The form and parameters of the HVdc frequency controller are shown in Fig. 5-7. The HVdc frequency controller is based on the CPAAUT-type HVdc auxiliary signal controller [PSSE 2013]. The controller gain used in the simulation is 120,000 MW per pu frequency (negative gain is for increasing power injection into WECC when its terminal frequency on the WECC side is low). These parameters were adjusted based on inherent frequency response and the required MW support from the HVdc system.

The CPAAUT model of Fig. 5-7 was implemented in the three lines that cross the EI and WI borders, as illustrated in Fig. 5-8, in both the Topology 3 and in the HVdc macrogrid.

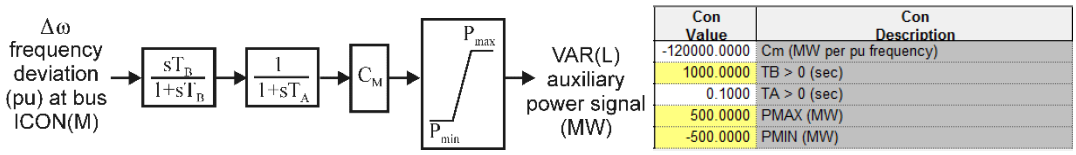

Con Value	Con Description
-120000.0000	Cm (MW per pu frequency)
1000.0000	TB > 0 (sec)
0.1000	TA > 0 (sec)
500.0000	PMAX (MW)
-500.0000	PMIN (MW)

Figure 5-7: Decentralized HVdc frequency control form and parameters for decentralized frequency controller. CPAAUT-type HVdc auxiliary signal controller in PSS®E [PSSE 2013].

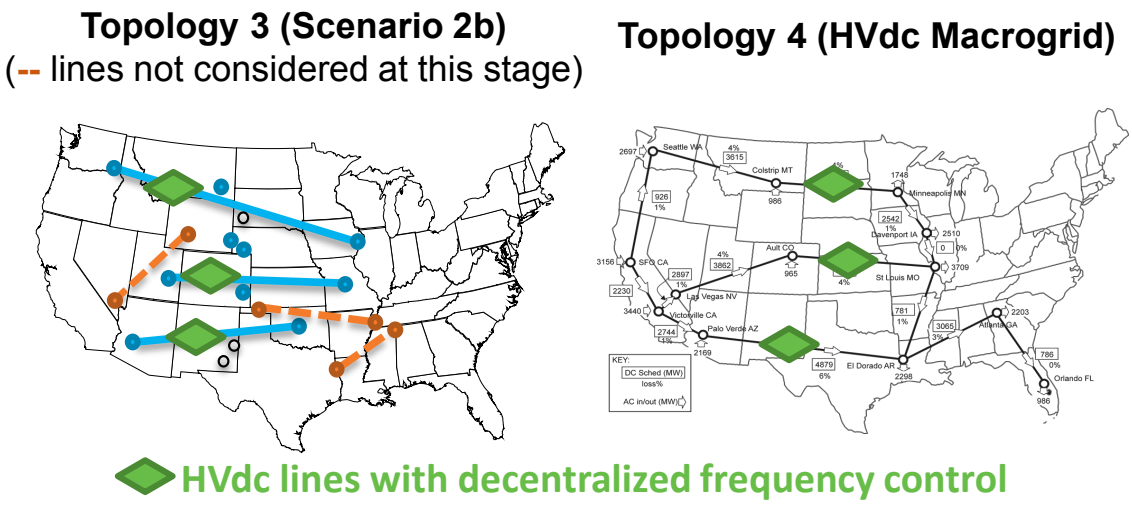

Figure 5-8: Decentralized controller implemented in HVdc lines that cross the WI and EI borders.

A large generator outage in the WECC system was used to test the response of the decentralized controllers. The results are shown in Fig. 5-9, and the comparisons are tabulated in Table 5-7. It can be seen that the decentralized frequency control improves the performance in both Topology 3 and the HVdc macrogrid.

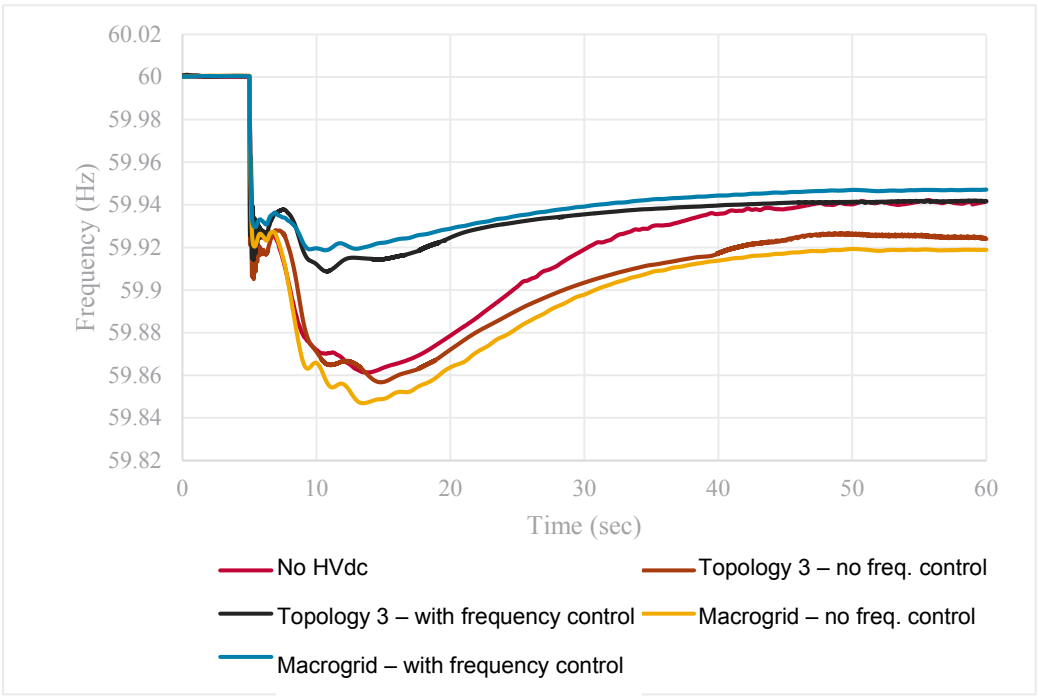

Figure 5-9: Results of simulations with and without decentralized frequency control.

Table 5-7: Results of simulations with and without decentralized frequency control

	Scenario	w/o freq. control	w/ freq. control	% Improvement
Nadir frequency	HVdc macrogrid	59.85 Hz	59.92 Hz	47%
	Topology 3	59.86 Hz	59.91 Hz	36%
Final frequency	HVdc macrogrid	59.92 Hz	59.94 Hz	34%
	Topology 3	59.93 Hz	59.95 Hz	26%

5.4 Congestion Management Comparison

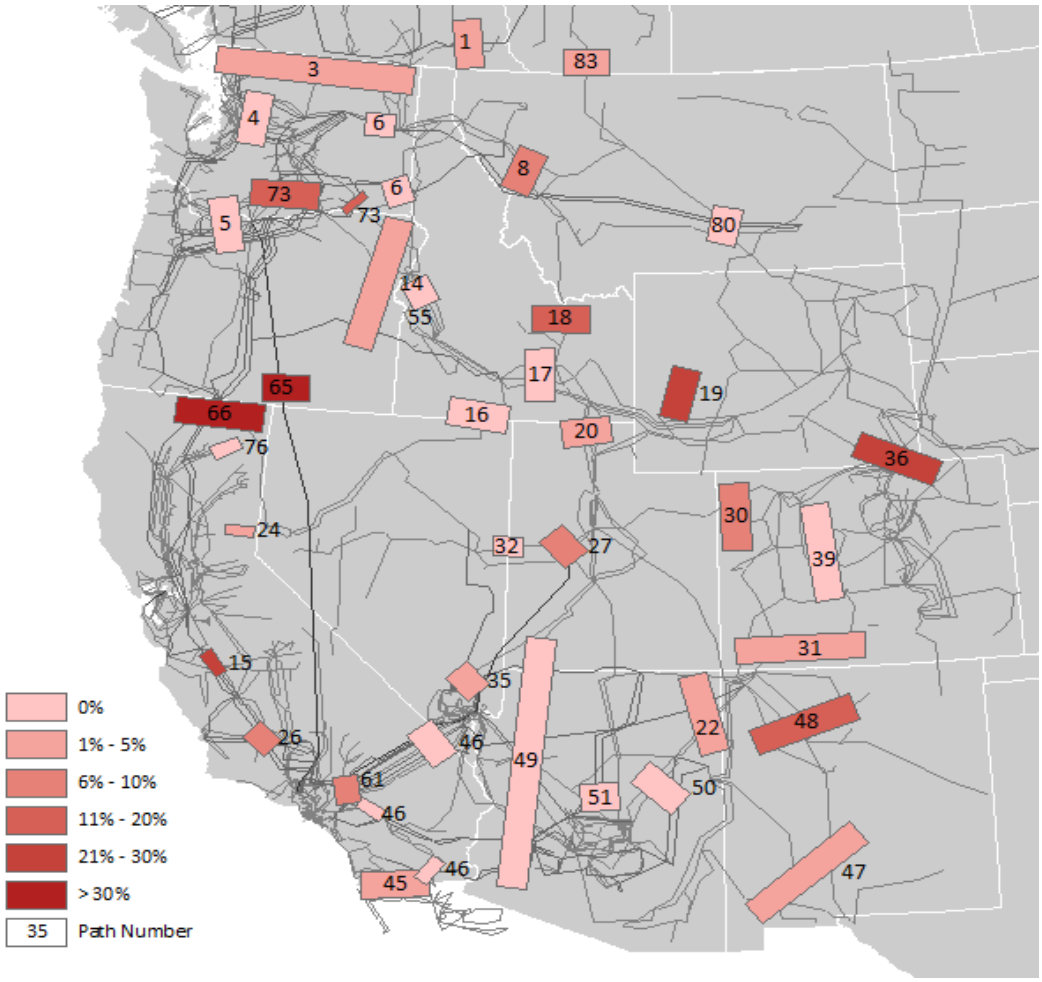

Figure 5-10: Main congested transmission paths in the WI system with the U75 metric shown in percentage.

To quantify the congestion relief benefits provided by the HVdc lines, a few major congested flow gates and transmission paths must be identified and compared with the base case of no HVdc lines. The

congested paths identified in WI are shown in Fig. 5-10. The U75 metric, shown as numbers in Fig. 5-10, measures the percentage of time when the path flow is above 75 percent of its operating limit.

Some paths in WI (e.g., Path 66 and Path 19) were built to carry electricity from large plants. High levels of power flow are not unusual in these paths. The paths monitored are 15, 18, 19, 36, 48, 65, 66, and 73. These are paths that are congested more than 10% of the time.

The comparison of the benefits accrued from congestion management is performed between the base case with no dc lines, Topology 3, and HVdc macrogrid.

The power flows in some of the major WI flow gates that have been monitored to investigate the impact of HVdc line injections are shown in Fig. 5-11. It can be observed that the HVdc macrogrid topology provides the maximum congestion relief. This is likely based on the seven points of HVdc injection available in the HVdc macrogrid, as compared to the three points of injection in Topology 3. The more the HVdc lines and points of connection, the more the congestion relief that can be provided to the ac system.

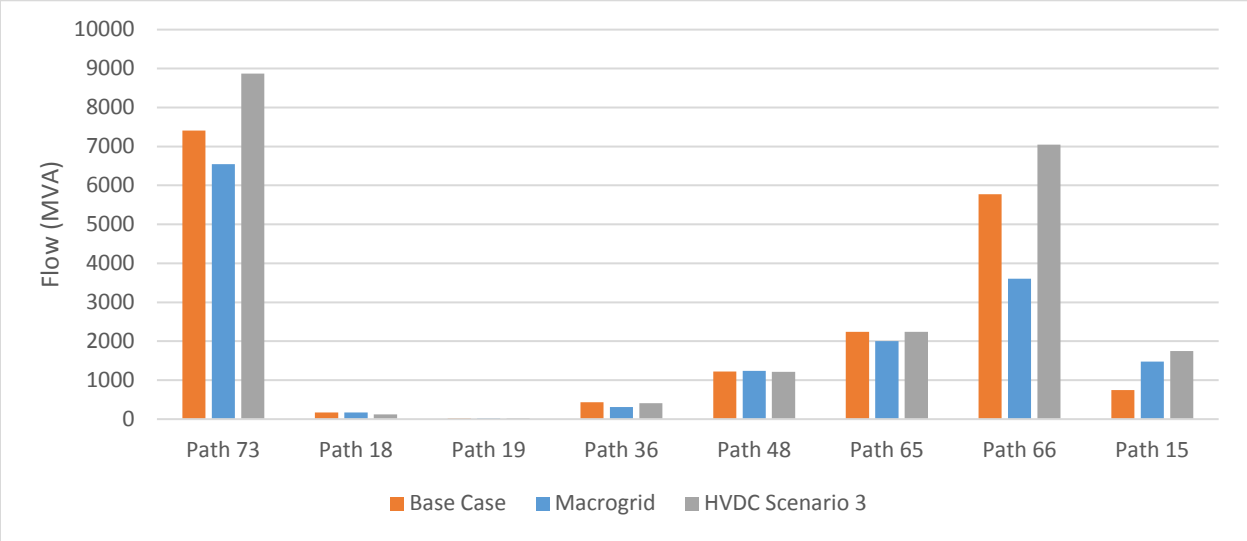

Figure 5-11: Results of loading in selected transmission paths in the WI system.

5.5 Combined Frequency Response and Congestion Management Comparison

The benefit of providing combined frequency response and congestion management is evaluated in this section. This benefit requires a combination of centralized and decentralized controllers. The decentralized controller consists of the frequency controller that locally controls the lines crossing the interconnection borders during a frequency event in the interconnection. The centralized controller can perform fast rescheduling of all HVdc lines. The fast controller can be implemented with an algorithm with pre-established rules and/or quick operator actions. This controller is envisioned to be slower than the decentralized controller, but it can be faster than the current re-dispatch technology. The faster response by the central controller than the current re-dispatch technology is possible as the HVdc lines can be ramped up very fast once the new dispatch values are identified. It may be noted that in [Makarov 2017], a central controller was proposed such that the power flow through the HVdc lines were

rescheduled as quickly as possible. In this work, the central controller is proposed to wait until the immediate action initiated by the decentralized controllers is completed on detecting a frequency event in the grid.

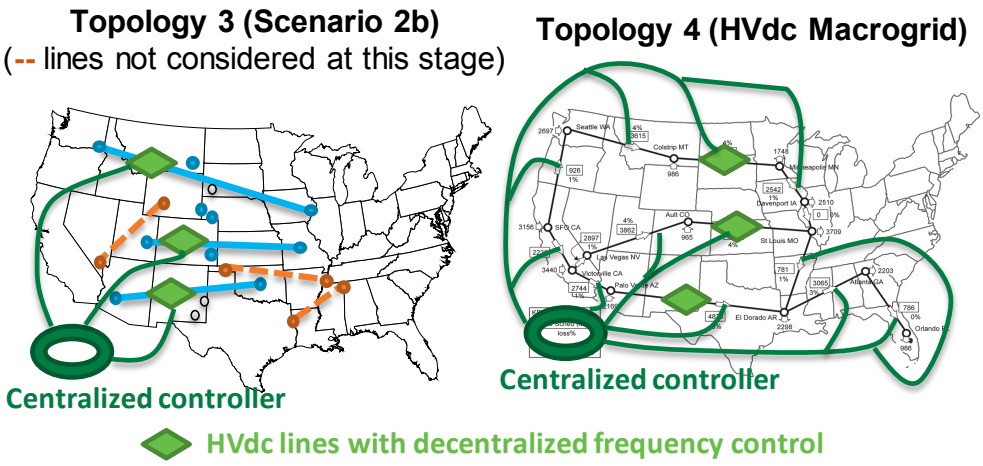

Figure 5-12: Decentralized controller implemented in HVdc lines that cross the WI and EI borders and centralized controller providing schedules to all HVdc lines.

The controller that provides a combination of frequency response and congestion management is evaluated in both Topology 3 and the HVdc macrogrid through simulations. An illustration of the implementation in the simulation examples is provided in Fig. 5-12. The decentralized controller's settings were the same as in the previous example explained in Section 5.3. The centralized controller is modeled here to take effect at 25 seconds after contingency.

The simulation results are shown in Fig. 5-13. It can be seen in Fig. 5-13(a) that the frequency improves further after the centralized fast rescheduling is applied as compared to the frequency results observed in Section 5.3. It can be observed in Fig. 5-13(b) that no significant improvement in congestion can be achieved in Topology 3 using the controller explained in this section. The bars in Fig. 5-13(b) and (c) provide the path power flows before the contingency ("HVDC 3 Base" and "Macrogrid"), before the central controller has acted (at 20 seconds in Fig. 5-13(a) and marked by "HVDC 3_before_central" and "Before Central" in the figures) and after the central controller has acted (at 60 seconds in Fig. 5-13(a) and marked by "HVDC 3_after" and "After Central" in the figures). However, as may be observed in Fig. 5-13(c), in the HVdc macrogrid scenario (or Topology 4), the centralized controller can reduce the ac congestion to pre-contingency levels. This example shows technical benefits of having more controllable HVdc lines in place in the system in addition to the benefits of transfers of large blocks of energy among regions.

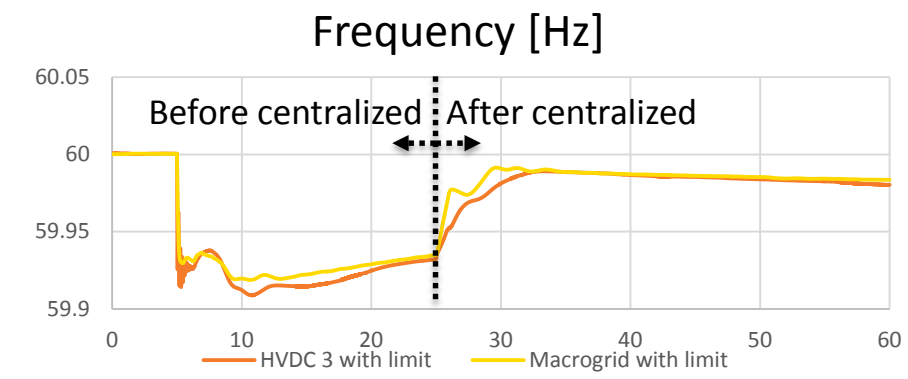

(a)

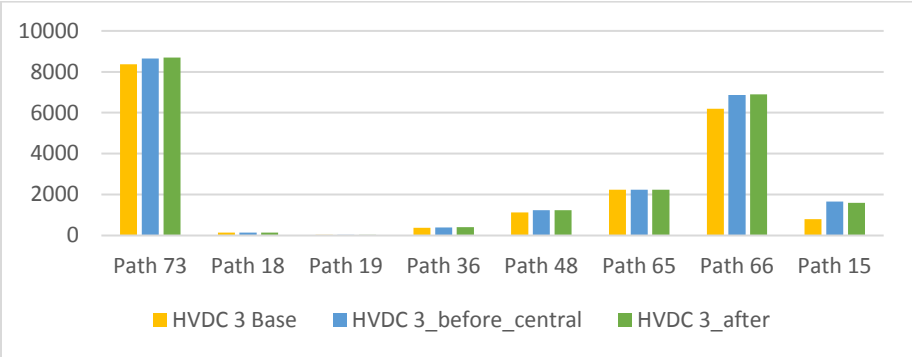

(b)

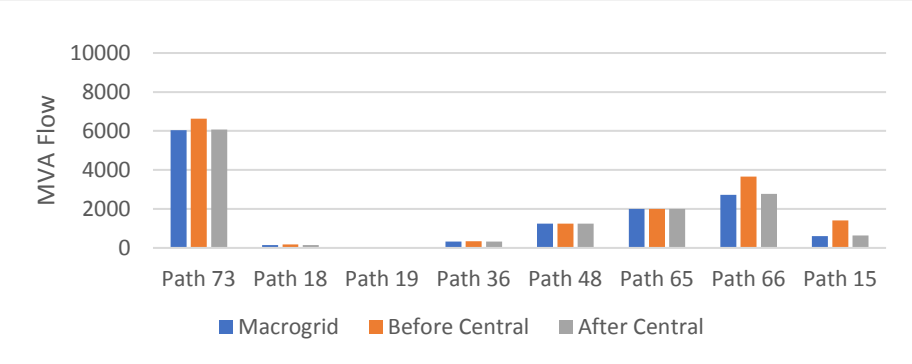

(c)

Figure 5-13: Results of combined frequency control and congestion management (a) Frequency of WI after generation contingency, (b) MVA flows in main WI paths for Topology 3 scenario, (c) MVA flows in main WI paths for Topology 4 (Macrogrid) scenario.

Chapter 6 Economic and Operational Impact and Analysis

Beyond the technical feasibility and impact assessment of different HVdc controls and configurations, the potential economic and operational impacts are important to evaluate. These potential impacts were examined through production cost modeling that represented the generation, load, and transmission network, including advanced HVdc controls and the macrogrid configuration design described in the previous chapters. The production cost model represented the EI and WI interconnections.
This evaluation found potential impacts from the studied scenarios and sensitivities, such as improved resource use efficiency, decreased production cost, changes to transmission congestion patterns, and decreased spinning reserve requirements. This study should be considered as a complement to the technical analysis performed in the previous chapters and is an initial modeling effort that captured only a limited set of potential impacts by HVdc control functions and configurations.

6.1 Methods

HVdc systems were developed in regions that can benefit from transferring large amounts of electricity. To plan these developments required economic and operational impact analysis across these large regions. The modeling and analysis performed in [GMLC 2019] showed the value of increasing HVdc interconnection between the EI and WI interconnections for the 2038 scenario. In this work, it is expanded further to identify benefits of advanced HVdc control methods in a macrogrid for a 2025/2026 scenario. The work launched the capability to simulate more than 200,000 nodes at a 5-minute time steps for a year.

6.2 PIDG 2.0

One of the first efforts in building a PCM was to create the transmission network representation of the buses, transmission lines, and all their characteristics. PIDG 2.0 was developed and deployed to accomplish this task. It translated PSS®E files and other power system characteristic information into a PLEXOS (NREL-1) database with minimal engineer intervention. As one of the most demanding tasks in creating a modeling database, the development and improvement to PIDG enables data processing that translates PSS®E transmission network data and merges with other data sources. Other data sources like generation and techno-economic parameters are included into the PLEXOS input format (Fig. 6-1). This task supported more complex data and increased automation in the process that took 160 hours of work to about 16 hours, an improvement by 10×.

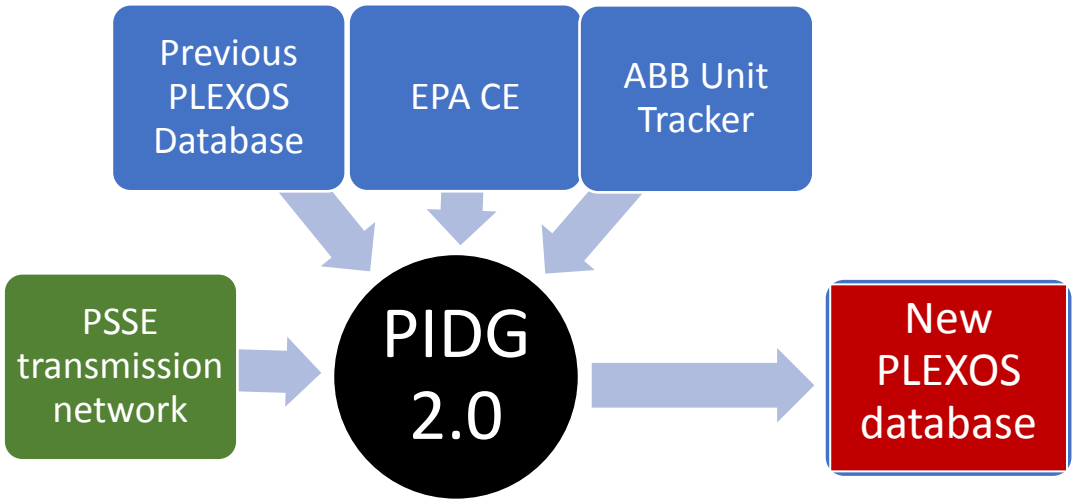

Figure 6-1: PIDG 2.0 tool inputs and output of a new PLEXOS PCM.

6.3 Production Cost Modeling and Analysis

The development and deployment of the geographic decomposition method in PCM (NREL-2) successfully enabled a continent-wide, year-long model to be simulated in 20 to 30 hours instead of 20 to 30 days. Geographic decomposition enabled this project through efficient simulation and more accurate representation of multisystem operator systems, such as the EI and WI.
A reference base case and a macrogrid scenario were prepared using the PIDG tool in PLEXOS as described in Table 6-1. The macrogrid scenario is studied with the various sensitivities defined in Table 6-1.

Table 6-1: Scenario and sensitivity description.

Scenarios	Sensitivity	Description
Base Case	N/A	The base reference case that includes 2025/2026 generation, transmission, and demand modeling.
Macrogrid	N/A	Built upon the base case with a macrogrid HVdc transmission network overlay
	2 GW reserve decrease	EI and WI interconnections each have 2 GW less spinning reserve requirement due to advanced HVdc control functions
	6 GW reserve decrease	EI and WI interconnections each have 6 GW less spinning reserve requirement due to advanced HVdc control functions

The economic and operational evaluation of advanced HVdc controls in a macrogrid were focused on three metrics.

1. Production Cost: The change in production cost of the study system reflects power system assets being utilized differently due to the change in scenarios or sensitivities. This impact should not be considered a full cost-benefit analysis, as it only looked at operational cost over a specific simulated year.
2. Spinning Reserves: One of the identified benefits of the advanced HVdc control functions was the decrease in spinning reserve. The presence of fast control functions in HVdc systems connecting asynchronous interconnections brought in an opportunity to increase reserve sharing. This study examined two different levels of spinning reserve reduction to bookend the potential impact advanced HVdc control functions could have on the EI and WI interconnections. The two spinning reserve reduction requirements of 2 GW and 6 GW from each interconnection was determined by performing the analysis documented in Chapters 4 and 5. The former represents the presence of the advanced control in the seven-terminal MTdc-type system (that includes only a portion of the HVdc macrogrid); the latter represents the presence of the advanced control in the macrogrid.
3. Congestion Relief: The congestion relief was measured in total TWh and average MW change due to the presence of the HVdc systems and advanced control methods in these systems.

The modeling approaches and valuation metrics that were developed to determine the value of the benefits of different dc controls and configurations are summarized in Table 6-2. The comparison of the metrics used in this study with respect to the metrics used in the study described in [GMLC 2019] is also summarized in the table.

Table 6-2: Evaluation metrics.

Valuation Metric of Interest	**Measured in [GMLC 2019]?**	**Modeling in This Work**
Efficient use of resources	Yes – main focus	Yes – in similar manner.
Congestion management	Modeled – but no explicit analysis	Yes - More detailed analysis of impact on congestion due to flexible/advanced operations of HVdc
Dynamic frequency support	No	Yes - Will access based on reduction of reserve provision requirements
Voltage support	No	No – Difficult to quantify directly in PCM.
Capacity value	No – except implicitly in capacity expansion modeling	No – This was not included due to requirement of another modeling database and tool. Future work could the examination of the effective load carrying capacity of HVdc lines.

6.4 Findings

1.2.1 PIDG 2.0

The findings are documented in this section based on the updates to the PIDG tool. The following are the findings:

1. PIDG was a heavily relied on tool and while it has had incremental development through other projects such as the one documented in [GMLC 2019], the work supported by this task has enabled the following major improvements:

2. Increased the transmission topology size that can be imported to enable processing of the combined EI and WI PSS®E case (approximately 100,000 transmission buses). For previous studies, such as in [GMLC 2019], PIDG 1.0 was limited to a maximum topology size (IE number of transmission buses). The EI and WI had to be manually preprocessed and separately processed into PIDG. The previous largest PSS®E topology studied is based on an Indian grid (approximately 6,000 transmission buses) that was processed by PIDG 1.0.

3. Improved process of creating new PLEXOS models by creating algorithms that automate matching new PSS®E transmission networks to PLEXOS databases and other data sources. Previously, the process to match transmission nodes to the corresponding load, generation, and other data was manually intensive. This improvement enabled PSS®E nodes to be merged with load participation factors and other techno-economic properties in existing PLEXOS databases. The nodes were also used to map and create memberships with the generators from an existing PLEXOS database [GMLC 2019], which had all the properties defined. This improvement also enabled automatic updates from other databases, such as generator retirement information from ABB and heat rate data from Environmental Protection Agency (EPA) continuous emissions monitoring systems (CEMSs).

4. Improved three-winding transformer translation capability by enabling six-digit or more transmission node numbers, from the previous five-digit node number limit.

5. Refined PIDG 2.0. PIDG 2.0 has been developed to be a more robust tool that enables translation of a larger diversity of systems and an improvement in automating manual tasks. These improvements reduced work hours by tenfold. PIDG 2.0 automates approximately 70% of the process needed to create a PLEXOS database; the remaining 30% still requires manual processing and review. It was challenging to automate the translation process and to account for many different versions of data and formats. The PLEXOS team experienced immediate and long-term benefits of the PIDG 2.0 development.

5.5.1 Production Cost Modeling and Analysis

Efficient Use of Resources
Advanced HVdc control functions reduce the cost of serving load by better connecting efficient and cheaper generation to load. The change in generation between the base case and the macrogrid is shown in Fig. 6-2. The macrogrid increases the use of coal, hydro, wind, and photovoltaic (PV) generation. All these resources are better utilized in the macrogrid scenario. The capacity factor of coal units increases, hydro spills less frequently, and the curtailment of wind and PV generation decreases.

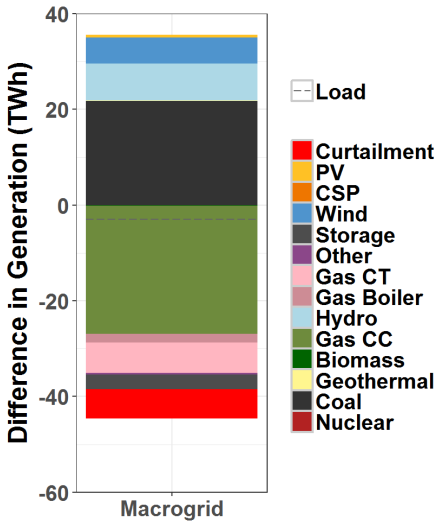

Figure 6-2: Generation by fuel and technology type (CSP stands for concentrated solar power)

Wind, PV, and hydro generators are all assumed to be zero or near-zero marginal cost units due to the lack of fuel costs. Coal in many parts of the country is cheaper than other fossil fuels. Increasing the use of those coal sources therefore decreases the total cost to serve load. The total operational costs of the base and macrogrid scenarios are shown in Table 6-3. In aggregate, the macrogrid reduces system costs by $1.8 billion in the one year of operations modeled. Most savings are from the reduced cost of fuel. However, approximately $300 million savings comes from reduced start and shutdown costs of generators. Increased connectivity, enabled by the HVdc macrogrid transmission network, which means that fewer units cycle on or off as frequently and that the demand for fast-starting, peaking units is lessened.

Table 6-3: Production cost results for base and macrogrid scenarios (millions $).

Production Cost Type (M$)	Base	Macrogrid
Fuel	$ 83,257	$ 81,769
Start & Shutdown	$ 1,856	$ 1,518
Variable operations and maintenance costs	$ 8,541	$ 8,569
Total	$ 93,654	$ 91,857

Congestion Management

The congestion relief provided by HVdc macrogrid is valued as part of the reduced production cost. The two metrics that illuminate the impact of the HVdc macrogrid configuration in noneconomic metrics are shown in Table 6-4. TWh congested measured the total amount of energy that flows over lines that were congested over the simulated year. Average MW congested measured the average power that was congested over the simulated year. The analysis performed on the HVdc macrogrid system shows higher total energy congested than the base case, but lower average power congested. This suggests that the HVdc lines in the macrogrid alleviated some congestion on major interfaces but also shifted congestion to other interfaces. These results highlighted the importance of considering ac transmission expansion in addition to HVdc system configuration to take full advantage of the HVdc lines.

Table 6-4: Congestion impact across scenarios (TWh and Average MW)

Scenario	TWh Congested	Average MW Congested
Base	305.9	1,230
Macrogrid	326.4	1,156

Dynamic Frequency Support

To understand the value of dynamic frequency support provided by the HVdc macrogrid, two sensitivities from the macrogrid scenario were analyzed as has been described in Section 6.3. An additional scenario of the HVdc macrogrid scenario is considered with no dynamic frequency support provided by the HVdc system.

The total amount of reserves held in each region for the base case, HVdc macrogrid, HVdc macrogrid (or seven-terminal MTdc system) with 2 GW reserve reduction, and HVdc macrogrid with 6 GW reserve reduction are shown in Fig. 6-3. The total amount to procure remained the same in the two scenarios, base case (labeled Base in Fig. 6-3) and HVdc macrogrid (labeled MG in Fig. 6-3). However, the type of generation that provided reserves did change, given that the addition of the HVdc lines changed the economics based on which of the units provided reserves.

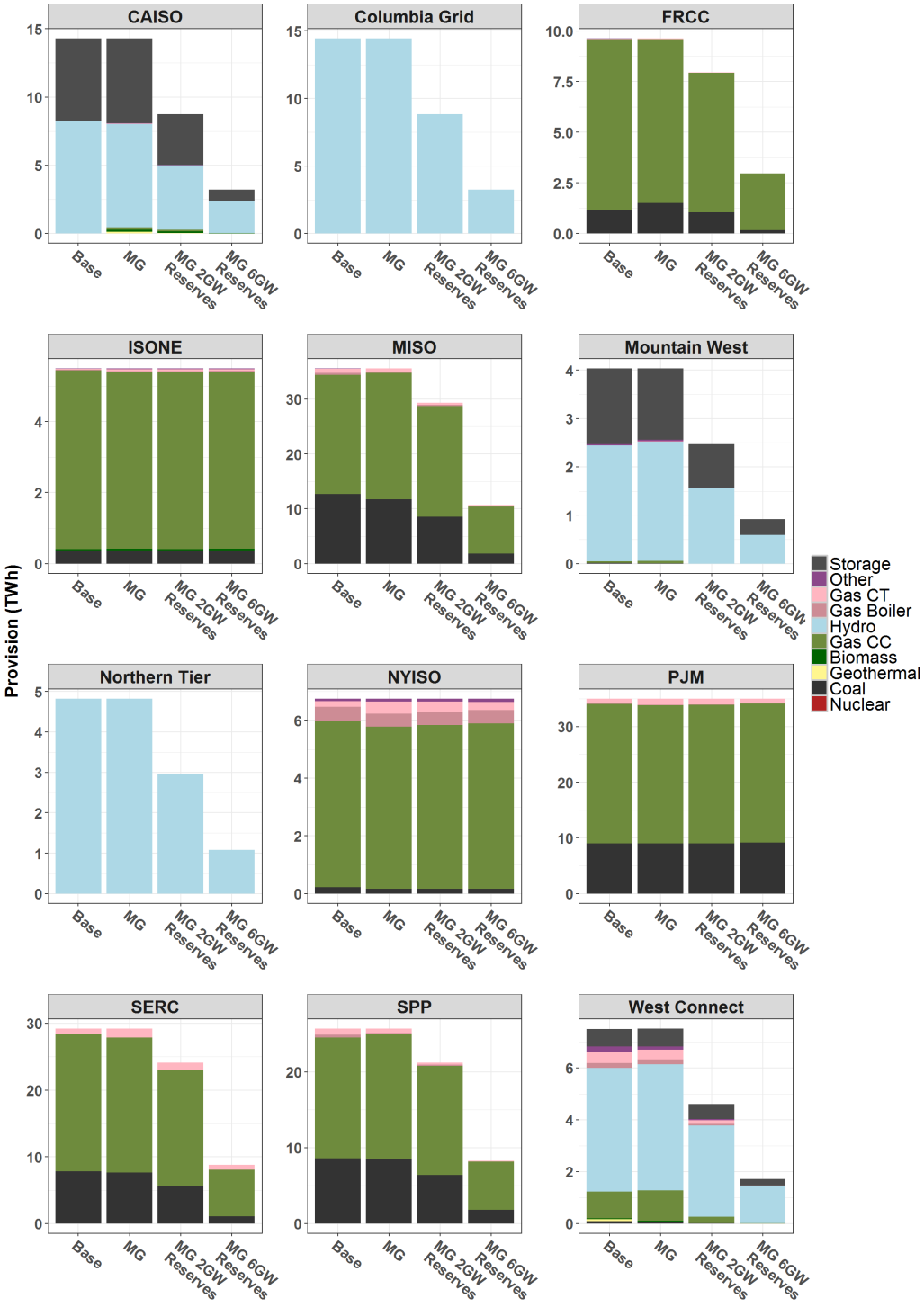

Figure 6-3: Spinning reserves provisions by fuel type and technology across two scenarios and two sensitivities.

One observation from Fig. 6-3 is that reducing the amount of reserves to procure does not necessarily eliminate the most expensive form of generation providing reserves. SERC Reliability Corporation (SERC), for example, still relies on gas combustion turbine (CT) units to provide between 5% and 8% of its total reserve provision when reserve procurement is reduced in its footprint, a slight increase compared

to the HVdc macrogrid scenario without any reserve procurement reduction. This was true even though Gas CTs are a more expensive unit to operate compared to natural gas combined cycle (CC) and coal units.

Even though expensive units are not eliminated from providing reserves, the decreased need to hold reserves through thermal generation leads to decreased total production costs, due to a reduction in their fuel costs. Reducing spinning reserve requirements by 2 GW in each interconnection reduces total annual system costs by $105 million when compared to the HVdc macrogrid scenario. In a 20-year span, the reduction in costs is of the order of $2 billion. Reducing the spinning reserve requirement further by 6 GW in each interconnection leads to a $241 annual million savings. In a 20-year span, the reduction in costs is of the order of $5 billion. Considering all benefits of the HVdc macrogrid with 6 GW reduction of spinning reserves compared to the base case scenario saved over $2 billion annually.

Chapter 7 Summary and Future Work

7.1 Conclusions

The high-fidelity models of VSCs like AAC and CTL converters were developed in this work. The high-fidelity models were based on EMT-type switched system models. Errors of less than 1% were observed in the developed models with respect to detailed reference models. A speed up of up to 12× was observed on a benchmarking system. The suite of VSC models for studying dc systems have been developed with the MMC models previously developed in [Makarov 2017].

The simulation tools and fidelity of models required to study fast control methods in VSCs (like voltage control) and their impact on ac transmission grids were established. The requirements are identified based on hybrid EMT-TS simulation of dc-ac systems. The fidelity of models in and the size of the buffer zones to perform hybrid simulation were also identified. While lumped transmission line models do not adequately capture the high-frequency dynamics, the distributed transmission line is computationally expensive. The larger buffer zone in hybrid simulations captured the dynamics of the VSC-HVdc control system that are important to tune controller parameters. The challenges associated with hybrid simulation were identified in this work. The challenges include speed of simulation (or equivalently, the computational burden) and the limitations in software (E-Tran). The results from hybrid simulations in PSCAD and PSS®E show that capturing the high-bandwidth dynamics is relevant to studying the impact of advanced control methods in VSCs, such as voltage control. In these simulations, a significant computational burden was imposed by PSCAD, which was mitigated using multi-rate simulation methods for power electronics.

EMT dynamic models of a continent-level mixed ac-MTdc grid model of North America with up to a seven-terminal MMC-based MTdc system were developed. The MTdc system connected the EI, ERCOT, and WI grids in North America. The ac transmission grid models were based on multi-area lumped models that capture main power flows among regions. The lumped models can simulate up to 100× faster than the full nodal models of the grid. The voltage behavior in these models utilized local buffer zones in the region of integration of the MMC substation. Based on these models, advanced control methods in MTdc systems like voltage control and multiple point of injection-based frequency support were studied. These methods showed up to 64% improvement in the observed frequency response in the simulations during defined contingency events.

The modeling of and the control coordination in various HVdc penetration scenarios to provide primary frequency response and congestion management in a North American continent-level power system have been described in this work. Scenarios of different levels of HVdc penetration were defined, where the lines are considered as strengthening the interconnection between the two largest North American power system interconnections: EI and WI. Power flow static and electromechanical transient dynamic models were built for the scenarios based on industry-grade models and databases. HVdc lines were modeled as controlled with both centralized power schedules and decentralized controllers to support primary frequency response. Congestion management was modeled as HVdc fast centralized rescheduling. Primary frequency response performance in one interconnection can be improved by immediately bringing support from the other interconnection. Additionally, HVdc lines can be used to alleviate congestion in the underlying ac system, especially when fast centralized rescheduling is used after a large generation contingency in combination with decentralized HVdc control. The model and simulations

demonstrated the technical benefits of having more controllable HVdc lines in place in the system, in addition to the benefits of transfers of large blocks of energy among regions.

The impact of an HVdc national network and accompanying HVdc controls were evaluated in an economic and operational context over a simulated year in PCM. To perform the study, PIDG 2.0, the tool that enables model conversion from PSS®E to PLEXOS, was updated to obtain a speedup by 10×. The speedup acts as an enabler to convert large systems from PSS®E to PLEXOS like the more than 100,000 bus models of the EI and WI grids. This study found potential impacts from the studied scenarios and sensitivities, such as improved resource use efficiency, decreased production cost, changes to transmission congestion patterns, and decreased spinning reserve requirements. Two spinning reserve reductions have been considered that have shown $105 million benefits annually with a 2 GW reduction and $241 million benefits annually with a 6 GW reduction. The former reduction can be obtained using the seven-terminal MTdc system studied and with the fast frequency support. The sensitivity analysis provides an understanding of the advantages of greater spinning reserve reduction using fast frequency support.

7.2 IAB Survey Results

A summary of the survey sent to the IAB members is provided in Appendix D.

7.3 Lessons Learned

Several HVdc penetration scenarios like a seven-terminal MTdc systems, VSC-LCC HVdc macrogrids, and point-to-point HVdc systems were studied in this work utilizing multiple tools (PSCAD, PSS®E, and PLEXOS). The requirement of high-fidelity models of these penetration scenarios to understand the stability and impact of advanced control methods like voltage and frequency control on ac transmission grid were identified. The models required included EMT switched system and hierarchical control system models of VSCs, distributed line model of transmission lines, EMT dynamic models of buffer zones in the region with VSCs, and TS model of ac transmission grids. The EMT dynamics models take a long time (or, more computational resources) to simulate, and there is a requirement for advanced simulation and modeling of components as has been performed with the EMT dynamic model of VSCs in this work. Future extensions of this work could include detailed EMT dynamic modeling and fast simulation of other components like transformers as well as buffer zones. It could also consider temporal parallelization that has been briefly studied in this project (see Appendix A).

The tools required to quantify the impact of the advanced control methods on ac-dc transmission grid include PSCAD, ETRAN, and PSS®E (or similar suite of tools). While the EMT dynamic models were simulated in PSCAD, the TS dynamic models were simulated in PSS®E. The co-simulation between the EMT and TS dynamic models were enabled by ETRAN. The ETRAN tool also enabled model conversion from TS dynamic model to EMT dynamic model, which was useful to develop EMT models of buffer zones.

Economic benefits were quantified from the impact of the advanced control methods in MTdc system/ HVdc macrogrid on the ac transmission grid. The tools utilized for the same included PSS®E, PIDG 2.0, and PLEXOS.

The ability to utilize information across multiple tools has been successfully demonstrated in this work, with the capability to identify economic benefits associated with advanced control methods applied to

power electronics. This is summarized in Fig. 7-1. One of the successes included the capability to identify the impact of advanced control in power electronics on the underlying ac transmission grid. The other included the means to evaluate the economic benefits associated with such advanced control methods through the impact quantified in ac transmission grids. While the former was achieved through hybrid simulation using ETRAN, the latter was achieved using PIDG 2.0. Some of the challenges associated with linking the tools have been identified:

1. Compatibility of models in different tools like PSCAD, PSS®E, and PLEXOS and
2. Limitations with respect to the size of the models utilized in individual tools while translating to another tool or co-simulating the models while performing hybrid simulation.

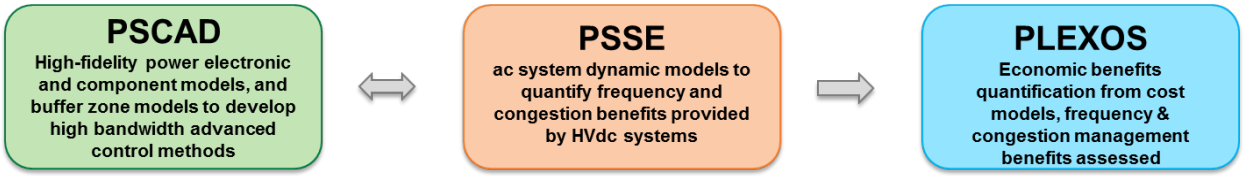

Figure 7-1: Tools and relationship to establish economic benefits from advanced control methods applied to large-scale dc-ac systems.

The feasibility of utilizing MTdc systems to provide fast frequency response at multiple points of injections has also been demonstrated in this project. The ability to provide combined congestion management and frequency response utilizing a higher penetration dc system (like the HVdc macrogrid) has also been demonstrated.

7.4 Future Work

Future extensions of this work could include the following:

1. Large-scale HVdc-ac system model that incorporates up to 15-terminal MTdc systems that will be needed in the MTdc macrogrid (or higher as desired for other HVdc configurations) with vendor agnostic VSC configurations. These models would provide means to explore other applications of MTdc grids like transportation electrification, integration of renewables (solar, wind), and others.
2. Detailed EMT dynamic modeling and fast simulation of other components (like HVdc breakers, transmission lines) as well as buffer zones. This work could also explore the advanced dynamic load models required for this type of analysis. These modeling efforts would equip planners to incorporate dc technologies into future grids.
3. Parallel-in-time simulation algorithm application to EMT simulations and/or hybrid simulations. The algorithm can speed up simulation and incorporate higher fidelity models that can be simulated in reasonable timeframe. The higher-fidelity models provide means to evaluate value models that are not explorable with lower fidelity models like the fast frequency support demonstrated in this work.
4. Contingency analysis in MTdc-ac systems with fault identification mechanism and post-fault operation methods. This analysis would provide further insights into the reliability of dc-ac systems from contingency studies in the dc systems, beyond the reliability aspects studied in the ac system in this work.
5. Hybrid simulation with large-scale HVdc-ac systems that incorporates advancements in hybrid simulation tools and simulation methods to enable and speed up such simulations. Such simulations to study contingencies in HVdc and ac systems to understand reliability and resiliency. This analysis enhances the tools to study large-scale dc-ac systems, systems considered by NERC-led IRPTF, and others.

6. Develop dynamic models for futuristic scenarios (like a 2038 grid) that include high-penetration of inverter-based resources (like generation and loads).
7. Additional modeling and analysis on the HVdc controls are necessary to expand industry expertise in the indirect benefit of reduced reserve requirements due to frequency support provided by HVdc. Another opportunity is to investigate coordinated control of multiple dc lines in both existing and future facilities. These opportunities could be explored not only from the point of view of automatic dynamic control in short timescales, but also including coordinated scheduling in longer terms and HVdc interactions and their roles in real-time electricity markets.

7.5 Presentations and Publications

The following presentations and publications were produced:

1. S. Debnath and M. Chinthavali, "Numerical-Stiffness-Based Simulation of Mixed Transmission Systems," in IEEE Transactions on Industrial Electronics, vol. 65, no. 12, pp. 9215-9224, Dec. 2018.
2. S. Debnath, P. R. Marthi and J. Sun, "Advanced Modeling & Fast Simulation Algorithms for Alternate Arm Converters," 2018 IEEE Electronic Power Grid (eGrid), Charleston, SC, 2018, pp. 1-6.
3. S. Debnath and P. R. Marthi, "Advanced Modeling & Fast Simulation Algorithms for Cascaded Two-Level Converters," 2018 IEEE Electronic Power Grid (eGrid), Charleston, SC, 2018, pp. 1-6.
4. S. Debnath and J. Sun, "Fidelity Requirements with Fast Transients from VSC-HVdc," IECON 2018 - 44th Annual Conference of the IEEE Industrial Electronics Society, Washington, DC, 2018, pp. 6007-6014.
5. S. Debnath, "Parallel-in-Time Simulation of Power Electronics: MMC-HVdc System," submitted.
6. Q. Zhang, M. A. Elizondo, Q. Huang, Y. V. Makarov, M. R. Vallem, Y. Liu, A. Tbaileh, H. Kirkham, S. Debnath, M. Chinthavali, “Adding Local Voltage Behavior to Large Equivalent Power System Models to Study Multi-Terminal dc Systems”, in press.
7. A. Tbaileh, M. A. Elizondo, Y. V. Makarov, Q. Huang, N. Mohan, M. R. Vallem, Y. Liu, H. Kirkham, N. A. Samaan, S. Debnath, M. Chinthavali, D. Osborn, “Centralized and Decentralized Frequency and Congestion Control by HVdc Macrogrid in North American Continental Interconnections”, in press.
8. Y. Liu, M. A. Elizondo, S. Debnath, A. Tbaileh, Y. V. Makarov, Q. Huang, M. R. Vallem, H. Kirkham, N. A. Samaan, “Hybrid (EMT-TS) Simulation Strategies to Study High Bandwidth MMC-Based HVdc Systems”, in press.
9. S. Debnath, P. R. Marthi, J. Sun, M. R. Vallem, M. A. Elizondo, H. Kirkham, A. Tbaileh, Q. Huang, Y. V. Makarov, S. Chinthavali, M. Lee, “Optimal Control of Multiple Injection MMC-Based MTdc System in US Asynchronous Interconnections”, in press.
10. Presentation on “HVDC Systems: Electro-Magnetic Transient Studies (EMTP/PSCAD)” to ERCOT dynamic working group meeting in November 2017.
11. Presentation on “High-Fidelity Modeling of High Bandwidth HVdc/MTdc Technologies and Methods to Assess their Impact” at EPRI workshop on “Industry Workshop on Planning and Integration of HVdc Technology” in November 2018.
12. Poster presentation at the GMLC project review in Washington DC in September 2018.
13. Presentations to IAB:
    a. November 2017: Teleconference kick-off of the project and introduction to the tasks
    b. February 2018: Teleconference presentation of scenarios and use cases to be studied with discussions on the survey submitted to IAB members.

c. October 2018: Meeting at ORNL to discuss the project methods and results obtained. Feedback provided to Electranix Corporations on issues faced with hybrid simulation.

Chapter 8 References

[Abdel-Moamen 2017] M. A. Abdel-Moamen, S. A. Shaaban and F. Jurado, "France-Spain HVDC transmission system with hybrid modular multilevel converter and alternate-arm converter," 2017 Innovations in Power and Advanced Computing Technologies (i-PACT), Vellore, 2017, pp. 1-6.

[Anderson 1990] P. M. Anderson and M. Mirheydar, "A low-order system frequency response model," in IEEE Transactions on Power Systems, vol. 5, no. 3, pp. 720-729, Aug. 1990.

[Barrows 2019] C. Barrows, B. McBennett, J. Novacheck, D. Sigler, J. Lau, and A. Bloom, "A Multi-operator Approach to Production Cost Modeling at Scale," IEEE Transactions (2019 Forthcoming)

[Chaudhuri 2011] N. R. Chaudhuri, R. Majumder, B. Chaudhuri, and J. Pan, "Stability analysis of VSC MTDC grids connected to multimachine AC systems," IEEE Transactions on Power Delivery, vol. 26, no. 4, pp. 2774–2784, oct 2011.

[Debnath 2015a] Debnath, Suman, "Control of Modular Multilevel Converters for Grid Integration of Full-Scale Wind Energy Conversion Systems" (2015).

[Debnath 2015b] S. Debnath, J. Qin, B. Bahrani, M. Saeedifard and P. Barbosa, "Operation, Control, and Applications of the Modular Multilevel Converter: A Review," in IEEE Transactions on Power Electronics, vol. 30, no. 1, pp. 37-53, Jan. 2015.

[Debnath 2016a] S. Debnath and M. Saeedifard, "Simulation-Based Gradient-Descent Optimization of Modular Multilevel Converter Controller Parameters," in IEEE Transactions on Industrial Electronics, vol. 63, no. 1, pp. 102-112, Jan. 2016.

[Debnath 2016b] S. Debnath and M. Chinthavali, "MMC-HVdc: Simulation and control system," in 2016 IEEE Energy Conversion Congress and Exposition (ECCE), Sept 2016, pp. 1–8.

[Debnath 2018a] S. Debnath and J. Sun, "Fidelity Requirements with Fast Transients from VSC-HVdc," IECON 2018 – 44th Annual Conference of the IEEE Industrial Electronics Society, Washington, D.C., 2018.

[Debnath 2018b] S. Debnath and M. Chinthavali, "Numerical stiffness-based simulation of mixed transmission systems," IEEE Trans. Ind. Electron., vol. 65, no. 12, pp. 9215-9224, Dec. 2018.

[Elizondo 2017] M. A. Elizondo, N. Mohan, J. O'Brien, Q. Huang, D. Orser, W. Hess, H. Brown, W. Zhu, D. Chandrashekhara, Y. V. Makarov, D. Osborn, J. Feltes, H. Kirkham, D. Duebner, Z. Huang "HVDC macrogrid modeling for power-flow and transient stability studies in north American continental-level interconnections," Chinese Society for Electrical Engineering. J. Power Energy Syst., vol. 3, no. 4, pp. 390–398, Dec. 2017

[Falgout 2012] R. Falgout, T. V. Kolev, S. MacLachlan, and J. Schroder, "A multigrid-in-time algorithm for solving evolution equations in parallel," 2012.

[GMLC 2019] Project 1.3.33, Grid Modernization Laboratory Consortium, U.S. Department of Energy, Midwest Interconnection Seams Study [online], Available https://gridmod.labworks.org/projects/1.3.33. Accessed 04/08/2019

[Gurrala 2016] G. Gurrala, A. Dimitrovski, S. Pannala, S. Simunovic, and M. Starke, “Parareal in time for fast power system dynamic simulations,” IEEE Transactions on Power Systems, vol. 31, no. 3, pp. 1820–1830, May 2016.

[Gustavsen 1999] B. Gustavsen, G. Irwin, R. Mangelrød, D. Brandt and K. Kent, "Transmission Line Models for the Simulation of Interaction Phenomena Between Parallel ac and dc Overhead Lines," in IPST '99 Proceedings, 1999.

[Haileselassie 2012] T. M. Haileselassie, “Control, dynamics and operation of multi-terminal VSC-HVDC transmission systems,” Ph.D. dissertation, Norwegian Univ. Sci. Technol., Trondheim, Norway, 2012.

[Jacobson 2010] B. Jacobson, P. Karlsson, G. Asplund, L. Harnefors and T. Jonsson, "VSC-HVdc Transmission with Cascaded Two-Level Converters," in CIGRE, Paris, 2010.

[Kou 2016] G. Kou, P. Markham, S. Hadley, T. King, and Y. Liu, “Impact of Governor Deadband on Frequency Response of the U.S. Eastern Interconnection”, IEEE Trans. on Smart Grid, vol. 7, no. 3, pp. 1368-1377, May 2016.

[Kundur 1994] Prabha Kundur. Power System Stability and Control. McGraw-Hill Professional, 1994.

[Makarov 2017] YV Makarov, MA Elizondo, JG O'Brien, Q Huang, H Kirkham, Z Huang, M Chinthavali, S Debnath, N Mohan, W Hess, D Duebner, D Orser, H Brown, D Osborn, J Feltes, DK Chandrashekhara, W Zhu, “Models and methods for assessing the value of HVDC and MVDC technologies in modern power grids,” Technical Report, PNNL-26640, Project GM 0074, Grid Modernization Laboratory Consortium, U.S. Department of Energy, July 2017.

[Mathew 2014] E. C. Mathew and A. Shukla, "Modulation, control and capacitor voltage balancing of alternate arm modular multilevel converter with DC fault blocking capability," 2014 IEEE Applied Power Electronics Conference and Exposition - APEC 2014, Fort Worth, TX, 2014, pp. 3329-3336.

[Merlin 2014] M. M. C. Merlin, T. C. Green, P. D. Mitcheson, D. R. Trainer, R. Critchley, W. Crookes and F. Hassan, "The Alternate Arm Converter: A New Hybrid Multilevel Converter With dc-Fault Blocking Capability," IEEE Transactions on Power Delivery, vol. 29, no. 1, pp. 310-317, Feb. 2014.

[Merlin 2015] M. M. C. Merlin and T. C. Green, "Cell capacitor sizing in multilevel converters: cases of the modular multilevel converter and alternate arm converter," in IET Power Electronics, vol. 8, no. 3, pp. 350-360, 3 2015.

[MISO 2014] MISO Transmission Expansion Plan (MTEP) report, MISO, 2014.

[Morched 1999] A. Morched, B. Gustavsen and M. Tartibi, "A Universal Model for Accurate Calculation of Electromagnetic Transients on Overhead Lines and Underground Cables," IEEE Transaction on Power Delivery, vol. 14, no. 3, pp. 1032-1038, July 1999.

[Najmi 2015] V. Najmi, R. Burgos and D. Boroyevich, "Design and control of modular multilevel alternate arm converter (AAC) with Zero Current Switching of director switches," 2015 IEEE Energy Conversion Congress and Exposition (ECCE), Montreal, QC, 2015, pp. 6790-6797.

[Peralta 2016] J. Peralta, H. Saad, S. Dennetiere, J. Mahseredjian, and S. Nguefeu, “Detailed and averaged models for a 401-level MMCHVDC system,” IEEE Trans. Power Del., vol. 27, no. 3, pp. 1501–1508, July 2012.

[PSSE 2013] Model Library, PSS®E Software documentation, Siemens PTI, October 2013.

[RUSK-PANOLA 2019] "About The RUSK-PANOLA Transmission Project." Available http://ruskpanolatransmissionproject.com/about-the-project/. Accessed 04/08/2019

[TransWest 2019] "Critical grid infrastructure to connect the West." Denver, CO. Available http://www.transwestexpress.net/. Accessed 04/08/2019

[Wickramasinghe 2016] H. R. Wickramasinghe, G. Konstantinou, J. Pou and V. G. Agelidis, "Asymmetric overlap and hysteresis current control of zero-current switched alternate arm converter," IECON 2016 - 42nd Annual Conference of the IEEE Industrial Electronics Society, Florence, 2016, pp. 2526-2531.

[Wickramasinghe 2017] H. R. Wickramasinghe, G. Konstantinou, Z. Li and J. Pou, "Development of an alternate arm converter benchmark model for HVDC applications," IECON 2017 - 43rd Annual Conference of the IEEE Industrial Electronics Society, Beijing, China, 2017, pp. 4506-4511.

Appendix A. Temporal Parallelization in Simulation of Power Electronics

Multigrid reduction-in-time (MGRIT) methods are applied to the simulations of modular multilevel convertors (MMC)s to parallelize the simulation in time. In general, the MGRIT methods evaluate simulation states in multiple levels with different update rates [Falgout 2012]. One special case of a MGRIT method is a two-level algorithm, also known as parareal method [Falgout 2012].

Parareal Simulation

The parareal algorithm is explained in detail in [Falgout 2012] and [Gurrala 2016] and is explained briefly here. In parareal methods, the differential algebraic equations (DAEs) representing the dynamics of the states of the system are discretized using two operators in different meshes (time steps): (i) a coarse operator on a coarse time step, and (ii) a fine operator on a fine time step. The coarse time step (T_{coarse}) is typically larger than or equal to the fine time step (T_{fine}). The coarse and fine operators depend upon the system model and the discretization algorithm chosen in each operator. The system model describes the dynamics of the states and is represented by a DAE. The states considered in the coarse time step (also known as coarse-mesh states) are a subset of the states in the fine time step (also known as the fine-mesh states). Based on the coarse-mesh and fine-mesh states, the final states of the system are determined. The different meshes and operators are graphically illustrated in Fig. A-1. The overview of the algorithm is provided below:

1. Initialization: The initial value of the states, like at $t = 0$ s, is propagated on the coarse time step (T_{coarse}) using the coarse operator to determine the value of the coarse-mesh and final states.

$$\tilde{\mathbf{x}}^0[0] = \mathbf{x}^0[0],$$

$$\text{Coarse Operation: } \tilde{\mathbf{x}}^0[k-1] \mapsto \tilde{\mathbf{x}}^0[k], \forall k \in [1, N_{\text{par}}],$$

$$\mathbf{x}^0[k] = \tilde{\mathbf{x}}^0[k], k \in [1, N_{\text{par}}],$$

   where $\mathbf{x}^0[k] = \mathbf{x}^0(k.T_{\text{coarse}})$.

2. Translation: The values of the final states in the $(i-1)^{\text{th}}$ iteration are translated to determine the initial values of the fine-mesh states in the i^{th} iteration on the same time steps as the coarse time step.

$$\text{Translation: } \mathbf{x}^{i-1}[k] \mapsto \hat{\mathbf{x}}^i[k], \forall k \in \left[0, N_{\text{par}}\right], i \geq 1.$$

3. Fine Operation: The fine operator is applied to the initial values of the fine-mesh states in the i^{th} iteration using a time step T_{fine} to determine the updated values of the fine-mesh states. That is, within each coarse time step (T_{coarse}), $\frac{T_{\text{coarse}}}{T_{\text{fine}}}$,serial operations occur on the system model considered by the fine operator to determine the updated values of the fine-mesh states. The fine operator across multiple coarse time steps in each simulation window is applied in parallel across multiple available parallel cores (with up to a maximum of N_{par} parallel cores).

$$\text{Fine Operation: } \hat{\mathbf{x}}^i[k-1] \mapsto \hat{\mathbf{x}}^i[k], \forall k \in \left[1, N_{\text{par}}\right].$$

4. Coarse and Final State Updates: The final states are updated based on the fine-mesh and coarse-mesh states in the i^{th} iteration. The coarse-mesh states in the i^{th} iteration are determined based on fine-mesh updates.

$$\text{Re} - \text{Initialization: } \tilde{\mathbf{x}}^i[k] = \hat{\mathbf{x}}^i[k], \forall k \in [0,1],$$

$$\text{Coarse Operation: } \tilde{\mathbf{x}}^i[k-1] \mapsto \tilde{\mathbf{x}}^i[k], \forall k \in [2, N_{\text{par}}],$$

$$\text{Update: } \mathbf{x}^i[k] = \tilde{\mathbf{x}}^i[k] + A_{\text{error}}\left(\hat{\mathbf{x}}^i[k] - \tilde{\mathbf{x}}^{i-1}[k]\right), k \in [1, N_{\text{par}}],$$

where A_{error} is the error matrix used to update the final states.

5. Iterations Error Check: Iterate to "Translation" step until the difference between the value of final states in consecutive iterations is within a predefined tolerance band. This difference is termed as iteration error (e_{tol}).

$$\text{Translation: } \tilde{\mathbf{x}}^i[k] \mapsto \hat{\mathbf{x}}^i[k], \forall k \in [0, N_{\text{par}}],$$

$$\sum_{k=0}^{k=N_{\text{par}}} \| \mathbf{x}^i[k] - \mathbf{x}^{i-1}[k] \| \leq e_{tol}.$$

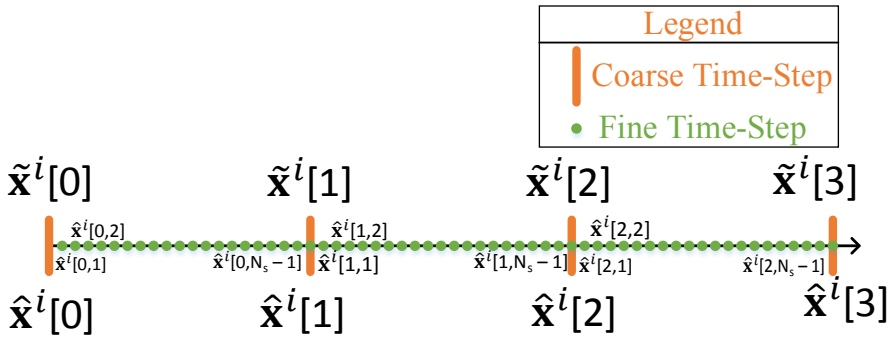

Figure Appendix A-1: An example coarse and fine meshes in a parareal simulation algorithm.

In this procedure, $\tilde{\mathrm{x}}^i$, $\hat{\mathrm{x}}^i$ and x^i represent the coarse-mesh, fine-mesh, and final states, respectively, in the i^{th} iteration. The simulation window size is $N_{\text{par}}T_{\text{coarse}}$. This procedure is summarized in Fig. A-2. Once the results converge in a simulation window, the process begins once again from the "Initialization" step based on the states determined at $N_{\text{par}}T_{\text{coarse}}$ in the previous simulation window. In different applications, different coarse and fine operators and time steps can be chosen. For example, in [Gurrala 2016], the coarse operator is a lower-order discretization algorithm and the fine operator is a higher-order discretization algorithm. The coarse and fine operators could be the same with only the corresponding time steps considered being different. In this paper, different models are used to represent the dynamics of the states of MMC in the coarse operator and the fine operator. Different time steps are also considered for the simulation in coarse and fine meshes.

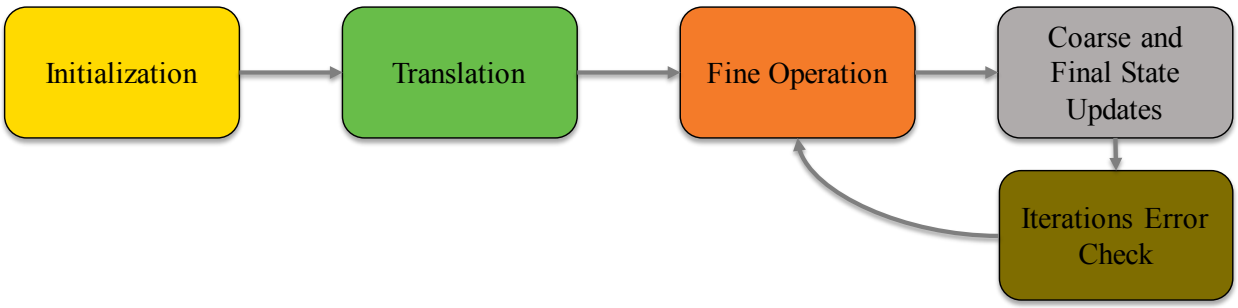

Figure Appendix A-2: Overview of parareal simulation algorithm.

Application of Parareal to Simulation of MMCs

The parareal simulation algorithm described in Section A.1 is applied to the simulation of MMCs in this section. The coarse operator is based on hybrid discretization of the average-value model described in [Peralta 2016]. The hybrid discretization algorithm utilized is explained in [Haileselassie 2012]. The operator also utilizes the upper-level control system of the MMC. The coarse time step is based on the control time step of the upper-level control system of the MMC, which is typically much smaller than the time constants associated with the dynamics of the states in the average-value model of the MMC. The fine operator is based on hybrid discretization of the detailed switch model described in [Makarov 2017]. It also utilizes the complete hierarchical control system of the MMC. The fine time step is based on the control time step of the lower-level control system of the MMC and the switching frequency of each SM. This time step is typically much smaller than the time constants associated with the dynamics of the states in the detailed switch model of the MMC. The translation of the final states to fine-mesh states of the MMC is achieved based on the lower-level control system of the MMC. The coarse and fine operators used in parareal algorithm to simulate MMCs are summarized in Fig. A-3.

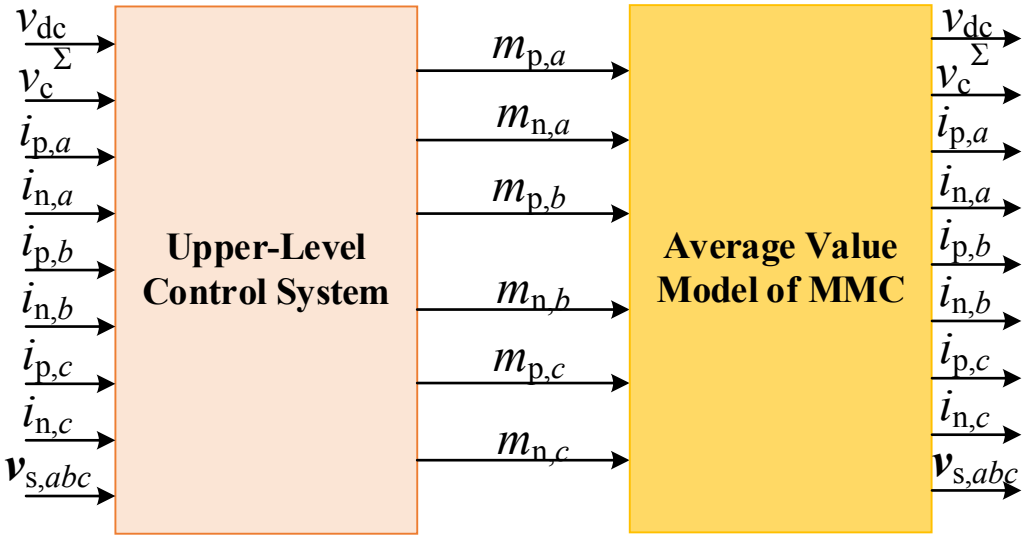

(a)

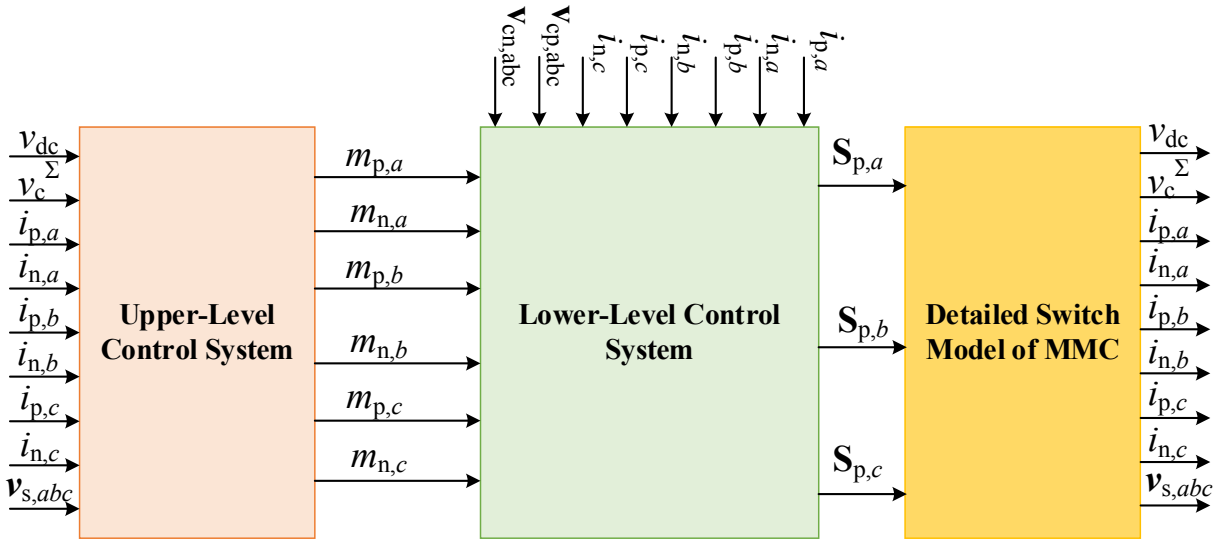

(b)

Figure Appendix A-3: Operators used in parareal algorithm to simulate MMCs: (a) Coarse operator, and (b) Fine operator.

The parameters that influence the speedup of the proposed algorithm are the following: (i) ratio of simulation window size to coarse time step, (ii) ratio of coarse time step to fine time step, and (iii) simulation window size. The total simulation time required may be different from the simulation window size. For example, to perform a 1 s simulation of the states of an MMC, a simulation window size of 300 μs may be considered. Within the 300 μs simulation window, coarse and fine time steps of 60 μs and 4 μs, respectively, may be considered. In this case, the maximum number of parallel cores that can be utilized by the fine operator is the ratio of simulation window size to coarse time step. The maximum number of parallel cores utilizable in this example is 5. The number of serial computations by the fine operator within each coarse time step is the ratio of coarse time step to fine time step (or, 15 in this example).

And, the number of serial computations by the coarse operator within the simulation window is the ratio of simulation window to coarse time step (or, 5 in this example). The lesser the serial computations and the greater the parallel computations possible, the higher is the speedup observed with the proposed algorithm compared to a serial-in-time algorithm. Since the iteration error is determined within the simulation window in each iteration, the convergence of the proposed algorithm is dependent on the simulation window size. The faster the convergence of the proposed algorithm, the lesser the number of iterations required and the higher the speedup observed with the proposed algorithm. The maximum number of parallel cores that can be utilized, the number of serial computations by the fine operator, the number of serial computations by the coarse operator, and the number of iterations required for convergence determine the speedup of the proposed algorithm.

The initial results from the parallel-in-time simulation of an MMC-HVdc system is provided in Fig. A-4. As may be noted in the figure, the arm currents that are observed from coarse simulation, fine simulation, and parallel-in-time simulation are very similar to each other. However, the summation of capacitor voltages that is observed from coarse simulation is different from the one observed in fine simulation. The summation of capacitor voltages that is observed from the parallel-in-time simulation and fine simulation are very similar to each other. These figures indicate that coarse simulation alone may not adequately represent the behavior of MMCs, but the parallel-in-time simulation results are accurate (with an error less than 1.5%). The speedup observed with parallel-in-time simulation is dependent upon the number of cores available for parallelization. In this case, the speedup observed was up to 5× with five parallel cores.

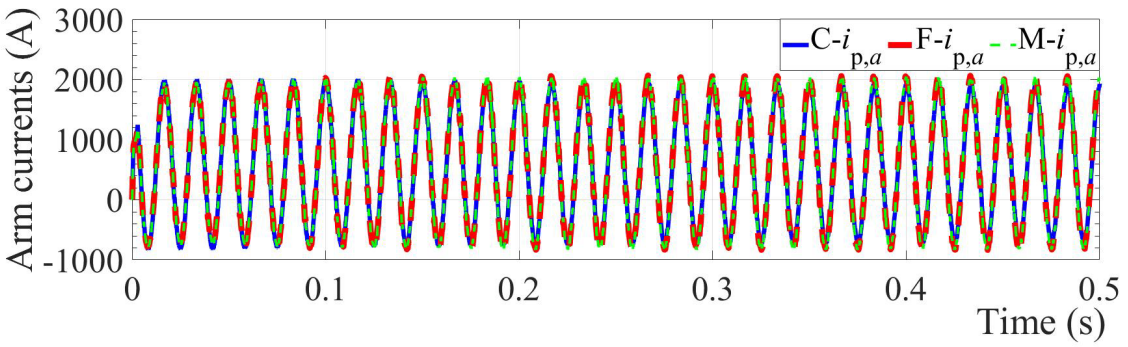

(a)

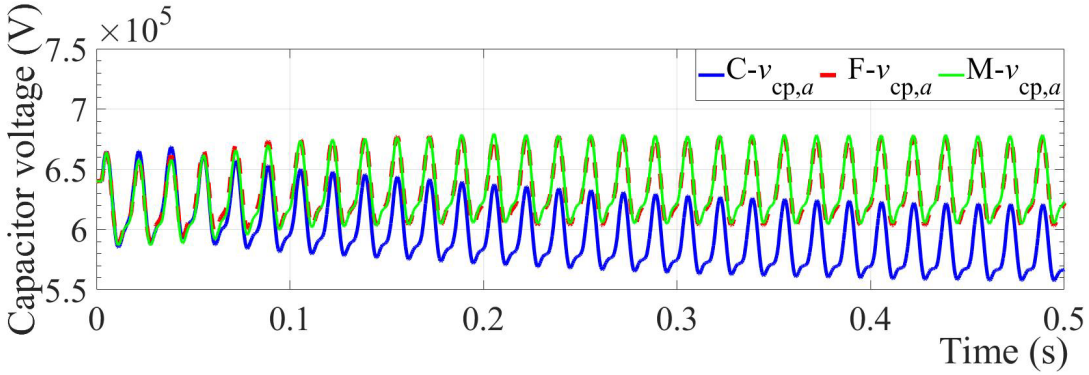

(b)

Figure Appendix A-4: MMC phase-a states with iq,ref = 2,828 A: (a) upper-arm current, and (b) summation of the upper-arm SM capacitor voltages. The states beginning with 'C-', 'F-', and 'M-' in the figure represent the results from coarse simulation, fine simulation, and parallel-in-time simulation.

Further developments in application of parallel-in-time concepts to EMT simulation and/or hybrid simulation will be considered as part of future work.

Appendix B. Initial Exploration of Fault Induced Delayed Voltage Recovery (FIDVR)

In the search for voltage control use cases, the FIDVR effect has been considered by modeling motor loads in PSSE. The loads considered in the buffer zones in the studies in this work was based on static loads. It was found that the FIDVR effect was important enough to be studied in analysis of ac transmission grid voltage control provided by voltage-source converter high-voltage direct-current (VSC-HVdc) lines. In the future, the models developed in PSSE will be converted into PSCAD and represented in the buffer zones.

The model developed to represent FIDVR-type effects in the Atlanta area was simulated; the corresponding results are shown in Fig. B-1. This model includes dynamic load modeling of the Atlanta buffer zone (14 load buses) and in the surrounding region within Georgia (365 load buses in total). The requirement to model a larger buffer zone is also highlighted in Fig. B-1, where the red curve closely matches the typical voltage profile observed during FIDVR-type events. The voltage profile for a longer duration during an FIDVR-type event with a larger buffer zone and dynamic modeling of loads in the buffer zone the for Atlanta area is shown in Fig. B-2.

There are several options on how to proceed with studying the impact of the ac transmission grid voltage control provided by VSC-HVdc substations during FIDVR-type events:

1. Model dynamic loads in the nearby PSS®E “zonal nodes” of the EI lumped model and buffer zones with the VSC-HVdc systems in PSCAD,
2. Define a much larger buffer zone model in PSCAD to study FIDVR-type events completely in PSCAD,
3. Utilize the full EI dynamic model in PSS®E and model smaller buffer zones in PSCAD with motor load models in both PSS®E and PSCAD models for the region of interest (where FIDVR-type studies are performed).

An important step for all the options presented above was the verification and comparison of motor load models to ensure that the models are comparable in PSS®E and PSCAD (upon conversion using ETRAN).

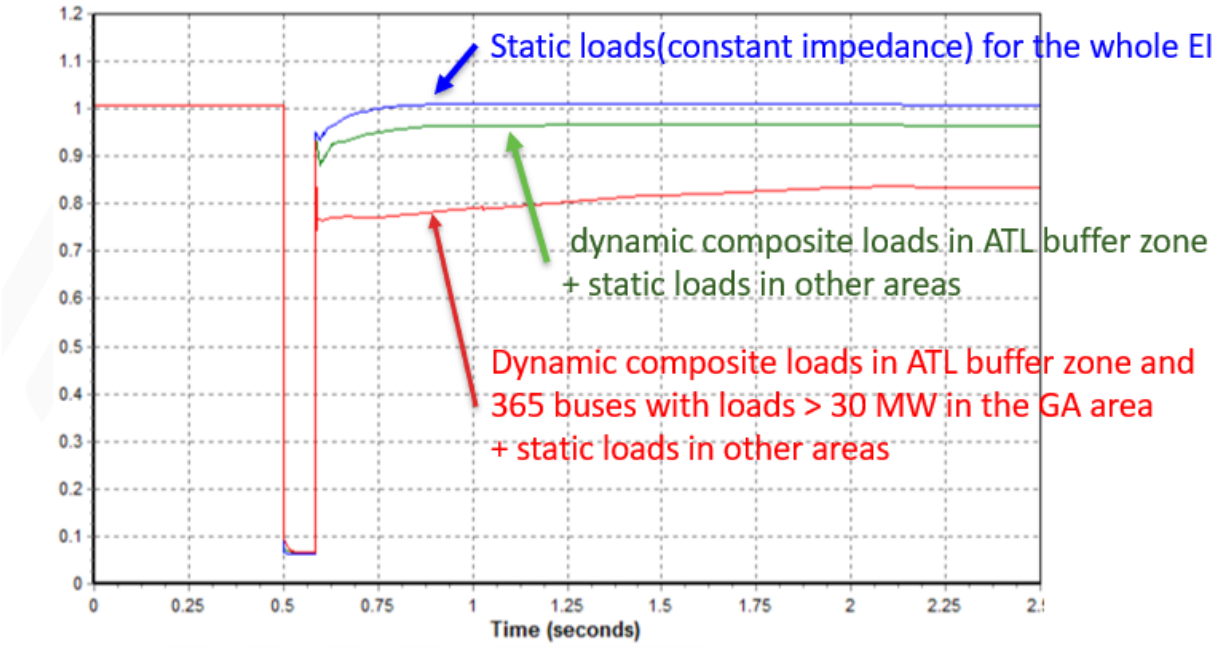

Figure Appendix B-1:Voltage at EI bus near Atlanta for FIDVR effect modeled in PSSE.

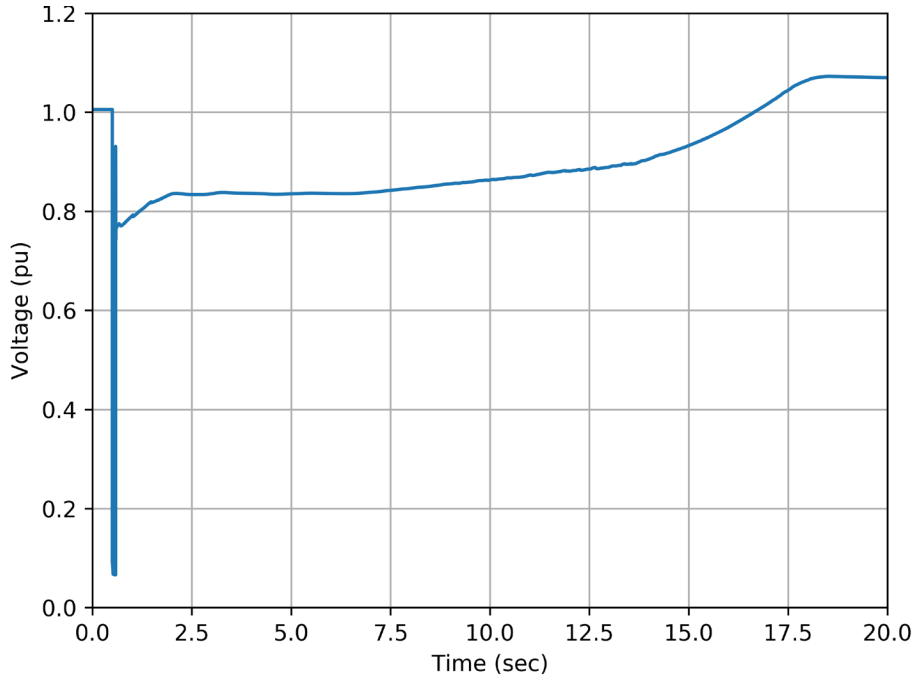

Figure Appendix B-2: Voltage at EI bus near Atlanta – 20 s PSSE simulation for the case with dynamic composite loads in ATL buffer zone and 365 buses with loads > 30 MW in the GA area plus static loads in other areas.

Appendix C. Optimization Results

The results from the optimization problem formulated in Chapter 4 for all the use cases are provided here.

Case Study-1:2 GW ±525 kV 7 Terminal MTdc System with Normal Power Flow

500 MW loss of generation in the Electric Reliability Council of Texas (ERCOT) grid

The initial and final optimized gains of the expert system are provided in Tables C-1 and C-2, respectively, in the case of 500 MW loss of generation in ERCOT grid. The performance of the optimization problem formulated in Chapter 4 was evaluated by comparing the performance of the expert system with initial gains and optimized gains in the multiterminal direct current (MTdc) systems. The comparison was performed based on the frequency responses observed in the simulation of the simplified models used in the optimization problem (as described in Section 4.2.2). Based on these comparisons, it was highlighted that the frequency deviation caused by the loss of generation in an asynchronous interconnection was reduced by use of the optimized gains in the expert system. The optimized gains in the expert system enable the transfer of the maximum amount of power between asynchronous interconnections. The corresponding comparison in the performance is shown in Fig. C-1 for the normal power flow case with a 500 MW loss of generation in the ERCOT grid. As shown in Fig. C-1 (b), the frequency deviation in ERCOT grid upon the loss of generation converges to -0.048, compared to -0.07 in Fig. C-1 (a). The nadir in the frequency deviation was seen to improve from -0.08 to -0.06 from the figures. The settling point and the nadir in the frequency response improve by 31% and 25%, respectively.

Table C-1: Initial gains of expert system for loss of generation in the ERCOT grid.

Terminal	Kpvdcs	Kpfp	Kvfp	F_upper	F_lower	Vdc_upper	Vdc_lower
1	10,000.0	0	0	0.03	-0.03	1.15641*10^6	1.12899*10^6
2	30,000	0	0	0.018	-0.018	1.14285*10^6	1.12022*10^6
3	40,000	0	0	0.006	-0.006	1.07968*10^6	1.04645*10^6
4	30,000	0	0	0.006	-0.006	1.05781*10^6	1.00621*10^6
5	20,000	0	0	0.006	-0.006	1.05585*10^6	984443
6	30,000	0	0	0.006	-0.006	1.12964*10^6	1.03235*10^6
7	0	-1*10^9	0	0.018	-0.018	1.09538*10^6	1.07369*10^6

Table C-2: Optimized gains of expert system for loss of generation in the ERCOT grid.

Terminal	Kpvdcs	Kpfp	Kvfp	F_upper	F_lower	Vdc_upper	Vdc_lower
1	10,000.0	0	0	0.0315	-0.0315	1.15352*10^6	1.12617*10^6
2	28,500.	0	0	0.0189	-0.0189	1.13999*10^6	1.11742*10^6
3	39,967.3	0	0	0.006	-0.006	1.0797*10^6	1.04643*10^6
4	29,980.8	0	0	0.006	-0.006	1.05782*10^6	1.00619*10^6
5	19,985.8	0	0	0.006	-0.006	1.05586*10^6	984433
6	29,970.6	0	0	0.006	-0.006047	1.12965*10^6	1.03235*10^6
7	0	-4.12774*10^9	0	0.018	-0.018	1.0954*10^6	1.07366*10^6

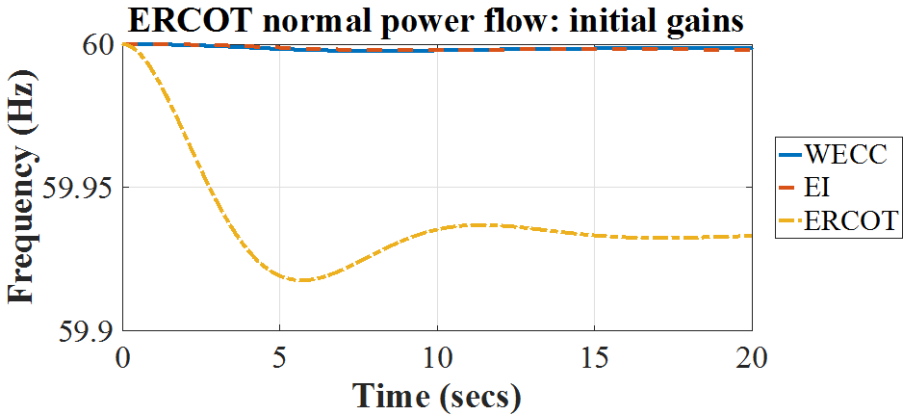

(a)

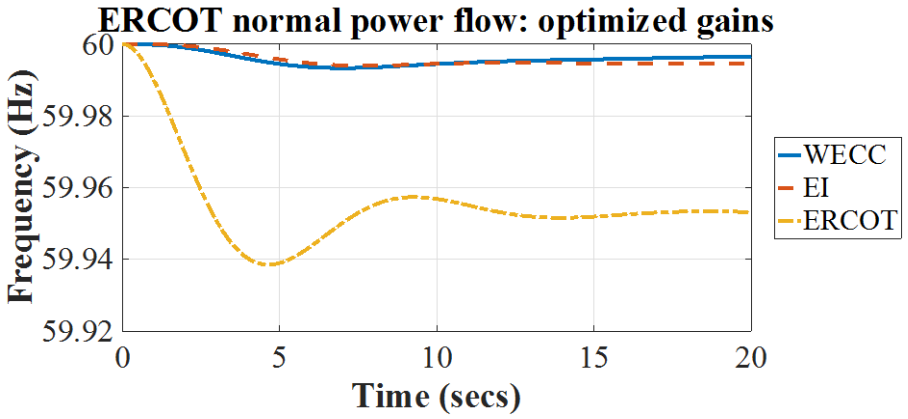

(b)

Figure Appendix C-1: Frequency response based on (a) initial gains, (b) optimized gains in the expert system of the MTdc system with loss generation in the ERCOT grid.

1,202 MW loss of generation in the Eastern Interconnection (EI) grid

The initial and final optimized gains of the expert system are provided in Tables C-3 and C-4, respectively, in the case of 1,202 MW loss of generation in the EI grid. The corresponding comparison in the performance is shown in Fig. C-2. As shown in Fig. C-2(b), the frequency deviation in the EI grid upon the loss of generation converges to -0.015, compared to -0.02 in Fig. C-2(a). The settling point in the frequency response improves by 25%.

Table C-3: Initial gains of expert system for loss of generation in the EI grid.

Terminal	Kpvdcs	Kpfp	Kvfp	F_upper	F_lower	Vdc_upper	Vdc_lower
1	30,000	0	0	0.03	-0.03	1.15641*10^6	1.12899*10^6
2	40,000	0	0	0.018	-0.018	1.14285*10^6	1.12022*10^6
3	0	-1*10^9	0	0.018	-0.018	1.07968*10^6	1.04645*10^6
4	0	-1*10^9	0	0.018	-0.018	1.05781*10^6	1.00621*10^6
5	0	-1*10^9	0	0.018	-0.018	1.05585*10^6	984,443
6	0	-1*10^9	0	0.018	-0.018	1.12964*10^6	1.03235*10^6
7	0	0	0	0.018	-0.018	1.09538*10^6	1.07369*10^6

Table C-4: Optimized gains of expert system for loss of generation in the EI grid.

Terminal	Kpvdcs	Kpfp	Kvfp	F_upper	F_lower	Vdc_upper	Vdc_lower
1	27,234.6	0	0	0.0145	-0.0145	1.15064*10^6	1.12335*10^6
2	39,001.0	0	0	0.0126	-0.01323	1.13714*10^6	1.11463*10^6
3	0	-6.91855*10^9	0	0.018	-0.018	1.07971*10^6	1.04642*10^6
4	0	-5.91758*10^9	0	0.018	-0.018	1.05783*10^6	1.00618*10^6
5	0	-4.38786*10^9	0	0.018	-0.018	1.05586*10^6	984428.
6	0	-6.6039*10^9	0	0.018	-0.018	1.12965*10^6	1.03235*10^6
7	0	0	0	0.018	-0.018	1.09541*10^6	1.07365*10^6

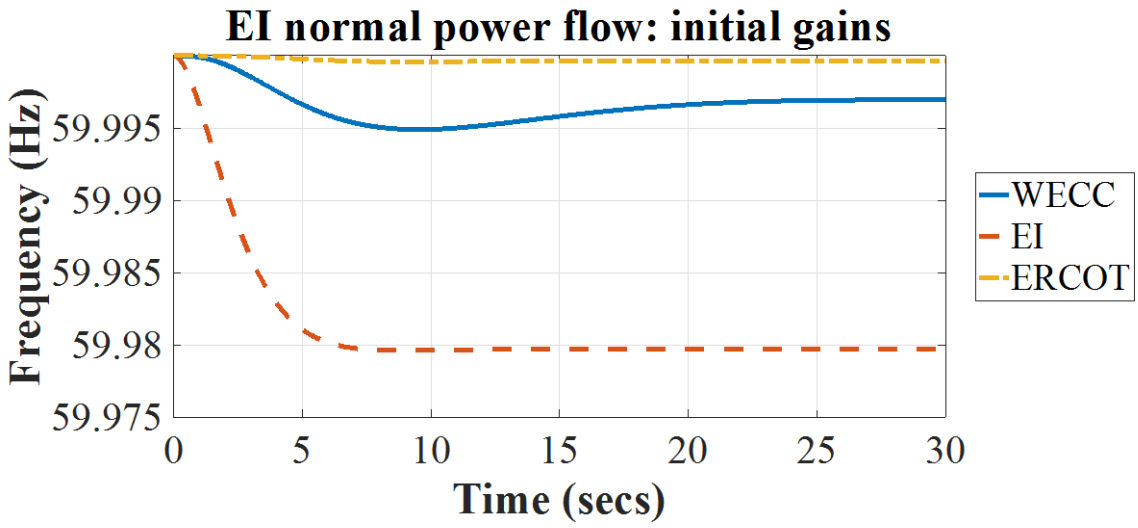

(a)

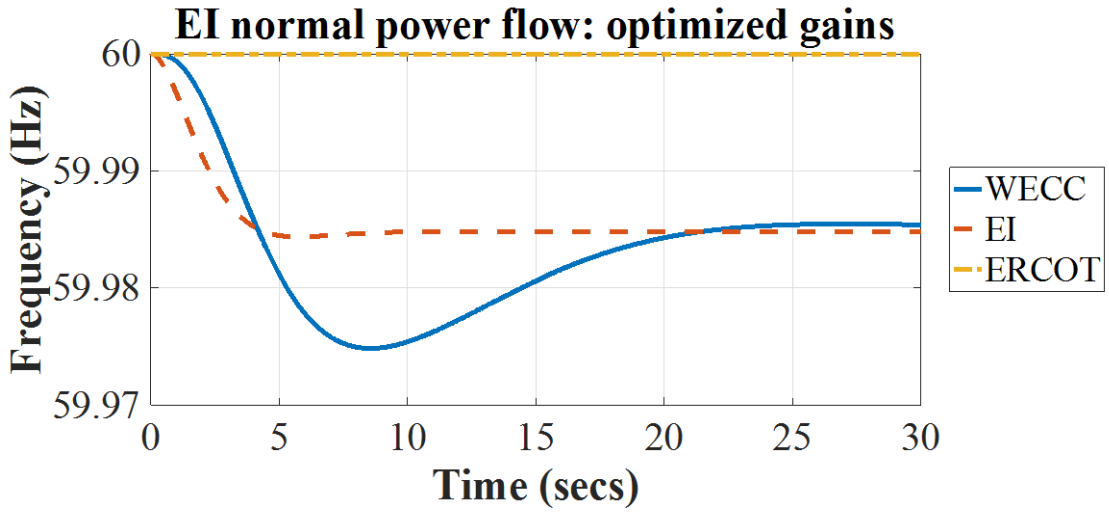

(b)

Figure Appendix C-2:Frequency response based on (a) initial gains, (b) optimized gains in the expert system of the MTdc system with loss generation in the EI grid.

2,756 MW loss of generation in the Western Interconnection (WI) grid

The initial and final optimized gains of the expert system are provided in Tables C-5 and C-6, respectively, in the case of 2,756 MW loss of generation in the WI grid. The corresponding comparison in the performance is shown in Fig. C-3. As shown in Fig. C-3(b), the frequency deviation in the WI grid upon the loss of generation converges to -0.07, compared to -0.10 in Fig. C-3(a). The nadir in the frequency deviation improves from -0.15 to -0.09. The settling point and the nadir in the frequency response improves by 30% and 40%, respectively.

Table C-5: Initial gains of expert system for loss of generation in the WI grid.

Terminal	Kpvdcs	Kpfp	Kvfp	F_upper	F_lower	Vdc_upper	Vdc_lower
1	0	-1*10^9	0	0.03	-0.03	1.15413*10^6	1.13127*10^6
2	0	-1*10^9	0	0.018	-0.018	1.14285*10^6	1.12022*10^6
3	40,000	0	0	0.006	-0.006	1.07968*10^6	1.04645*10^6
4	40,000	0	0	0.006	-0.006	1.05781*10^6	1.00621*10^6
5	40,000	0	0	0.006	-0.006	1.05585*10^6	984443.0
6	40,000	0	0	0.006	-0.006	1.12964*10^6	1.03235*10^6
7	0	0	0	0.018	-0.018	1.09538*10^6	1.07369*10^6

Table C-6: Optimized gains of expert system for loss of generation in the WI grid.

Terminal	Kpvdcs	Kpfp	Kvfp	F_upper	F_lower	Vdc_upper	Vdc_lower
1	0	-7.68148*10^9	0	0.0224593	-0.0294196	1.11359*10^6	1.09154*10^6
2	0	-7.06324*10^9	0	0.0215812	-0.0215812	1.09902*10^6	1.07726*10^6
3	40,323.7	0	0	0.007547	-0.004279	1.05449*10^6	1.02205*10^6
4	39,901.3	0	0	0.007547	-0.004279	1.03648*10^6	985913.0
5	39,896.1	0	0	0.007547	-0.004279	1.03713*10^6	966986.0
6	39,925.3	0	0	0.007547	-0.004279	1.10484*10^6	1.00969*10^6
7	0	0	0	0.0198	-0.0162	1.06397*10^6	1.0429*10^6

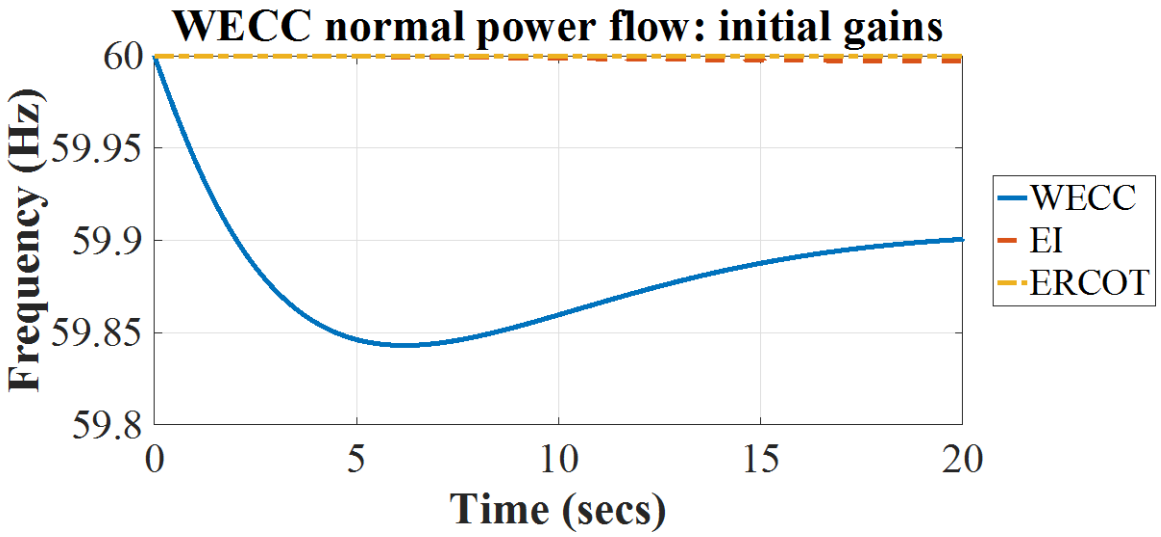

(a)

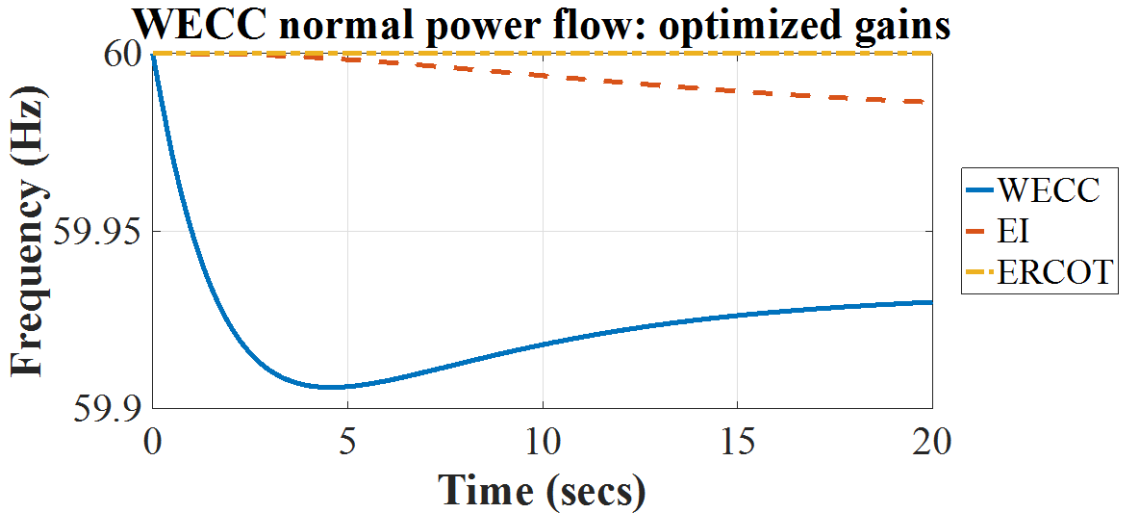

(b)

Figure Appendix C-3: Frequency response based on (a) initial gains, (b) optimized gains in the expert system of the MTdc system with loss of generation in the WI grid.

Case Study-2:2 GW ±525 kV 7 Terminal MTdc System with Reverse Power Flow

500 MW loss of generation in the ERCOT grid

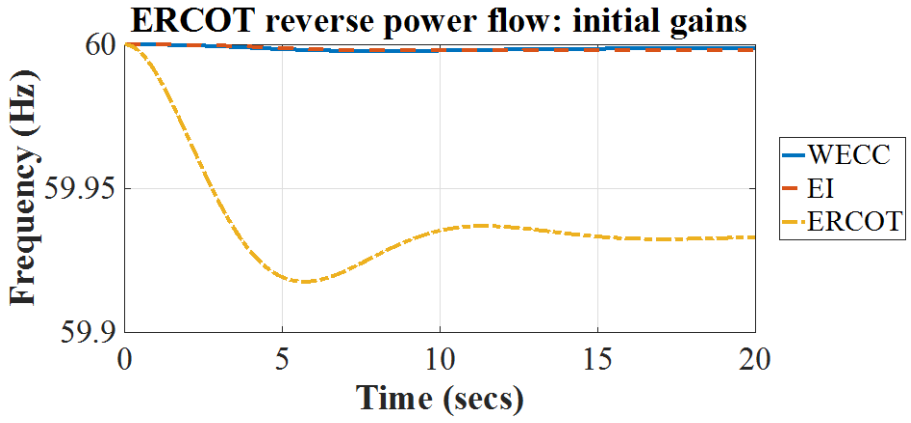

(a)

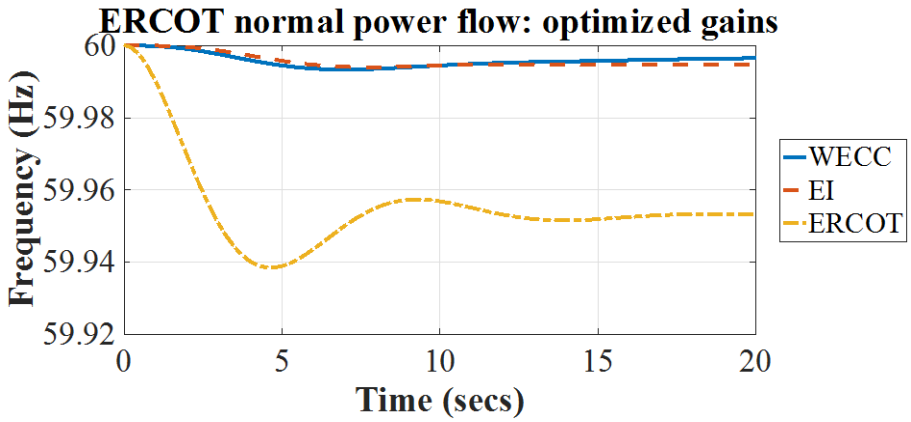

(b)

Figure Appendix C-4: Frequency response based on (a) initial gains, (b) optimized gains in the expert system of the MTdc system with loss of generation in the ERCOT grid.

The initial and final optimized gains of the expert system are provided in Tables C-7 and C-8, respectively, in the case of 500 MW loss of generation in the ERCOT grid during reverse power flow. The corresponding comparison in the performance is shown in Fig. C-4. As shown in Fig. C-4(b), the frequency deviation in the ERCOT grid upon the loss of generation converges to -0.048, compared to -0.07 in Fig. C-4(a). The nadir in the frequency deviation improves from -0.08 to -0.045. The settling point and the nadir in the frequency response improves by 31% and 43.75%, respectively.

Table C-7: Initial gains of expert system for loss of generation in the ERCOT grid.

Terminal	Kpvdcs	Kpfp	Kvfp	F_upper	F_lower	Vdc_upper	Vdc_lower
1	10,000.0	0	0	0.03	-0.03	1.00108*10^6	977340
2	30,000	0	0	0.018	-0.018	1.00876*10^6	988781
3	40,000	0	0	0.006	-0.006	1.0863*10^6	1.05287*10^6
4	30,000	0	0	0.006	-0.006	1.13255*10^6	1.0773*10^6
5	20,000	0	0	0.006	-0.006	1.15397*10^6	1.07593*10^6
6	30,000	0	0	0.006	-0.006	1.10097*10^6	1.00615*10^6
7	0	-1*10^9	0	0.018	-0.018	1.05831*10^6	1.03735*10^6

Table C-8: Optimized gains of expert system for loss of generation in the ERCOT grid.

Terminal	Kpvdcs	Kpfp	Kvfp	F_upper	F_lower	Vdc_upper	Vdc_lower
1	10,000.0	0	0	0.033075	-0.033075	1.05114*10^6	928473
2	24,435.2	0	0	0.0208373	-0.0208373	1.05919*10^6	939342
3	39,338.2	0	0	0.006	-0.006	1.08631*10^6	1.05286*10^6
4	29,457.9	0	0	0.006	-0.006	1.13256*10^6	1.07729*10^6
5	19,527.6	0	0	0.006	-0.006	1.15398*10^6	1.07592*10^6
6	29,509.8	0	0	0.006	-0.006047	1.10097*10^6	1.00615*10^6
7	0	-8.80909*10^9	0	0.018	-0.018	1.05832*10^6	1.03734*10^6

1,202 MW loss of generation in the EI grid

The initial and final optimized gains of the expert system are provided in Tables C-9 and C-10, respectively, in the case of 1,202 MW loss of generation in the EI grid during reverse power flow. The corresponding comparison in the performance is shown in Fig. C-5. As shown in Fig. C-5(b), the frequency deviation in the EI grid upon the loss of generation converges to -0.015, compared to -0.02 in Fig. C-5(a). The settling point in the frequency response improves by 25%.

Table C-9: Initial gains of expert system for loss of generation in the EI grid.

Terminal	Kpvdcs	Kpfp	Kvfp	F_upper	F_lower	Vdc_upper	Vdc_lower
1	30,000	0	0	0.03	-0.03	1.00108*10^6	977340
2	40,000	0	0	0.018	-0.018	1.00876*10^6	988781
3	0	-1*10^9	0	0.018	-0.018	1.0863*10^6	1.05287*10^6
4	0	-1*10^9	0	0.018	-0.018	1.13255*10^6	1.0773*10^6
5	0	-1*10^9	0	0.018	-0.018	1.15397*10^6	1.07593*10^6
6	0	-1*10^9	0	0.018	-0.018	1.10097*10^6	1.00615*10^6
7	0	0	0	0.018	-0.018	1.05831*10^6	1.03735*10^6

Table C-10: Optimized gains of expert system for loss of generation in the EI grid.

Terminal	Kpvdcs	Kpfp	Kvfp	F_upper	F_lower	Vdc_upper	Vdc_lower
1	25,234.6	0	0	0.0132	-0.0132	1.05114*10^6	928,473
2	35,051.0	0	0	0.01323	-0.0138915	1.05919*10^6	939,342
3	0	-8.07457*10^9	0	0.018	-0.018	1.08631*10^6	1.05286*10^6
4	0	-6.92975*10^9	0	0.018	-0.018	1.13256*10^6	1.07729*10^6
5	0	-5.09092*10^9	0	0.018	-0.018	1.15398*10^6	1.07592*10^6
6	0	-7.70589*10^9	0	0.018	-0.018	1.10097*10^6	1.00615*10^6
7	0	0	0	0.018	-0.018	1.05832*10^6	1.03734*10^6

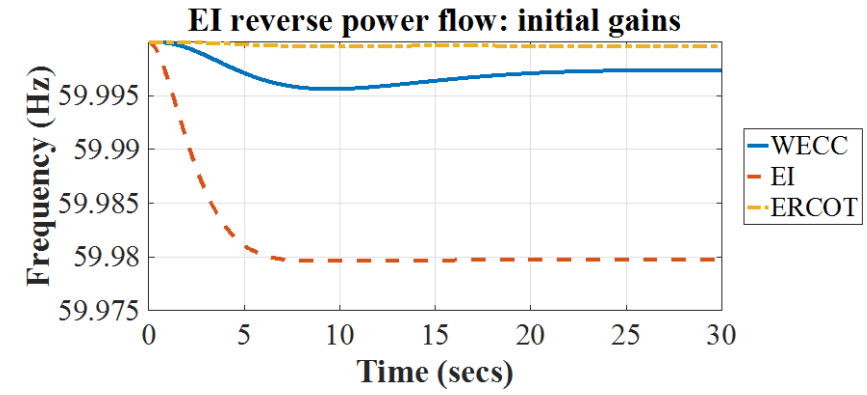

(a)

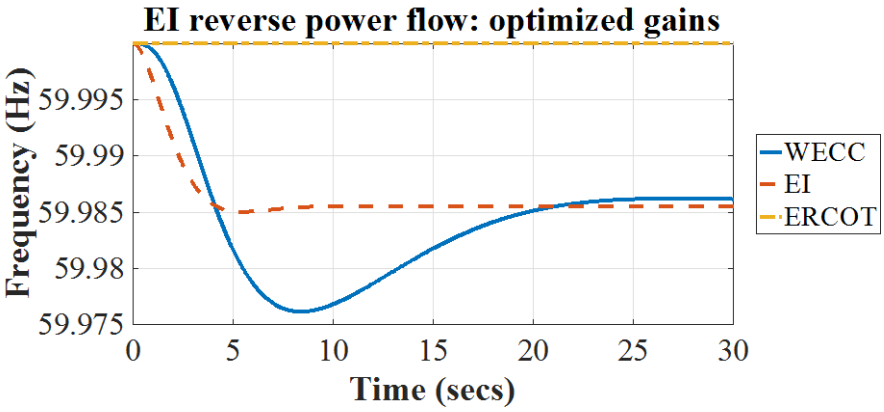

(b)

Figure Appendix C-5: Frequency response based on (a) initial gains, (b) optimized gains in the expert system of the MTdc system with loss of generation in the EI grid.

2,756 MW loss of generation in the WI grid

The initial and final optimized gains of the expert system are provided in Tables C-11 and C-12, respectively, in the case of 2,756 MW loss of generation in the WI grid during reverse power flow. The corresponding comparison in the performance is shown in Fig. C-6. As shown in Fig. C-6(b), the frequency deviation in EI grid upon the loss of generation converges to -0.07, compared to -0.1 in Fig. C-6(a). The nadir in the frequency deviation improves from -0.15 to -0.1. The settling point and the nadir in the frequency response improves by 30% and 33.33%, respectively.

Table C-11: Initial gains of expert system for loss of generation in the WI grid.

Terminal	Kpvdcs	Kpfp	Kvfp	F_upper	F_lower	Vdc_upper	Vdc_lower
1	0	-1*10^9	0	0.03	-0.03	998,100.0	978,330.0
2	0	-1*10^9	0	0.018	-0.018	1.0084*10^6	988,189.0
3	40,000	0	0	0.006	-0.006	1.08196*10^6	1.05223*10^6
4	40,000	0	0	0.006	-0.006	1.12992*10^6	1.07555*10^6
5	40,000	0	0	0.006	-0.006	1.14672*10^6	1.07506*10^6
6	40,000	0	0	0.006	-0.006	1.09535*10^6	1.00583*10^6
7	0	0	0	0.018	-0.018	1.05784*10^6	1.03719*10^6

Table C-12: Optimized gains of expert system for loss of generation in the WI grid.

Terminal	Kpvdcs	Kpfp	Kvfp	F_upper	F_lower	Vdc_upper	Vdc_lower
1	0	-6.89205*10^9	0	0.0238273	-0.026923	998100.0	978,330.0
2	0	-6.60491*10^9	0	0.0206173	-0.0206173	1.0084*10^6	988,189.0
3	41,852.3	0	0	0.007547	-0.004279	1.08196*10^6	1.05223*10^6
4	39,924.2	0	0	0.007547	-0.004279	1.12992*10^6	1.07555*10^6
5	39,116.5	0	0	0.007547	-0.004279	1.14672*10^6	1.07506*10^6
6	39,442.2	0	0	0.007547	-0.004279	1.09535*10^6	1.00583*10^6
7	0	0	0	0.0198	-0.0162	1.05784*10^6	1.03719*10^6

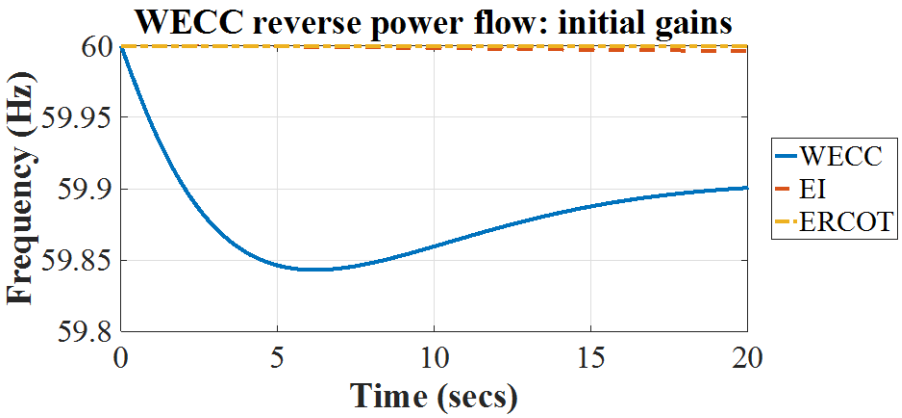

(a)

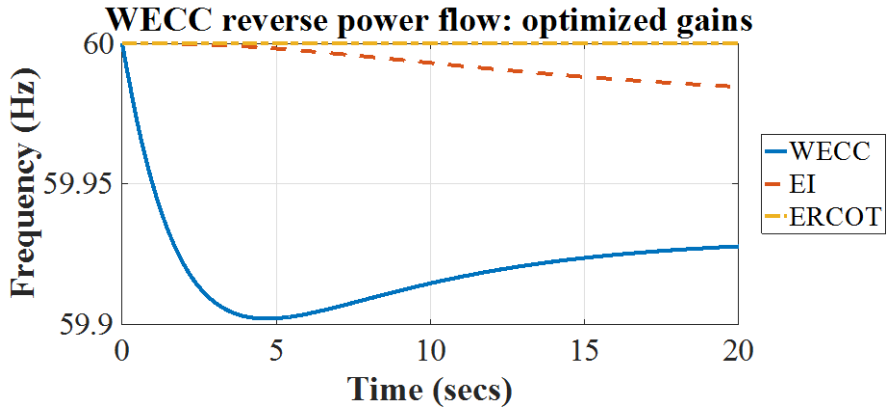

(b)

Figure Appendix C-6: Frequency response based on (a) initial gains, (b) optimized gains in the expert system of the MTdc system with loss of generation in the WI grid.

Simulation Results

Case Study-1:2 GW ±525 kV 7 Terminal MTdc system with normal power flow

In this case study, the MTdc system shown in Fig. 4-2 as connected to EI, ERCOT, and WI grids. The powers injected into the MTdc system at terminals: Victorville (terminal 1), Palo Verde (terminal 2), and St. Louis (terminal 6). The powers are drawn out of the MTdc system at terminals: Panola County (terminal 3), Atlanta (terminal 4), and Orlando (terminal 5). The power dispatch commands for this case study are tabulated in Table C-13.

Table C-13: Power dispatch commands for normal power flow scenario.

Terminal	Power Dispatch (Pdis) (W)
1: Victorville (VV)	-2,018,000,000
2: Palo Verde (PV)	-1,480,720,000
3: Panola County (PC)	1,532,000,000
4: Atlanta (AT)	1,482,000,000
5: Orlando (OR)	1,700,000,000
6: St. Louis (STL)	-1,733,800,000
7: Sweetwater (SW)	0

500 MW loss of generation in ERCOT grid at 10 s

The 500 MW loss of generation in ERCOT grid with the MTdc system connecting the asynchronous grids was simulated using electromagnetic transient (EMT) simulation; the corresponding results from the simulation are shown in Fig. C-7. F_VV, F_PV, F_PC, F_AT, F_OR, F_STL, and F_SW indicate the frequency measured at substation terminals Victorville (VV), Palo Verde (PV), Panola County (PC), Atlanta (ATL), Orlando (ORL), St Louis (STL), and Sweetwater (SW), respectively, in Fig. C-7 (a). F_VVbase, F_PVbase, and F_SWbasewere the frequency profiles at the substation terminals in VV, PV, and SW, respectively, without any primary frequency support. Pout1-Pout7 in Fig. C-7 (b) indicate the output power profiles at substation terminals VV through SW as in the same order tabulated in Table C-13. Vdc1-Vdc7 in Fig. C-7(c) indicate the output dc voltage profiles of the terminals VV through SW as in the same order tabulated in the table. idc1-idc7 in Fig. C-7(d) indicate the output current profiles of terminals VV through SW as in the same order as tabulated in the table.

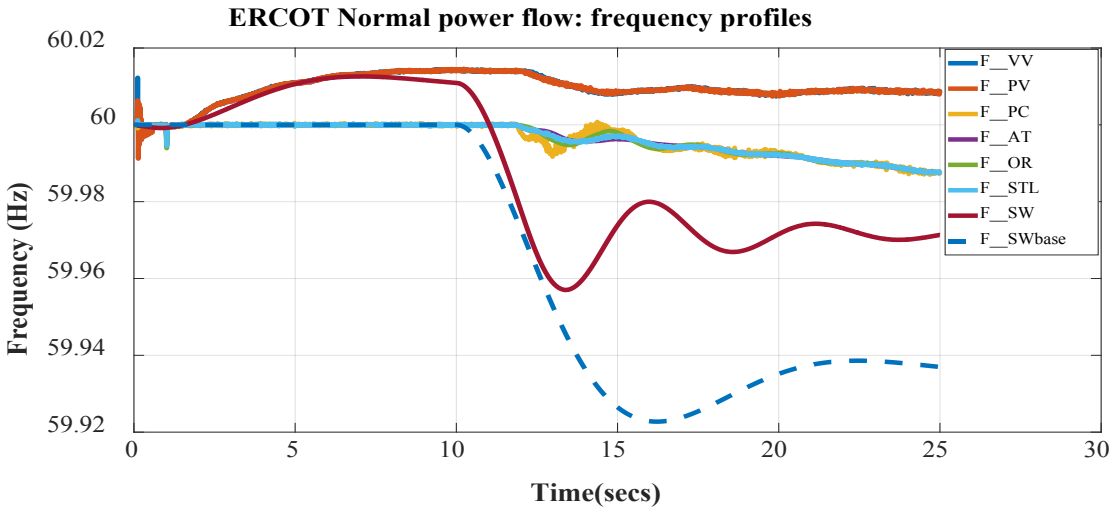
ERCOT Normal power flow: frequency profiles
Frequency (Hz)
Time(secs)
F__VV
F__PV
F__PC
F__AT
F__OR
F__STL
F__SW
F__SWbase

(a)

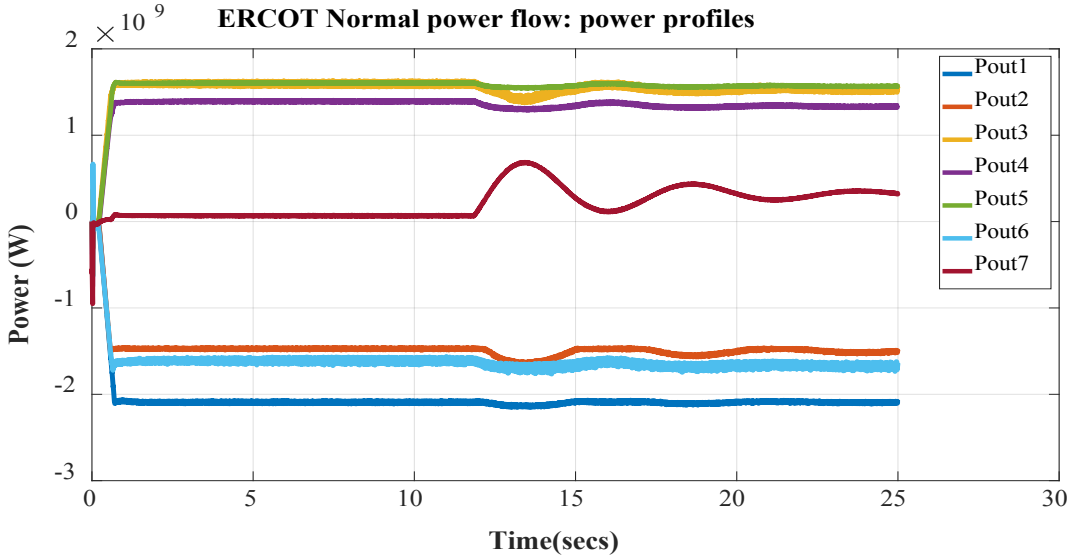
ERCOT Normal power flow: power profiles
Power (W)
Time(secs)
Pout1
Pout2
Pout3
Pout4
Pout5
Pout6
Pout7

(b)

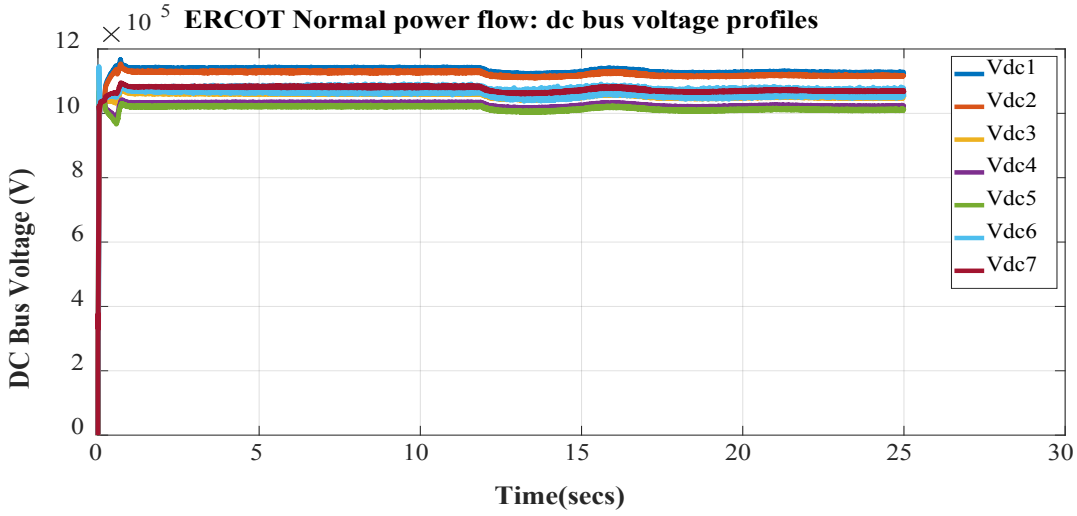

(c)

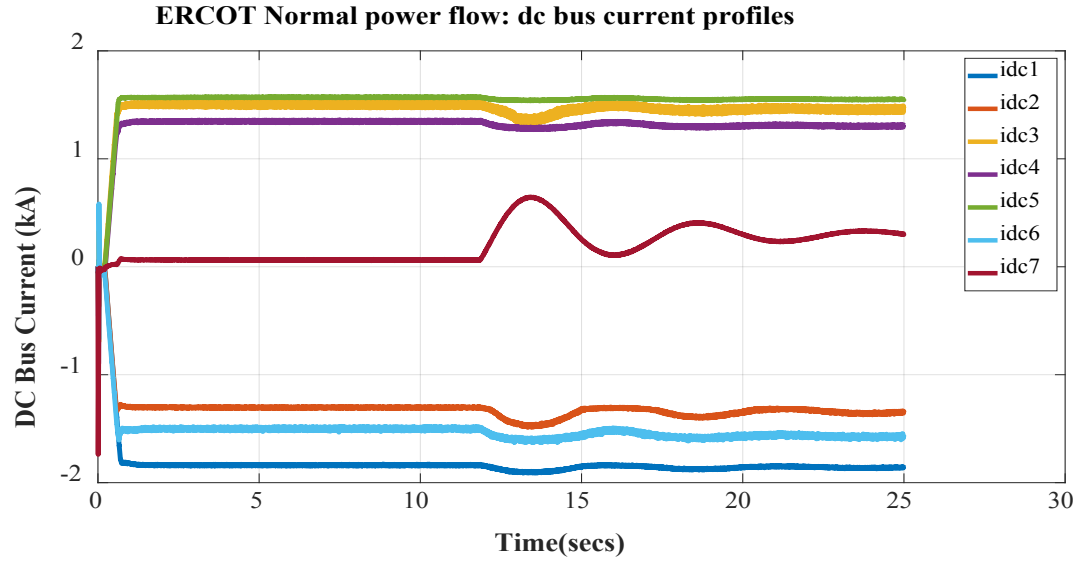

(d)

Figure Appendix C-7: Loss of generation in ERCOT grid in normal power flow case study: (a) frequency profiles with and without WI and EI grids' support (b) output power profiles (c) dc bus voltage profiles (d) dc bus current profiles.

From Fig. C-7(a), it can be noticed that the inclusion of advanced frequency control in MTdc system improves the frequency response. Frequency response of the ERCOT grid was improved by up to 38.8% in the nadir and 44.4% in the settling point. It can be observed from Figs. C-7(b) and (d) that in the event of generation loss in ERCOT grid, the support was provided to the grid by changing the power and current flow through the MTdc system. During the contingency, the dc voltages at all the MTdc substation terminals were within the defined permissible limits, as seen from Fig. C-7 (c).

1,202 MW loss of generation in EI grid at 10 s

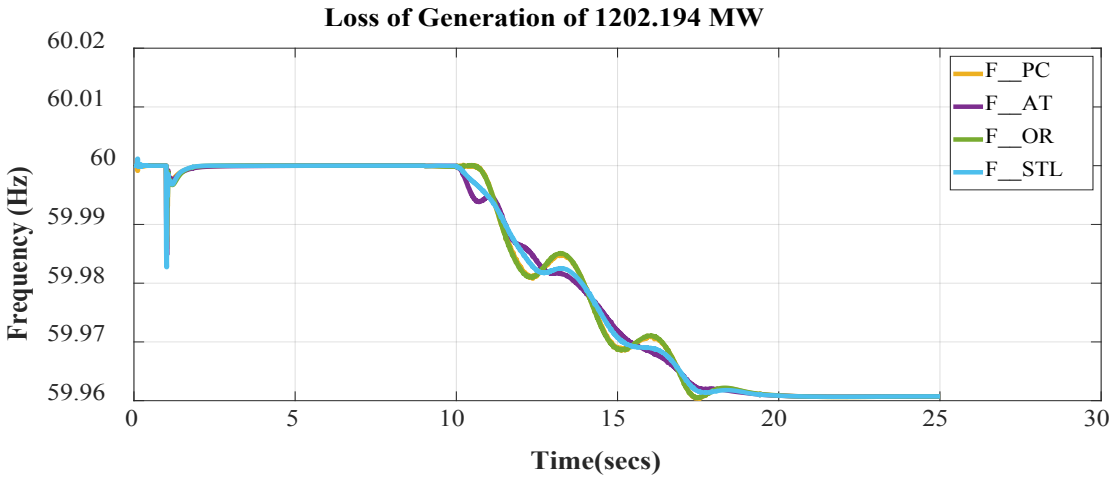

Figure Appendix C-8: Frequency profiles of the terminals in the EI grid without any support from the WI and ERCOT grids.

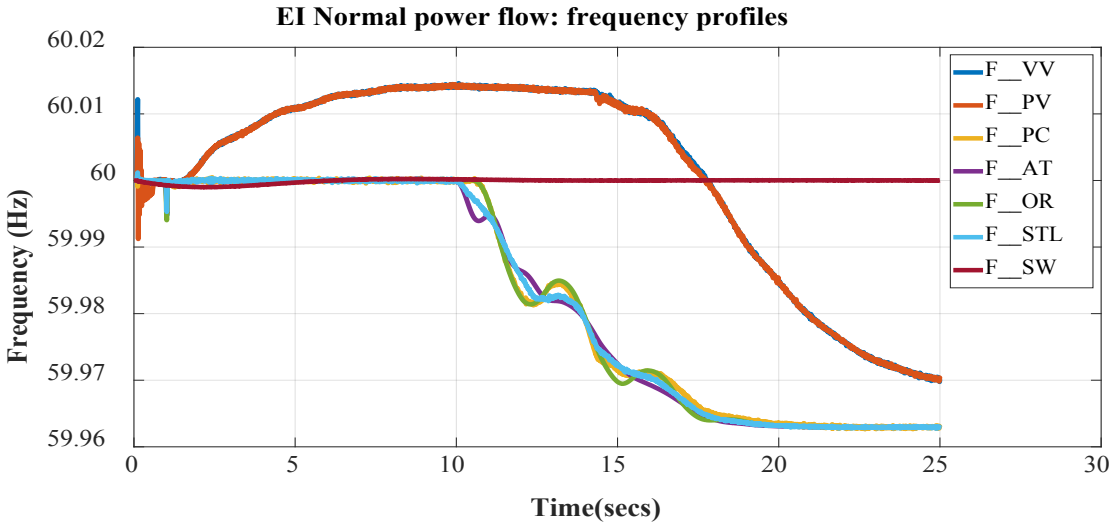

(a)

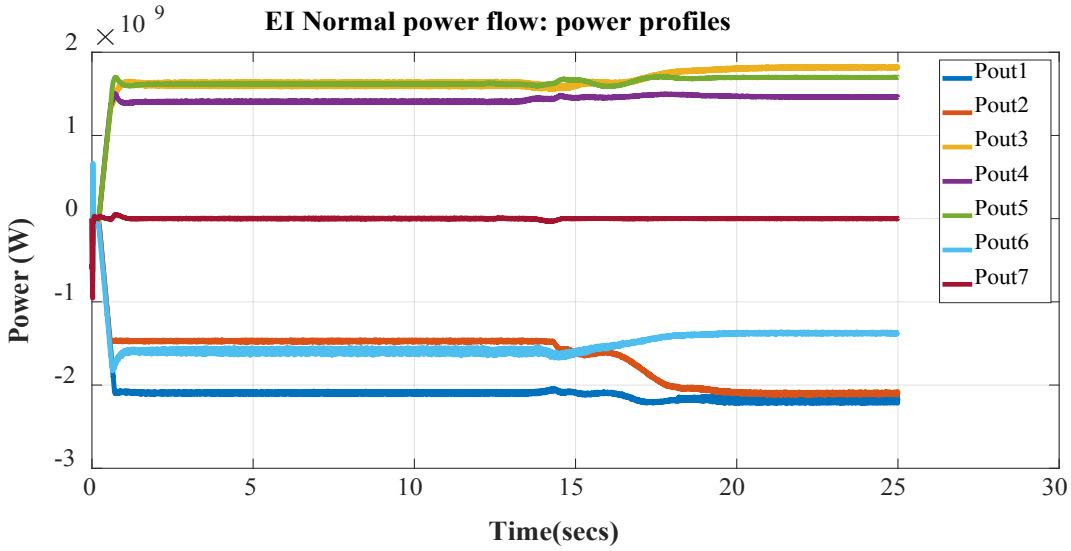
EI Normal power flow: power profiles
×10^9
Power (W)
Time(secs)
Pout1
Pout2
Pout3
Pout4
Pout5
Pout6
Pout7

(b)

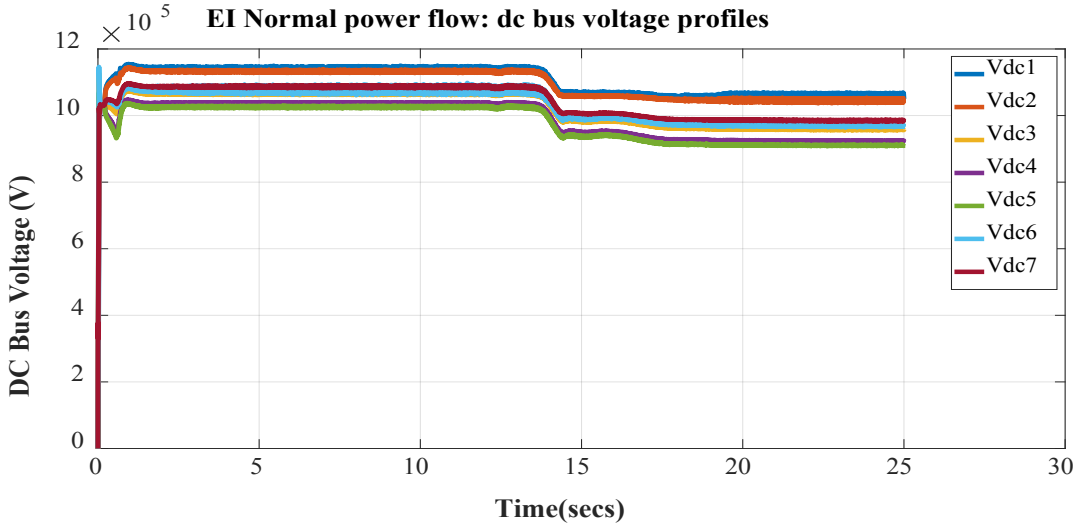
EI Normal power flow: dc bus voltage profiles
×10^5
DC Bus Voltage (V)
Time(secs)
Vdc1
Vdc2
Vdc3
Vdc4
Vdc5
Vdc6
Vdc7

(c)

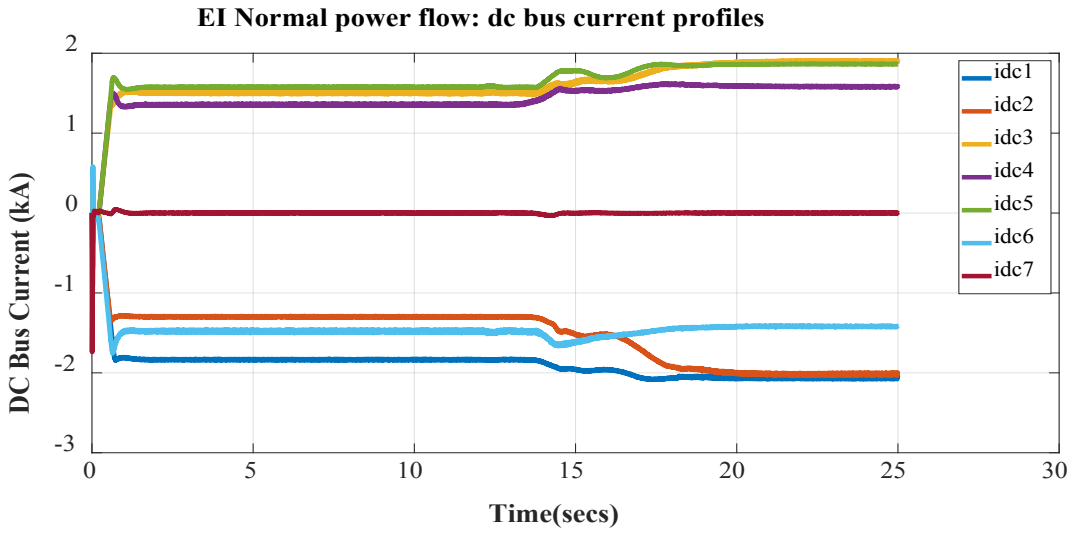

(d)

Figure Appendix C-9: Loss of generation of 1,202 MW in the EI grid in normal power flow case study: (a) frequency profiles (b) output power profiles (c) dc bus voltage profiles (d) dc bus current profiles.

The 1,202 MW loss of generation in the EI grid with the MTdc system connecting the asynchronous grids was simulated using EMT simulation; the corresponding results from the simulation are shown in Fig. C-8–C-9. The frequency response of the MTdc substation terminals in the EI grid without the advanced frequency control in the MTdc system is shown in Fig. C-8. From Fig. C-9 (a), it can be noticed that the inclusion of advanced frequency control in the MTdc system improves the frequency response. Frequency response of the EI grid was improved by up to 5% in the settling point. In the event of generation loss in the EI grid, the support was provided to the EI grid by the MTdc substation terminals in the WI grid. This phenomenon can be clearly noticed in Figs. C.9 (b) and (d). These figures also show that the MTdc substations in the WI grid were sending rated power prior to the loss of generation. Therefore, it was difficult to provide power to the EI grid from the WI grid upon the loss of generation. The dc voltages at all MTdc substation terminals were within the defined permissible limits, as seen in Fig C.9 (c).

2,756 MW loss of generation in the WI grid at 10 s

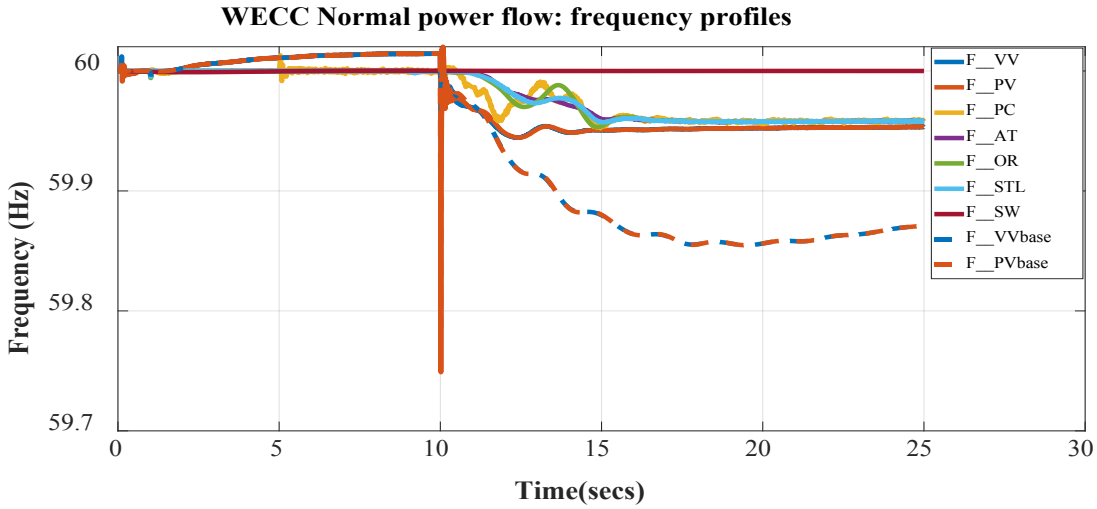

(a)

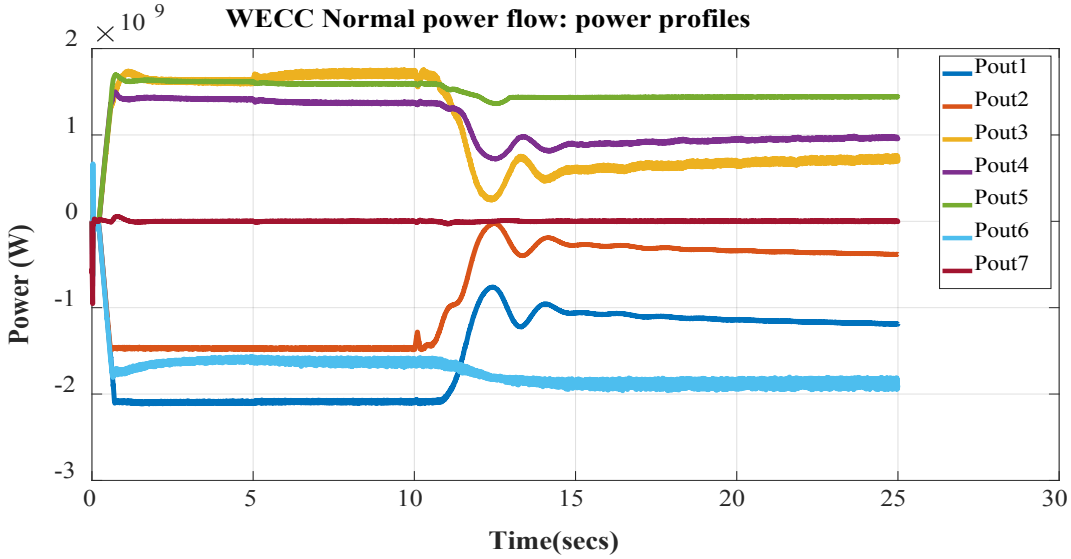

(b)

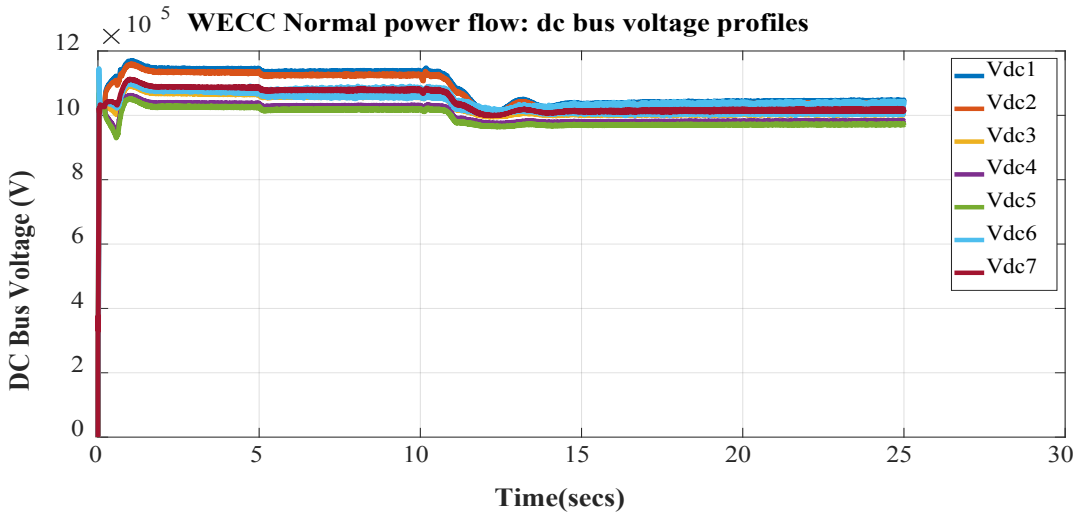

(c)

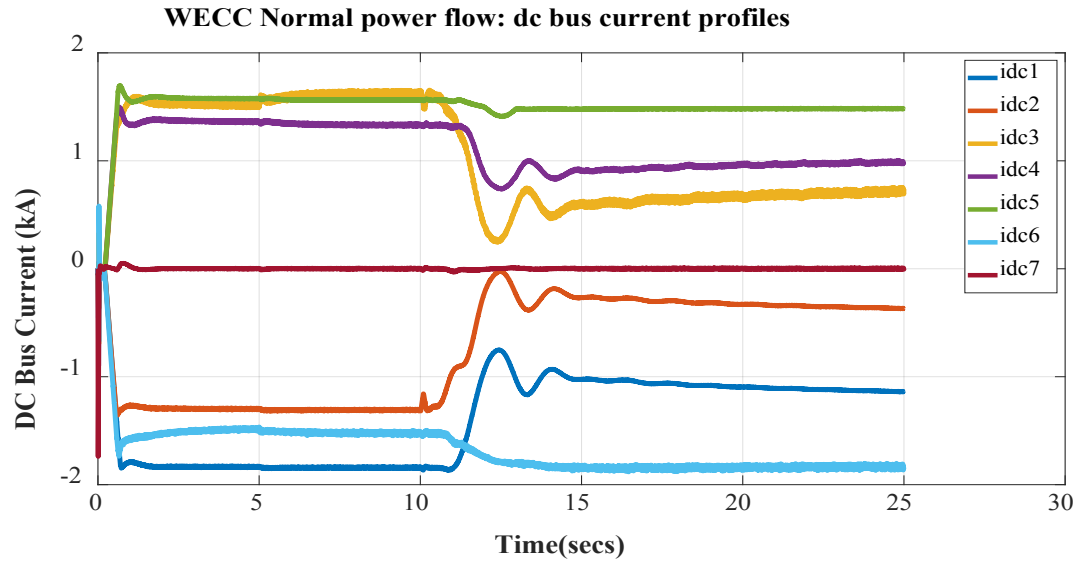

(d)

Figure Appendix C-10: Loss of generation in the WI grid in normal power flow case study: (a) frequency profiles with and without EI and ERCOT grids' support (b) output power profiles (c) dc bus voltage profiles (d) dc bus current profiles.

The 2,756 MW loss of generation in WI grid with the MTdc system connecting the asynchronous grids was simulated using EMT simulation; the corresponding results from the simulation are shown in Fig. C-10. From Fig. C-10(a), it can be noticed that the inclusion of advanced frequency control in the MTdc system improves the frequency response. Frequency response of the WI grid was improved by up to 62.5% in the nadir and 64.3% in the settling point. In the event of generation loss in the WI grid, the support was provided to WI by the MTdc substation terminals in the EI grid. This phenomenon can be clearly noticed in Figs. C-10(b) and (d). The dc voltages at all MTdc substation terminals were within the defined permissible limits, as seen in Fig C-10(c).

Case Study-2: 2 GW ±525 kV 7 Terminal MTdc system with reverse power flow

In this case study, the powers were injected into the MTdc system at Panola County (terminal 3), Atlanta (terminal 4), and Orlando (terminal 5). The powers were drawn out of the MTdc system at Victorville (terminal 1), Paloverde (terminal 2), and St. Louis (terminal 6). The power dispatch commands for this case study are tabulated in Table C-14.

Table C-14: Power dispatch commands for reverse power flow scenario.

Terminal	Power Dispatch (Pdis) (W)
1 (Victorville) (VV)	2,018,000,000
2 (Paloverde) (PV)	1,480,720,000
3 (Panola County) (PC)	-1,900,000,000
4 (Atlanta) (AT)	-1,900,000,000
5 (Orlando) (OR)	-1,900,000,000
6 (St. Louis) (STL)	1,733,800,000
7 (Sweetwater) (SW)	0

500 MW loss of generation in the ERCOT grid at 10 s

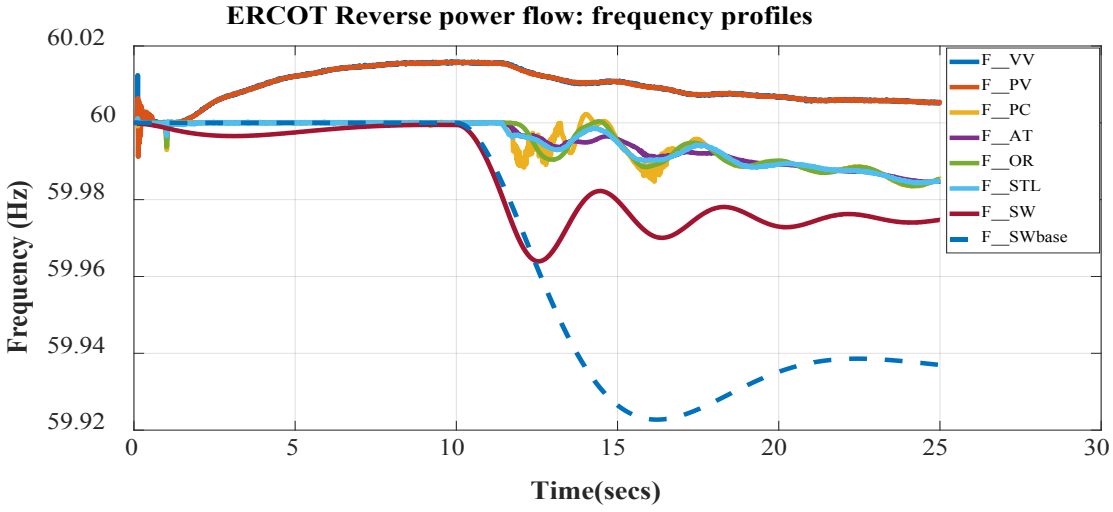

(a)

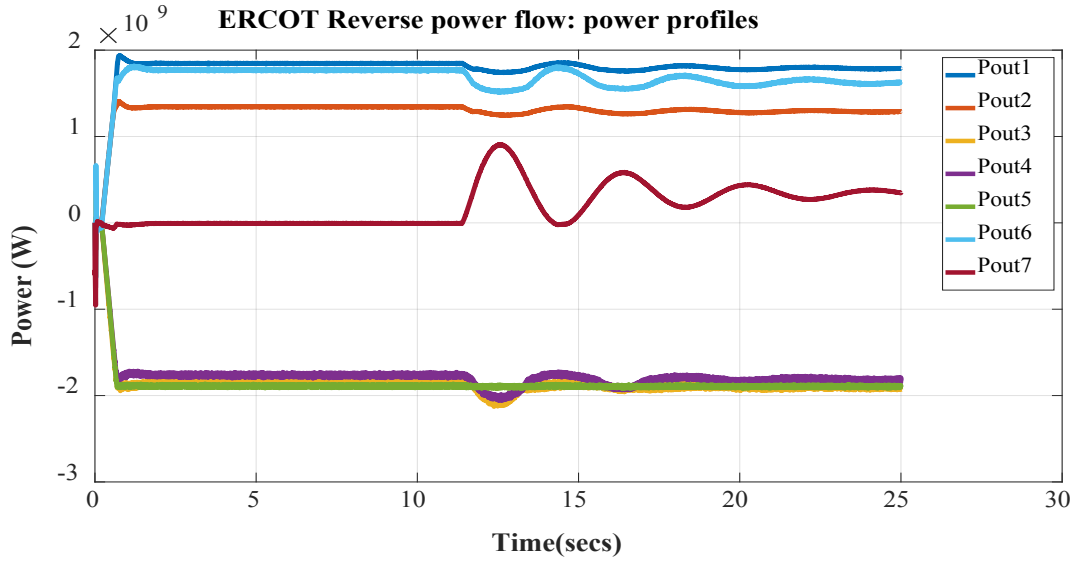
ERCOT Reverse power flow: power profiles
× 10 9
2
1
0
-1
-2
-3
Power (W)
0
5
10
15
20
25
30
Time(secs)
Pout1
Pout2
Pout3
Pout4
Pout5
Pout6
Pout7

(b)

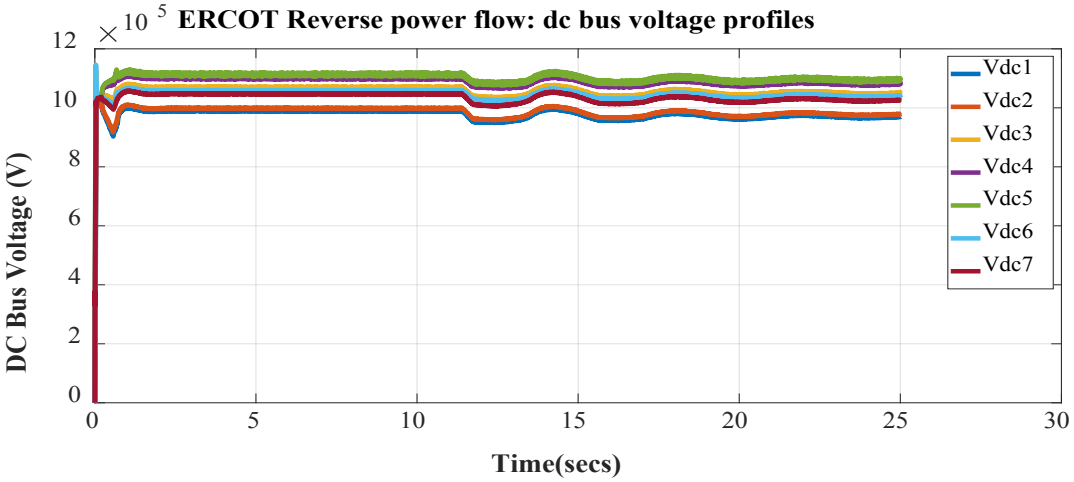
ERCOT Reverse power flow: dc bus voltage profiles
× 10 5
12
10
8
6
4
2
0
DC Bus Voltage (V)
0
5
10
15
20
25
30
Time(secs)
Vdc1
Vdc2
Vdc3
Vdc4
Vdc5
Vdc6
Vdc7

(c)

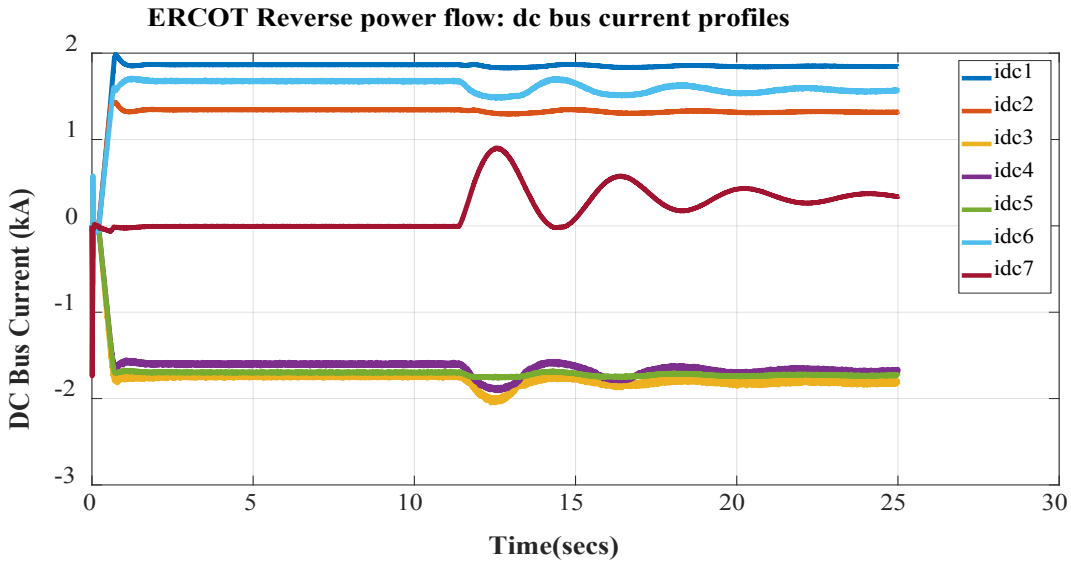

(d)

Figure Appendix C-11: Loss of generation in the ERCOT grid in a reverse power flow case study: (a) frequency profiles with and without EI and WI grids' support (b) output power profiles (c) dc bus voltage profiles (d) dc bus current profiles.

The 500 MW loss of generation in the ERCOT grid with the MTdc system connecting the asynchronous grids was simulated using EMT simulation; the corresponding results from the simulation are shown in Fig. C-11. From Fig. C-11(a), it can be noticed that the inclusion of advanced frequency control in the MTdc system improves the frequency response. The frequency response of the ERCOT grid was improved by up to 49% in the nadir and 55% in the settling point. In the event of generation loss in the ERCOT grid, the support was provided to ERCOT by the MTdc substation terminals in the EI and WI grids. This phenomenon can be clearly noticed in Figs. C-11(b) and (d). The dc voltages at all MTdc substation terminals are within the defined permissible limits, as seen in Fig C-11(c).

1,202 MW loss of generation in EI grid at 10 s

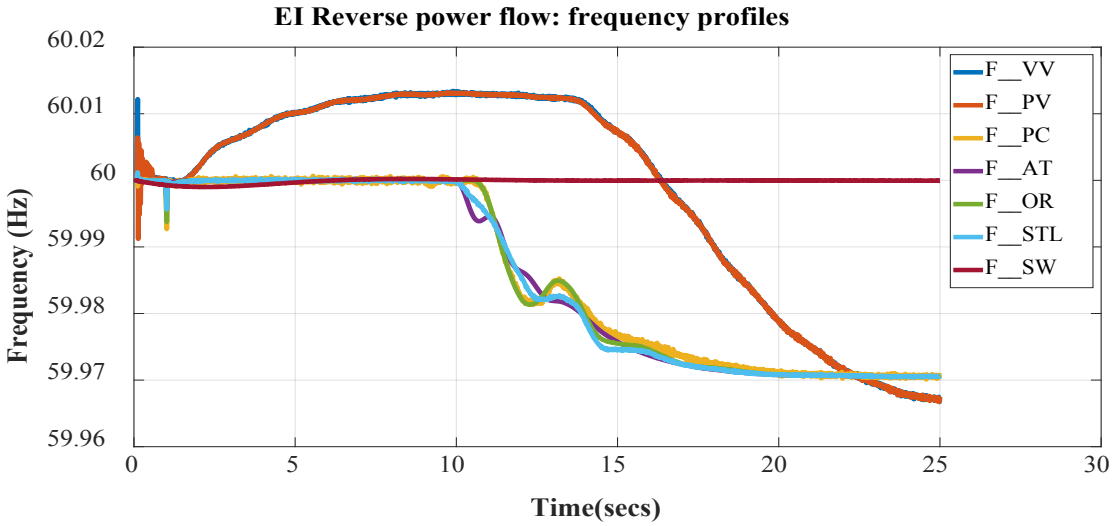

(a)

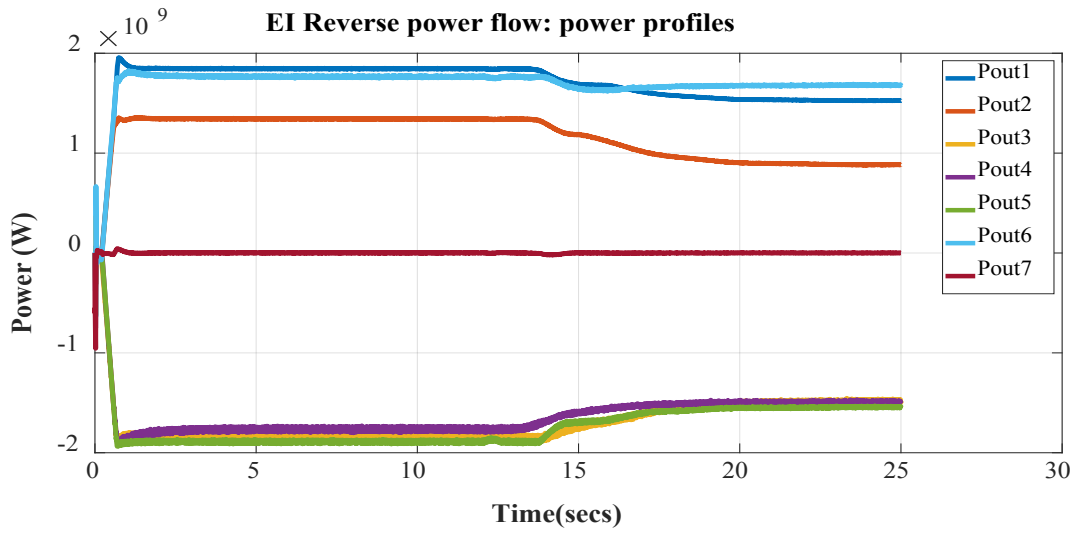
EI Reverse power flow: power profiles
× 10 9
2
1
0
-1
-2
Power (W)
0
5
10
15
20
25
30
Time(secs)
Pout1
Pout2
Pout3
Pout4
Pout5
Pout6
Pout7

(b)

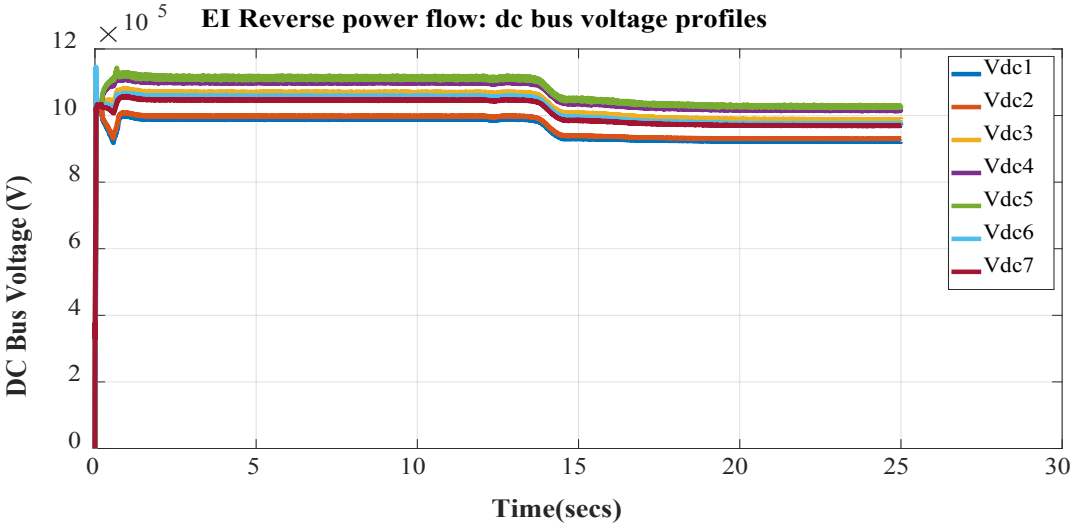
EI Reverse power flow: dc bus voltage profiles
× 10 5
12
10
8
6
4
2
0
DC Bus Voltage (V)
0
5
10
15
20
25
30
Time(secs)
Vdc1
Vdc2
Vdc3
Vdc4
Vdc5
Vdc6
Vdc7

(c)

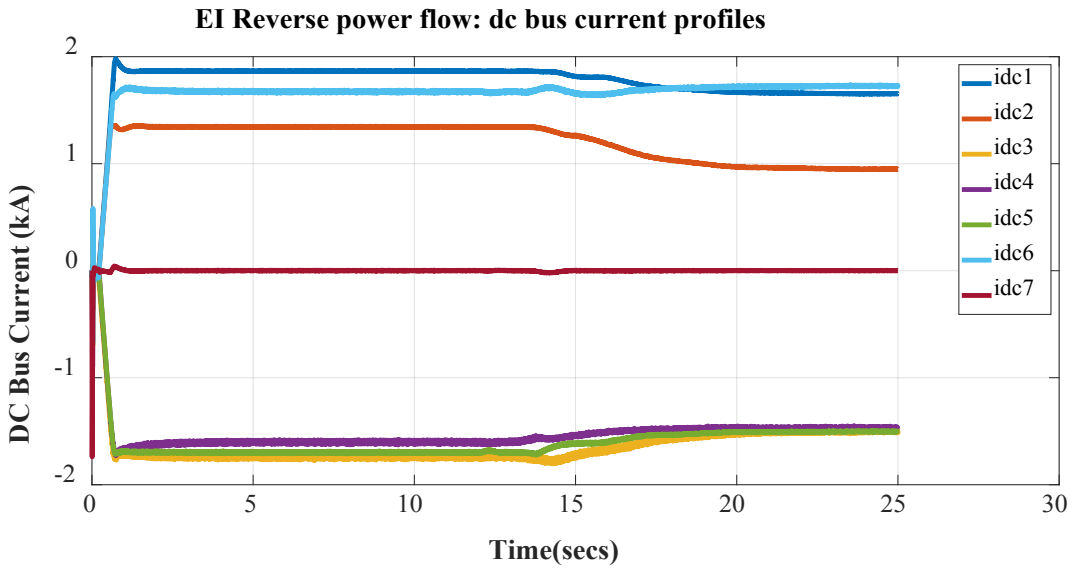

(d)

Figure Appendix C-12: Loss of generation of 1,202 MW in the EI grid in reverse power flow case study: (a) frequency profiles (b) output power profiles (c) dc bus voltage profiles (d) dc bus current profiles.

The 1,202 MW loss of generation in EI grid with the MTdc system connecting the asynchronous grids was simulated using EMT simulation; the corresponding results from the simulation are shown in Fig. C-12. From Fig. C-12(a), it can be noticed that the inclusion of advanced frequency control in the MTdc system improves the frequency response. Frequency response of the EI grid was improved by up to 25% in the settling point. In the event of generation loss in the EI grid, the support was provided to the EI grid by the MTdc substation terminals in the WI grid. This phenomenon can be clearly noticed in Figs. C-12(b) and (d). The dc voltages at all MTdc substation terminals were within the defined permissible limits, as seen in Fig C-12(c).

2,756 MW loss of generation in WI grid at 10 s

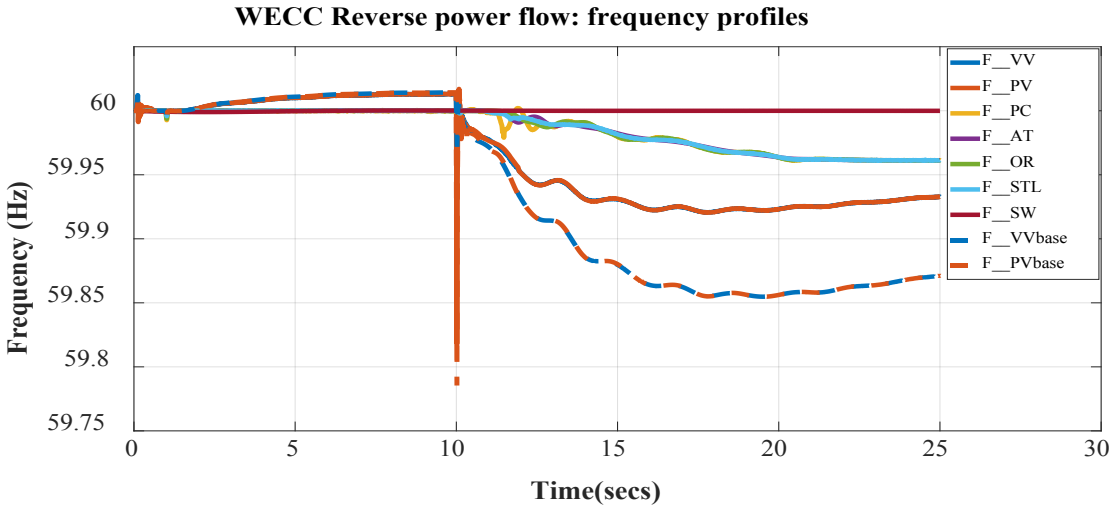

(a)

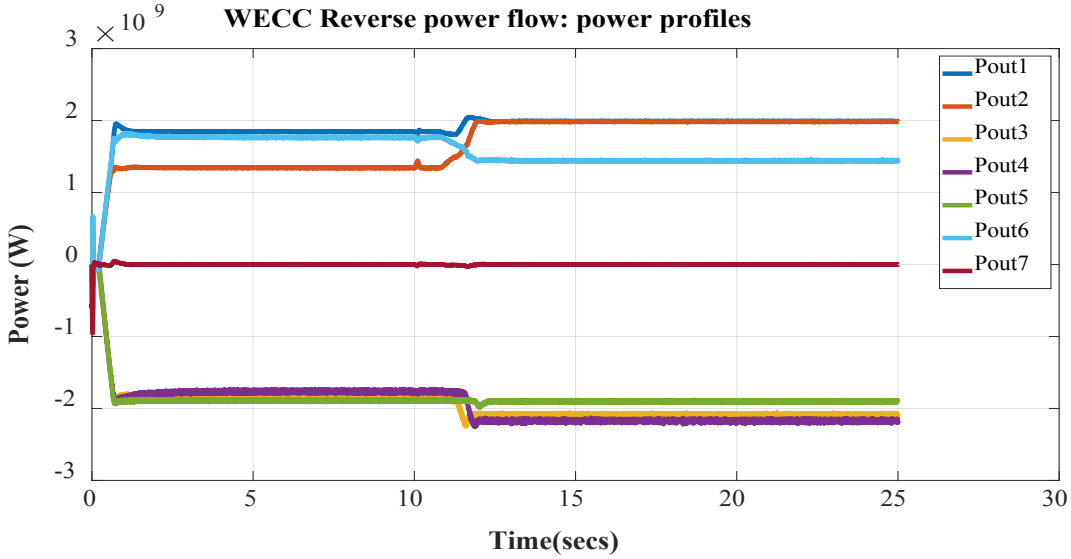

(b)

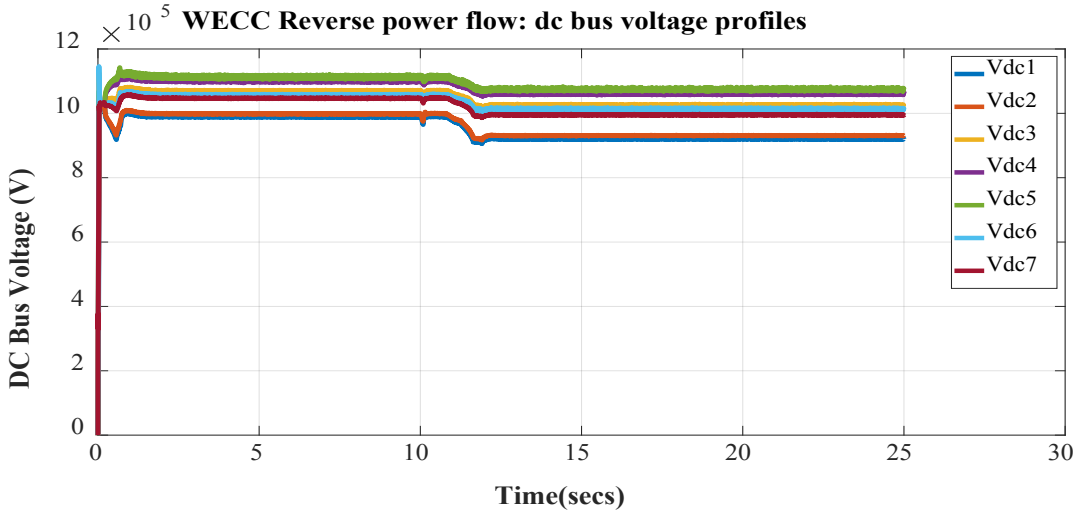

(c)

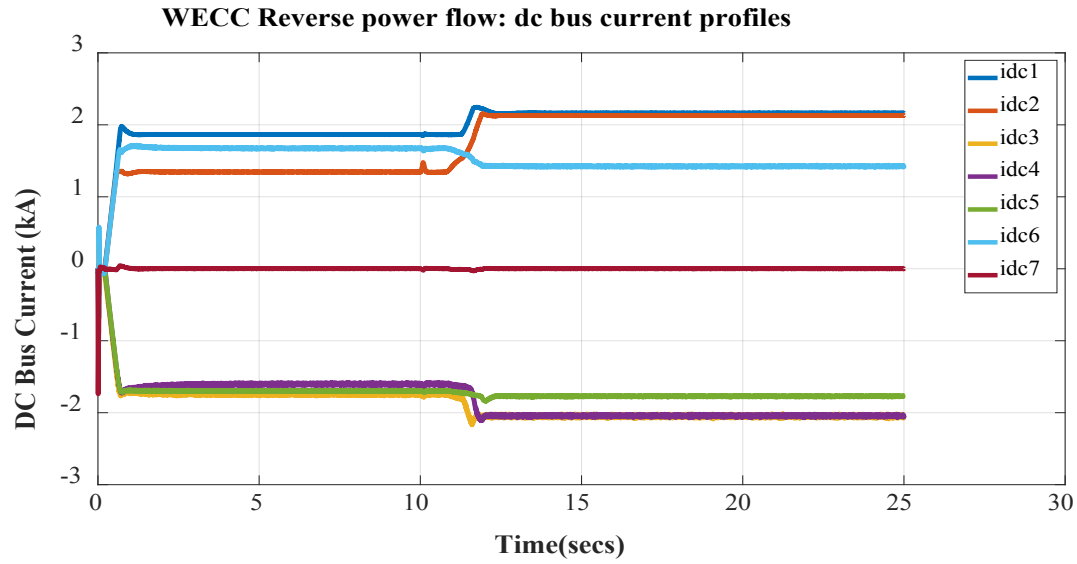

(d)

Figure Appendix C-13: Loss of generation in WI grid in reverse power flow case study: (a) frequency profiles with and without support from EI and ERCOT (b) output power profiles (c) dc bus voltage profiles (d) dc bus current profiles.

The 2,756 MW loss of generation in WI grid with the MTdc system connecting the asynchronous grids was simulated using EMT simulation; the corresponding results from the simulation are shown in Fig. C-13. From Fig. C-13(a), it can be noticed that the inclusion of advanced frequency control in the MTdc system improves the frequency response. Frequency response of the WI grid was improved by up to 46% in the nadir and 42% in the settling point. In the event of generation loss in the WI grid, the support was provided to the WI grid by the MTdc substation terminals in the EI grid. This phenomenon can be clearly noticed in Figs. C.13 (b) and (d). The dc voltages at all MTdc substation terminals were within the defined permissible limits, as seen in Fig C.13 (c).

Visualization Framework

The visualization framework to enable better understanding of the multiple objectives and constraints involved in the control of MTdc systems to provide primary frequency-sharing capability between asynchronous interconnections is shown in Fig. C-14. In Fig. C-14, the boundaries of the asynchronous interconnections (EI, ERCOT, and WI) are shown. The balancing areas within EI are also shown. The color of each region indicates the frequency variation in the corresponding region. The circles indicate the location of the modular multilevel convertor (MMC) substation in the MTdc system; the lines indicate the dc transmission lines. The size of each circle indicates the power processed at each MMC substation; the color of the circles indicates the dc-link voltage at each MMC substation. The color of the lines indicates the power processed by each dc transmission line. The results shown in the visualization framework visualize the 2,756 MW loss of generation in the WI grid and the support provided by the EI and ERCOT grids through the MTdc system. It may be noted that the constrained optimization solved to determine the optimal control method in the MTdc system had enabled higher power transferred at MMC substations in WI closer to the interconnection boundary to maximize the efficiency of power transfer. This is indicated by the larger circle representing the MMC substation closer to the interconnection boundary in WI. The stress on dc lines between EI and WI is higher, without violating the constraints imposed by their ratings. Similarly, the dc-link voltage at each MMC substation are within the imposed constraints, with the voltages of the MMC substations in WI closer to the lower constraints imposed on the dc-link voltages.

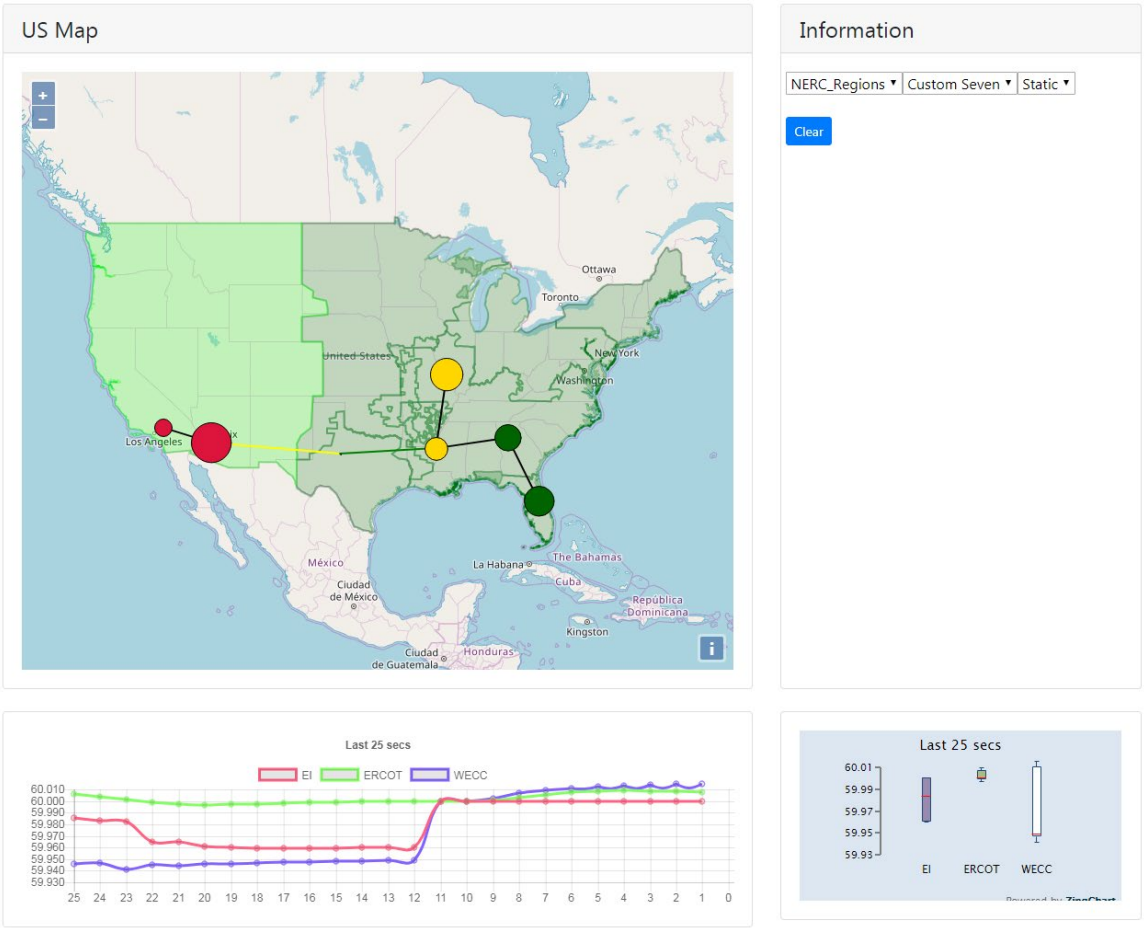

Figure Appendix C-14: Visualization framework to understand the behavior of MTdc systems as they provide the capability to share primary frequency reserves across multiple asynchronous interconnections in the United States.

Appendix D. Summary of Industry Advisory Board Response

A summary of the different responses received as part of the GMLC "HVDC Models & Methods" survey sent to the industry advisory board (IAB) members is provided in this section.

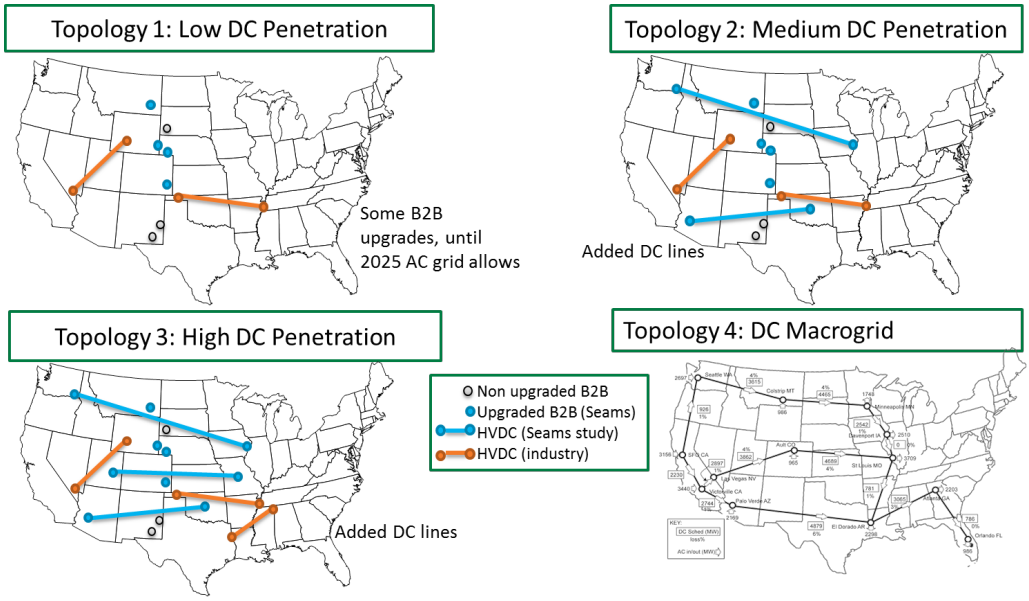

Figure Appendix D-1: Scenarios of dc penetration.

1. Four topologies are shown for connecting the Interconnections. We have labeled them Low dc Penetration, Medium dc Penetration, High dc Penetration, and Macrogrid. Within these topologies, do you think the dc lines that have been considered are sufficient, or can you add others?

While most responders believed that the lines considered in the topologies were sufficient, a few believed that there was potential for considering more dc lines. There were recommendations on methods to develop dc lines in each topology.

One of the methods recommended the development of co-optimized high-voltage direct current (HVdc) and extra high-voltage (EHV) alternating current (ac) flexible transmission plan to incorporate the potential >200 GW inverter-based resources. This plan may consider western interconnection (WI) – eastern interconnection (EI) ac synchronous operation, optimal seam boundary, and sub-HVdc transmission-distribution network to interconnect inverter resources. Moreover, it may define the future grid continent-wide EHV overlay options, define key corridors, and determine an appropriate voltage class for corridor upgrades (example >= 765 kV).

The other response advised the use of transmission adequacy and reliability assessment (TARA) for power flow analysis and combining TARA with production cost simulation to identify the optimal design of transmission expansions. It also recommended the use of PSCAD to evaluate the control system interactions of high-speed electronic controls like voltage-source converter (VSC)-HVdc. The other studies that were recommended in PSCAD include HVdc control coordination with static volt-ampere

reactive compensators, static synchronous compensators (STATCOMs), series capacitors, controllable series capacitors, storage in batteries in Type 4 wind and solar converters, water heater control, etc.

2. Do you think this is a sufficient set of interconnecting topologies to consider, or can you add others?

Some of the responses suggested additional interconnection topologies or methods to generate the topologies like the following:

- The segmentation of large interconnections (EI and WI) using HVdc back-to-back (B2B) lines to minimize area during major outages and blackouts.
- Loop the dc macrogrid into MAAC/Midwest (east of IL), leveraging the ac transmission and load centers there.
- Additional topologies could be generated based on co-optimized resource and transmission solutions.

In addition to only HVdc topologies, one of the responses advised to consider the solution of developing HVdc along with energy storage (possibly embedded within HVdc). This solution can be used to reduce area control error and reduce frequency events. It can also allow the markets to adjust continuously, rather than the 5-minute period now, due to the higher bandwidths supported by the power electronics (HVdc, solar/wind converters) and battery systems.

3. Among the four topologies shown above, which do you see as having the most value to the overall US grid? Please explain why you consider it to have the most value.

Majority of the responses supported the dc macrogrid topology (Topology 4) that allows the diversification of renewable energy sources to save overall energy costs. The other reason for selecting Topology 4 was the difficulty in upgrading the B2B dc ties located in remote areas beyond the current power transmitted. One of the responses supported Topology 2 due to the interconnect between pacific northwest and EI and to Las Vegas and Phoenix giving access to southern California load center. Another response supported the Topology 3 due to lower costs over Topology 4.

4. What do you consider to be the near-term benefits of the four topologies shown above?

A summary of the near-term benefits from the various dc topologies is provided here based on the responses. The benefits expected from the dc topologies include improved grid resiliency, reduced energy costs, access to renewable generation and other cheap generation to load centers, use of time zones to manage peak demands, fully controllable power flow to enhance system stability and security, and ability to provide benefits in the current business-as-usual policies design (Renewable Portfolio Standard enforced and no CO_2 costs) and the Comprehensive Energy Plan base designs (Renewable Portfolio Standard not enforced and includes CO_2 costs).

5. Are you aware of any additional ac reinforcements expected in the WECC or the EI ac models in the near future? If yes, do you know if it is possible for the project team to have access to them or get the corresponding inputs?

The responses from utilities and regional transport organizations (RTOs) have referred to information in TEAC and PC (partially public) and listed other developments.

6. There are 70,000+ bus Eastern Interconnection (EI) and 20,000+ bus WECC grid models available for the year 2025/2026. These models are computationally expensive. In this project, lumped models and methods to reduce the size of such models are being looked at to represent the voltage and frequency dynamics at certain locations of interest. Do you have any suggestions on such lumped equivalent models of EI or WECC grid?

One of the responses suggested the use of methods used to develop the EI lumped model based on frequency measurements (available at http://fnetpublic.utk.edu/). The model considers scenarios in 2030, and not in 2025/2026. Another response suggested the reduction of models to the number of buses specified using generation-2 wind turbine models that replace the type 3 and 4 wind turbine models. However, benchmarking against full models was required. There were other suggestions to use RTO support to develop these models.

7. Would you be interested in using the lumped models developed in this project to represent the EI and WECC grid dynamics? If so, please explain some of the applications of such models.

The responses suggested the use of lumped models or methods used to develop the models to characterize inter-area oscillations and higher-level control benefits of HVdc, evaluate economic benefits, understand the value of some new technologies, create options to implement in a smaller case set, and assist in developing knowledge for system reduction within current models.

8. The team would like to validate the accuracy of the improved models and the performance of the proposed control strategies developed in this project. Are there any near-term HVdc projects where the models and control strategies can be evaluated or tested? If so, please provide further details on the project.

Some of the HVdc lines suggested to test the proposed models and control strategies include the clean line energy proposals (that were not yet concrete), Southern Cross HVdc Classic, and other lines suggested in WECC HVdc modeling group planning studies.

9. The recent developments in HVdc technologies have included the development of efficient Voltage-Source Converters (VSCs) and Multi-Terminal dc (MTdc) systems. Are you aware of any further advances that the team should be aware of?

One of the recent developments was the increased capacity of VSCs, with the capability to connect to ±640 kV dc and process 3,000 MW. Another development was the ongoing research/development of meshed dc networks (or, dc grids) and MTdc systems. Based on these developments, there was a need to research the economical interconnection of 100s GW of inverter-based resources at transmission voltages (using hybrid HVdc and ac transmission grids).

10. MTdc system has been successfully built with as many as 5 terminals in the Zhoushan MTdc project. It is being planned or developed with 7 and 12 terminals in the Zhangbei project and Atlantic Wind Connection project, respectively. In this project, up to 6 terminals of MTdc is considered, with possible expansion to more terminals of the Macrogrid topology shown in the figure above. Do you sense that there is some limit to the number of terminals? If so, please explain.

Most of the responses suggested that there were no limits to the number of terminals in MTdc systems (especially, with the use of dc circuit breakers), except when dictated by reliability and probability of loss of load conditions.

Another suggestion recommended that lower EHV transmission lines (<230 kV) may be transformed to HVdc distribution grid to efficiently control inverter-based resources and loads (examples include renewable wind, solar, battery storage, transportation network, micro-grids) injection to the existing EHV ac and HVdc infrastructure. The existing EHV ac/HVdc infrastructure could be transformed to transport the dc grid energy to large load centers across the continent and fully take advantage of the rich energy resource and load diversity.

11. What problems do you anticipate in the power system with greater penetration of fast-switching power electronics like VSCs? For the identified problems, will high-fidelity detailed component models help identify and bound the problems?

Most responses suggested that high-fidelity models of VSCs could help with studying control interaction issues, sub or super-synchronous resonance issues, voltage control problems, and voltage droop tuning or sub-synchronous control interaction (SSCI) oscillations.

12. What problems do you anticipate in the power system because of faster dynamics from power electronics? If you anticipate problems, do you think high-fidelity detailed component models would help identify and bound the problems?

One of the responses suggested that the HVdc system full power responses need to be scheduled to controlled ramps rather than ramp rates faster or slower than system response. The control of HVdc systems need to be coordinated with other equipment controls with changes in system response.

13. Simulation of both electromagnetic and electromechanical transients was being considered in our analysis of the proposed ac/dc power systems to understand the bounds on the faster dynamics of power electronics and high-penetration of power electronics. Do you have any comments from previous experience of such simulations? If so, please explain your thoughts.

Most responses suggested that hybrid simulation can reduce computational burden. One of the users of hybrid simulation has setup the system in a parallel computing setup. This setup was used to study detailed sub-networks with weak ac transmission grids (with wind resources) in PSCAD and the remaining network in PSSe.

14. What grid services can be expected from power electronic systems like VSCs?

A summary of the grid services expected from VSCs include the following (based on the responses): (i) real and reactive power control, (ii) voltage control, (iii) frequency control, (iv) black start, (iv) power modulation to damp oscillations similar to power system stabilizers, (v) integration into weak systems, (vi) four-quadrant controllability, (vii) possible continuous control of power systems that redefine "services".

15. There have been recent developments in emulating power electronic systems (like VSCs) as synchronous generators or controlled transmission lines (like in Mackinac Back-to-Back system). Do you have any comments on advanced control benefits that could be obtained from the faster dynamics afforded by VSCs?

One of the responses suggested to consider the Power Systems Engineering Research Center (PSERC) Systems project on "Stability, Protection and Control of Systems with High Penetration of Converter Interfaced Generation" that shows controls exists for 100% inverter-based generation schemes. Coordination with these control-settings and any HVdc transmission could be investigated.

16. The economic benefits arising from the improvements in ac system dynamics afforded by HVdc and the faster switching VSCs are being studied in this project (like frequency response and voltage regulation). Do you any comments on the methods to quantify these benefits or other benefits that need to be studied?

One of the suggestions was to run PLEXOS at shorter periods than an hour. The shorter period studies compared to the hourly study results can be differenced to identify potential values. Another response asked if economic benefits from whole-life expectancy (say 30 years) was being evaluated in this project.

17. What are your interests or take-aways expected from this project?

The various take-aways highlighted from this project, based on the responses, include:

- VSC HVdc technology could be a key transmission technology for national or regional grids in the US.
- Different set of validated models and benefits of integrated ac-dc system.
- Better practical modeling of HVdc system in established simulation tools (PSSe).
- Impact of larger penetration of dc lines on the system as of today.
- Behavior of the system interconnected largely through inverters, under different circumstances.
- Move modeling towards expanded robust macro grid that captures as much value as possible and improves reliability.

18. Any additional comments?

One of the additional comments suggested to consider conversion of ac lines to dc to increase capacity on existing lines, especially with many utilities actively considering it.

Another comment summarized some of the issues involved with higher penetration of power electronics. The addition of power electronics to the power system brings on the possibility of introducing more harmonics to the system. Increasing harmonics causes increased current flow in transformers which causes them to wear out prematurely. K-factor transformers were not commonly in use in the transmission system.

Some of the other comments include:

- Work with industry and use annual planning processes to increase study efficiency.
- Implement modeling that advances into the industry planning processes.
- Development of long-term plan for future studies that cannot be funded with budget estimates and time estimates.
- Augment the SEAM and NARIS studies by coordinating studies that provide continuous development.

http://gridmodernization.labworks.org/